# Insights into Mechanisms of Amyloid Toxicity: Molecular Dynamics Simulations of the Amyloid β-peptide (Aβ) and Islet Amyloid Polypeptide (IAPP)

Anne Michael Brown

Dissertation submitted to the Faculty of the Virginia Polytechnic Institute and State University in partial fulfillment of the requirements for the degree of

Doctor of Philosophy
In
Biochemistry

David R. Bevan, Chair
Florian D. Schubot
Robert H. White
Bin Xu

March 17, 2016
Blacksburg, VA

Keywords: amyloid proteins, amyloid β-peptide (Aβ), islet amyloid polypeptide (IAPP), peptide-membrane interactions, molecular dynamics simulations

# Insights into Mechanisms of Amyloid Toxicity:

# Molecular Dynamics Simulations of the Amyloid β-peptide (Aβ) and Islet Amyloid Polypeptide (IAPP)

Anne Michael Brown

ACADEMIC ABSTRACT

Aggregation of proteins into amyloid deposits is a common feature among dozens of diseases. Two such diseases that feature amyloid deposits are Alzheimer's disease (AD) and type 2 diabetes (T2D). AD toxicity has been associated with the aggregation and accumulation of the amyloid β-peptide (Aβ); Aβ exerts its toxic effects through interactions with neuronal cell membranes. A characteristic feature of T2D is the deposition of the islet amyloid polypeptide (IAPP) in the pancreatic islets of Langerhans. It is currently unknown if IAPP aggregation is a cause or consequence of T2D, but it does lead to β-cell dysfunction and death, exacerbating the effects of diabetes. Characterizing the fundamental interactions between both Aβ and IAPP with lipid membranes and in solution will give greater insight into mechanisms of toxicity exhibited by amyloid proteins. In this work, molecular dynamics (MD) simulations were used to study the secondary, tertiary, and quatnary structure of Aβ and IAPP, in addition to peptide-membrane interactions and membrane perturbation as independently caused by both peptides. Studies were conducted to address the following questions: (1) what influence do solution conditions and oxidation state have on monomeric Aβ; (2) how and in what way does monomeric Aβ interact with model lipid membranes and what role does sequence play on these peptide-membrane interactions; (3) can MD simulations be utilized to understand Aβ tetramer formation, rearrangement, and tetramer-membrane interactions; (4) how does IAP interact with model membranes and how does that vary from non-toxic (rat) IAPP peptide-membrane interactions. These studies led to conclusions that showed variance in lipid affinity and degree of perturbation as based on peptide sequence, in addition to insight into the type of perturbation caused to membranes by these amyloid peptides. Understanding the differences in peptide-membrane interactions of amyloidogenic and non-amyloidogenic (rat) peptides gave insight into the overall mechanism of amyloidogenicity, leading to the detection of specific amino acids essential in peptide-membrane perturbation. These residues can then be targeted for novel therapeutic design to attenuate the perturbation and potential cell death as caused by these peptides.

# Insights into Mechanisms of Amyloid Toxicity:

# Molecular Dynamics Simulations of the Amyloid β-peptide (Aβ) and Islet Amyloid Polypeptide (IAPP)

Anne Michael Brown

PUBLIC ABSTRACT

Aggregation of misfolded proteins into plaques is a common feature among dozens of diseases. Two such diseases that feature plaques of misfolded proteins are Alzheimer's disease (AD) and type 2 diabetes (T2D). AD toxicity has been associated with the aggregation and accumulation of the amyloid β-peptide (Aβ). T2D is exacerbated by is the deposition of the islet amyloid polypeptide (IAPP) in and around pancreatic cells. Peptide-membrane interactions have been hypothesized to be associated with neuronal (AD) and pancreatic cell death (T2D). By studying both peptides at the atomistic ($10^{-10}$ m) level, we can understand certain aspects relevant to their folding and interaction with membranes that will provide insight into their toxicity. The structure of these peptides is indicative of stage in the aggregation pathway and a measurable factor we are interested in studying for this work. The following work was performed to determine how and in what ways does Aβ and IAPP interact with various membranes that mimic the cellular environment in which it is causing cell death. In addition, the rat version of these peptides does not result in the disease state as observed in humans. The rat version of both peptides was also studied to compare against the human peptides to determine any difference in interactions with membranes that might cause differences observed in toxicity. The results of these studies showed that membrane composition influenced degree and depth of insertion of these peptides in the membrane. Cholesterol was found to attenuate the degree of membrane disruption. Understanding the differences in peptide-membrane interactions of amyloidogenic (human) and non-amyloidogenic (rat) peptides gave insight into the overall mechanism of these diseases, leading to the detection of specific amino acids essential in peptide-membrane perturbation. These residues can then be targeted for novel therapeutic design to attenuate the perturbation and potential cell death as caused by these peptides.

ACKNOWLEDGEMENTS

First and foremost, I owe my deepest gratitude to my mentor and advisor, Dr. David Bevan, for his support, invaluable guidance, and encouragement throughout my graduate career. He has afforded me numerous opportunities that have challenged me to expand my skill-set and base knowledge in areas of research, professional development, and teaching. With his direction, I developed an appreciation of protein structure-function relationships that will last my entire career. Finally, without his support and mentorship, I would have never developed the passion and enjoyment for working with undergraduate researchers nor have the breadth of experience and amount of feedback from teaching courses at the undergraduate and graduate level.

I would like to express great appreciation to all the members of my committee, Dr. Florian Schubot, Dr. Robert White, and Dr. Bin Xu. My development as a biochemist is largely attributed to their desire to constantly challenge me and provide insight from various perspectives. I thank Dr. Webster Santos for the opportunity to participate in new avenues of research and providing solid advice for pursuing future directions in drug design. I also wish to share my deepest appreciation for the advice and knowledge shared by Dr. Justin Lemkul. Thank you for setting the bar and challenging me to reach it.

I would be remiss if I did not mention the help and friendship provided by Nikki Lewis. Your input and perspective on my work has been invaluable. In addition, you have provided solid support as I learn the ropes of mentoring and working with undergraduates. Your dedication and desire to improve student experiences has profoundly influenced my future directions.

I thank all of my Graduate Teaching Scholar colleagues for their conversations and feedback on my own teaching practices. Our weekly meetings have been a wonderful part of my graduate career and I look forward to continued discussions on teaching experiences with this group.

I also thank my Center of Gerontology colleagues; especially Dr. Rosemary Bliezner and Dr. Shannon Jarrott, for welcoming me into their field, exposing me to an entirely different area of academia, and providing me with opportunities to fulfill my desire to help the aging population on multiple levels.

Finally, I wish to express my gratitude to my family and friends. Thank you for providing me with a network of support; I would be lost without you. To my parents, for supporting me on this journey. To Michael, for constantly pushing me to better myself and being my biggest cheerleader and constructive critic.

The presented work as been supported by the Virginia Tech College of Agriculture and Life Sciences Graduate-Teaching Scholars Fellowship. Computing resources on the Athena and BlueRidge supercomputers was provided by Advanced Research Computing at Virginia Tech.

# Table of Contents

# List of Figures

# List of Tables

# List of Abbreviations

| Abbreviation | Description |
|---|---|
| Aβ | amyloid β-peptide |
| $A\beta_{(40)}$ | 40-residue alloform of Aβ |
| $A\beta_{(42)}$ | 42-residue alloform of Aβ |
| $A\beta_{40}$-Met35 | reduced amyloid β-peptide |
| $A\beta_{40}$-Met35$^{ox}$ | oxidized amyloid β-peptide |
| AD | Alzheimer's disease |
| AFM | atomic force microscopy |
| APP | amyloid precursor protein |
| CPE | carboxypeptidase E |
| COM | center of mass |
| ER | endoplasmic reticulum |
| GM1 | ganglioside GM1 - galactosyl-*N*-acetylgalactosaminyl-(sialyl)-galactosylglucosylceramide |
| $HA\beta_{(42)}$ | human $A\beta_{(42)}$ |
| hIAPP | human islet amyloid polypeptide |
| IAPP | islet amyloid polypeptide |
| MD | molecular dynamics |
| MS | mass spectrometry |
| Met35 | methionine-35 |
| Met35$^{ox}$ | sulfoxide form of methionine-35 |
| NMR | nuclear magnetic resonance spectroscopy |
| PAM | Peptidylglycine alpha-amidating monooxygenase |
| PC1/3 | prohormone convertases 1/3 |
| PC2 | prohormone convertases 2 |
| PME | particle mesh Ewald |
| POPC | palmitoyloleoylphosphatidylcholine |
| POPE | palmitoyloleoylphosphatidylethanolamine |
| POPS | palmitoyloleoylphosphatidylserine |
| proIAPP | proislet amyloid polypeptide |

| | |
|---|---|
| PSM | palmitoylsphingomyelin |
| P-LINCS | parallel Linear Constraint Solver |
| RMSD | root-mean-square deviation |
| $RA\beta_{(42)}$ | rat $A\beta_{(42)}$ |
| rIAPP | rat islet amyloid polypeptide |
| SASA | solvent-accessible-surface area |
| TEM | transmission electron microscopy |

# Attributions

All chapters included in this dissertation document were written by the candidate. Dr. David Bevan served as primary research advisor and provided editorial comments and suggestions for improvement all manuscripts for publication. The specifics of author contributions are listed below by chapter. Each author's initials are used to specify which author contributed each part. Author names used are as follows:

Anne M. Brown (AMB)
David R. Bevan (DRB)
Justin A. Lemkul (JAL)
Nick Schuam (NS)

Chapter 2
AMB wrote this paper with input on content and corrections prior to publication from JAL and DRB. AMB performed a majority of the simulations and analysis, with NS performing initial simulations of oxidized Aβ. All authors collectively conceived the initial project idea and direction. AMB was responsible for submission of the completed manuscript and response to reviewers. This chapter has been published in Archives of Biochemistry and Biophysics

Chapter 3
AMB wrote this paper with input on content and corrections prior to publication from DRB. All authors collectively conceived the initial project idea and direction. AMB was responsible for submission of the completed manuscript and response to reviewers. This chapter is to be submitted to BBA Biomembranes.

Chapter 4
AMB performed all of the data collection, analysis, and prepared the manuscript with editorial support from DRB. All authors collectively conceived the initial project idea and direction. AMB is responsible for pending submission of the completed manuscript and response to reviewers. This chapter is to be submitted to Biophysical Journal.

Chapter 5

AMB performed all of the data collection, analysis, and prepared the manuscript with editorial support from DRB. All authors collectively conceived the initial project idea and direction. AMB is responsible for pending submission of the completed manuscript and response to reviewers.

# 1 Introduction

## 1.1 Amyloid Diseases

Typically, misfolded proteins are degraded by proteases or refolded by chaperone activity. Certain proteins (Table 1.1) are classified as amyloidogenic because they elude these processes and accumulate into insoluble protein aggregates over time [1, 2]. These amyloidogenic proteins form long, highly ordered β-sheet protein fibrils that are linked to incurable diseases [3]. While the amyloid insoluble fibrils typically exhibit low toxicity in the presence of cells [4], the soluble oligomeric forms of amyloidogenic proteins are extremely toxic, causing membrane disruption and ultimately cell death [2]. For the research described in this dissertation, focus is on the amyloidogenic peptide associated with Alzheimer's disease (AD), amyloid β-peptide (Aβ), and the peptide associated with Type 2 diabetes mellitus (T2D), islet amyloid polypeptide (IAPP).

**Table 1.1.** Diseases associated with amyloidogenic proteins

| Disease | Protein |
|---|---|
| Alzheimer's | amyloid β-peptide ( Aβ) |
| Atherosclerosis | apolipoprotein A1 |
| Dialysis-related amyloidosis | $\beta_2$microglobulin |
| Huntington's | huntingtin |
| Parkinson's | α-synuclein |
| Prolactinomas | prolactin (APro) |
| Rheumatoid arthritis | serum amyloid A |
| Transmissible spongiform encelphalopathy | $PrP^{Sc}$ |
| Type 2 diabetes mellitus | islet amyloid polypeptide (IAPP) |

### 1.1.1 Alzheimer's Disease

AD is the 6$^{th}$ leading cause of death in the United States and until recently was considered a normal part of the aging process [5]. AD is no longer considered a part of the normal aging process, but rather is classified as a disorder/disease given the severity and progression of symptoms as compared to "age-associated memory impairment" [6]. AD is a progressive, neurodegenerative disease that is characterized by memory and motor skill impairment,

dementia, increased aggressive behavior, decreased ability to communicate, weight loss, and susceptibility to infection [5]. These disease characteristics contribute to the overall mental and physical health decline of AD patients, ultimately resulting in death. AD typically affects individuals ages 65 and older, with one in nine individuals in the 65-75 age group and one in three individuals ages 85+ developing the disease [5]. With individuals living longer due to advances in health care and medicine, the average lifespan of individuals is increasing worldwide. Therefore, the incidence of the disease is expected to increase in coming years, with rates of individuals 65 and older tripling in the next 50 years [7].

Currently, the National Institute on Aging estimates that 5.2 million individuals in the United States have AD. Direct costs paid annually by Medicare and Medicaid for health care, long-term care, and hospice for people with AD and other associated dementias are projected to increase from $200 billion in 2015 to $1.1 trillion by 2050, making AD a critical challenge for future generations [5]. Worldwide, the Alzheimer's Association estimates that 36 million individuals are currently living with AD, with approximately 115 million expected to be diagnosed by 2050 [7, 8]. With over 65% of individuals suffering from AD living in low-to middle-income countries, there is a lack of awareness and understanding of AD [7, 8]. AD impacts patients and caregivers in a physical, psychological, and economic way, giving rise to a pressing need for increased understanding of disease progression and development of therapeutics. Current therapies, including the often-prescribed Aricept® (donepezil, Pfizer) and Namenda® (memantine, Forest), only temporarily suppress Alzheimer's disease symptoms. These drugs cause substantial side effects and do not stop the continual deterioration and eventual death of neurons [9]. AD is a fundamentally important problem to solve, requiring detailed insight into the origins of the disease in order to deal with the expected drastic increase in sufferers in the next forty years.

### 1.1.2 Type 2 Diabetes

Type 2 diabetes mellitus (T2D), classified as noninsulin-dependent diabetes, is a complex metabolic disorder drastically increasing in prevalence worldwide. T2D is diagnosed by the presence of high blood glucose levels caused by insulin resistance and eventually insufficient insulin production. Health problems related to diabetes include heart disease, stroke, hypertension, blindness, and kidney disease. Diabetes, including type 1 and type 2, is the seventh-leading cause of death in the United States, with 8.3% of the U.S. population diagnosed [10]. As of 2011, 285 million cases worldwide had been reported, equivalent to 6% of the world's population [11]. Direct and indirect costs in the United States, including medical costs, work loss, and disability associated with diabetes, reached approximately $245 billion in 2012 [10]. T2D is increasing rapidly due to an aging global population, a decrease in exercise, and an increase in obesity [10]. One element of T2D pathology is the death of β-cells, eventually decreasing overall insulin production and compounding the effects of insulin resistance [12]. Understanding how β-cell death occurs can lead to the development of therapeutic compounds that will ameliorate the compounded effects of insulin resistance and β-cell death. With the rate of diagnosis T2D increasing rapidly, there is a need to reduce β-cell death and maintain production of insulin to aid in long-term management of the disease.

## 1.2 The Amyloid Hypothesis of Alzheimer's Disease and Aβ

Hardy and Higgins first described and proposed what is now called the "amyloid hypothesis" of AD [13]. Hardy and Higgins based their hypothesis on the work of Masters *et al*., whose work described a protein known as $A_4$ to be identical to an aggregated peptide found in individuals with Down syndrome [14]. The connection between Down syndrome and Aβ is discussed in 1.2.1. During the same year, Wong *et al*. also published results on a peptide named "β-peptide", where immunohistochemical analysis was performed and showed the β-peptide presence in the neuronal tissue of AD and Down syndrome patients, but not in healthy individuals [14]. Utilizing their own work and the work of Masters *et al.* and Wong *et al.,* Hardy and Higgins hypothesized that deposition of the amyloid β-peptide (Aβ) in and around neuronal tissue was linked to the pathological events resulting in AD [15]. The naming for Aβ was a combination of the naming set forth by Masters *et al.* ($A_4$) and Wong *et al*. (β-peptide), resulting in the amyloid β-peptide (Aβ). Herein, Aβ has been considered the principal toxic species in AD, with other peptides such as Tau also contributing to the etiology of AD [16].

Another interesting aspect of Aβ is the dynamic nature of its structure and its structural relationship to the amyloidogenic pathway. Secondary structure changes within Aβ are a driving force for aggregation [17, 18] and the hydrophobic C-terminal region (residues 29–40) of Aβ is particularly important for Aβ oligomerization and the formation of higher-order aggregates in solution [19-21]. By studying Aβ in the presence of multiple environments (salt, pH, membrane, oxidation state), we can begin to understand the effect of these environmental factors on the secondary structure of Aβ and the amyloidogenic pathway in relationship to both the amyloid hypothesis and the etiology of AD.

### 1.2.1 Production and Function of Aβ

Aβ is produced after sequential proteolysis of the human amyloid precursor protein (APP) [22]. APP is a type I transmembrane protein with three predominant isoforms consisting of 695, 751, and 770 amino acids. These isoforms are expressed at varying levels in tissues throughout the body; however, the 695-residue isoform is predominantly expressed in neuronal cells [22]. Interestingly, the APP gene is located on chromosome 21, which is present in triplicate in Down syndrome. This additional copy of chromosome 21 and increased expression of APP in Down syndrome aids in explaining similarities between the AD phenotype and the Down syndrome phenotype as linked to excess Aβ production [23].

Sequential proteolysis by secretases (α- or β- and γ-secretase) is carried out as APP is trafficked through the endoplasmic reticulum (ER) and Golgi apparatus to the plasma membrane [24, 25]. During these cellular trafficking and cleavage events, production of an extracellular domain protein called sAPP (sAPPα or sAPPβ depending on secretase) and an APP intracellular protein domain (AICD) occurs [26]. The cleavage product sAPPα/β is considered essential given its function in synaptic development and cell differentiation [27, 28]. AICD has been suggested to act as a transcription factor, interacting with several DNA-binding domains [29].

β-secretase cleavage of APP results in multiple alloforms, varying in total residue numbers of, (38-43) of Aβ being produced, with the most prevalent alloforms containing 40 ($Aβ_{(40)}$) or 42 ($Aβ_{(42)}$) residues. The sequence of $Aβ_{(42)}$ is as follows:

$$DAEFRHDSGY_{10}EVHHQKLVFF_{20}AEDVGSNKGA_{30}IIGLMVGGVV_{40}IA_{42}$$

β-secretase activity is primarily carried out by the protease classified as β-site APP cleaving enzyme 1 (BACE-1) [30], located in the endosome and late *trans* Golgi [31, 32]. γ-secretase activity is largely attributed to protein complexes consisting of presenilin, nicastrin, APH-1, and PEN-2 [33]. A third secretase, α-secretase, can preclude β-secretase processing by cleaving APP in the middle of the Aβ sequence to create a non-amyloidogenic peptide, p3 [26]. P3 is considered to be an off-pathway product of amyloidogenesis as related to cleavage of APP and relevance to the etiology of AD [34].

The function of Aβ is unknown [35] but experimental studies propose that Aβ maintains metal ion homeostasis [36] and decreases synaptic activity to prevent excitotoxicity associated with seizures [37]. In addition, recent studies have hypothesized that Aβ functions as a part of the immune system by acting as an antimicrobial agent against numerous types of bacteria, including *Staphylococcus* and *Streptococcus* species [38]. This putative function of Aβ is particularly interesting, since antimicrobial peptides like polymyxin typically work by causing disruption of the cell membrane [39].

## 1.3 The Role of Islet Amyloid Polypeptide in Type 2 Diabetes

When first recognized in the early twentieth century, islet amyloids were not originally attributed to any pathological event related to T2D [40] and derived from a protein known as islet amyloid polypeptide (IAPP) [41]. Conflicting evidence currently questions if IAPP is a cause or consequence of β-cell dysfunction and death. However, it has been determined that there is a clear linkage of islet amyloids to T2D [42]. Experimental studies have focused on the fundamental mechanism by which human IAPP aggregates affect β-cells by membrane perturbation and how the aggregation process can be modulated by therapeutic intervention [43, 44].

IAPP is a regulatory peptide that contributes to glycemic control by acting locally in the islets to inhibit insulin and glucagon secretion and by binding to receptors in the brain to slow gastric emptying and provide satiety regulation [12, 45, 46]. Insulin and IAPP are co-secreted from β-cells, found in the pancreatic islets of Langerhans. IAPP is a 37-residue peptide that is cleaved from an 89-residue preproprotein, which contains a 22-residue signal peptide and a 67-residue proislet amyloid polypeptide (proIAPP) [47]. The signal peptide directs the preproprotein to the ER where it is cleaved. Subsequent cleavage of IAPP from proIAPP occurs in secretory vesicles. ProIAPP is processed by prohormone convertases 2 and 1/3 (PC2 and PC1/3), which are the same proteases that process proinsulin. PC1/3 cleaves IAPP at the N-terminus and PC2 cleaves at the C-terminus [48]. Following this cleavage event, carboxypeptidase E (CPE) removes a lysine and arginine at the C-terminus, exposing a glycine residue that is amidated. A disulfide bond is formed between two cysteine residues in the N-terminal region (Cys2 and Cys7), resulting in biologically active IAPP [42, 48]. With residues 20-29 (SNNFGAILSS) being classified as one of the most amyloidogenic sequences known, this residue section of IAPP is of particular interest in the proposed work. IAPP is natively unfolded in its monomeric state in solution and has helical characteristics in the presence of a membrane [42]. These structural elements of IAPP are essential in understanding the mechanistic details of IAPP toxicity.

## 1.4 The Importance of Protein-Membrane Interactions

The disruption of the plasma membrane by amyloidogenic peptides has been identified as a principal cause of toxicity in amyloid diseases [1, 49]. Understanding the mechanism by which Aβ and IAPP compromise the structural integrity of the membrane and promote ion leakage is crucial to understanding how AD and T2D progress. The structure and aggregation state of human IAPP and human Aβ have been found to be critical in the mechanism of toxicity and interaction with phospholipid membranes [50, 51].

It has been proposed that Aβ inserts into the lipid bilayer, leading to membrane thinning, increased membrane conductance, calcium influx, and the triggering of apoptoptic pathways in neuronal cells [51][52]. Electron microscopy studies show that oligomeric IAPP disrupts membranes in three possible ways: the formation of transmembrane pores, nonspecific ion permeation, or membrane fragmentation through the growth of amyloid fibrils on the membrane surface [50, 51]. While hypothesis of mechanisms of membrane interaction vary for both Aβ and IAPP, fibrillation of hIAPP and Aβ is known to be accelerated in the presence of anionic membranes *in vitro* [53]. Herein, understanding the degree and type of binding and insertion of Aβ or IAPP to multiple membranes is of interest, in addition to studying the effect of the membrane environment on Aβ or IAPP. Are there similar mechanisms of insertion and membrane perturbation as caused by both Aβ and IAPP?

Currently, the mechanism of toxicity within a membrane environment is unclear for both peptides. Interestingly, the rat forms of Aβ and IAPP do not exhibit the toxicity seen with the human forms. There are only three and six amino acid differences between the homologous human and rat forms of Aβ and IAPP, respectively. These residue differences may provide insight into the reduced aggregation, membrane perturbation, and cell death that is seen in rats [12, 54, 55]. Comparing the membrane interactions and binding events of human Aβ, hIAPP, rat Aβ and rat IAPP (rIAPP) will lead to a greater understanding of the mechanism and specific residue interactions that lead to membrane perturbation and cell death.

## 1.5 Role of MD Simulations in Studying Amyloidogenic Peptides

Studying the interactions of Aβ and IAPP in solution and in the membrane environment experimentally is challenging. Aβ and IAPP are prone to rapid aggregation in an aqueous solution, a process that interferes with techniques such as NMR, circular dichroism, and neutron and x-ray diffraction [12, 43, 53, 56, 57]. Typically, organic solvents are added to the solution to aid in peptide solubilization; however, these solvents may also affect interactions between the peptide and the membrane [58-61]. Thus, it is difficult to experimentally characterize the interactions of Aβ and IAPP with the membrane, as a monomer, or as a low-molecular weight oligomer, leading to uncertainties about amyloidogenicity as caused by these two peptides.

Secondary structure is indicative of aggregation potential for both Aβ and IAPP, which can provide insight into the influence of solution conditions, oxidation state, and a membrane environment on secondary structure evolution given the microenvironment. Understanding the influence of microenviroments on both peptides can provide insight into on-pathway aggregation events and relate to the toxicity manifested by these two peptides. MD simulations have been widely used to study peptide-membrane interactions, ultimately producing insights with

atomistic resolution and producing mechanistic details to explain experimental results [62-65]. In addition, MD simulations add a level of detail and control on peptide species studied (monomer, tetramer, etc.) and can provide insight into the degree and type of membrane perturbation as caused by peptide binding. The most relevant parameters that MD can examine are the conformations and the orientations of peptides and lipid membrane properties such as order, diffusion, packing, and thickness. These parameters, taken together, can then aid in understanding the extent of perturbation as linked to toxicity as caused by Aβ to neuronal or β-cells. Currently, there are only four studies that have simulated IAPP in the presence of a membrane [52, 53, 66, 67]; however, none of the simulations have been performed using a physiologically representative membrane. Aβ-membrane simulations have also been successful in providing insight into the underlying molecular mechanism of membrane perturbation [63, 65]. Prior to completion of this dissertation, no all-atom MD studies had been performed on a peptide unit larger than a dimer in the presence of a model membrane.

## 1.6 MD System Construction and Validation

All simulations were conducted with the freely available GROMACS package, which at the start of simulation construction was version 4.6.1 [68, 69]. Peptide force field parameters used in all cases came from the GROMOS96 53A6 parameter set [70], while force field parameters of Berger *et al*. were applied to all lipids [71]. The GROMOS96 53A6 force field was selected given its ability to adequately simulate monomeric Aβ relative to experimental information [72, 73]. Given that a long term goal of this work was to compare in-solution and peptide-membrane simulations of Aβ and IAPP, the GROMOS96 53A6 force field was used for all simulations presented to allow for this comparison. A physiologically representative environment was utilized in all simulations by maintaining temperature for all systems at 310 K using the Nosé-Hoover thermostat [74, 75] and regulating pressure at 1 bar with the Parrinello-Rahman barostat [76, 77]. Water was represented by the SPC model [78] and the aqueous phase included 150 mM NaCl in all simulations expect for those in chapter 2, where the influence of salt concentration on the secondary structure of Aβ was tested. Long-range electrostatics were calculated with the smooth Particle Mesh Ewald (PME) method [79, 80]. Three-dimensional periodic boundary conditions were applied to all simulations. Analysis of simulations was conducted using programs incorporated in the GROMACS package or by software written in-house.

For the presented work, determination of which alloform of Aβ to use was essential. Experimental studies commonly use either the 40-residue alloform ($A\beta_{40}$) or the 42-residue alloform ($A\beta_{42}$) of Aβ. After an extensive literature review, comparable amounts of literature on both $A\beta_{42}$ and $A\beta_{40}$ were found. $A\beta_{42}$, classified as the "more toxic" alloform of Aβ, was chosen as the peptide to be used in the peptide-membrane simulations. In the diseased state, both $A\beta_{40}$ and $A\beta_{42}$ accumulate in the brain, with $A\beta_{42}$ being present at a 9:1 ratio with respect to $A\beta_{40}$ [81, 82]. Oligomer formation has been experimentally reported to be initiated by plasma membrane-bound $A\beta_{42}$ [82]. The prevalence of $A\beta_{42}$ in the AD brain makes $A\beta_{42}$ an appropriate choice for modeling the toxic effects of Aβ on the membrane [82, 83], in addition understanding the oligomerization of this peptide. In addition to membrane-bound $A\beta_{42}$ promoting the formation of oligomeric and fibril forms of $A\beta_{42}$, it is reasonable to hypothesize that when monomeric $A\beta_{42}$ inserts into the membrane to facilitate plaque formation, it also disrupts and compromises the integrity of the membrane. This insertion event is thought to be the primary mechanism by which

$A\beta_{42}$ causes neuronal cell death [4]. For the Aβ oxidation and solution condition study, the $A\beta_{40}$ version was utilized given the corresponding experimental work.

There is only one relevant full-length alloform of IAPP and an NMR-derived structure of the peptide determined in a neutral pH will be used for this study [60]. This structure was amidated at the C-terminus and all disulfide bonds were retained during simulations to mimic the biologically active form of IAPP.

In all peptide-membrane simulations conducted, the following lipids are found in eukaryotic plasma membranes were utilized as indicated in the individual chapters: palymitoyloleoylphosphatidylcholine (POPC), palymitoyloleoylphosphatidylserine (POPS), palymitoyloleoylphosphatidylethanolamine (POPE), a lipid raft composed of POPC, palmitoylsphingomyelin (PSM), and cholesterol, and the raft with galactosyl-*N*-acetylgalactosaminyl-(sialyl)-galactosylglucosylceramide (GM1). In the simulations, the peptide center of mass (COM) was placed 3 nanometers (nm) away from the model membrane in order to produce an unbiased starting point for the simulations. Placing the peptide 3 nm away from the model membrane ensures nonbonded interactions are not influencing the dynamics of the peptide at the start of the simulation. Peptide binding to the membrane was defined as the peptide inserting into the phospholipid head group and glycerol region of the membrane. Peptide-membrane binding was further characterized by the number and types of interactions between the phospholipid moieties (headgroups, glycerol esters, acyl chains) and the peptide. Depth of insertion into the membrane was monitored over time by measuring the COM distance between the peptide and the core of the membrane or phospholipid headgroups, as appropriate. The depth of insertion was characterized by describing the sidechain residues responsible for binding interactions.

## 1.7 Organization of the dissertation

This dissertation is compiled as a collection of a published peer-reviewed paper (Chapter 2), two submitted manuscripts (Chapter 3, Chapter 4), and a manuscript in preparation for submission (Chapters 5). Chapter 1 serves as a general introduction to amyloid proteins, with specific focus on Aβ and IAPP as relevant to AD and T2D. Chapter 1 also provides background information on peptide-membrane interactions and the general set-up of MD simulations performed for this dissertation work. Chapter 2 is a published paper on the effects of methionine oxidation and solution conditions on the structure and dynamics of Aβ, giving insight into the role of these conditions on the secondary structure of the peptide. The citation for Chapter 2 is provided on the title page. Chapter 3 is a submitted article detailing simulations that examined human Aβ-peptide membrane interactions in the presence of five membrane compositions to determine the role of lipid type on Aβ membrane interactions. In addition, simulations with the rat Aβ-peptide in the presence of the same membranes were performed to determine the influence of sequence on peptide-membrane interactions. Chapter 4 is a manuscript prepared for submission that details the formation of an Aβ tetramer and subsequent Aβ-tetramer membrane interactions. Chapter 5 is a manuscript prepared for submission that details human and rat IAPP-membrane interactions in order to determine the influence of sequence on secondary structure and degree and type of membrane perturbation caused by IAPP-membrane interactions. Chapter 6 contains concluding remarks that tie all of the chapters together and address goals of the dissertation in determining the influence of solution conditions on amyloid proteins and subsequent peptide-membrane

interactions. Chapter 6 is followed by the bibliography of references cited. The dissertation ends with appendices that contain executive summaries of other publications completed during the PhD process and parameter files used in MD simulations.

# 2 Simulations of Monomeric Amyloid β-Peptide (1-40) with Varying Solution Conditions and Oxidation State of Met35: Implications for Aggregation

Anne M. Brown[1], Justin A. Lemkul [1], Nicholas Schaum[1], and David R. Bevan[1]

[1]Department of Biochemistry (0308), Virginia Polytechnic Institute and State University, 201 Engel Hall, Blacksburg, VA 24061.



**Attribution:** AMB wrote this paper with input on content and corrections prior to publication from JAL and DRB. AMB performed a majority of the simulations and analysis, with NS performing initial simulations of oxidized Aβ. All authors collectively conceived the initial project idea and direction. AMB was responsible for submission of the completed manuscript and response to reviewers.

Citation: Brown, A. M., J. A. Lemkul, N. Schaum and D. R. Bevan (2014). "Simulations of monomeric amyloid β-peptide (1–40) with varying solution conditions and oxidation state of Met35: Implications for aggregation." Archives of Biochemistry and Biophysics 545: 44-52.

## 2.1 Abstract

The amyloid β-peptide (Aβ) is a 40-42 residue peptide that is the principal toxic species in Alzheimer's disease (AD). The oxidation of methionine-35 (Met35) to the sulfoxide form ($Met35^{ox}$) has been identified as potential modulator of Aβ aggregation. The role $Met35^{ox}$ plays in Aβ neurotoxicity differs among experimental studies, which may be due to inconsistent solution conditions (pH, buffer, temperature). We applied atomistic molecular dynamics (MD) simulations as a means to probe the dynamics of the monomeric 40-residue alloform of Aβ ($Aβ_{40}$) containing Met35 or $Met35^{ox}$ in an effort to resolve the conflicting experimental results. We found that Met35 oxidation decreases the β-strand content of the C-terminal hydrophobic region (residues 29-40), with a specific effect on the secondary structure of residues 33-35, thus potentially impeding aggregation. Further, there is an important interplay between oxidation state and solution conditions, with pH and salt concentration augmenting the effects of oxidation. The results presented here serve to rationalize the conflicting results seen in experimental studies and provide a fundamental biophysical characterization of monomeric $Aβ_{40}$ dynamics in both reduced and oxidized forms, providing insight into the biochemical mechanism of $Aβ_{40}$ and oxidative stress related to AD.

## 2.2 Introduction

Alzheimer's disease (AD) is a progressive, neurodegenerative disease that is characterized by memory and motor skill impairment, dementia, increased aggressive behavior, decreased ability to communicate, weight loss, and increased susceptibility to infection [5]. These disease characteristics contribute to the overall mental and physical health decline of AD patients, ultimately resulting in death. Currently, the National Institute on Aging estimates that 5.2 million individuals in the United States have AD [5]. AD has been associated with the aggregation and accumulation of the amyloid β-peptide (Aβ) in neural tissue, with Aβ believed to be the principal toxic species of AD [13]. Aβ is cleaved from a larger, transmembrane protein known as the amyloid precursor protein (APP) [26, 84]. Multiple alloforms of Aβ are produced, ranging in length from 38 – 43 residues, with the most common alloforms containing 40 ($A\beta_{40}$) or 42 ($A\beta_{42}$) residues.

Currently, there are two principal hypotheses that aim to explain the role of Aβ in AD. While AD is a complex disease, the prevailing theory, the "amyloid hypothesis" [13], states that Aβ oligomers are the primary toxic entity in AD [4]. These oligomers exert toxicity via interactions with the cell membrane [49], which lead to increased membrane conductance and calcium influx, ultimately triggering apoptotic pathways in the neuronal cell [85]. The "oxidation/inflammation hypothesis", states that AD occurs due to increased oxidative stress from age-dependent increases in amounts of $Cu^{2+}$, $Fe^{2+}$, and $Hg^{2+}$ in the brain [86-90], which catalyze reactions that produce free radicals that are toxic to neural cells. The accumulation of metals and concomitant increase in free radicals and decrease in antioxidant presence lead to a harmful, highly oxidative environment in the AD brain. In addition, autopsy studies of AD brains show extensive oxidative damage, as determined by protein oxidation, lipid peroxidation, and advanced glycation end products [91-95]. It is in the scope of this study to understand the effects of oxidation of monomeric $A\beta_{40}$ to better understand how this oxidation contributes to either or both of these hypotheses.

Several studies suggest that the methionine residue in Aβ (Met35) is prone to oxidation and contributes to AD oxidative stress and neurotoxicity [91, 96-98]. Met35 can undergo 2-electron oxidation to form methionine sulfoxide ($Met35^{ox}$) or 4-electron oxidation to form methionine sulfone [96]. In addition, it has been proposed that the close proximity of the carbonyl backbone group of isoleucine-31 (Ile31) relative to the sulfur of Met35, can lead to the formation of an S-O bonded radical cation intermediate [99]. Moreover, theoretical calculations have shown that a free radical on the sulfur atom of Met35 could attack glycine 33 (Gly33) on an adjacent peptide, creating a free radical on Gly33 that would form a peroxyl free radical upon binding oxygen [98]. This peroxyl radical formation could contribute to neurotoxicity and lipid peroxidation that is seen in autopsied AD brains.

The oxidation of Met35 to $Met35^{ox}$ has been reported to alter the rate of Aβ aggregation, but the outcomes of these studies disagree. Some groups report that aggregation is attenuated in the presence of oxidized Aβ [61, 100-102], while others report an increase in aggregation [103] or free radical production following oxidation of Met35 [104]. An NMR study by Hou et al. established that oxidation impedes Aβ aggregation and fibrillation, and their results suggested a reduced propensity for β-strand structure in Aβ [101]. Conversely, the work of Snyder et al.

found that oxidation of Met35 increased the rate of Aβ aggregation [103]. In addition, a study by Kou et al. found that post-mortem AD plaques contain approximately 10-50% oxidized Aβ [105]. The Kou et al. study and other studies on AD plaque composition have led to the assumption that oxidation leads to aggregation [105-107]; however, it has not yet been determined if oxidation occurs before or after plaque formation. Manipulation of solution conditions is commonplace when working with Aβ, given its propensity to aggregate. The conflicting results of the experimental work on Aβ-Met35$^{ox}$ may be attributed to differences in experimental conditions used to perform these studies, including pH, temperature, buffer, use of organic solvents and/or detergents, and peptide length ($A\beta_{40}$ or $A\beta_{42}$).

In the current study, we performed molecular dynamics (MD) simulations to provide atomistic insight into the structural dynamics of monomeric Aβ in varying solution conditions and oxidation state to determine the main driving force for potential aggregation and to resolve discrepancies in the literature. Secondary structure changes within Aβ are the driving force for aggregation [17, 18] and the hydrophobic C-terminal region (residues 29-40) of Aβ is particularly important for Aβ oligomerization and the formation of higher-order aggregates in solution [19-21]. A transition from helix to β-sheet in this region is believed to be necessary for aggregation, given that fibrils are characterized by parallel, in-register β-strands [17, 108]. Monomeric Aβ enriched in β-strand structure typically undergoes rapid aggregation, whereas random coil forms of Aβ aggregate more slowly [101, 108, 109]. Thus, it was of particular emphasis in this study to understand secondary structure changes of Aβ and relate these changes to varying experimental conditions that have been used. The present work is the first to systematically analyze the effects of both pH and salt concentration on the structural transition of monomeric Aβ. This study provides insight into the dynamic structure of monomeric Aβ in a physiologically relevant environment, one that is devoid of organic solvents and detergents that can influence secondary structure and thus aggregation.

## 2.3 Methods

### 2.3.1 System Construction

The coordinates of Aβ were taken from PDB entry 1BA6, a solution NMR structure for monomeric, oxidized $A\beta_{40}$ ($A\beta_{40}$-Met35$^{ox}$) [102]. Reduced $A\beta_{40}$ ($A\beta_{40}$-Met35) was produced by removing the oxygen from the sulfoxide moiety of Met35$^{ox}$ of 1BA6. The influence of different pH values was modeled by protonating all titratable groups according to their predominant forms at either pH 5 or pH 7. The only difference between these two pH values occurs with respect to histidine residues ($pK_a$ = 6.5), which can either bear no charge or a net +1 charge, depending on the pH of the surrounding medium. There are three histidine residues in the $A\beta_{40}$ sequence, at positions 6, 13, and 14. At pH 5, these histidine residues were treated as fully protonated (net +1 charge on each), while at pH 7 they were protonated only on the ε-nitrogen in the imidazole ring (net charge of zero on each). $A\beta_{40}$ has 3 Glu and 3 Asp residues, which, based on canonical pKa values, remain charged (-1) at both pH 5 and 7. We note that $pK_a$ values in $A\beta_{40}$ may differ from canonical values, but experiments have only established $pK_a$ values for the $A\beta_{1-28}$ fragment, not the full-length peptide [110]. Given that fact, as well as the lack of $pK_a$ information about $A\beta_{40}$-Met35$^{ox}$, we built our models based on canonical $pK_a$ values in order to concentrate on more defined differences. While experiments examining the effect of oxidation of Met35 on Aβ were

performed at pH 4 [102], simulating Aβ at pH 4 is difficult due to the mixture of protonated and deprotonated sidechain forms of Asp and Glu. Therefore, we assigned protonation states according to dominant forms at pH 5, a condition that approximates the pH 4 experiments. pH 5 is also significant in that it is the pH at which Aβ aggregates the most rapidly [111, 112],so our simulations serve as a useful model of experiments conducted at pH 4 and 5. $A\beta_{40}$ termini were protonated such that the C-terminal carboxylate group bore a charge of -1 and the N-terminal amine had a charge of +1. Thus, in our simulations, $A\beta_{40}$ and $A\beta_{40}$-Met35$^{ox}$ bore a -3 charge at pH 7 and no net charge at pH 5. All protein parameters were assigned from the GROMOS96 53A6 force field [70]. Charges for the Met35$^{ox}$ sulfoxide moiety of the sidechain were taken from dimethyl sulfoxide [113], as shown in Figure 2.1.

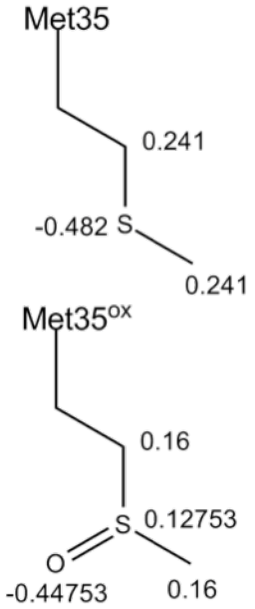


**Figure 2.1.** Diagram of Met35 and Met35$^{ox}$ sidechains showing the charges on atoms of the thioether and sulfoxide moieties.

Systems were constructed in the following way. Reduced and oxidized $A\beta_{40}$ were centered in a dodecahedral box with a minimum solute-box distance of 1.0 nm, which was subsequently solvated with SPC water [114]. $Na^+$ counterions were added to balance the net charge of Aβ (–3 at pH 7), while no counterions were added in the case of pH 5 systems since Aβ carries no net charge at this pH value, in accordance with our method of assigning charges to side chain residues. These systems will be referred to as containing "0 mM NaCl," otherwise representative of minimal or no salt present. For systems denoted "150 mM NaCl," additional $Na^+$ and $Cl^-$ ions were added for a final concentration of approximately 150 mM NaCl, including any counterions already present. The following condition sets were tested for reduced and oxidized $A\beta_{40}$: 0 mM NaCl-pH 5, 150 mM NaCl-pH 5, 0 mM NaCl-pH 7, and 150 mM NaCl-pH 7. Five replicates were performed for each condition set for reduced and oxidized $A\beta_{40}$, resulting in 40 total simulations.

## 2.3.2 MD Simulations

After system construction, energy minimization was performed using the steepest descent method and equilibration was performed in two steps, NVT and NPT. All simulations were

performed using the GROMACS software package, version 4.5.3 [68, 115]. During equilibration, position restraints were imposed on all protein heavy atoms. NVT was first applied to the system for 100 ps and utilized the Berendsen weak coupling method [116] to maintain temperature at 310 K. NPT was then applied to the system for 100 ps, using the Nosé-Hoover thermostat [74, 75] and Parrinello-Rahman barostat [76, 77] to maintain temperature (310 K), and pressure (1 bar), respectively.

All MD simulations employed three-dimensional periodic boundary conditions. All bond lengths were constrained using P-LINCS [117], allowing an integration time step of 2 fs. A short-range cutoff of 1.4 nm was applied to all nonbonded interactions, and long-range electrostatic interactions were determined with the smooth particle mesh Ewald (PME) method [79, 80] using cubic interpolation and a Fourier grid spacing of 0.16 nm. Simulations were then allowed to run until backbone root-mean-square deviation (RMSD) and peptide secondary structure stabilized for 100 ns, as determined by block averaging. These criteria were the first indicator of convergence, which is explored more thoroughly below. Simulation times ranged from 200 to 375 ns, and each simulation condition set contained 5 independent trajectories, initiated with different random starting velocities at the outset of NVT. Analysis was conducted using programs in the GROMACS package or scripts written in-house. Secondary structure was determined according to the DSSP algorithm [118]. Backbone RMSD clustering was performed using the method of Daura et al., employing a cutoff of 0.2 nm [119]. Intrapeptide contacts were also assessed, with a contact being defined as any two heavy (non-hydrogen) atoms being separated by no more than 0.6 nm. PyMOL was used for visualization [120]. Results were subjected to statistical analysis using a two-tailed *t*-test, with statistical significance determined if $p < 0.05$.

## 2.4 Results

### 2.4.1 Selection of Force Field and Conditions

The solution conditions modeled here were designed to mimic experimental studies and provide insight into the effects of pH and solution ionic strength on the dynamics of monomeric $A\beta_{40}$, especially with respect to which factor, pH or salt concentration, has a greater influence on the conformational dynamics of $A\beta_{40}$. In this regard, we identified parameters that we could measure from the MD simulations to assess differences in structure and dynamics. For example, we examined the overall secondary and tertiary structure of monomeric $A\beta_{40}$, focusing on certain areas including the hydrophobic C-terminal region (residues 29-40), which plays a critical role in aggregation [19-21, 121, 122]. Given this information, we focused our analysis of secondary structure, hydrophobic contacts, and solvent-accessible surface area (SASA) of residues 29 – 40 in light of properties of $A\beta_{40}$ as a whole.

In order to effectively perform an in-depth analysis on structural properties of monomeric $A\beta_{40}$, we set a strict standard to determine if the duration of the simulation was long enough to achieve convergence and equilibrium sampling. In order to determine convergence of each simulation, we utilized block averaging of the backbone RMSD and RMSD clustering. Block averaging of the backbone RMSD was a preliminary step to determine if any significant conformational changes of Aβ were occurring. When there was no systematic change among four overlapping blocks of time (final 25 ns, final 50 ns, final 75 ns, and final 100 ns) covering the last 100 ns, the

simulation was terminated and RMSD clustering was carried out. The first 5 clusters of each replicate were analyzed to assess the homogeneity between all clusters, which serves as an indicator of how effective the sampling was during the last 50 ns of each trajectory (Supporting Figures 2.S1 – 2.S4). The first 5 clusters of each replicate represented at least 85% of the structures contained in the final 50 ns of each trajectory, indicating that sampling during this time was reasonably homogeneous and that our analysis reflects equilibrium sampling. Among the first five clusters of a given replicate, secondary structural features were all very similar. These outcomes gave us confidence that our simulations were sufficiently converged. Finally, it is important to note that statistically significant differences are difficult to achieve in MD simulations of a disordered peptide like Aβ, thus we focus the interpretation of our results in terms of general features and trends, drawing comparisons with all available experimental evidence, giving us confidence that our results aid in explaining the effect of oxidation and solution conditions of monomeric Aβ. It should be noted that many quantities presented in the Results bear large standard deviations. While our assessments indicate that each individual trajectory has converged and represents equilibrium sampling, it is clear that there is considerable homogeneity in the structure of Aβ across replicates. This outcome reflects the intrinsically dynamic nature of the Aβ peptide, which is a challenge to simulate.

### 2.4.2 Secondary and Tertiary Structure of $A\beta_{40}$-Met35 and $A\beta_{40}$-Met35$^{ox}$

In simulations at pH 7 and 0 mM NaCl (neutralizing counterions only), $A\beta_{40}$-Met35$^{ox}$ showed decreased formation of β-strand in both the C-terminal region and the whole peptide, as compared to reduced $A\beta_{40}$-Met35 (Table 2.1, Figure 2.S1). The coil content in $A\beta_{40}$-Met35$^{ox}$ was higher than in $A\beta_{40}$-Met35 in both the full peptide and the C-terminal region (Table 2.S1). In $A\beta_{40}$-Met35, extended β-strands formed more readily than in $A\beta_{40}$-Met35$^{ox}$, in which shorter, transient β-strand structures were observed (Figure 2.S1).

**Table 2.1.** Average β-strand content (shown in %) in the C-terminal region (residues 29 – 40) of $A\beta_{40}$.[a]

| Solution Conditions | $A\beta_{40}$-Met35 (%) | $A\beta_{40}$-Met35$^{ox}$ (%) |
|---|---|---|
| 0 mM NaCl, pH 5 | 36 ± 31 | 9 ± 4 |
| 150 mM NaCl, pH 5 | 26 ± 17 | 19 ± 15 |
| 0 mM NaCl, pH 7 | 39 ± 15 | 23 ± 11 |
| 150 mM NaCl, pH 7 | 32 ± 14 | 26 ± 5 |

[a] Percentages represent averages over the final 50 ns of simulation time, with corresponding standard deviations.

RMSD clustering of $A\beta_{40}$-Met35 showed a substantial amount of β-strand in the central structure of the most populated clusters. $A\beta_{40}$-Met35$^{ox}$ RMSD clustering results indicate that all replicates in the first two clusters are populated by at least 35% of all structures in the last 50 ns and visually show substantially less β-strand content in the C-terminal region, with only one replicate (Replicate 5) involving Met35$^{ox}$ in a β-strand (Figure 2.S1). In addition, $A\beta_{40}$-Met35$^{ox}$ RMSD clustering showed reduced β-strand content and showed that Met35$^{ox}$ was not involved in β-strand structures, but rather coil (Figure 2.2, Figure 2.S2, and Table 2.S1). In the structure clustering data, it was also observed that in $A\beta_{40}$-Met35, the Met35 residue tended to be directed toward the interior of the peptide, while Met35$^{ox}$ in $A\beta_{40}$-Met35$^{ox}$ was more solvent-exposed

(Figure 2.S1). Ramachandran plots of individual residues for the C-terminal region (residues 29 – 40) of Aβ were analyzed in order to determine which residues were most likely causing localized changes in secondary structure. Free energy values were calculated by generating histograms from backbone f and y dihedral angles according to the equation

$$\Delta G(\phi, \psi) = -\mathrm{k_b T} \ln[P(\phi, \psi) - P_{max}]$$

where $P_{max}$ is the (f,y) pair with maximum probability, thus corresponding to a free energy value of zero.

Ramachandran plots confirmed the observed shift in secondary structure at 0 mM NaCl, pH 7 (Figure 2.3, third column), with Gly33, Leu34, and Met35 being the most strongly affected. The secondary structure shift was especially prominent in Gly33, which is normally involved in a bend connecting β-strands when Met35 is in its reduced form, but converts to a random coil when Met35 is in its sulfoxide form (Figure 2.S1).

We next examined the effects of increased salt concentration (150 mM) while keeping pH fixed at 7. In simulations of $A\beta_{40}$-Met35, the initial α-helical structure was largely lost during the first 100 ns of the simulation in favor of random coil and β-strand structures in the C-terminal region; some small amounts of helicity transiently broke and re-formed over time (Table 2.S2). The β-strand content in both the total peptide and the C-terminal region was decreased in the simulations of $A\beta_{40}$-Met35$^{ox}$ relative to $A\beta_{40}$-Met35 (Table 2.1). This outcome was similar to the simulations at 0 mM NaCl, pH 7, though the decrease in β-strand content attributed to oxidation of Met35 was reduced as compared to the simulations at low ionic strength.

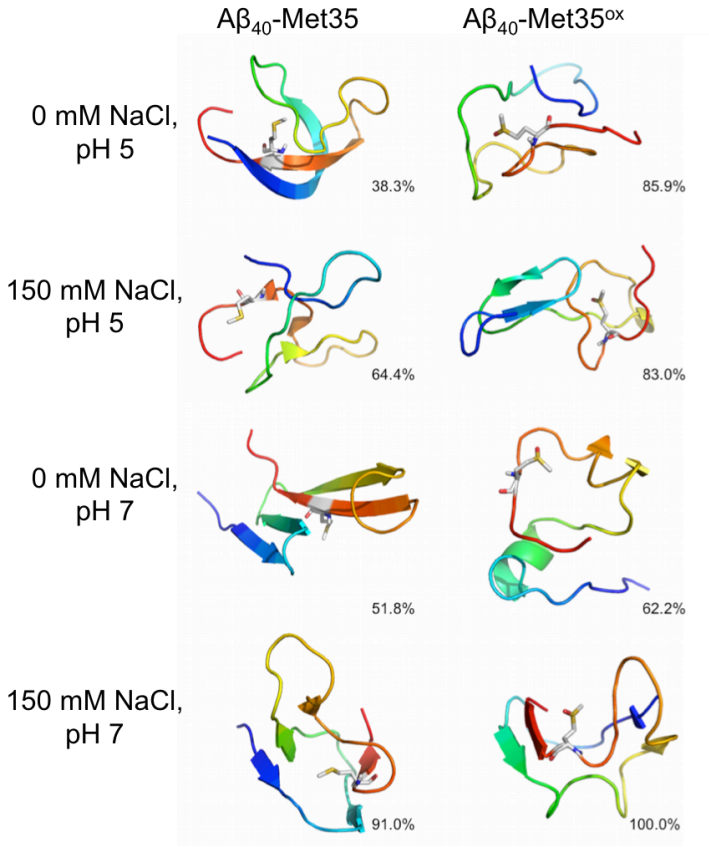


**Figure 2.2.** Dominant morphologies from RMSD clustering Met35 and Met35$^{ox}$. The structures shown are the central structures of the first cluster of a representative replicate. Representative replicates were chosen based on secondary structure similarity of the C-terminal region to the average. The percentages represent the number of frames during the last 50 ns of simulationthat belong to each cluster. The peptide is shown as a cartoon, colored as a rainbow gradient from N-terminus (blue) to C-terminus (red), with Met35 highlighted in stick representation.

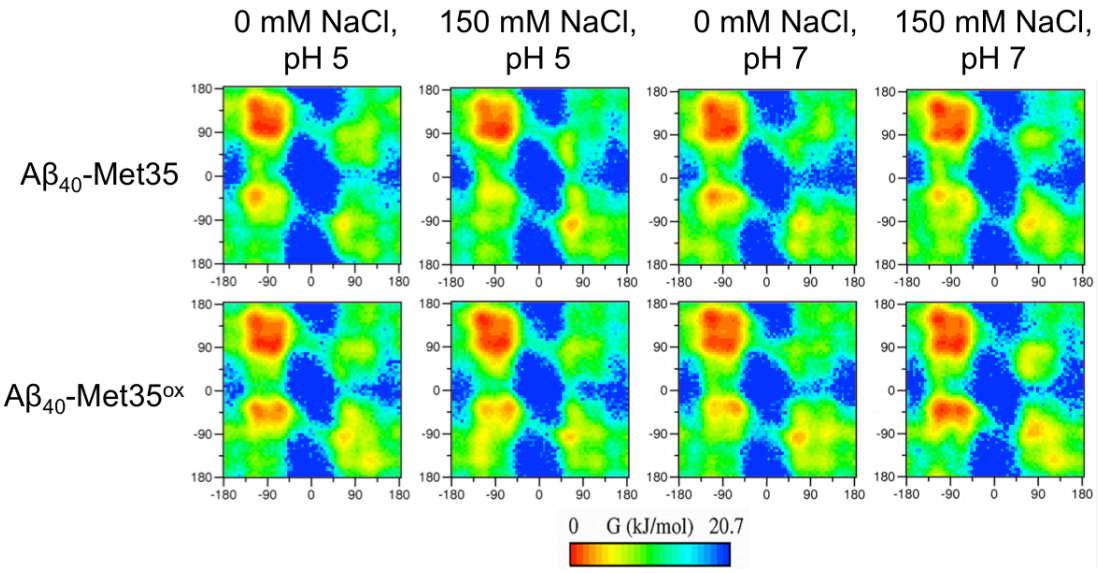


**Figure 2.3.** Free energy surfaces constructed from Ramachandran plots of C-terminal residues 29-40. Backbone Φ and Ψ dihedral angles are plotted on the x- and y-axes, respectively.

Secondary structure propensities were confirmed in the clustering results, with $A\beta_{40}$-Met35 producing more β-strand than $A\beta_{40}$-Met35$^{ox}$ (Figure 2.2, Figure 2.S2). Whereas $A\beta_{40}$-Met35 configurations were characterized by a single antiparallel β-sheet involving central (residues 16-22) and C-terminal residues, the simulations of $A\beta_{40}$-Met35$^{ox}$ showed β-strands at numerous positions along the $A\beta_{40}$ sequence, including N-terminal, central (residues 11-14), and C-terminal residues. Interestingly, there was no change in coil secondary structure propensity between $A\beta_{40}$-Met35 and $A\beta_{40}$-Met35$^{ox}$, though bend and turn content were increased in $A\beta_{40}$-Met35$^{ox}$ relative to $A\beta_{40}$-Met35 (Table 2.S2). In addition, Met35$^{ox}$ was not involved in any β-strand structures. Ramachandran plots of each residue in the C-terminal region confirmed a shift from β-strand to coil, turn, and helix at 150 mM NaCl, pH 7 (Figues 2.2 and 2.3, fourth column). From the Ramachandran plots, it was determined that Gly33, Leu34, and Met35 had the greatest shifts in their secondary structure, from bend and β-strand to coil (Figures 2.4 and 2.5). The change from bend to coil for Gly33 and Leu34 represent a destabilization of β-strand formation caused by Met35$^{ox}$ becoming more solvent-accessible and interacting less with the hydrophobic C-terminal region. These findings are similar to the results at 0 mM NaCl, pH 7 discussed above.

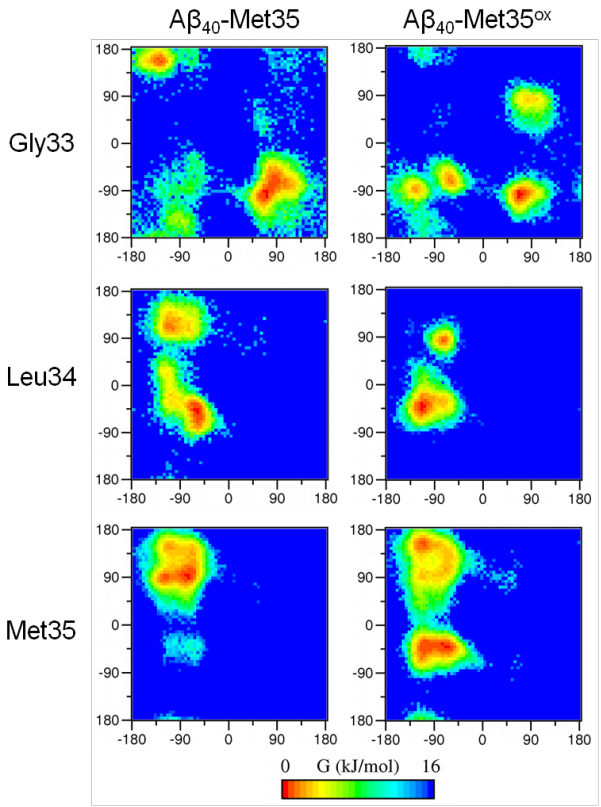


**Figure 2.4.** Free energy surfaces generated from Ramachandran plots of the residues indicated. Data are from simulations under the 150 mM NaCl, pH 7 conditions. Backbone Φ and Ψ dihedral angles are plotted on the x- and y-axes, respectively.

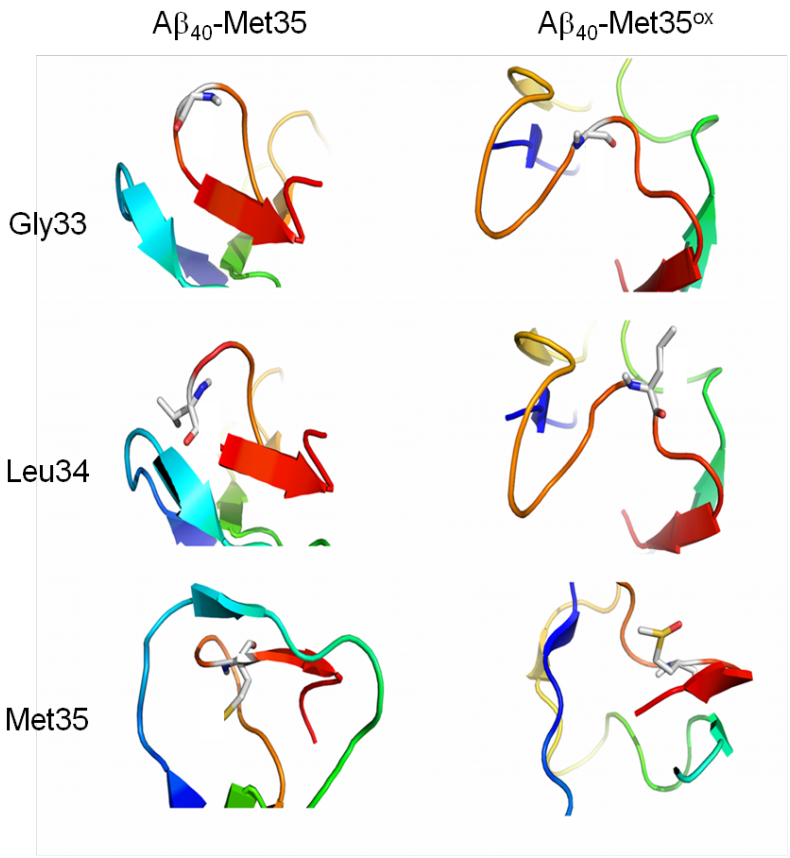


**Figure 2.5.** Selected residues that show the greatest shifts in secondary structure propensity in simulations conducted in the presence of 150 mM NaCl, pH 7. Images are rendered as in Figure 2.2, with the selected residue being highlighted in stick representation.

Having examined the dynamics of $A\beta_{40}$ at a physiologically relevant pH, we next considered a solution pH of 5. Acidic conditions are often used to control the ability of Aβ to aggregate to facilitate data collection [61], and thus it is important to consider the effects that pH may have on $A\beta_{40}$-Met35$^{ox}$, as well. In simulations at 0 mM NaCl, pH 5, $A\beta_{40}$-Met35 showed substantial amounts of β-strand in the C-terminal region, while $A\beta_{40}$-Met35$^{ox}$ had minimal amounts of β-strand structure and substantially more coil (Figure 2.2 and Table 2.S3). Ramachandran plots also show a shift from β-strand structure to more bend and turn in this region at 0 mM NaCl, pH 5 (Figure 2.3, first column) for $A\beta_{40}$-Met35$^{ox}$. Gly33 had the most substantial shift, populating β-strand configurations in $A\beta_{40}$-Met35 and coil configurations in $A\beta_{40}$-Met35$^{ox}$. This same outcome was observed in the rest of the C-terminal region, which showed a measurable shift from β-strand and bend to coil and turn (Table 2.1). In these simulations, $A\beta_{40}$-Met35$^{ox}$ had the lowest amount of β-strand (9 ± 4%) of all the conditions tested, whereas $A\beta_{40}$-Met35 showed similar amounts of β-strand (36 ± 31%) as other $A\beta_{40}$-Met35 data sets.

In the final simulation set we considered, solution conditions were set at 150 mM NaCl, pH 5. For $A\beta_{40}$-Met35, the principal secondary structure element in the C-terminal region was β-strand, which was observed in 4 replicates (Figure 2.S4). β-strand was observed in $A\beta_{40}$-Met35$^{ox}$ between residues 3 – 12 rather than the C-terminal region. Overall, a decrease in C-terminal region β-strand structure was observed in $A\beta_{40}$-Met35$^{ox}$ compared to$A\beta_{40}$-Met35 (Table 2.1);

however, both reduced and oxidized $A\beta_{40}$ showed substantial heterogeneity in results. This observation suggests that many conformations are sampled at 150 mM NaCl, pH 5 and that $A\beta_{40}$ is highly dynamic. Ramachandran plots also showed a shift from β-strand and bend in $A\beta_{40}$-Met35 to coil in $A\beta_{40}$-Met35$^{ox}$ at 150 mM NaCl, pH 5 (Figure 2.4, second column). In $A\beta_{40}$-Met35$^{ox}$, Gly33 participated in fewer bend configurations in favor of random coil, while Leu34 and Met35 were more frequently found in random coils than β-strand. In $A\beta_{40}$-Met35$^{ox}$ at pH 5, Val36 and Gly37 shifted toward coil structures rather than turn or bend, as compared to $A\beta_{40}$-Met35, in contrast to observations at pH 7. This coil involving residues Gly33, Val36, and Gly37 is easily observed in RMSD clustering results of $A\beta_{40}$-Met35$^{ox}$ (Figure 2.5, Figure 2.S4). There are bends in this same region that are observed in $A\beta_{40}$-Met35, enhancing the ability of this region to form β-strand as compared to $A\beta_{40}$-Met35$^{ox}$. It should be noted that there was a difference in the location of the coil structural elements between $A\beta_{40}$-Met35 and $A\beta_{40}$-Met35$^{ox}$, though the total coil content of $A\beta_{40}$ remained very similar overall (Table 2.S4). For example, there was a change in location of coil, such that more coil was found in the C-terminal region of $A\beta_{40}$-Met35$^{ox}$ (46 ± 8%) than $A\beta_{40}$-Met35 (39 ± 16%), indicating an increase in coil content of N-terminal residues 1 – 29 in $A\beta_{40}$-Met35 such that the overall coil content was unaffected at 150 mM NaCl, pH 5. The absence of any change in coil propensity was also observed at pH 7, indicating that the effect of salt on coil formation and secondary structure of $A\beta_{40}$ acts independently of pH.

### 2.4.3 Hydrophobic Contacts and Solvent Accessible Surface Area

At 0 mM NaCl, pH 7, oxidation of Met35 substantially reduced the number of hydrophobic contacts in the C-terminal region (Table 2.2). There was a significant ($p < 0.05$) difference in SASA of residues 26, 28, and 34 such that they were more solvent-exposed in $A\beta_{40}$-Met35$^{ox}$. Our results confirm that oxidation of Met35 perturbs this region, especially with respect to Leu34, which is very hydrophobic and is normally shielded from solvent in the absence of oxidation. There was also a significant ($p < 0.05$) difference between the C-terminal region SASA of reduced and oxidized $A\beta_{40}$, with $A\beta_{40}$-Met35$^{ox}$ having a higher hydrophobic SASA (Table 2.3). The larger SASA represents greater solvent exposure of residues 29 – 40, which indicates fewer intra-peptide interactions and greater affinity of the peptide for the solvent, an outcome that is driven by oxidation of Met35. The increased solvent exposure consequently disrupted β-strand formation by disturbing backbone hydrogen bonding that otherwise favors β-strand formation and sidechain interactions that give rise to a hydrophobic nucleus that is shielded from solvent. These findings suggest that Met35$^{ox}$ drives the solvent exposure of the hydrophobic C-terminal region, counteracting the unfavorable nature of water-hydrophobic residue interactions, concomitant with a destabilization in the bend structure in Gly33 normally found in the C-terminal region, resulting in a localized loss of β-strand structure. This observation and explanation can be used for each condition set tested, given the similar trends in comparison of reduced and oxidized Aβ. This effect on $A\beta_{40}$-Met35$^{ox}$ is greater at 0 mM NaCl than it is at 150 mM NaCl (discussed below), contributing to the lower occurrence of β-strand and higher SASA seen in the C-terminal region (Tables 2.1 and 2.3).

**Table 2.2**. Heavy atom hydrophobic contacts within C-terminal residues 29 – 40.[a]

| Solution Conditions | $A\beta_{40}$-Met35 | $A\beta_{40}$-Met35$^{ox}$ |
|---|---|---|
| 0 mM NaCl, pH 5 | 121 ± 15 | 100 ± 9 |
| 150 mM NaCl, pH 5 | 134 ± 22 | 81 ± 6 |
| 0 mM NaCl, pH 7 | 120 ± 9 | 99 ± 7 |
| 150 mM NaCl, pH 7 | 132 ± 26 | 97 ± 14 |

[a] Averages are shown over the last 50 ns of simulation time, with corresponding standard deviations.

**Table 2.3.** Hydrophobic solvent-accessible surface area ($nm^2$) in C-terminal residues 29 – 40.[a]

| Solution Conditions | $A\beta_{40}$-Met35 | $A\beta_{40}$-Met35$^{ox}$ |
|---|---|---|
| 0 mM NaCl, pH 5 | 5.0 ± 0.3 | 5.9 ± 0.7 |
| 150 mM NaCl, pH 5 | 5.4 ± 0.6 | 6.1 ± 0.4 |
| 0 mM NaCl, pH 7 | 4.9 ± 0.2 | 6.1 ± 0.3 |
| 150 mM NaCl, pH 7 | 4.9 ± 0.8 | 5.2 ± 0.4 |

[a] Averages are shown over the last 50 ns of simulation time, with corresponding standard deviations.

At 150 mM NaCl, pH 7, oxidation also resulted in a decrease in hydrophobic contacts (Table 2.2) and a slight increase in SASA (Table 2.3) relative to $A\beta_{40}$-Met35. It is also important to note that there was a decrease in SASA between $A\beta_{40}$-Met35$^{ox}$ upon increasing the solution ionic strength, indicating $A\beta_{40}$-Met35$^{ox}$ interacts more with the solvent when there is no salt present, preventing collapsed structure formation. At pH 5, an increase in SASA and decrease in hydrophobic contacts in $A\beta_{40}$-Met35$^{ox}$ (Tables 2.2 and 2.3) were observed relative to $A\beta_{40}$-Met35 for both 0 mM NaCl and 150 mM NaCl. However, it is clear that independent of pH, at 0 mM NaCl, $A\beta_{40}$-Met35 had similar amounts of β-strand (39 ± 15% at pH 5 and 36 ± 31% at pH 7), whereas the results for $A\beta_{40}$-Met35$^{ox}$ were very different (9 ± 4% at pH 5 and 23 ± 11% at pH 7). This observation leads us to propose that solution conditions affect $A\beta_{40}$-Met35$^{ox}$ in a more pronounced way than $A\beta_{40}$-Met35, ultimately explaining the different results and conclusions gathered from experimental studies that use varying buffer conditions.

## 2.5 Discussion

The paradigm of oxidized Aβ causing neurotoxicity has been present for decades; however, experimental studies focusing on oxidized Aβ and its relationship to aggregation have produced conflicting results [4, 13, 49, 85]. Inhibiting or otherwise modifying the aggregation pathway is likely to be beneficial to AD patients. Understanding different components that affect aggregation, like oxidation state of Met35, can provide a better understanding of the properties of Aβ that affect aggregation, as influenced by the surrounding environment.

An important indicator of potential for aggregation is secondary structure. Aβ proceeds through many intermediate forms as it transitions from helix to β-strand in the aggregation of monomeric Aβ to fibrillar Aβ. This transition of secondary structure is especially prominent in the hydrophobic C-terminal region of Aβ, and parallel β-strand formation is a characteristic of Aβ fibrils. NMR studies have observed changes in secondary structure and aggregation rates between reduced and oxidized Aβ, with the Met35$^{ox}$ form aggregating more slowly [101, 102].

The present work utilizes this transition of secondary structure as a predictor of aggregation at the level of the monomer to explain these experimental studies. We modeled the experimental solution conditions of Watson et al. (0 mM NaCl, pH 5), Hou et al. (0 mM NaCl, pH 7), and Snyder et al. (150 mM NaCl, pH 7) to resolve the conflicting outcomes of these experimental studies, and we also modeled conditions of 150 mM NaCl, pH 5 that would help to determine if pH or salt concentration was more influential on the dynamics of $A\beta_{40}$. Of particular interest are results at 150 mM NaCl, pH 7, which is most representative of physiological conditions. This study is unique in that we have systematically studied monomeric $A\beta_{40}$ in multiple solution conditions in order to determine influencing factors on Aβ aggregation in relation to oxidation state.

In addition to modeling experimental studies and a physiologically relevant environment, we took special care in deciding which force field would be best suited for studying a disordered peptide like Aβ. Common atomistic force fields, such as the AMBER parameter sets [44, 123-128], CHARMM [120, 129], OPLS-AA [130], and GROMOS96 [70, 131, 132], have been developed with different parameterization techniques and are calibrated against different criteria. Thus, the outcome of a simulation under a given force field is not necessarily the same as a simulation carried out under a different force field. Secondary structure propensity is crucial in our analysis and it was important to choose a force field that compares well with experimental results. AMBER03 and CHARMM22+CMAP have been shown to over-stabilize α-helical secondary structure, whereas GROMOS96 53A6 under-stabilizes helices in favor of extended configurations [133], an outcome that motivated the development of the newer GROMOS96 54A7 parameter set [132]. There is a unique challenge in modeling Aβ, an intrinsically disordered peptide, and studies have shown that GROMOS96 43A1 and OPLS-AA modeled Aβ well, in terms of reproducing NMR J-coupling constants [134]. More recent work by Olubiyi and Strodel has indicated that GROMOS96 53A6 reproduces NMR chemical shifts effectively for Aβ [135]. Recent work from our group has indicated that GROMOS96 53A6 performs well in reproducing a variety of structural features of monomeric Aβ [72], thus in conjunction with existing studies by other groups, GROMOS96 53A6 was chosen as the force field used in this work.

A recent MD study on Aβ with and without Met35 oxidation at 150 mM NaCl, pH 7 showed Asp23 – Lys28 salt bridge stabilization and turn formation between residues 24 – 27 were essential in stabilizing a β-hairpin structure [136], a finding that was not observed. In addition, in our simulations we observed greater β-strand content in both reduced and oxidized forms of Aβ, especially in the C-terminal region, which can be correlated with propensity for aggregation. These differences can be attributed to several factors. First, the work of Triguero et al. employed short (50 ns) simulations and did not utilize replicate simulations. In addition, no assessment of convergence was conducted so it is possible that the results presented are not reflective of equilibrium sampling. Further, the force field employed by Triguero et al., GROMOS96 53A5 [70], was designed for simulations of amino acids and proteins in nonpolar media, not water. Thus, the structures they observed may not reflect the true conformational ensemble of Aβ in physiological conditions, or even the *in vitro* conditions that have been used experimentally.

In our simulations, when Met35 was oxidized, C-terminal β-strand content and hydrophobic contacts decreased, while SASA increased (Tables 2.1 – 2.3) relative to $A\beta_{40}$-Met35. This

outcome was independent of solution conditions and thus reflects the influence of the sulfoxide moiety, which is strongly attracted to water. We explain this phenomenon by noting the change in dipole around the sulfur atom when oxidized; the partial negative charge of the sulfoxide oxygen atom interacts favorably with the polar solvent (water). In Met35, when the thioether is not oxidized, the hydrophobicity of the neighboring $CH_2$ and $CH_3$ groups shield the sulfur atom (which bears a partial negative charge in our model) from water (Figure 2.1). The favorable interaction of the sulfoxide moiety with water provides the driving force for exposing residues 29 – 40 to water, ultimately modulating the secondary structure propensities in this region. The decrease in hydrophobic contacts and increase in SASA represent a change in the dynamics of the C-terminal region such that Met35$^{ox}$ impedes the formation of a collapsed structure.

Having determined the effect of the sulfoxide moiety on nearby residues, we sought to determine how solution conditions affected both reduced and oxidized Aβ. Our results suggest that solution conditions affected Aβ$_{40}$-Met35$^{ox}$ in a more pronounced and consistent way by influencing C-terminal β-strand content across solution conditions, whereas there were only slight differences in C-terminal β-strand content in Aβ$_{40}$-Met35 under the various solution conditions. This concept is best illustrated by comparing C-terminal β-strand propensity for Aβ$_{40}$-Met35 at 0 mM NaCl, pH 5 and pH 7 (36 ± 31% and 39 ±15%, respectively) and Aβ$_{40}$-Met35$^{ox}$ at pH 5 and pH 7 (9 ± 4% and 23 ± 11%). These results show that with varying pH, β-strand formation in Aβ$_{40}$-Met35 remained similar, whereas, when Aβ$_{40}$ was oxidized, pH did affect secondary structure propensity. Changes in overall secondary and tertiary structure between Aβ$_{40}$-Met35 and Aβ$_{40}$-Met35$^{ox}$ were minimal, but when focusing on the C-terminal region, which is critical for aggregation, greater differences became clear. In a physiologically relevant environment (150 mM NaCl, pH 7), Aβ$_{40}$-Met35$^{ox}$ produced less β-strand structure in the C-terminal region when compared to Aβ$_{40}$-Met35 for reasons described above. Our results are in good agreement with the experimental work of Snyder et al., who found an increase in aggregation rate for Aβ$_{40}$-Met35$^{ox}$ [103] above 200 mM NaCl. Our results agree with respect to secondary structure (as a predictor of aggregation) and the finding that SASA is influenced by salt and pH. Similar to our study, Snyder et al. found that aggregation was accelerated by increasing salt concentration and decreased with lower pH, an outcome that was due to changes in secondary structure. They noted that below approximately 200 mM NaCl (which encompasses all of our simulations, which were conducted at either 0 mM or 150 mM NaCl), they saw a decrease in aggregation directly proportional to salt concentration, while above 200 mM NaCl, aggregation increased. Ultimately, this finding confirms that solution conditions do affect Aβ, especially when Met35 is oxidized, and hopefully helps clarify the overall effect of oxidation of Met35 on Aβ from varying experimental studies. Our results indicate that Met35 oxidation impedes aggregation across different solution conditions

Based on the results shown in Table 2.1, pH was a greater influence on β-strand formation than salt concentration, especially on Aβ$_{40}$-Met35$^{ox}$, indicating that the protonation state of His6, His13, and His14 influences the dynamics of the peptide more than surrounding salt concentration, though these histidine residues do not interact directly with Met35 (data not shown). Experimental studies on the effect of pH on Aβ found a decrease in Aβ aggregation at acidic pH (pH 3.5) by stabilizing helix formation [137] and changes to the electrostatic surface in the N-terminal region [135, 138]. Atomic force microscopy studies have indicated that at a lower pH, Aβ displays rod-shaped aggregates that are not as cytotoxic as aggregates formed at pH 7

[139]. In addition, pH affects $A\beta_{40}$-Met35 in a similar way, which indicates an intrinsic change in the overall nature of monomeric $A\beta_{40}$ that is independent of oxidation state. In our study, this difference was caused by the change in charge state of the histidine residues, influencing a reduction in the amount of β-strand structure in the C-terminal region.

Greater solution ionic strength caused the C-terminal region of $A\beta_{40}$-$Met35^{ox}$ to become less solvent-exposed at pH 7, thus causing an increase in β-strand when a higher concentration of salt was present, since $Met35^{ox}$ was not as strongly driven towards the solvent. This difference is most likely due to charge screening that arises from the presence of salt, thus reducing the influence of the change in dipole between $A\beta_{40}$-$Met35^{ox}$ and $A\beta_{40}$-Met35. This phenomenon aids in explaining why there was not as much of a difference in secondary structure composition between $A\beta_{40}$-$Met35^{ox}$ and $A\beta_{40}$-Met35 with 150 mM NaCl present compared to the simulations containing 0 mM NaCl. Greater ionic strength did not cause the C-terminal region of $A\beta_{40}$-$Met35^{ox}$ to become more solvent exposed, as there was not much difference between SASA between 0 mM NaCl and 150 mM NaCl with $A\beta_{40}$-$Met35^{ox}$; however, there was a substantial decrease in β-strand content. Ultimately, solvent accessibility decreases the hydrophobic interactions of $Met35^{ox}$ with nearby residues in the C-terminal region and disrupts the bend that normally forms involving Gly33 and Leu34. This phenomenon causes a reduction in β-strand in the C-terminal region, a behavior that should ultimately slow aggregation.

Overall, oxidation of Met35 in monomeric $A\beta_{40}$ resulted in a decrease in C-terminal β-strand formation, a behavior that was influenced by solution conditions. Across all conditions, irrespective of peptide protonation state or solution ionic strength, oxidation of Met35 resulted in a decrease in β-strand content in the C-terminal region of $A\beta_{40}$, indicating that it is a global property of $Met35^{ox}$. While β-strand content of monomeric $A\beta_{40}$-Met35 did not change significantly between pH 5 and pH 7 conditions, additional salt produced small decreases in β-strand content, irrespective of pH. The opposite was true for $A\beta_{40}$-$Met35^{ox}$, with increased salt giving rise to increased β-strand content. Thus, it is important to interpret experimental studies in light of the different outcomes that arise simply by virtue of differences in solution pH and ionic strength. Our simulations have provided insight into the conflicting body of literature on this topic. The reduced β-strand content produced as a result of oxidation of Met35 is consistent with a decrease in aggregation rate that was observed experimentally [101, 103]. Our findings fit well within the experimental model that oxidative stress in the AD brain likely induces toxicity in a manner independent of Aβ fibril formation, since our findings are consistent with oxidized Aβ having attenuated aggregation capacity. The simulation results we present here provide mechanistic insight into this dynamic process. Understanding properties like oxidation state of Aβ will allow for further investigations to determine which molecular events give rise to the devastating characteristics of AD.

## 2.6 Acknowledgments

The authors thank Advanced Research Computing at Virginia Tech for computing time on the SystemX and Athena supercomputers. This work was supported by the Institute for Critical Technology and Applied Science (ICTAS) at Virginia Tech.

## 2.7 Supporting Information

**Table 2.S1.** Secondary structure percentages for 0 mM NaCl, pH 7 systems.[a]

| | $A\beta_{40}$-Met35 | $A\beta_{40}$-Met35$^{ox}$ |
|---|---|---|
| Coil | 33± 6 | 44 ± 7 |
| β-Strand | 27± 14 | 17 ± 8 |
| Bend | 29 ± 8 | 26± 11 |
| Turn | 8 ± 6 | 10 ± 9 |
| Helix | 3 ± 5 | 3± 6 |

[a] Averages are shown over the last 50 ns of simulation time, with corresponding standard deviations.

**Table 2.S2.** Secondary structure percentages for 150 mM NaCl, pH 7 systems.[a]

| | $A\beta_{40}$-Met35 | $A\beta_{40}$-Met35$^{ox}$ |
|---|---|---|
| Coil | 37 ± 5 | 37 ± 6 |
| β-Strand | 27 ± 7 | 19 ± 3 |
| Bend | 27 ± 10 | 32± 7 |
| Turn | 8 ± 4 | 12 ± 6 |
| Helix | 1 ± 3 | 0 ± 0 |

[a] Averages are shown over the last 50 ns of simulation time, with corresponding standard deviations.

**Table 2.S3.** Secondary structure percentages for 0 mM NaCl, pH 5 systems.[a]

| | $A\beta_{40}$-Met35 | $A\beta_{40}$-Met35$^{ox}$ |
|---|---|---|
| Coil | 38± 8 | 52 ± 9 |
| β-Strand | 24 ± 20 | 7 ± 4 |
| Bend | 22 ± 9 | 30± 5 |
| Turn | 9 ± 3 | 8 ± 5 |
| Helix | 7 ± 13 | 3 ± 6 |

[a] Averages are shown over the last 50 ns of simulation time, with corresponding standard deviations.

**Table 2.S4.** Secondary structure percentages for 150 mM NaCl, pH 5 systems.[a]

| | $A\beta_{40}$-Met35 | $A\beta_{40}$-Met35$^{ox}$ |
|---|---|---|
| Coil | 43 ± 3 | 44 ± 5 |
| β-Strand | 16 ± 3 | 17 ± 7 |
| Bend | 26 ± 6 | 27 ± 3 |
| Turn | 11 ± 4 | 9 ± 3 |
| Helix | 4 ± 5 | 3 ± 5 |

[a] Averages are shown over the last 50 ns of simulation time, with corresponding standard deviations.

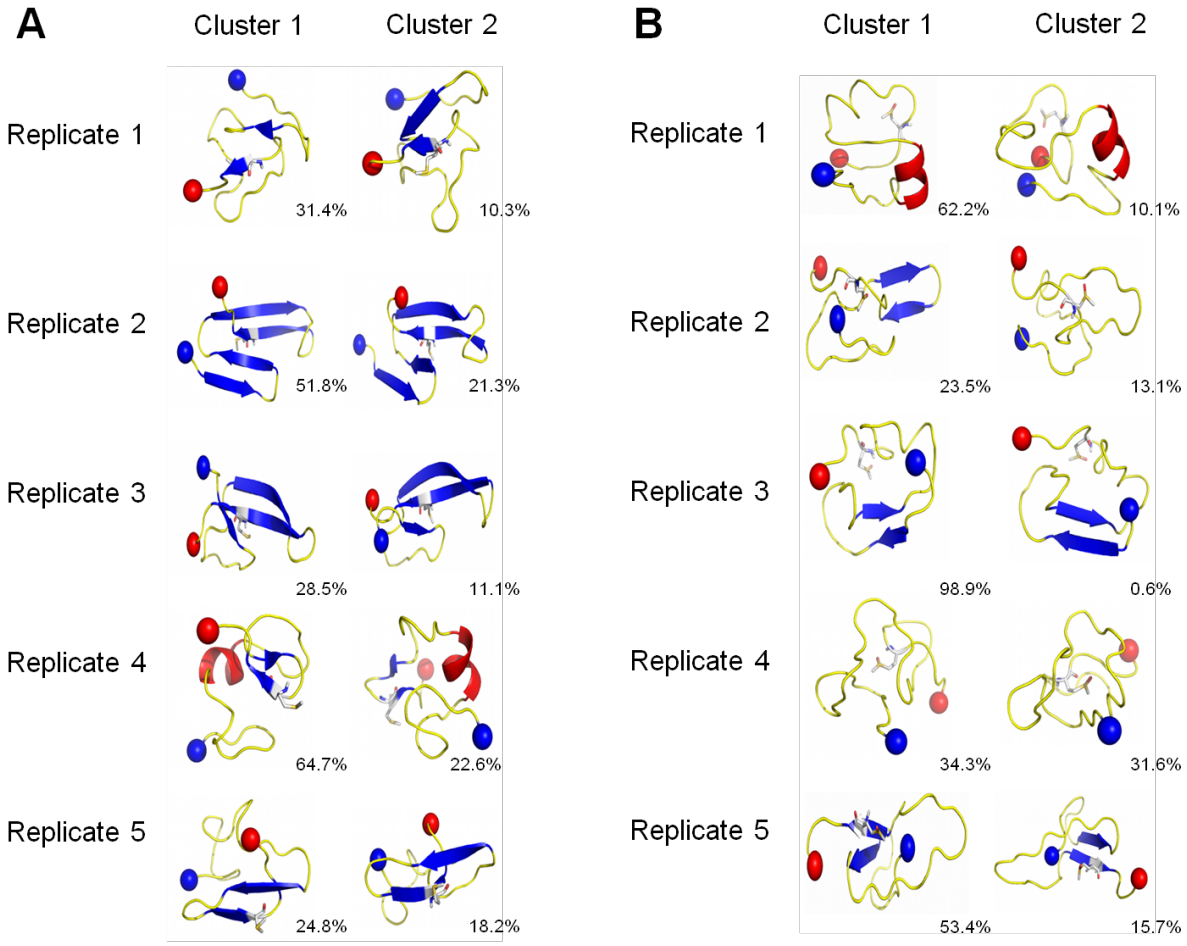


**Figure 2.S1.** Dominant morphologies from RMSD clustering for 0 mM NaCl, pH 7 reduced and oxidized Aβ for (A) $A\beta_{40}$-Met35 and (B) $A\beta_{40}$-$Met35^{ox}$. The structures shown are the central structures of the cluster for each replicate. The percentages shown represent the number of configurations during the last 50 ns of simulation that differ by no more than 0.2 nm RMSD from the central structure. The peptide is shown as a cartoon, colored by secondary structure (blue = β-strand, red = helix, and yellow = coil) with N- and C-termini indicated by blue and red spheres, respectively. Met35 is highlighed in stick representation.

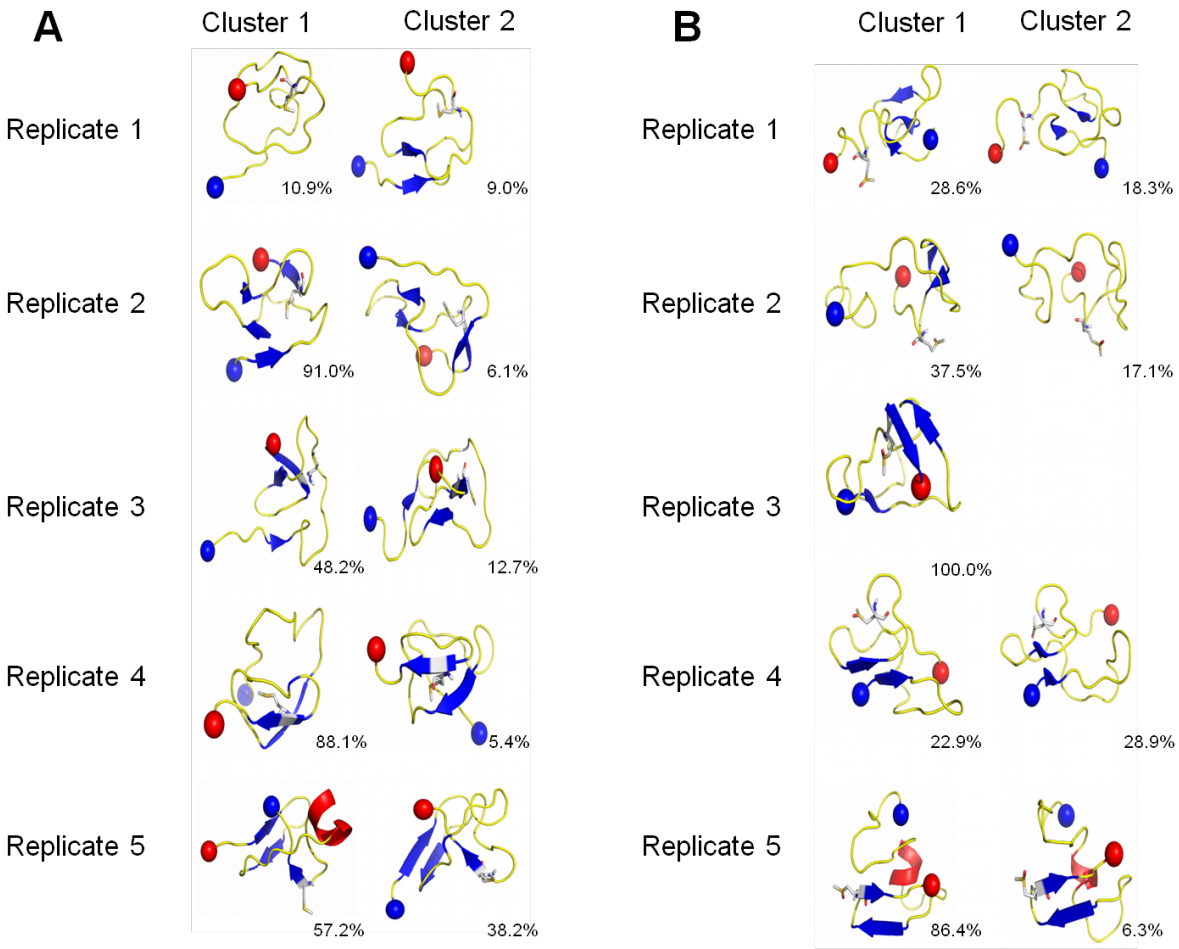


**Figure 2.S2.** Dominant morphologies from RMSD clustering for 150 mM NaCl, pH 7 reduced and oxidized Aβ for (A) $A\beta_{40}$-Met35 and (B) $A\beta_{40}$-$Met35^{ox}$. The structures shown are the central structures of the cluster for each replicate. The percentages shown represent the number of configurations during the last 50 ns of simulation that differ by no more than 0.2 nm RMSD from the central structure. The peptide is shown as a cartoon, colored by secondary structure (blue = β-strand, red = helix, and yellow = coil) with N- and C-termini indicated by blue and red spheres, respectively. Met35 is highlighted in stick representation.

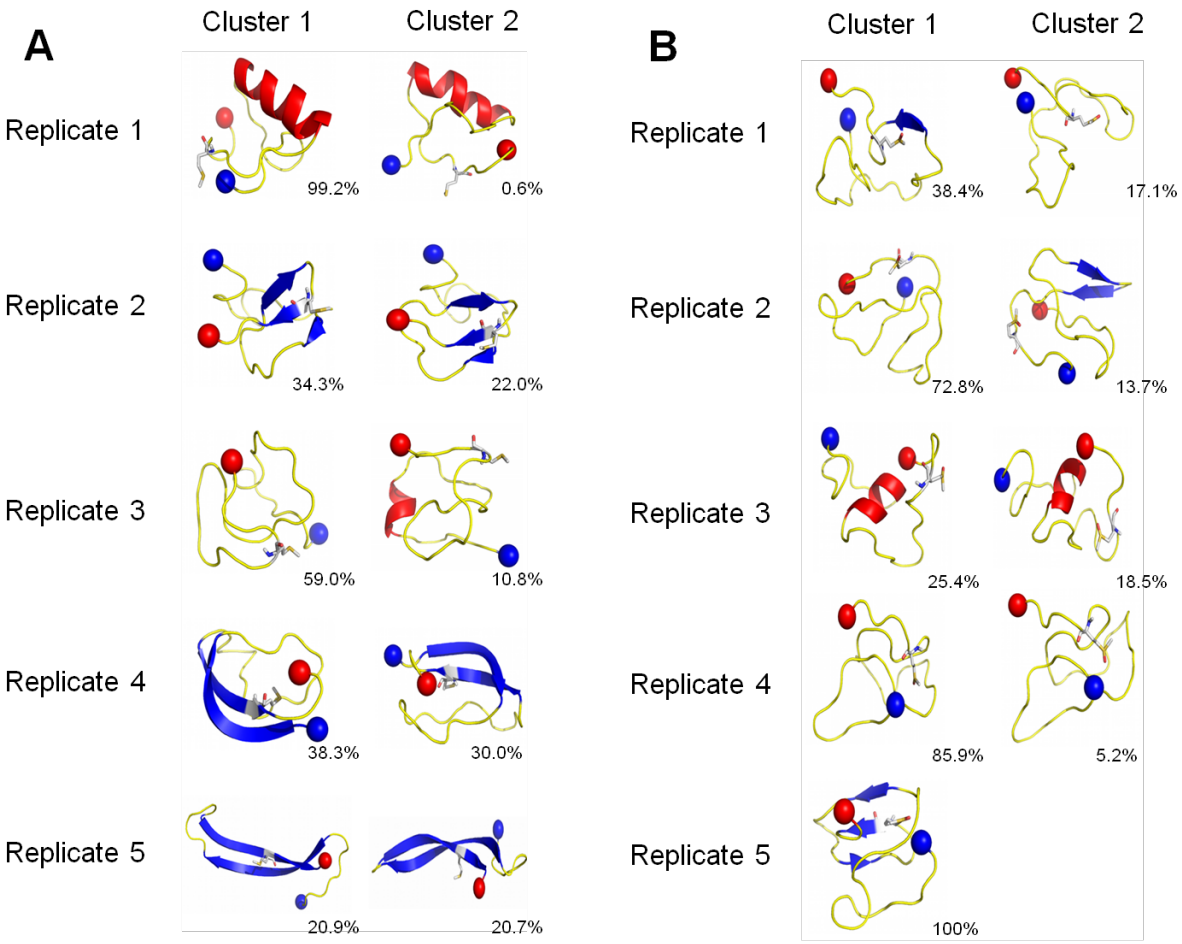


**Figure 2.S3.** Dominant morphologies from RMSD clustering for 0 mM NaCl, pH 5 reduced and oxidized Aβ for (A) $A\beta_{40}$-Met35 and (B) $A\beta_{40}$-$Met35^{ox}$. The structures shown are the central structures of the cluster for each replicate. The percentages shown represent the number of configurations during the last 50 ns of simulation that differ by no more than 0.2 nm RMSD from the central structure. The peptide is shown as a cartoon, colored by secondary structure (blue = β-strand, red = helix, and yellow = coil) with N- and C-termini indicated by blue and red spheres, respectively. Met35 is highlighed in stick representation.

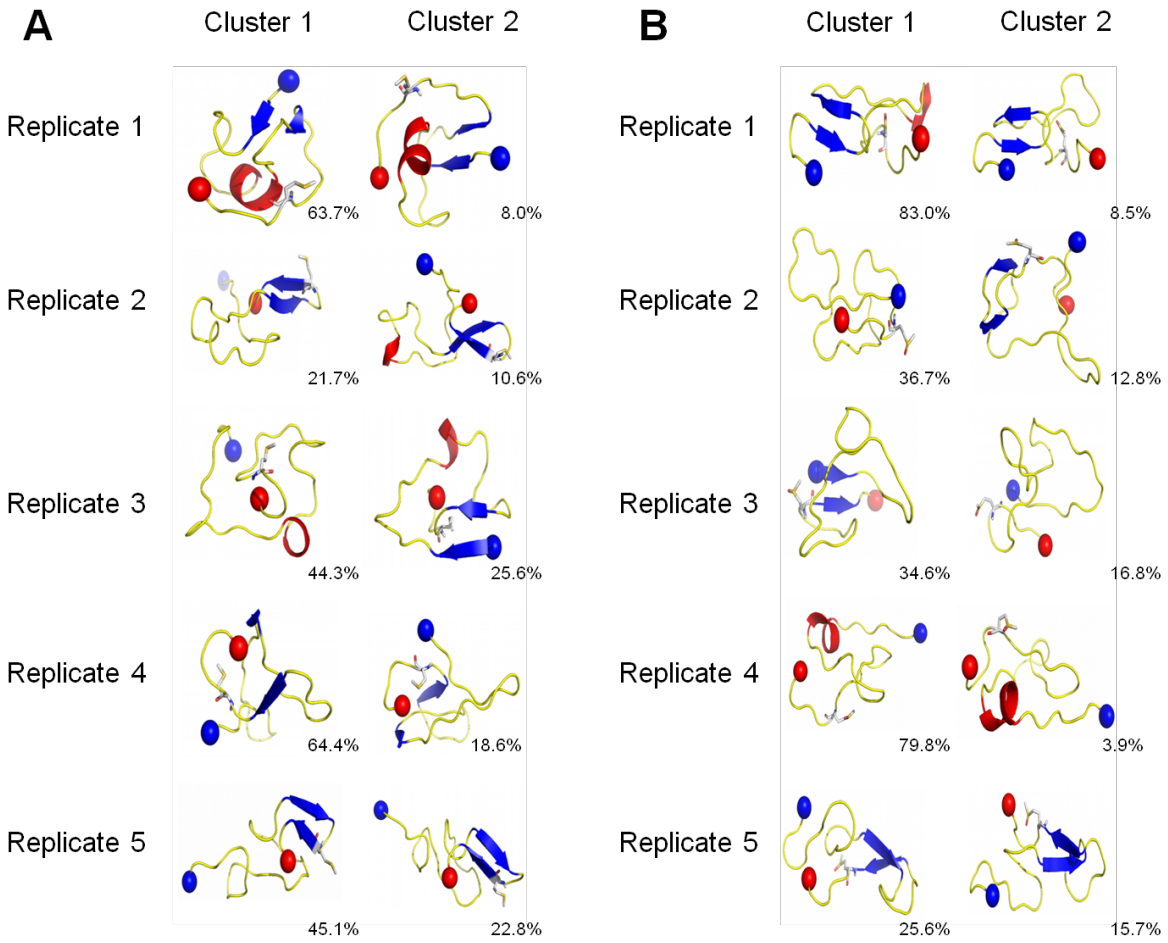


**Figure 2.S4.** Dominant morphologies from RMSD clustering for 150 mM NaCl, pH 5 reduced and oxidized Aβ for (A) $A\beta_{40}$-Met35 and (B) $A\beta_{40}$-$Met35^{ox}$. The structures shown are the central structures of the cluster for each replicate. The percentages shown represent the number of configurations during the last 50 ns of simulation that differ by no more than 0.2 nm RMSD from the central structure. The peptide is shown as a cartoon, colored by secondary structure (blue = β-strand, red = helix, and yellow = coil) with N- and C-termini indicated by blue and red spheres, respectively. Met35 is highlighed in stick representation.

# 3 Influence of Sequence and Lipid Type on Membrane Perturbation by Human and Rat Amyloid β-Peptide (1-42)

Anne M. Brown[1] and David R. Bevan[1]

[1]Department of Biochemistry (0308), Virginia Polytechnic Institute and State University, 201 Engel Hall, Blacksburg, VA 24061.

**Attribution:** AMB wrote this paper with input on content and corrections prior to publication from DRB. All authors collectively conceived the initial project idea and direction. AMB was responsible for submission of the completed manuscript and response to reviewers. This chapter is to be submitted to BBA Biomembranes.

## 3.1 Abstract

The hallmark characteristics of plaque formation and neuronal cell death in Alzheimer's disease (AD) are caused principally by the amyloid β-peptide (Aβ). Current research focuses on understanding the interactions between Aβ and neuronal cell membranes, given the relationship between membrane perturbation and neurotoxicity. Aβ sequence and lipid composition are essential variables to consider when elucidating the impact of the biological membrane on Aβ structure and the effect of Aβ on membrane integrity. Atomistic molecular dynamics simulations testing two Aβ sequences (Human $A\beta_{(1-42)}$ (HAβ) and Rat $A\beta_{(1-42)}$ (RAβ)), five lipid types, and totaling 9 μs in simulation time, were performed in order to explain the effect of these variables on membrane perturbation and to assess the potential link to AD toxicity. All metrics used to assess membrane perturbation agree insomuch that it can be concluded that HAβ and RAβ contribute to membrane perturbation by causing a more rigid, gel-like lipid phase. The presence of cholesterol in a model raft membrane was found to moderate the amount of perturbation caused by HAβ and RAβ. Differences between HAβ and RAβ membrane perturbations were seen based on lipid headgroup charge and hydrogen bonding capacity. The position of arginine in the N-terminal region was determined to be the mediating factor in these differences in lipid affinity and disruption between HAβ and RAβ. Overall, this work increases our understanding of the influence of sequence and lipid type on Aβ-membrane interactions, providing mechanistic insight into the etiology of AD.

## 3.2 Introduction

Alzheimer's disease (AD), a progressive, neurodegenerative disease, is currently estimated to affect 5.3 million individuals in the United States and is expected to increase in prevalence by forty percent by the year 2025 [5]. AD is the sixth leading cause of death in the United States and currently cannot be prevented or cured. Current therapies focus on temporarily slowing symptoms of AD and preserving neurotransmitters by inhibiting cholinesterase or by antagonizing N-methyl-D-aspartate (NMDA) receptors [140]. Development of novel therapeutics to prevent or cure AD requires further insight into the principal mechanisms of toxicity related to AD.

AD toxicity is typically classified by the aggregation and accumulation of the amyloid β-peptide (Aβ) in and around neuronal cells [15]. Aβ is cleaved from the amyloid precursor protein (APP) by sequential proteolysis by α- or β-secretase and γ-secretase [26, 84]. α-secretase cleavage results in a product named p3, which consists of residues 17-40/42 of Aβ [141]. β-secretase cleavage of APP results in multiple alloforms of Aβ being produced, with the most prevalent alloforms containing 40 ($A\beta_{(40)}$) or 42 ($A\beta_{(42)}$) residues. This study focuses on $A\beta_{(42)}$, given that it is found in the disease state at a 9:1 ratio as compared to $A\beta_{(40)}$ [81, 82, 142].

One of the main theories of Aβ toxicity, the "amyloid hypothesis" [13], states that Aβ can exert toxic effects through aggregation and interactions with neuronal cell membranes [4]. These Aβ interactions with the cell membrane [49] can result in increased membrane permeability and calcium ion leakage, activating apoptotic pathways [85, 143, 144]. In addition, the influence of non-Aβ factors, like membranes, have been implicated to play a major role in the toxicity exerted by Aβ [145]. Experimental studies show that monomeric Aβ can interact with neuronal membranes and then seed the aggregation pathway [57], cause membrane destabilization of a raft membrane [146], and bind electrostatically to the polar headgroups of a phosphatidylcholine (PC) membrane [147]. Computational studies suggest that Aβ forms aggregates in the membrane and does not exit the membrane [148] and that dimerization can occur in the membrane and prevent Aβ release [149]. In addition, experimental and computational studies show that secondary structure of Aβ can also influence type and degree of interaction with various membrane environments [150-152], in addition to membranes influencing the secondary structure of Aβ [153-155]. Taken together, it becomes evident that the starting structure, species (monomer, dimer, trimer, etc.), and position of Aβ relative to model membranes can critically influence aggregation of Aβ and its interaction with membranes. Lipid type and composition of the membrane can also greatly affect these protein-membrane interactions.

Lipid type and composition have often been variables in studies that detail the interaction of Aβ with membranes, making it hard to compare between studies with different experimental design and conditions. Some studies focus on a specific membrane composition (zwitterionic or anionic) [156-158] or the role of cholesterol or ganglioside-GM1 [67, 150, 159-162] related to Aβ-membrane interactions. In order to assess the influence of lipid type on Aβ membrane-interactions, a variety of model membranes were utilized in the present study to systematically compare effects of lipid type under the same conditions and parameters. Lipids most commonly found in eukaryotic cell membranes were utilized to mimic peptide-membrane interactions that

may be physiologically relevant [163, 164]. In addition, since the focus of this study is to assess the influence of Aβ toxicity, lipid types and domains most frequently found in neuronal cells were utilized [165, 166]. Model membrane systems used in this study included single component phospholipid bilayers (zwitterionic palmitoyloleoylphosphatidylcholine (POPC) and anionic palmitoyloleoylphosphatidylserine (POPS)), a two component bilayer (1:1 POPC: palmitoyloleoylphosphatidylethanolamine (POPE)), a raft bilayer (Raft) containing 1:1:1 POPC:cholesterol:palmitoylsphingomyelin (PSM), and the previously mentioned raft bilayer containing 6.67% ganglioside-GM1 on one leaflet (Raft + GM1). These model membranes are comparable to those used in a previous study, allowing for comparison with those results [65].

Finally, in order to assess Aβ-membrane interactions and their relationship to toxicity, both human and rat versions of Aβ were studied in the presence of the model membranes discussed above. Studies have indicated that the hallmark characteristics of AD are absent in wild-type rodents [167-169]. Moreover, transgenic mice and rats expressing the human Aβ variant are used to study AD and they are observed to form plaques and exhibit symptoms characteristic of cognitive dysfunction. Murine and rat (*Rattus norvegicus*) Aβ display high sequence identity to human Aβ, with only three amino acid differences (R5G, Y10F, and H13R) (Figure 3.1), but murine/rat Aβ exhibits decreased fibril formation with age [170-172]. A notable difference between rat Aβ and human Aβ sequences is the positioning of an arginine residue. The role of electrostatics influencing the protein-membrane interactions has been briefly discussed [147] and provides an interesting avenue for deepening our understanding of mechanistic details of AD. By studying both the human and rat variants of $A\beta_{(42)}$, assessment and comparison based on position of a positively charged residue can be performed. It is hypothesized that the position of arginine is influential in Aβ-membrane interactions given the role of electrostatics in peptide-membrane interactions. From here, assessment on the role of sequence and lipid type on membrane perturbation and the influence of the membrane on Aβ can be performed.

The use of molecular simulations to study the atomistic detail of Aβ-membrane interactions and complement experimental work has greatly increased. Molecular dynamics (MD) simulations are well-suited to explore peptide-membrane interactions and determine the degree of influence of lipid types on Aβ-membrane interactions as well as to also assess key residues of Aβ that are dictating the interaction [173]. In this study, particular care was taken in selecting the starting structure of Aβ and its initial position relative to the model membranes. It is in the scope of this report to show the interactions of monomeric human or rat $A\beta_{(42)}$ ($HA\beta_{(42)}$ and $RA\beta_{(42)}$, respectively) in what might mimic the events after proteolytic cleavage and release from the membrane, without bias related to peptide placement on the model membranes. This simulation system follows the generally accepted progression of the aggregation pathway, in that monomeric $A\beta_{(42)}$ can progress to form oligomers and fibrils or interact with the neuronal cell membranes as monomers or higher order structures [174]. The center of mass (COM) of each equilibrated $A\beta_{(42)}$ starting structure was placed at least 3.0 nm away from each model membrane to provide non-biased interactions with the membrane (Figure 2). Herein, this study seeks to comparatively assess how $HA\beta_{(42)}$ and $RA\beta_{(42)}$ interact with various model membranes and the role of electrostatics on peptide-membrane interactions, ultimately providing insight into the molecular mechanisms of toxicity leading to AD.

## 3.3 Methods

### 3.3.1 System Construction and MD Simulations - Starting Structures of $A\beta_{(42)}$

The starting structure of $A\beta_{(42)}$ utilized in MD simulations can greatly influence peptide-membrane interactions. To mimic the structure of $A\beta_{(42)}$ in solution, molecular dynamics simulations were performed on human (*Homo sapiens*) and rat (*Rattus norvegicus*) $A\beta_{(42)}$ ($HA\beta_{(42)}$ and $RA\beta_{(42)}$, respectively) in water and salt, with the resulting structures being used in subsequent simulations with model membranes. The starting coordinates of $HA\beta_{(42)}$ were taken from PDB entry 1IYT [175], a NMR solution structure in an apolar environment. $RA\beta_{(42)}$ coordinates were generated by taking the 1IYT structure and changing three residues, R5G, Y10F, and H13R (Figure 3.1), using DeepView-Swiss-PdbViewer [176] (http://www.expasy.org/spdbv/). The sequence reference for $RA\beta_{(42)}$ is UniProtKB - P08592, residues 671-713. The lowest energy rotamer of each altered amino acid sidechain was selected. Residues were deprotonated or protonated to mimic the most prevalent ionized species at pH 7.4, with the ionizable residue sidechains charged as follows: Glu and Asp (-1), His net-neutral, and Lys and Arg (+1). Structures were then centered in a dodecahedral box with a minimum solute-box distance of 1.0 nm and solvated with SPC water [114]. $Na^+$ and $Cl^-$ ions were added to mimic a concentration of 0.150 M NaCl and to maintain a net-neutral system. All simulations, including peptide-membrane simulations described below, were performed using the GROMACS software package, version 4.6.0 [68, 115] and the GROMOS53A6 force field [70]. Energy minimization on the structures was performed using the steepest descent method. System equilibration was performed in two steps, NVT and NPT. Three replicates, defined as independent trajectories started with different random starting velocities in NVT, were performed for both $HA\beta_{(42)}$ and $RA\beta_{(42)}$ in 0.150 M NaCl. The first equilibration step, NVT, was applied to the system for 100 ps using the Berendsen weak coupling method [116] to maintain a temperature of 310 K. Following NVT, NPT was performed for 100 ps, using the Nosé-Hoover thermostat [74, 75] and Parrinello-Rahman barostat [76, 77] to maintain temperature (310 K), and pressure (1 bar). For both NVT and NPT, position restraints were imposed on all protein heavy atoms. After equilibration, position restraints were removed and MD simulations were performed using three-dimensional periodic boundary conditions, with bond lengths constrained using P-LINCS [117], allowing an integration time step of 2 fs. Short-range cutoffs for all nonbonded interactions were set to 1.2 nm and the smooth particle mesh Ewald (PME) method [79, 80], with cubic interpolation and Fourier grid spacing of 0.16 nm, was used to calculate long-range electrostatic interactions. Simulations were run to 200 ns, when it was observed that backbone root-mean-square deviation (RMSD) and secondary structure of $HA\beta_{(42)}$ and $RA\beta_{(42)}$ were stabilized, with stabilization classified as no major structural changes during the last 100 ns of simulation time. Secondary structure was evaluated according to the DSSP algorithm [118]. Backbone RMSD clustering, using a cutoff of 0.2 nm was performed using the method of Daura et al. [119], and structures that were the center structure of the largest cluster for the last 100 ns of simulation time were then placed in the presence of model membranes (Fig. 3.S1).

### 3.3.2 System Construction and MD simulations – Peptide-Membrane Systems

Each structure of $HA\beta_{(42)}$ and $RA\beta_{(42)}$, derived from clustering as described above (Fig. 3.S1), was randomly placed above a model membrane so that the minimum atom distance between a protein atom and membrane atom was at least 2.4 nm (Figure 3.S2, Table 3.1). Allowing the peptide to potentially change structure and direction before interaction with the model

membranes can provide insight into what amino acids are acting as the driving force of interaction, rather than biasing interaction by placing the peptide on or within long-range interaction distances to the membrane. Model membranes used in this work include: **(1)** POPC, **(2)** 1:1 POPC/POPE, **(3)** POPS, **(4)** Raft (1:1:1 POPC/PSM/cholesterol) and **(5)** Raft + 6.67% ganglioside-GM1 (Raft + GM1). The coordinates and topologies for the membranes were based on previous work [71, 177-180]. Details of membrane composition, size, and minimum distance of human or rat $A\beta_{(42)}$ to the membrane are shown in Table 3.1. Three replicates, with each replicate containing a starting structure from replicates 1-3 of the peptide in 0.150 M NaCl solution simulations, were run for each model membrane for human and rat $A\beta_{(42)}$. In total, 15 simulations of 300 ns were run with $HA\beta_{(42)}$ and each lipid type and 15 simulations were run with $RA\beta_{(42)}$ and each lipid type, totaling 9 μs of simulation time for peptide-membrane simulations.

**Table 3.1.** Details of System Contents.

| Membrane | Membrane Composition | Membrane Dimensions (nm - *x* x *y* x *z* ) after energy minimization | Minimum Distance between Peptide + Membrane (nm) | |
|---|---|---|---|---|
| | | | $HA\beta_{(42)}$ | $RA\beta_{(42)}$ |
| POPC | 128 POPC | 6.34 x 6.31 x 15 | Rep 1: 3.2<br>Rep 2: 2.8<br>Rep 3: 3.1 | Rep 1: 2.8<br>Rep 2: 3.0<br>Rep 3: 3.0 |
| POPS | 128 POPS | 5.48 x 5.74 x 15 | Rep 1: 2.8<br>Rep 2: 3.0<br>Rep 3: 3.0 | Rep 1: 2.8<br>Rep 2: 2.8<br>Rep 3: 2.9 |
| POPC:POPE | 144 POPC<br>144 POPE | 8.90 x 8.90 x 15 | Rep 1: 3.1<br>Rep 2: 2.9<br>Rep 3: 3.1 | Rep 1: 3.0<br>Rep 2: 3.1<br>Rep 3: 3.0 |
| Raft | 129 POPC<br>119 PSM<br>121 Cholesterol | 8.75 x 8.75 x 15 | Rep 1: 2.9<br>Rep 2: 3.0<br>Rep 3: 2.8 | Rep 1: 2.6<br>Rep 2: 2.6<br>Rep 3: 2.5 |
| Raft + GM1 | 129 POPC<br>94 PSM<br>121 Cholesterol<br>25 GM1 | 8.67 x 8.67 x 15 | Rep 1: 2.5<br>Rep 2: 2.4<br>Rep 3: 2.5 | Rep 1: 2.5<br>Rep 2: 2.7<br>Rep 3: 2.6 |

After the peptide was randomly placed at least 2.4 nm away from the membrane, the peptide-membrane system was solvated with SPC water [114], and $Na^+$ and $Cl^-$ ions were added to mimic a concentration of 0.150 M NaCl and to maintain a net-neutral system. The equilibration (energy minimization, NVT, NPT) and MD simulation protocols for the peptide-membrane simulations were the same as the protein in solvent simulations, with the following additions or modifications. An annealing step was added after NVT equilibration, which linearly heated from 100 to 310 K, at 1 bar pressure for 1 ns using the Berdensen algorithm [116]. The protein, membrane, and solvent (water and ions) were coupled separately and position restraints were held on all protein heavy atoms during all steps of equilibration (NVT, annealing, NPT) and released during MD simulations. Short-range nonbonded interactions were set to 1.2 nm. MD simulations were run for 300 ns, which exceeds literature values of 100-200 ns in simulation

time as being appropriate and adequate to observe changes in both the peptide and membrane as a result of their interaction [63, 65, 149]. In addition, backbone RMSD and secondary structure of the peptide were used to determine convergence, which was defined as $A\beta_{(42)}$ being stable and unchanging in its interaction with the membrane. A simulation to 1.5 μs of $HA\beta_{(42)}$ with POPC was performed to test for further insertion into the membrane. This longer simulation showed that the peptide did not insert further into the membrane and remained in a position similar to that at the end of 300 ns (Fig. S2), also indicating that 300 ns was an adequate duration for peptide-membrane simulations. All analysis was performed using programs within the GROMACS program suite or in-house written scripts. In addition to DSSP, assessment of secondary structure was performed by using free energy calculated by generating histograms from backbone f and y dihedral angles according to equation (1)

$$\Delta G(\phi,\psi) = -\mathrm{k_b T}\ln[P(\phi,\psi) - P_{max}] \quad (1)$$

where $P_{max}$ is the (f,y) pair with maximum probability, thus corresponding to a free energy value of zero. Deuterium order parameter analysis was performed to assess the order of the lipid acyl chains, relative to the bilayer normal. Equation (2) explains the how these parameters are calculated.

$$-S_{CD} = \langle \frac{3cos^2\theta - 1}{2} \rangle \ , \quad (2)$$

where θ is the angle between the C-D bond and bilayer normal and angle brackets represent that the θ value is averaged over all equivalent atoms (e.g., all C2 on the lipid acyl chain) over the time period analyzed. In addition, in order to determine local and global affects of $A\beta_{(42)}$ binding to the membrane, a lipid tier analysis (Fig. 3.S5) based on the work of Bachar and Becker was performed [181]. Analysis on area-per-lipid (APL) and membrane bilayer thickness was performed using GridMAT-MD [182]. All averages presented represent the average of three replicates for that simulation set. PyMOL was used for visualization of results [120]. Results were subjected to statistical analysis using a two-tailed *t*-test, with statistical significance determined if $p < 0.05$.

## 3.4 Results and Discussion

The aggregation pathway of $A\beta_{(42)}$ is not well understood and focus is currently shifting towards understanding the generation and actions of low-molecular-weight oligomers of $A\beta_{(42)}$ that may be the most toxic species [174]. Cleavage and release of $A\beta_{(42)}$ from the neuronal cell membrane is an important part of this aggregation pathway, and $A\beta_{(42)}$ typically proceeds through several intermediate structural forms, transitioning from helix to random coil to β-hairpin/β-strand in the aggregation of monomeric Aβ to fibrillar Aβ [183, 184]. Because one of the primary routes hypothesized for Aβ toxicity is neuronal cell membrane disruption, the interaction of Aβ species present in the extracellular region of neuronal cells must be understood in detail.

Another novel component of this study was to include the rat variant of $A\beta_{(42)}$. Few MD studies of rat $A\beta_{(42)}$ are reported in the literature [185, 186], providing an avenue to explore how the three amino acid differences (Figure 3.1) affect the structure and dynamics of $A\beta_{(42)}$ and interaction with model membranes. Rat $A\beta_{(42)}$ does not display the hallmark traits of plaque formation or neuronal cell death, providing an interesting, unexplored comparison to $HA\beta_{(42)}$

[167-169]. It is proposed that the change in position of arginine between $HA\beta_{(42)}$ and $RA\beta_{(42)}$ can influence the conformational state of the peptide and its degree and type of perturbation on model membranes. By studying both $HA\beta_{(42)}$- and $RA\beta_{(42)}$-membrane interactions, we can assess the role and position of arginine in the $A\beta_{(42)}$ sequence and its potential for toxicity. The influence of the position of the arginine is discussed below in regards to its role in membrane perturbation and its role in potential toxicity relevant to $HA\beta_{(42)}$.


**Figure 3.1.** Sequence comparison of human and rat $A\beta_{(42)}$. Residues are represented as hydrophobic (black), polar (green), positive charge (blue), and negative charge (red). Arrows indicate variance between sequences.

We begin the discussion by describing the approach and results found for this study to answer the following questions: (1) What effect do model membranes with varying lipid composition have on the secondary structure of $A\beta_{(42)}$? , (2) How does $A\beta_{(42)}$ cause membrane perturbation?, and (3) By comparing $HA\beta_{(42)}$- and $RA\beta_{(42)}$-membrane interactions, what role does sequence play in these peptide-membrane interactions?

### 3.4.1 Effect of Model Membranes on the Secondary Structure and Aggregation Potential of $HA\beta_{(42)}$ and $RA\beta_{(42)}$

For these simulations, the selection of the GROMOS53A6 force field was appropriate given that it has been shown to reasonably reproduce key structural features of monomeric Aβ [72], has been used in used in multiple Aβ-membrane simulations [64, 65, 149, 157], and contains parameters for a commonly used lipid force field [71]. Starting structures of $HA\beta_{(42)}$ and $RA\beta_{(42)}$ for simulations in the presence of membranes were selected after equilibration and MD simulations of the NMR structure (PDB ID: 1IYT) in water and 0.150 M NaCl. The structure of $RA\beta_{(42)}$ was generated by using SwissModel [176] to alter amino acids (R5G,Y10F, H13R) in the NMR structure of $HA\beta_{(42)}$ to match the $RA\beta_{(42)}$ sequence. $HA\beta_{(42)}$ and $RA\beta_{(42)}$ lost most of the initial α-helical structure during MD simulations and adopted a mixture of random coil and β-strand structure, consistent with reports in both experimental and computational studies (Table 3.2) [101, 185, 187]. Three replicates of both $HA\beta_{(42)}$ and $RA\beta_{(42)}$ in solution were performed and a representative structure from each replicate, as determined by RMSD clustering (Fig. 3.S1), was randomly placed above each model membrane at a distance beyond the cutoff for long-range interactions (Figure 3.2). This specific approach has not yet been utilized in all-atom MD simulations and provides an interesting perspective, as well as extensive sampling, in how extracellular, monomeric species of $A\beta_{(42)}$ interact with model membranes.

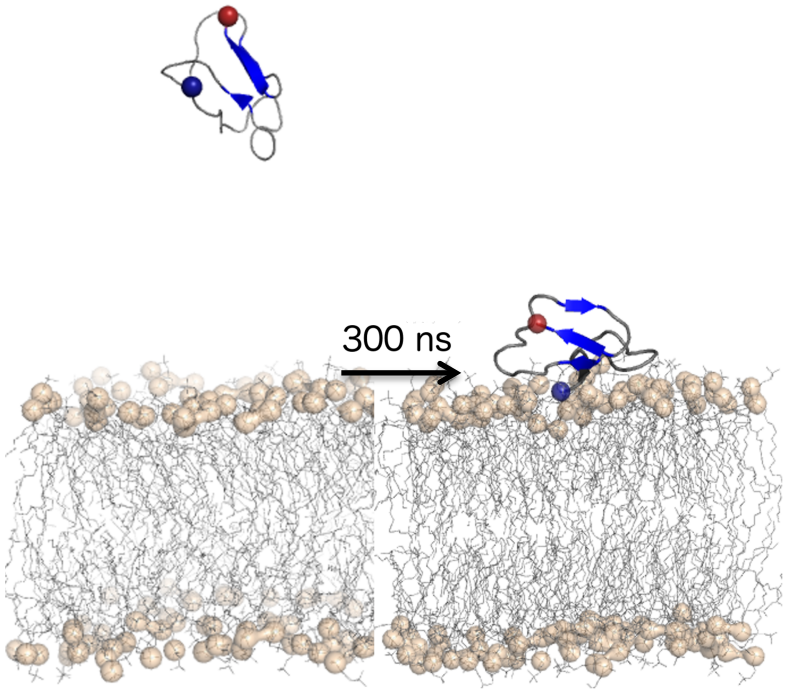


**Figure 3.2.** Depiction of starting and final position of $HA\beta_{(42)}$ relative to POPC membrane. The peptide is shown as a cartoon, with secondary structure colored blue (β-strand) and gray (coil). N-(blue) and C-(red) termini are shown as spheres. Lipids are shown as gray lines, with the phosphate atom shown as tan spheres. The left panel shows the starting position of $HA\beta_{(42)}$ relative to a POPC membrane at the start of MD simulation, whereas the right panel shows the cluster structure of the last 100 ns of simulation time of $HA\beta_{(42)}$ interacting with the POPC membrane.

The structures of $HA\beta_{(42)}$ and $RA\beta_{(42)}$ after MD simulations in solution exhibited large percentages of random coil (73 ± 4 and 66 ± 7), with regions of β-strand structure (23 ± 4 and 27 ± 5, respectively) developing primarily in the C-terminal region (Table 3.2, Figure 3.3). There are no amino acid differences from residues 30-42 in the human and rat $A\beta_{(42)}$ variants, so the similar amounts of β-strand structure in the C-terminal region were expected. Slight variation between $HA\beta_{(42)}$ and $RA\beta_{(42)}$ manifests in residues 10-20, which houses the central hydrophobic core (CHC – residues 17-21), with the presence of α-helical structure being slightly greater in $RA\beta_{(42)}$ than in $HA\beta_{(42)}$. This increase in α-helical structure in $RA\beta_{(42)}$ is most likely influenced by Arg-13, given that arginine has a higher propensity of being found in α-helical structure [188], and may affect the structure of the CHC region due to its proximity to that region (Figure 3.3). Studies have shown that residues 17-21 are the shortest fragment of Aβ to form β-strand structure and are essential in full length Aβ oligomer formation [189], which makes the increase of β-strand structure in residues 10-20 in $HA\beta_{(42)}$, as compared to starting structures, interesting and relevant to potential aggregation ability. The higher propensity for the CHC region of

$RA\beta_{(42)}$ to adopt α-helical structure compared to the CHC region of $HA\beta_{(42)}$ was even more evident in the simulations with model membranes, further confirming a role for Arg-13 in $RA\beta_{(42)}$ in influencing secondary structure and aggregation potential (Figure 3.3).

**Table 3.2.** Average secondary structure composition (shown in %) of $HA\beta_{(42)}$ or $RA\beta_{(42)}$.[a]

| | Coil | | β-strand | | α-helix | |
|---|---|---|---|---|---|---|
| System | $HA\beta_{42}$ | $RA\beta_{42}$ | $HA\beta_{42}$ | $RA\beta_{42}$ | $HA\beta_{42}$ | $RA\beta_{42}$ |
| Starting Structure | 73 ± 4 | 66 ± 7 | 23 ± 4 | 27 ± 5 | 4 ± 4 | 7 ± 7 |
| POPC | 73 ± 5 | 71 ± 9 | 27 ± 5 | 23 ± 10 | 0 ± 0 | 6 ± 8 |
| POPS | 75 ± 6 | 63 ± 15 | 23 ± 4 | 28 ± 9 | 2 ± 3 | 9 ± 8 |
| POPC:POPE | 77 ± 10 | 72 ± 10 | 23 ± 9 | 27 ± 5 | 0 ± 0 | 1 ± 1 |
| Raft | 72 ± 2 | 66 ± 10 | 28 ± 3 | 28 ± 13 | 0 ± 0 | 6 ± 11 |
| Raft + GM1 | 74 ± 9 | 63 ± 10 | 23 ± 7 | 30 ± 13 | 3 ± 1 | 7 ± 9 |

[a] Percentages represent averages over the final 100 ns of simulation time for three replicates of each system, with corresponding standard deviations.

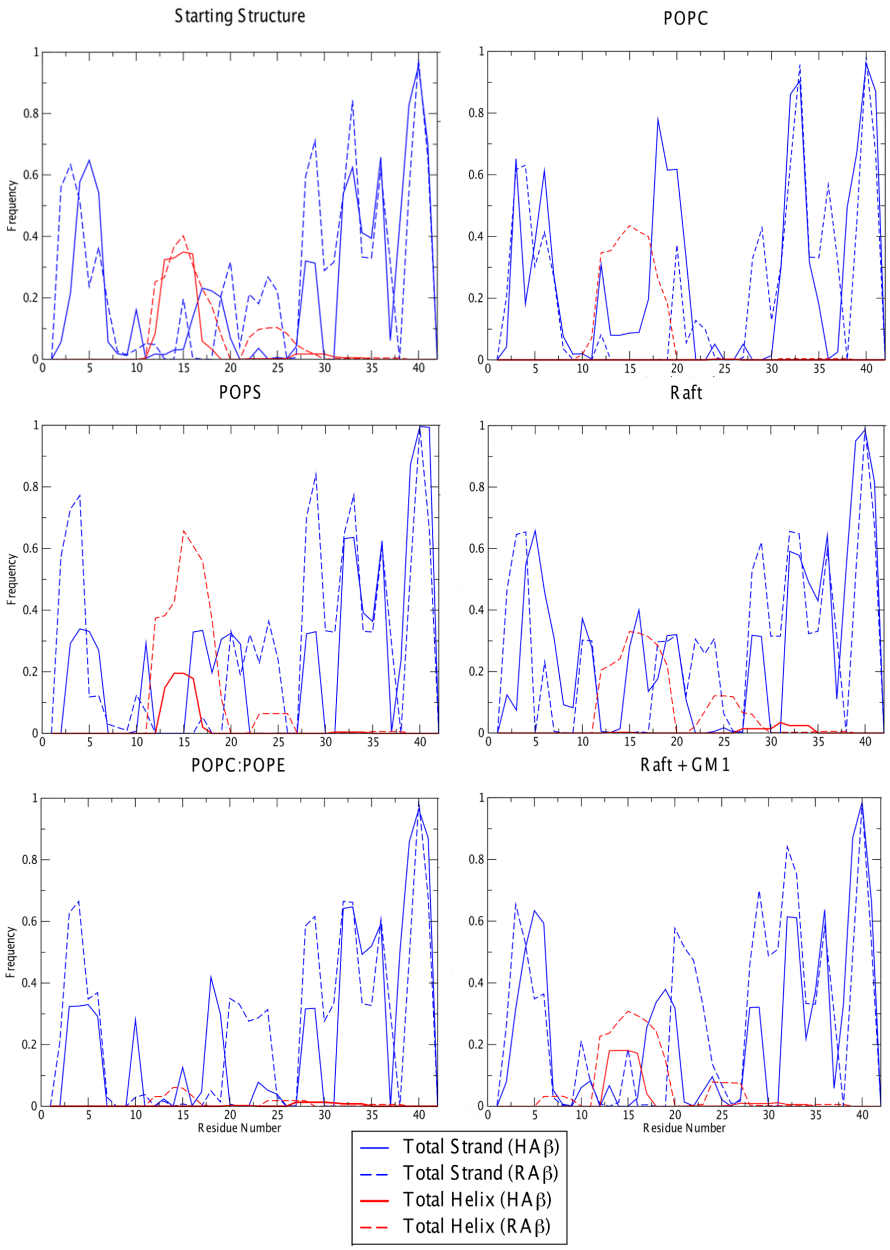


**Figure 3.3.** Frequency of average secondary structure per residue of $A\beta_{42}$ in the presence of model membranes. Frequency is calculated over the last 100 ns of simulation time for each replicate. β-strand structure is shown in blue, α-helix is in red (Human $A\beta_{42}$ –solid line, Rat $A\beta_{42}$ – dashed line).

Although some differences in secondary structure were apparent in particular segments of $HA\beta_{(42)}$ and $RA\beta_{(42)}$ when evaluated by residue, including some changes in the presence of the membrane systems (Figure 3.3), an analysis of secondary structure for the entire peptides did not show statistically significant differences (Table 3.2). However, some general trends were evident. For example, secondary structure of $HA\beta_{(42)}$ and $RA\beta_{(42)}$ was not influenced by POPS, POPC:POPE, and Raft + GM1 membranes. This result was interesting in that Manna et al. have reported an increase in β-strand formation in the presence of GM1 containing membranes [160].

A measurable, but not significant, increase in β-strand content was observed in the presence of pure POPC and Raft membranes (23 ± 4 to 27 ± 5 and 28 ± 3, respectively) for $HA\beta_{(42)}$ but not $RA\beta_{(42)}$ (Table 3.2). These results were further supported by Ramachandran plots (Fig. 3.S3), which showed a decrease in sampling of α-helical structure and an increase in β-strand structure for $HA\beta_{(42)}$ with POPC and Raft membranes relative to the starting structures based on visual analysis. The change in secondary structure in $HA\beta_{(42)}$ with POPC and Raft membranes was not observed with $RA\beta_{(42)}$ with POPC and Raft membranes, indicating this measurable difference was specific to $HA\beta_{(42)}$ interactions with POPC and Raft membranes.

Visual analysis of the structures of $HA\beta_{(42)}$ and $RA\beta_{(42)}$ in the presence of membranes revealed interesting differences. When qualitatively looking at results in the presence POPC and Raft, it was observed that $HA\beta_{(42)}$ was interacting with the membrane in a way that indicates potential for another peptide to form an extended β-sheet structure with the bound $HA\beta_{(42)}$ (Figure 3.4). This aggregation potential is best described by the positioning of the β-sheet structure as parallel to the plane of the bilayer and exposed to solvent, rather than vertical or masked by another region of $A\beta_{(42)}$ not exhibiting β-strand structure. This difference in positioning of β-strand structure was observed when comparing $HA\beta_{(42)}$ with POPC and Raft membranes to $HA\beta_{(42)}$ with POPS or any $RA\beta_{(42)}$ membrane system (Figure 3.4). These quantitative (Table 3.2) and visual (Figure 3.4) data reveal that the structure of $HA\beta_{(42)}$ was slightly influenced by POPC and Raft membranes only, whereas membranes had little to no influence over $RA\beta_{(42)}$ structure, suggesting the potential for greater aggregation of HAβ(42) over RAβ(42) in the presence of these lipid microdomains.

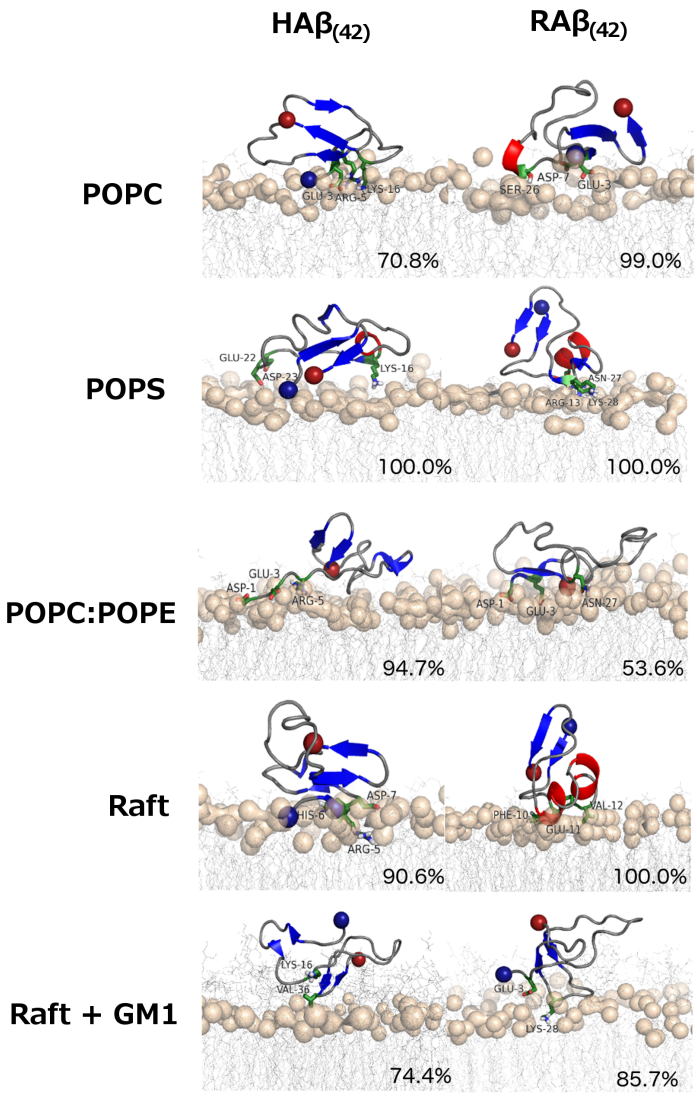


**Figure 3.4.** Dominant morphologies of Aβ interaction with model membranes from RMSD clustering. A representative replicate from each simulation set was chosen for clarity. The representative replicate was chosen based on similarity to secondary structure average. The structures shown are the central structure of the first cluster, as based on RMSD clustering with a cutoff of 0.2 nm. Percentages represent the number of frames each structure represented over the last 100 ns. The peptide is shown as a cartoon, with secondary structure colored blue (β-strand), red (α-helix), and gray (coil). N-(blue) and C-(red) termini are shown as spheres. Lipids are shown as gray lines, with the phosphate atom shown as tan surface for perspective. Key residues based on distance plots are shown in green stick and labeled.

### 3.4.2 HAβ$_{(42)}$ and RAβ$_{(42)}$ Binding Causes Membrane Rigidification

By placing the peptides above each model membrane at a distance beyond the cutoff for long-range interactions, so as not to bias the regions of Aβ$_{(42)}$ that interacted with the model membranes, we could assess key residues that might drive the interaction between the peptide and model membranes. To insure that 300 ns was an adequate length of time for simulations, a simulation of HAβ$_{(42)}$ with POPC was also run for 1.5 μs. There was no observable change in

residue insertion depth or effect on the membrane between 300 ns and 1.5 μs (Fig. 3.S2), indicating that our simulation time of 300 ns was appropriate. While other studies have shown that Aβ can penetrate below the headgroup region and into membranes [49, 152, 190], this observation is most likely influenced by the starting structure, typically α-helical, and the position of the peptide relative to the membrane. It is concluded that by not pre-embedding or positioning Aβ into/on the membrane and using a starting structure consisting of mostly random coil and β-strand structure, it is not favorable for $HA\beta_{(42)}$ and $RA\beta_{(42)}$ to insert into the bilayer under our simulation conditions. Instead, $HA\beta_{(42)}$ and $RA\beta_{(42)}$ interact predominantly with the polar headgroups, supporting the proposed carpeting effect model [191] or sinking-raft model of peptide-membrane interactions [192]. The surface interaction that was observed in our study, rather than penetration, can potentially allow other $A\beta_{(42)}$ peptide species to interact with $A\beta_{(42)}$ monomers already associated with the surface of the membrane. This finding relates well to other studies that discuss the role of monomeric Aβ–membrane interactions being the start of a seeding event for Aβ aggregation and fibril formation [193].

Experimental studies indicate that membrane fluidity decreases when Aβ interacts with model membranes [194-196]. The effect of $HA\beta_{(42)}$ and $RA\beta_{(42)}$ on membrane fluidity in our simulations was determined by calculating area-per-lipid (APL) (Table 3.3), bilayer thickness (Table 3.4), and deuterium order parameters (Figure 3.5). To assess the degree of perturbation that was caused by $A\beta_{(42)}$ interaction and binding to the polar headgroups, control simulations of the model membranes in a solution of water and 0.150 M NaCl were performed and run to 300 ns. One of the interesting and significant indications of membrane perturbation as caused by $HA\beta_{(42)}$ or $RA\beta_{(42)}$ binding were the results relevant to APL (Table 3.3) and the supporting trends observed in bilayer thickness (Table 3.4). A reduction in APL, as compared to controls, corresponds to a rigidification of the membrane as the lipids pack closer together as a result of peptide binding. The increase in rigidification of the membranes produced by $HA\beta_{(42)}$ compared to the controls, from greatest effect to least effect, was POPC > POPC:POPE > POPS > Raft > Raft + GM1. As noted in Table 3, the effects of $HA\beta_{(42)}$ binding are statistically significant, compared to controls, in systems with POPC, POPS, POPC:POPE, and Raft with $HA\beta_{(42)}$. $RA\beta_{(42)}$ also caused rigidification, usually to a lesser extent as compared to $HA\beta_{(42)}$, in the following order: POPS > POPC:POPE > POPC > Raft > Raft + GM1 (Table 3.3). Bilayer thickness provides a corresponding measure of membrane fluidity, with increasing thickness indicating greater rigidification, as the lipid tails become more ordered and extended as the lipids pack closer together. Although the effects of $HA\beta_{(42)}$ and $RA\beta_{(42)}$ on bilayer thickness were not as dramatic as those for APL since thickness is for the entire bilayer rather than leaflet, the general trend again was indicative of increased rigidity in the same order of effect described above for $HA\beta_{(42)}$ and $RA\beta_{(42)}$ (Table 3.4). APL and bilayer thickness showed no change as compared to the control for $HA\beta_{(42)}$ and $RA\beta_{(42)}$ in the presence of Raft + GM1 (Tables 3.3 and 3.4), which will be discussed below in greater detail.

**Table 3.3.** Area per lipid head group (mean ± SD) in $Å^2$ (% difference from controls) for the interacting leaflet over the last 100 ns of each trajectory. [a]

| | Control | $HA\beta_{(42)}$ | $RA\beta_{(42)}$ |
|---|---|---|---|
| POPC | 62 ± 1 | 51 ± 1 (-18%)* | 53 ± 1 (-14%)* |
| POPS | 50.6 ± 0.3 | 45 ± 2 (-11%)* | 42.6 ± 0.3 (-16%)* |
| POPC:POPE | 54.5 ± 0.4 | 48 ± 1 (-12%)* | 47 ± 2 (-14%)* |
| Raft | 41.2 ± 0.1 | 38 ± 2 (-8%)* | 40 ± 2 (-3%) |
| Raft + GM1 | 42.4 ± 0.2 | 41.9 ± 0.2 (-1.2%) | 41.5 ± 0.2 (-2.2%) |

[a] Statistically significant differences from controls are designated with an asterisk.

**Table 3.4.** Bilayer thickness (mean ± SD) in nm (% difference from controls) over the last 100 ns of each trajectory.

| | Control | $HA\beta_{(42)}$ | $RA\beta_{(42)}$ |
|---|---|---|---|
| POPC | 3.9 ± 0.2 | 4.2 ± 0.1 (+7%) | 4.1 ± 0.1 (+5%) |
| POPS | 4.5 ± 0.1 | 4.7 ± 0.1 (+4%) | 4.8 ± 0.1 (+7%) |
| POPC:POPE | 4.2 ± 0.2 | 4.4 ± 0.1 (+6%) | 4.4 ± 0.2(+6%) |
| Raft | 4.3 ± 0.2 | 4.3 ± 0.1 (±0%) | 4.3 ± 0.1(±0%) |
| Raft + GM1 | 4.4 ± 0.3 | 4.4 ± 0.1 (±0%) | 4.4 ± 0.3 (±0%) |

APL and bilayer thickness analysis metrics allowed for an understanding on the type and degree of perturbation on the global level of the model membrane, whereas deuterium order parameters ($S_{CD}$) on lipids in closest proximity to the peptides, termed first tier lipids by Bachar and Becker [181], were studied to understand perturbation at the local site of peptide-membrane interaction. $S_{CD}$ on all lipid tiers and full leaflets were performed and showed similar trends to the first tier. $HA\beta_{(42)}$ binding to all membranes except Raft + GM1 increased the $S_{CD}$ value of the sn-1 chain of lipids closest to peptide binding compared to the control. $RA\beta_{(42)}$ binding to all membranes except Raft and Raft + GM1 similarly showed increased values of $S_{CD}$ relative to the controls. An increased $S_{CD}$ value represents more ordering of the lipid tails, consistent with APL and bilayer thickness results supporting rigidification of the lipids as a result of peptide binding. The increase in $S_{CD}$ value varied among lipid types based on $HA\beta_{(42)}$ or $RA\beta_{(42)}$ binding and agrees with results and order of effect observed in APL and bilayer thickness analysis metrics (Figure 3.5). For example, $HA\beta_{(42)}$ binding showed greater disruption and ordering of POPC and POPC:POPE membranes than POPS membranes in all analysis metrics. This observation indicates an ability to disrupt zwitterionic membranes to a greater extent than anionic membranes, most likely due to side chain insertion depth dictated by position of charge, either at the membrane/water interface or in the phosphate region of the membrane.

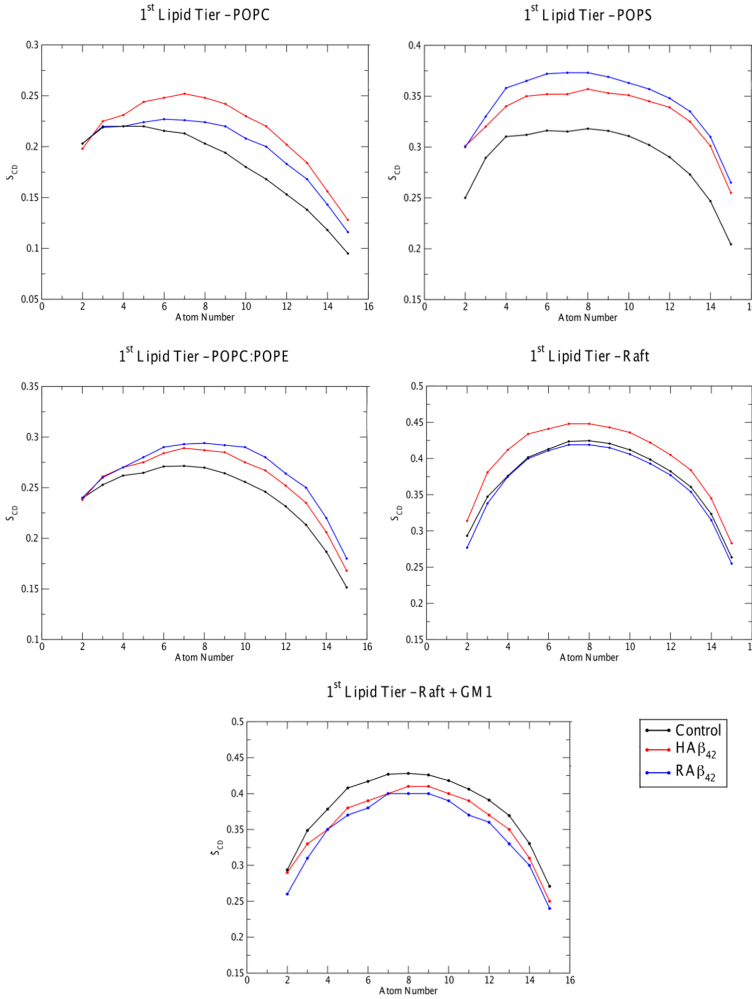


**Figure 3.5.** Deuterium order parameters on lipids in closest proximity to $AB_{42}$. Average deuterium order parameters ($S_{CD}$) of palmitoyl (sn-1) chain of PO lipids in model membrane simulations. For clarity, only the sn-1 chain is shown; however, parameters were also analyzed on the sn-2 chain and showed similar trends. The 1st tier of lipids, as based on the method of Bachar and Becker [181] was determined as the 16 lipids in closest proximity to the COM of $AB_{42}$ on the model membrane. Control (no peptide present) parameters for each carbon in the lipid chain are shown in black, with the average parameter over three replicates being shown for $HAB_{(42)}$(red) and $RAB_{(42)}$(blue) for each membrane simulation set.

In order assess if either $HA\beta_{(42)}$ or $RA\beta_{(42)}$ binding effected the degree of membrane perturbation for each lipid type, it was also of interest to compare deuterium order parameters, APL, and bilayer thickness for each membrane type after interaction with either $HA\beta_{(42)}$ or $RA\beta_{(42)}$. An interesting trend was observed related to degree of membrane perturbation in certain lipid types. This observation is best shown by comparing degree of perturbation in APL and deuterium order parameters, where it was observed that POPS lipids were perturbed to a greater extent in the presence of $RA\beta_{(42)}$ than $HA\beta_{(42)}$. Interestingly, POPC and Raft lipids were perturbed to a greater extent in the presence of $HA\beta_{(42)}$ than $RA\beta_{(42)}$ (Figure 3.5, Table 3.3). While not statistically significant in difference, we felt that this trend was worth discussion and can aid in the

discussion on the role of sequence in Aβ-membrane interactions. POPC and Raft membranes both have net-neutral lipid headgroups that do not have the ability to hydrogen bond with $A\beta_{(42)}$, whereas POPS and POPE lipids have either negatively charged or lipid headgroups capable of hydrogen bonding. $HA\beta_{(42)}$ perturbed lipid types whose headgroups lacked charged and hydrogen bonding capacity to a greater extent compared to $RA\beta_{(42)}$, which perturbed lipid types whose headgroups were charged or had hydrogen bonding capacity. Interestingly, POPC and Raft membranes are found in higher concentration in the exofacial leaflet of cell membranes, whereas POPS and POPE lipid types are found in higher concentration in the cytofacial leaflet.

Finally, the results discussed above also indicate that lipid composition plays a major role in the amount of perturbation that $HA\beta_{(42)}$ or $RA\beta_{(42)}$ binding can impose on a model membrane. The role of lipid composition, specifically the influence of the added cholesterol in a Raft membrane, on degree of membrane perturbation was also observed for Raft simulations with both $A\beta_{(42)}$ variants. By comparing the difference in extent and amount of perturbation caused by $HA\beta_{(42)}$ and $RA\beta_{(42)}$ to a pure POPC membrane compared to a Raft membrane (18% vs. 8 % and 14% vs. 3%, respectively for change in APL relative to the control), a decrease in perturbation effects is observed. This decrease in perturbation effects, as characterized by a minimal change in deuterium order parameters, APL, and bilayer thickness relative to the control, indicates that while $HA\beta_{(42)}$ or $RA\beta_{(42)}$ bound to the membrane headgroup region, with some positively charged residues interacting with the phosphate region (Figure 3.6), $HA\beta_{(42)}$ or $RA\beta_{(42)}$ binding did not effect lipid order to the extent that was observed in other model membranes. Therefore, it was concluded that cholesterol appeared to moderate the effect of $A\beta_{(42)}$ binding on membrane integrity based on all analysis metrics related to membrane integrity (Figure 3.5, Table 3.3 and 3.4) in our simulations, correlating with experimental findings [151].

### 3.4.3 Positively Charged Residues Influence $HA\beta_{(42)}$ and $RA\beta_{(42)}$ Binding

Some studies have noted the potential role of the N-terminal region in Aβ-membrane interactions [64, 65], though other studies disregard this region because it is not well resolved in structures that are reported [152, 197]. Our study concludes that the N-terminal region is important in that the change in position of the arginine ultimately affects the interaction of $HA\beta_{(42)}$ and $RA\beta_{(42)}$ with model membranes and influences the degree of perturbation observed (Figure 3.6). In order to assess what aspects of $A\beta_{(42)}$ binding were causing the rigidification previously discussed, analysis of residue insertion depth was performed. By examining residues that had the highest probability of inserting into the membrane, it is concluded that positively charged residues consistently get the closest to the phosphate atom in the lipid headgroups, as would be expected, but the position of the positive charges in the sequence influences the nature of the interactions (Figures 3.4 and 3.6).

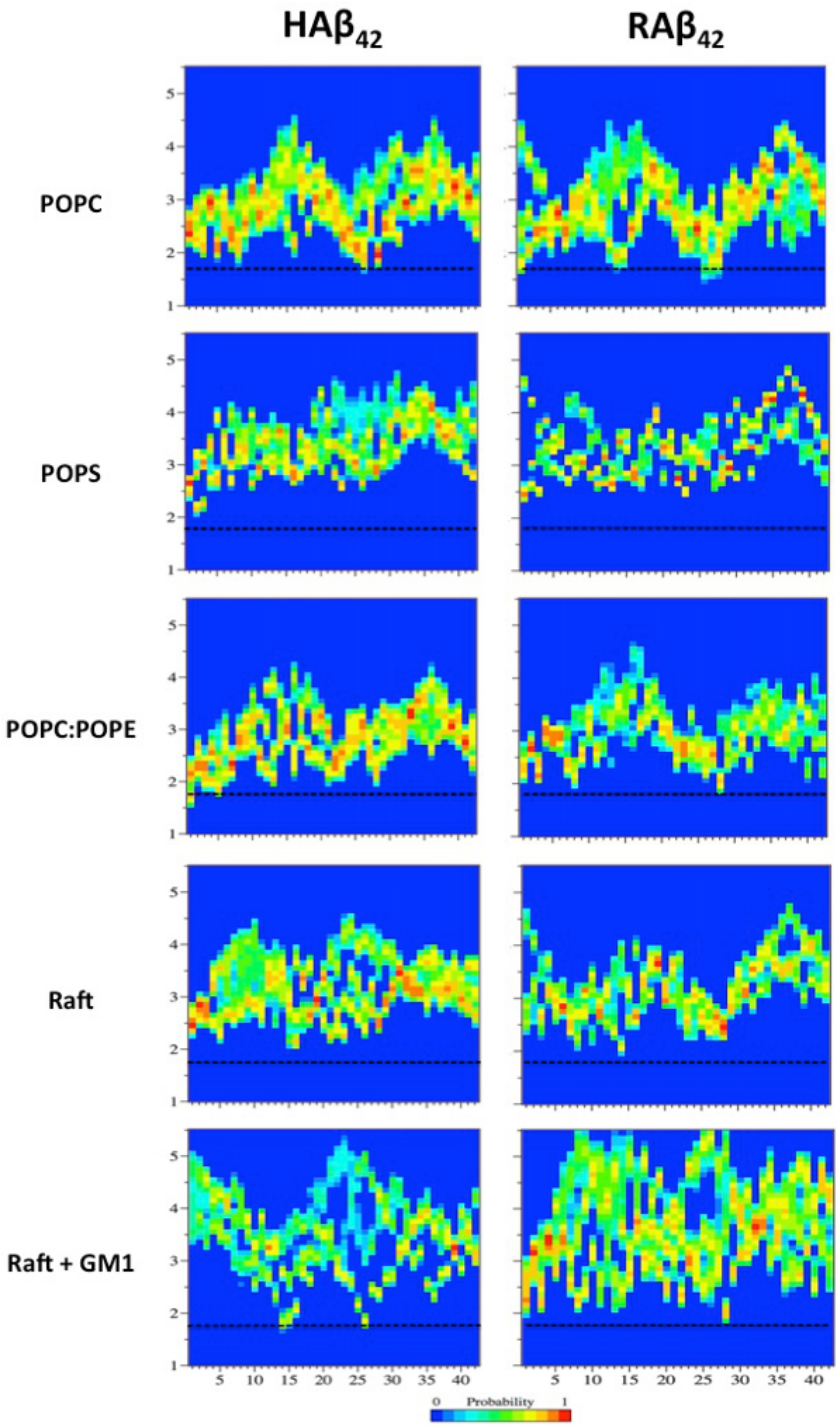


**Figure 3.6.** Global normalization of the frequency of Aβ residue center of mass (COM) occurrence at a distance, on the z-axis, from the COM of the membrane bilayer**.** Each plot contains all data points from 3 replicates in each simulation over the last 100 ns of simulation time. Residue number and distance (nm) are plotted on the x- and y- axis, respectively. The black dotted line represents the position of the phosphate atom in the lipid headgroup.

With $HA\beta_{(42)}$, close interactions are observed at residues Arg-5, Lys-16, and Lys-28 for most lipid types (Figure 3.6). However, the absence of the positive charge at position 5 in $RA\beta_{(42)}$ affects the interaction of the N-terminal region with the membranes, most notably with POPC, POPS, and raft membranes. With $HA\beta_{(42)}$, the N-terminal region has a very high probability of being embedded in the phosphate headgroups (the notable exception with Raft + GM1 will be discussed below). However, the N-terminal region (residues 1-5) in $RA\beta_{(42)}$ samples two positions relative to the bilayer (Figure 3.6). One region is closer to the phosphate headgroups as is seen with $HA\beta_{(42)}$, whereas the second region is approximately 2 nm further away from the phosphate headgroups. This trend in sampling of the N-terminal position relative to POPC, POPS, and Raft membranes indicates that by changing arginine to glycine at position 5, key interactions are lost with these membranes. Lys-16 and Lys-28, which are common to both $HA\beta_{(42)}$ and $RA\beta_{(42)}$, appear with high probability at or near the phosphate atoms for all model membrane interactions, and Arg-13 in $RA\beta_{(42)}$ likely contributes to these interactions. This finding gives insight as to why molecular tweezers that target Lys-16 and Lys-28 have been successful in attenuating Aβ toxicity [198, 199] and suggests a rational way to target $A\beta_{(42)}$-membrane interactions.

Further support for a role for Arg-5 in influencing $HA\beta_{(42)}$-membrane interactions comes from quantitating the number of hydrogen bonds between amino acid side chains and model membranes in the N-terminal region (Fig. 3.S4). An increased number of hydrogen bonds is particularly apparent in the N-terminal region, and more specifically at position 5 in $HA\beta_{(42)}$ relative to $RA\beta_{(42)}$. In addition, with an arginine at position 13 in $RA\beta_{(42)}$, an increased probability of hydrogen bonds is observed relative to $HA\beta_{(42)}$, but that region of the peptide would be expected to have an increased frequency of hydrogen bonds due to K16. The role and position of Arg-5 in $HA\beta_{(42)}$ was also confirmed by visually examining each replicate cluster structure (Figure 3.3) and monitoring the MD trajectories. In simulations of $HA\beta_{(42)}$ with POPC and Raft, the trajectories very clearly show the peptide reorienting as it approaches the membrane such that the N-terminal region is directed towards the membrane. The N-terminal region, including Arg-5, then bound to the model membrane. This change in orientation from the randomly placed starting structure was not observed in simulations of $RA\beta_{(42)}$ with POPC and Raft. While the N-terminal region of $RA\beta_{(42)}$ was observed to interact with other membranes (POPS, POPC:POPE), the change in orientation in the solvent and movement towards the membrane were not as distinct in terms of specific rearrangement before interacting with the membrane. These results, including depth of penetration, hydrogen bonding, and visual analysis, together indicate that the change in position of Arg-5 to Arg-13 influences the entire N-terminal region of residues 1-10, affecting the type and degree of interaction with model membranes.

Ganglioside-GM1 essentially blocked $HA\beta_{(42)}$ from interacting with the lipid headgroups of POPC and PSM. Ganglioside-GM1 carbohydrate groups bound with the N-terminal region of $HA\beta_{(42)}$, specifically Arg-5, and blocked $HA\beta_{(42)}$ binding and insertion into the polar headgroup regions of POPC and PSM. $RA\beta_{(42)}$ with Raft + GM1 results showed that the N-terminal region, which lacks the positively charged Arg-5, inserted closer towards the lipid headgroups (Figure 3.6). The N-terminus of $RA\beta_{(42)}$ is able to insert deeper and interact more with the polar headgroups of the Raft + GM1 membrane (Figure 3.6), given that the N-terminus of $RA\beta_{(42)}$ is lacking positive charge at position 5 and not hydrogen bonding as strongly to the carbohydrate headgroup as $HA\beta_{(42)}$ (Fig. 3.S4).

These results combined gives precedence for the role and position of Arg-5 in mediating these peptide-membrane interactions. Therefore, it is concluded that the specific positioning of Arg-5 in $HA\beta_{(42)}$ is essential to the dynamics and interactions of $A\beta_{(42)}$ with model membranes, ultimately relating into aggregation potential, as shown with secondary structure data (Figure 3.4, Table 3.3) and membrane perturbation abilities (Figure 3.5, Tables 3.3 and 3.4). Herein, based on the results obtained by membrane perturbation analysis metrics and the influence of the position of Arg-5 in the Aβ sequence and consequent membrane interactions, it is concluded that the environment in which Aβ peptides are found is influential on their amyloidogenic properties, which is also supported by recent experimental results [145]. These recent studies also suggest that aspects that contribute to differences in peptide neurotoxicity between $HA\beta_{(42)}$ or $RA\beta_{(42)}$ are primary structure, assembly structure, and non-Aβ factors [145]. Note that the rat referred to in that study is *Octodon degus,* for which the common name is "degu", which distinguishes it from *Rattus norvegicus*, the sequence of which was used in our study and previous ones referring to rat Aβ [167-171]. Most notably, only one amino acid sequence difference is present between human and degu Aβ (H13R). In this study, we have shown that primary structure, relevant to the change in position of arginine between $HA\beta_{(42)}$ and $RA\beta_{(42)}$ can influence folding properties and potential for aggregation. We also find that non-Aβ factors, represented here as multiple model membranes, are influenced by the variation between $HA\beta_{(42)}$ and $RA\beta_{(42)}$ sequence, shown by difference in type and degree of perturbation. Subsequent work on higher order structures of $HA\beta_{(42)}$ and $RA\beta_{(42)}$ is of great interest, and understanding the role of primary structure on these difference in toxicity and can give important insight into therapeutic design.

### 3.4.4 Conclusions

This study applied MD simulations to systematically compare degree and type of membrane perturbation caused by interaction and binding of Aβ, the principal toxic species in AD. In particular, variance in perturbation and binding based on lipid type and Aβ sequence were studied to assess the role of sequence and non-Aβ factors on peptide-membrane interactions. Starting structure and position of the peptide were found to be influential on Aβ-membrane interactions in these simulations compared to previous computational studies. By placing $A\beta_{(42)}$ above and outside of long-range interactions with model membranes, we were able to test how extracellular, monomeric $HA\beta_{(42)}$ or $RA\beta_{(42)}$ interacted with model membranes. This approach has not been utilized in previous MD simulations and gives a new perspective on $A\beta_{(42)}$–membrane interactions and the influence of sequence, most notably a change in position of an arginine. POPC and Raft membranes influenced secondary structure changes in $HA\beta_{(42)}$, with the changes suggesting an increase in potential aggregation ability (Figure 3 and 4). $HA\beta_{(42)}$ and $RA\beta_{(42)}$ were both found to cause membrane perturbation, to varying extents based on lipid composition, that resulted in the membrane becoming more gel-like and rigid (Figure 3.5, Tables 3.3 and 3.4). Cholesterol and ganglioside-GM1 attenuated the degree of perturbation that $A\beta_{(42)}$ exerted on the model membranes. While a test simulation run until 1.5 μs did not show $HA\beta_{(42)}$ or $RA\beta_{(42)}$ insertion into the membrane, this observation could be a limitation of MD simulations. Our results also highlight the susceptibility of certain lipid microdomains by $A\beta_{(42)}$ binding and the degree and type of perturbation in that positively charged residues were determined to be of key influence and a driving force in Aβ-membrane interactions. This observation may explain why targeting these residues has been successful in inhibiting the toxicity of Aβ [198, 199]. The variance in membrane perturbation observed between peptides

was determined to be due to the change of position of arginine (Figure 3.6), which ultimately affected the dynamics and membrane interactions of $RA\beta_{(42)}$ as compared to $HA\beta_{(42)}$ (Figures 3.3 and 3.6). This study rationalizes the role of lipid type and sequence on Aβ-membrane interactions and demonstrates that a non-Aβ factor, membranes, is an important factor to consider.

## 3.5 Acknowledgments

The authors thank Advanced Research Computing at Virginia Tech for computing time on the BlueRidge supercomputer and the Virginia Tech College of Agriculture and Life Sciences for the Graduate Teaching Scholars Fellowship (to A.M.B.).

## 3.6 Supporting Information

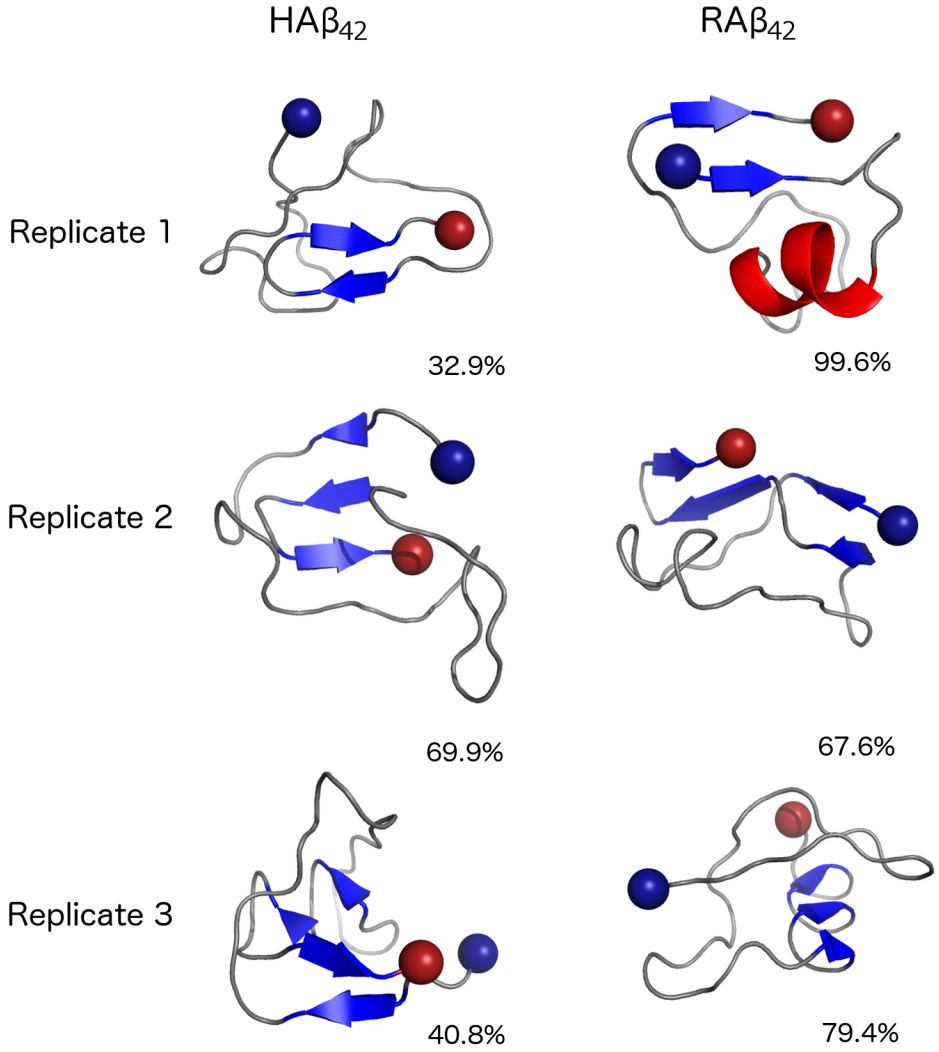


**Figure 3.S1.** Dominate morphologies of human or rat $A\beta_{42}$ from RMSD clustering. Each structure was respectively placed 2.4 nm away from model membranes to assess unbiased interaction. The peptide is shown as cartoon, colored by secondary structure (grey-coil, blue-β-strand, red-α-helix). N-terminus is shown as blue sphere, while the C-terminus is shown as red sphere. Percentages represent the number of frames during the last 100 ns of simulation time that

are in the dominant cluster.

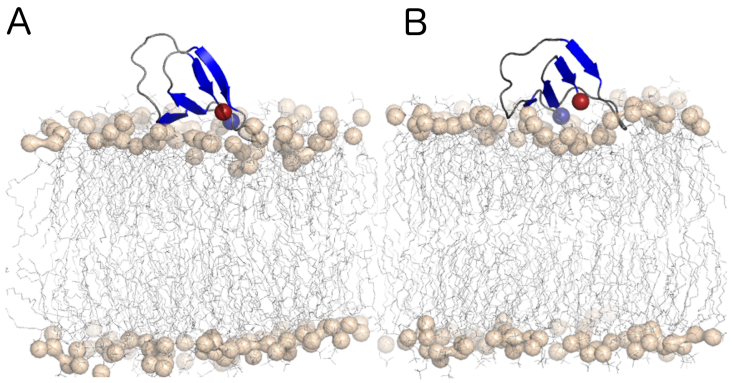


**Figure 3.S2.** Dominant morphologies of Aβ interaction with POPC at (A) 300 ns and (B) 1.5 μs. The peptide is shown as a cartoon, with secondary structure colored blue (β-strand), red (α-helix), and gray (coil). N-(blue) and C-(red) termini are shown as spheres. Lipids are shown as gray lines, with the phosphate atom shown as tan surface for perspective

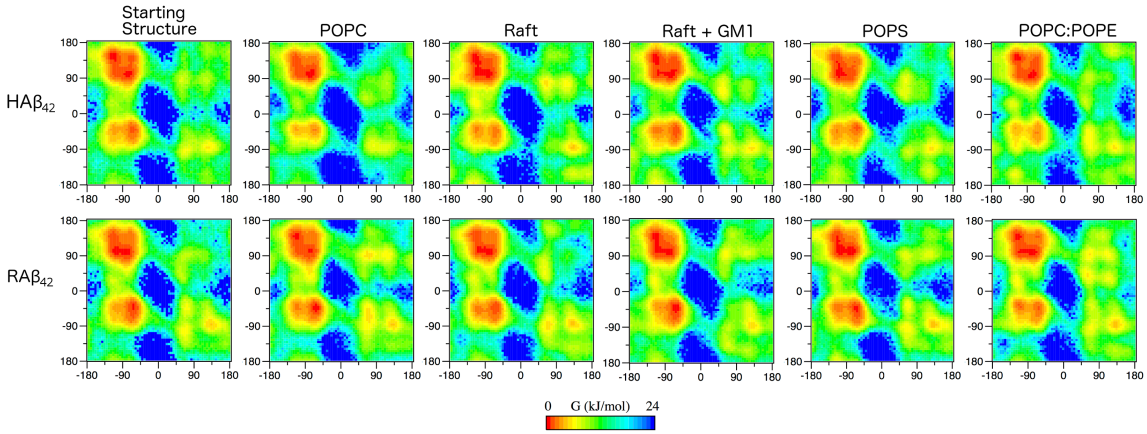


**Figure 3.S3.** Free energy surfaces constructed from Ramachandran plots of $HA\beta_{42}$ and $RA\beta_{42}$ before interaction with a membrane (starting structure) and after interaction with a membrane (as labeled). Each plot is a composite image of the 3 replicates run for each simulation set. Backbone $\phi$ and $\psi$ dihedral angles are plotted on the *x*- and *y*-axes, respectively.

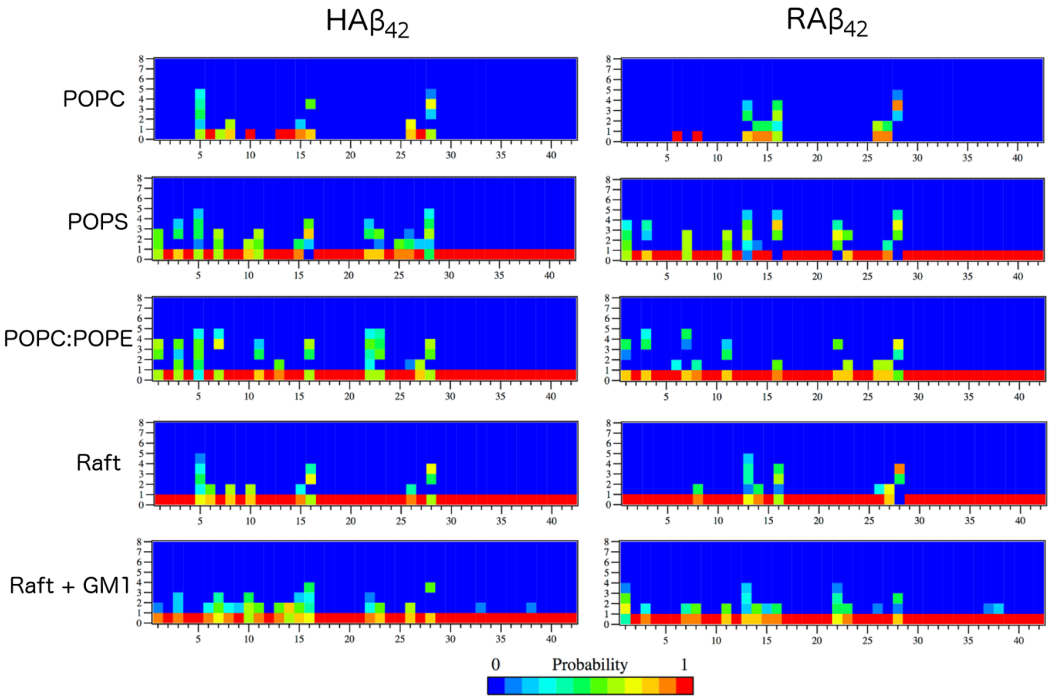


**Figure 3.S4.** Probability distribution of the occurrence and amount of hydrogen bonds between $A\beta_{(42)}$ side chains and the respective membrane. Each plot is an average of all 3 replicates in each simulation set. Residue number and amount of hydrogen bonds are plotted on the x- and y- axis, respectively.

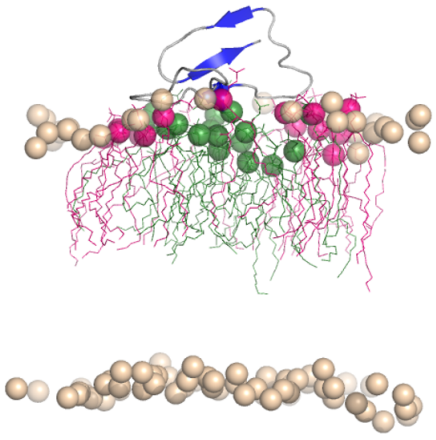

**Figure 3.S5.** Lipid Tiers. The usage of lipid tiers, as discussed by Bachar and Becker [181], was essential to analysis of local and global affects on the model membranes. The 1st lipid tier, defined as the first 16 closest lipids to the COM of $A\beta_{42}$, is shown as green, whereas the 2nd lipid tier, defined as the second 16 closest lipids to the COM of $A\beta_{42}$ is shown in pink. Phosphate atoms are shown as tan sphere. $A\beta_{42}$ is shown as cartoon and colored by secondary structure (grey-coil, blue-β-strand). Lipid tails not in the 1st or 2nd tier are not shown for clarity.

# 4 Atomistic Molecular Dynamics Simulations of Amyloid β-Peptide (1-42): Tetramer Formation, Rearrangement, and Membrane Interactions

Anne M. Brown[1] and David R. Bevan[1]

[1]Department of Biochemistry (0308), Virginia Polytechnic Institute and State University, 201 Engel Hall, Blacksburg, VA 24061.

**Attribution:** AMB wrote this paper with input on content and corrections prior to publication from DRB. All authors collectively conceived the initial project idea and direction. AMB was responsible for submission of the completed manuscript and response to reviewers. This chapter is to be submitted to Biophysical Journal.

## 4.1 Abstract

The aggregation cascade and peptide-membrane interactions of the amyloid β-peptide (Aβ) are implicated as toxic events in the development and progression of Alzheimer's disease. $A\beta_{42}$ forms oligomers and ultimately plaques; these oligomeric species have been hypothesized as the main toxic species contributing to neuronal cell death. To better understand oligomerization events and subsequent oligomer-membrane interactions of $A\beta_{42}$, unbiased, all-atom molecular dynamics (MD) simulations were performed to characterize both inter-peptide interactions and perturbation of model membranes by the peptides. MD simulations were utilized to first show formation of a tetramer unit by four separate $A\beta_{42}$ peptides. $A\beta_{42}$ tetramers adopted an oblate ellipsoid shape and showed a significant increase in β-strand formation in the final tetramer unit relative to the monomers, indicative of on-pathway events for fibril formation The $A\beta_{42}$ tetramer unit formed in the initial simulations was used in subsequent MD simulations in the presence of a pure POPC or cholesterol-rich raft model membrane. Tetramer-membrane simulations resulted in elongation of the tetramer in the presence of both model membranes, with tetramer-raft interactions giving rise to rearrangement of key hydrophobic regions in the tetramer and the formation of a more rod-like structure indicative of a fibril-seeding aggregate. Membrane perturbation by the tetramer was manifested in the form of more ordered, rigid membranes, with the pure POPC being affected to a greater extent than the raft membrane. These results provide critical atomistic insight into the aggregation pathway of $A\beta_{42}$ and a putative toxic mechanism in the pathogenesis of Alzheimer's disease.

## 4.2 Introduction

Aggregation of proteins into amyloid deposits is a common feature among dozens of diseases [200]. Alzheimer's disease (AD) is an amyloid disease that currently affects 5.3 million people in the United States, with no current treatment to stop or slow the progression of the disease [5]. AD toxicity is associated with the aggregation and accumulation of the amyloid β-peptide (Aβ) in and around neural tissue [13, 16]. Aβ is generated by sequential proteolysis by β- and γ-secretase within the amyloid precursor protein (APP) [16, 27, 37], and variations in the processivity of γ-secretase give rise to multiple Aβ alloforms of different length [201, 202]. The $A\beta_{42}$ alloform aggregates faster [203, 204] and is more cytotoxic than shorter alloforms [205]. Recent evidence suggests that low-molecular-weight oligomers of $A\beta_{42}$ share common structures and possible mechanisms of pathogenesis and are the most toxic agents contributing to AD [83, 206-208]. In addition, neuronal cell membrane perturbation by Aβ is central to the pathology of AD [173]. Understanding mechanistic details related to the formation of low-molecular-weight oligomers and their role in membrane perturbation leading to neuronal cell death is essential in assessing the cascade of events that results in AD.

An unambiguous definition of the most cytotoxic low-molecular-weight Aβ oligomer in terms of structure and size remains elusive [209, 210]. Some argue that it is not necessarily the size of the Aβ oligomer that correlates with the highest toxicity, but rather the structure and organization of the peptide. These structural states are assessed based on secondary structure elements retained by the peptide, the density of the oligomer, and order of events leading to fibrillization [211]. The structural transition from the primarily α-helical monomer of Aβ after γ-secretase cleavage to a disordered ensemble in solution, and subsequent enrichment in β-strand structure [212] is indicative of on-pathway aggregation [17, 18] and suggests an important role for the Aβ monomer structure in oligomer and fibril formation [19, 203]. Events leading to the aggregation of multiple Aβ monomers into oligomeric forms can vary [4, 213]. In regards to the structural makeup and size of toxic, oligomer Aβ species, multiple pathways are possible and structural diversity of Aβ oligomers drives the aggregation pathway [211, 214, 215]. Multiple mechanisms of toxicity may exist for different Aβ oligomers and each may be related to different conformations adopted by the polymorphic Aβ [215]. Structural characterization of these various oligomer species would provide necessary information into the various toxic states of Aβ; however, details necessary for mechanistic insight are unattainable with the resolution of current experimental techniques [216].

MD simulations are an essential complement to experimental studies and can provide key insights into the aggregation pathways of low-molecular-weight Aβ oligomers and their subsequent interactions with membranes and other proteins. Simulations of monomeric Aβ in various solution environments have been performed [185, 187, 212, 217, 218], with a few all-atom MD simulations on dimer formation [219, 220]. Discrete molecular dynamics (DMD), replica exchange MD (REMD), and use of implicit solvent are techniques that have been used to characterize structural ensembles of higher-order Aβ aggregates [220-223]; however, differences in conclusions related to equilibrium ensembles are most likely associated with force fields and sampling [173]. The present study utilizes unbiased, all-atom MD simulations of full-length

$A\beta_{42}$ on the microsecond scale to understand and provide insight into tetramer formation of $A\beta_{42}$ as a foundation for studying higher-order oligomeric $A\beta_{42}$ aggregate formation.

Interactions of low-molecular-weight Aβ oligomers with membranes is also of interest, given that membrane perturbation by Aβ is central to the pathology of AD [173]. Aβ aggregation is accelerated in the presence of membranes, with electrostatic interactions potentially driving the peptide-membrane interactions [224, 225]. However, few computational studies exist that examine the dynamics of low-molecular-weight oligomers, like an $A\beta_{42}$ tetramer, in the presence of a membrane. Computational studies have looked at the effect of rafts on membrane binding and dimerization of Aβ [149, 226], whereas others have utilized pre-embedded oligomeric Aβ to understand transmembrane structures [157, 227]. Currently, no study has utilized all-atom MD to understand the effects of any $A\beta_{42}$ oligomer of three or more peptides on membranes from a starting position that is external to the membrane. By studying the interactions of an $A\beta_{42}$ tetramer binding to model membranes of a composition similar to those found in the eukaryotic plasma membranes and in neuronal cells [163, 164, 166], the ability of low-molecular weight $A\beta_{42}$ species to perturb membranes can be characterized.

## 4.3 Methods

### 4.3.1 Tetramer Formation Simulations

A schematic image detailing experimental design can be seen in Figure 4.1. Simulations were first performed to characterize $A\beta_{42}$ tetramer formation. In doing so, it was important to carefully consider the starting monomer structure that would be utilized in these simulations. The on-pathway, monomeric species sample a diverse conformational ensemble, consisting of a mixture of random coil and β-strand structures, as shown in reports in both experimental and computational studies [101, 185, 187]. As such, a starting structure that mimicked these properties was preferred. To obtain this monomer starting structure, the structure of $A\beta_{42}$ (PDB 1IYT) [175] was equilibrated and simulated in water and 0.150 M NaCl for 300 ns using the protocol described below. Clustering was performed based on root-mean-square deviation (RMSD) of backbone atoms to obtain a representative structure over the last 100 ns of simulation time. Four copies of the representative structure (defined as the center structure of the most populated cluster) were then placed randomly four times in a 12.7-nm cubic box, separating each monomer by at least 1.7 nm to be beyond the non-bonded cutoff for van der Waals interactions. A minimum solute-box distance of 3.0 nm was enforced. This system design resulted in a box containing four equilibrated monomeric Aβ peptides that were separated by enough solvent and ions to negate any bias due to van der Waals interactions. Each system was then solvated with SPC water [114] and 0.150 M NaCl was added, including counterions to maintain a net neutral system.

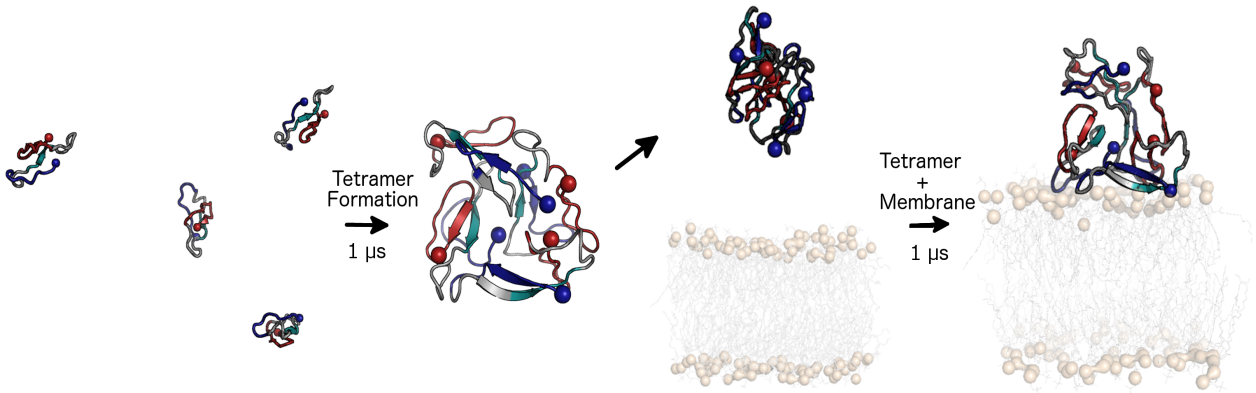


**Figure 4.1.** Schematic for experimental design to understand interpeptide interactions and potential rearrangement of interpeptide interactions when placed in the presence of membranes. Interpreted from left to right, the far left segment shows the initial configuration for four $A\beta_{42}$ peptides placed at least 3 nm apart. Tetramer formation occurs during 1 μs MD simulations. The resulting tetramer is placed 3 nm away from either a POPC or raft model membrane and another 1 μs MD simulation is conducted. $A\beta_{42}$ is shown as cartoon, colored by region (blue: residues 1-10, grey: residues 11-16, 22-29, teal: residues 17-21, and red: residues 30-42). N- and C-termini are indicated by blue and red spheres, respectively. Membranes are shown as grey sticks, with the phosphorus atoms shown as tan spheres for perspective.

### 4.3.2 Tetramer – Membrane Simulations

Representative tetramer structures were identified using RMSD clustering (as above) from each replicate in tetramer formation simulations and were placed at a center of mass (COM) distance of 3.0 nm away from pre-equilibrated POPC and raft [1:1:1 POPC:cholesterol:palmitoylsphingomyelin (PSM)] model membranes, yielding a minimum atom distance between the tetramer and membrane of at least 2.4 nm. The coordinates and topologies for the membranes were based on previous work [71, 178, 180]. The placement of the tetramer far from the membrane was chosen to avoid biasing the initial approach of the tetramer towards the membrane. Details on tetramer-membrane distance and membrane composition are listed in Table 4.S1. Tetramer-membrane systems were solvated with SPC water [114] and 0.150 M NaCl. Three independent simulations, initiated from different structures generated from the three replicates of the tetramer-formation simulations described above were carried out with each model membrane for 1 μs each, resulting in 3 μs of sampling time for the tetramer-membrane simulations of each lipid type. Two control simulations of the POPC and raft membranes were carried out in the absence of $A\beta_{42}$. These membranes were solvated with SPC water and 0.150 mM NaCl and simulated for 1 μs to assess membrane stability over long MD simulations and to serve as a control for assessing membrane perturbation effects caused by interactions with the $A\beta_{42}$ tetramer. All results presented for the control membrane simulations are averages over the last 250 ns of simulation time.

### 4.3.3 General MD Simulation Protocol

All simulations were run using the GROMACS software package, version 4.6 [68, 115] and the GROMOS96 53A6 force field [70]. Systems were energy-minimized using the steepest descent method, and three replicates, defined as independent trajectories initiated with different random velocities in a canonical (NVT) ensemble, were performed separately for tetramer formation and tetramer-membrane simulations. One simulation was performed to obtain the monomer starting structure of Aβ. NVT was applied to the system for 100 ps using the Berendsen weak coupling method [116] to maintain temperature at 310 K. An additional annealing step was added after NVT equilibration for tetramer-membrane simulations, which linearly heated the system from 100 to 310 K, at 1 bar pressure for 1 ns using the Berendsen algorithm [116]. Following either NVT or annealing depending on the system, an isothermal-isobaric (NPT) ensemble was performed to maintain temperature (310 K) and pressure (1 bar) using the Nosé-Hoover thermostat [74, 75] and Parrinello-Rahman barostat [76, 77]. For NVT, annealing, and NPT, position restraints were imposed on all peptide heavy atoms and all restraints were released at the outset of production MD simulations. For tetramer-membrane simulations, peptide, membrane, and solvent (water and ions) were attached to separate thermostats. All simulations were performed using three-dimensional periodic boundary conditions. Bond lengths were constrained using P-LINCS [117], allowing an integration time step of 2 fs to be used. Cutoffs for all nonbonded interactions were set to 1.4 nm for monomer equilibration and tetramer-formation simulations and 1.2 nm for tetramer-membrane simulations. The smooth particle mesh Ewald (PME) method [79, 80] using cubic interpolation and Fourier grid spacing of 0.16 nm was utilized to calculate long-range electrostatic interactions. Simulations of $A\beta_{42}$ tetramer-formation and tetramer-membrane simulations were carried out for 1 μs, yielding a total of 9 μs of simulation time, in order observe inter-peptide and peptide-membrane interactions. Backbone RMSD and secondary structure of $A\beta_{42}$ were used to assess simulation convergence and peptide

equilibration. Analysis was performed over the last 250 ns for all tetramer-formation and tetramer-membrane simulations. All averages, except for starting structure, were calculated over three replicates for that simulation set and are presented with the corresponding standard deviation. To obtain representative structures of each replicate, RMSD clustering was performed using the method of Daura et al. [119] using the peptide backbone atoms, with a cutoff of 0.3 nm for tetramer formation and 0.2 nm for selection of a monomer structure to begin tetramer formation simulations. Representative structures shown in all Figures are the central structure of the largest cluster over the last 250 ns of simulation time. GridMAT-MD was used to calculate area per lipid (APL) and bilayer thickness in simulations involving membranes [182]. Deuterium order parameters were calculated to assess the order of the sn-1 POPC lipid acyl chains along the bilayer normal, per equation (1):

$$-S_{CD} = \langle \frac{3cos^2\theta - 1}{2} \rangle \quad (1)$$

where θ is the angle between the C-D bond and bilayer normal and angle brackets indicate the time-average over all equivalent atoms during the last 250 ns of simulation. PyMOL [228] was used to visualize snapshots and render figures. A two-tailed *t*-test was used for statistical analysis, with statistical significance determined if $p < 0.05$. Central hydrophobic core (CHC) residues are defined as residues 17-21, C-terminal residues (Cterm) are defined as residues 29-42.

## 4.4 Results and Discussion

Understanding the formation of low-molecular-weight Aβ oligomers and their interactions with membranes are essential in providing more insight into their toxicity [229, 230]. Given the variability in experimental conditions, aggregation rates, and limits of experimental resolution to fully characterize these toxic, intermediate species of Aβ, MD simulations have an important role in providing essential, mechanistic details into the formation of low-molecular-weight oligomer structures and can suggest possible mechanisms of interaction with model membranes and contributions to the aggregation pathway of Aβ. This study utilized all-atom MD simulations to determine the formation pathway of an $A\beta_{42}$ tetramer and to subsequently place that tetramer in the presence of two model membranes, pure POPC and a cholesterol-rich raft. Aβ oligomers of this size have not been studied in the presence of model membranes and can provide essential knowledge in understanding the type and extent of perturbation caused by peptide binding.

The approach taken in the present work was driven by known experimental information on low-molecular-weight oligomer structures of $A\beta_{42}$ [19, 229], and previous DMD simulations of an Aβ tetramer [221]. Prior to this research, no reported study has utilized all-atom MD simulations to show formation of $A\beta_{42}$ species larger than a dimer. In addition, many questions exist regarding the membrane-perturbing effects exhibited by low-molecular-weight $A\beta_{42}$ oligomers. By simulating a preformed tetramer in the presence of two model membranes, insight into potential toxicity of this oligomeric species can be attained. While it has been suggested that larger (dodecamer and larger) oligomers of $A\beta_{42}$ exhibit the most toxicity [231], the availability of model structures of an $A\beta_{42}$ tetramer as determined by ion mobility and mass spectrometry [229], coupled with sufficient computational power to simulate such large systems, made studying tetramer formation the most practical approach for all-atom MD simulations of $A\beta_{42}$

aggregation. The GROMOS96 53A6 force field was selected in this study given its ability to adequately simulate monomeric Aβ relative to experimental information [72, 73]. In addition, this force field selection allows for comparison to previous studies on monomer and dimer Aβ-membrane interactions (A.M.B and D.R.B-submitted) [65, 149] and application of frequently utilized lipid parameters to simulate physiologically relevant model membranes [71, 178, 180].

### 4.4.1 Tetramer Formation

Increase in β-strand structure of $A\beta_{42}$ as a function of aggregation state is indicative of on-pathway aggregation, and thus studying the evolution of secondary structure is relevant to the formation of an Aβ tetramer [17, 18]. Analysis was first performed to quantify changes in secondary structure of Aβ monomers as the tetramer formed. In addition, tertiary and quaternary structure was studied to better understand inter-peptide interactions and any trends related to these levels of structure that may give insight into the order of events surrounding $A\beta_{42}$ tetramer formation and structure. When the $A\beta_{42}$ structure from PDB 1IYT [175] was simulated in an aqueous 0.150 mM NaCl environment, it lost all α-helical structure. The resulting $A\beta_{42}$ monomer that was utilized in tetramer formation simulations consisted of 75% random coil structure and 25% β-strand structure (Table 4.1). An NMR study on $A\beta_{42}$ monomers found that the average β-strand structure was 20% based on Hα chemical shifts [101], indicating that secondary structure assignment and development as observed in these simulations were in agreement with previous experimental and computational work [72, 73].

**Table 4.1.** Average secondary structure content (shown in %), with corresponding standard deviation, of $A\beta_{42}$ after tetramer formation and after interaction of the tetramer with a POPC or Raft membrane. [a, b]

| System | Coil | β-strand | α-helix |
|---|---|---|---|
| Starting Structure | 75 ± 1 | 25 ± 1 | 0 ± 0 |
| Tetramer Formation | 66 ± 6 | 34 ± 5 | 0 ± 0 |
| Tetramer + POPC | 68 ± 6 | 32 ± 6 | 0 ± 0 |
| Tetramer + Raft | 60 ± 4 | 40 ± 4 | 0 ± 0 |

[a] Tetramer percentages represent structural properties of $A\beta_{42}$ tetramers formed in the indicated simulation, averaged over the final 250 ns of three replicate trajectories for a cumulative sampling time of 750 ns, with corresponding standard deviations.

[b] Starting structure percentages represent the average secondary structure of the four $A\beta_{42}$ peptides after energy minimization and before equilibration and MD simulation.

The time at which inter-peptide contact initially occurred during the MD simulations of tetramer formation varied among replicates; however, a similar trend emerged in the sequence of inter-peptide contact events (Figure 4.S1). In all replicates, two $A\beta_{42}$ peptides (denoted as peptides 1 and 2) interacted and formed a dimer, with peptides 3 and 4 binding to the dimer sequentially. Tetramer formation was complete within the first 250 ns of simulation time (Figure 4.S1); however, to observe any potential rearrangement and increase in inter-peptide β-strand structure, simulations were continued out to 1 μs. The tetramer was determined to be stable and unchanging at this time based on RMSD time series and clustering percentage results (Figure 4.2). The last 250 ns of simulation time for tetramer formation simulations were utilized for analysis to reflect the dominant features of the tetramers formed during these simulations. Clustering results show that a clear dominant morphology emerged in each replicate, with the

central structure of the first cluster representing 44.5%, 71.4%, and 73.4% of frames over the last 250 ns for each of the three replicates.

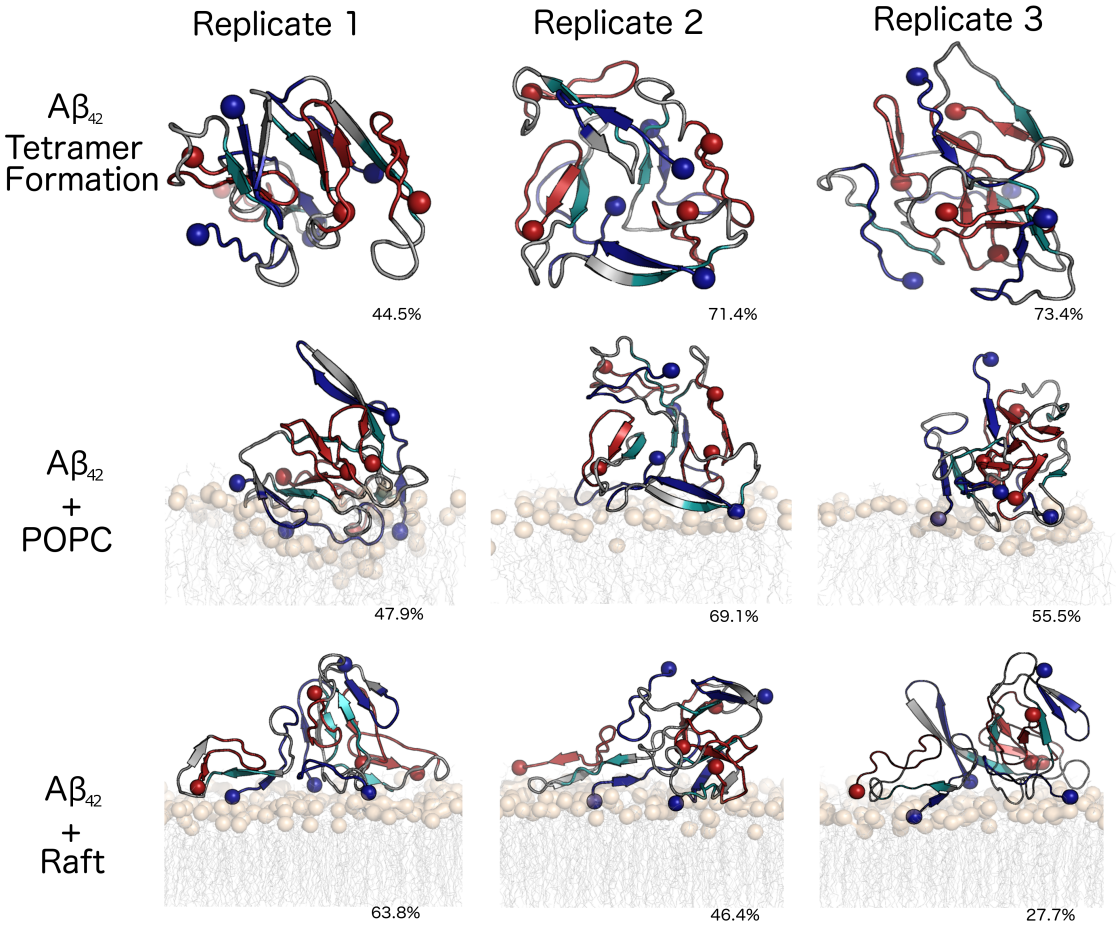


**Figure 4.2.** Images represent the central structure of the largest cluster from the last 250 ns of each simulation, with percentages representing the cluster size (percentage of frames belonging to the cluster). The rendering of $A\beta_{42}$ and the membranes is the same as in Figure 4.1.

A statistically significant increase in average percent β-strand structure was observed for $A\beta_{42}$ tetramers (34 ± 5%) compared to starting, monomeric structures (25 ± 1%, Table 4.1). This structural conversion was driven by an increase in the β-strand content in the C-terminal region of each peptide (41 ± 9% vs. 36 ± 5% in the starting monomer, respectively). Such an increase in β-strand content in the hydrophobic C-terminal region of $A\beta_{42}$ has been linked to $A\beta_{42}$ fibrillation and implicates the role of this hydrophobic region of $A\beta_{42}$ in on-pathway aggregation as shown by circular dichroism (CD) spectroscopy and electron microscopy experiments. Such as increase in β-strand structure overall and in C-terminal residues indicates that the tetramer unit that was formed via all atom MD simulation is on-pathway with known aggregation events. The $A\beta_{42}$ tetramer in all replicates was compact, with an average radius of gyration ($R_g$) of 1.6 ± 0.1 nm (Table 4.2) and an average self-diffusion coefficient of 2.6 ± 0.8 × $10^{-6}$ $cm^2$ $s^{-1}$ (Table 4.S2). Initial $R_g$ values of $A\beta_{42}$ monomers were 1.0 ± 0.1 nm, in agreement with single-molecule level fluorescence values for monomeric $A\beta_{42}$ $R_g$ (0.9 ± 0.1 nm) [232]. The structural ensembles of all

$A\beta_{42}$ species were characterized by non-specific interactions between the central hydrophobic core (CHC) and C-terminal region (Table 4.3, Figure 4.2, Figure 4.S3).

**Table 4.2.** Average $R_g$ values of $A\beta_{42}$ tetramers, with corresponding standard deviation. [a,b]

| System | $R_g$ (nm) |
|---|---|
| Tetramer Formation | 1.6 ± 0.1 |
| Tetramer + POPC | 2.1 ± 0.2 |
| Tetramer + Raft | 2.4 ± 0.3 |

[a] Average represents $R_g$ of $A\beta_{42}$ tetramers in the indicated simulation, averaged over the final 250 ns of three replicate trajectories for a cumulative sampling time of 750 ns, with corresponding standard deviations.
[b] Initial, monomeric peptide $R_g$ values of $A\beta_{42}$ were 1.0 ± 0.1 nm, which agrees with literature values [232].

**Table 4.3.** Average percent of intermolecular side chain contacts between key regions of $A\beta_{42}$. [a]

| System | CHC-CHC | CHC-Cterm | Cterm-Cterm |
|---|---|---|---|
| Tetramer Formation | 27 ± 25 | 26 ± 10 | 47 ± 25 |
| Tetramer + POPC | 20 ± 23 | 20 ± 24 | 59 ± 35 |
| Tetramer + Raft | 43 ± 2 | 24 ± 8 | 33 ± 6 |

[a] Average percent represents the intermolecular contacts of $A\beta_{42}$ specified region-region contacts formed in the indicated simulation, averaged over the final 250 ns of three replicate trajectories for a cumulative sampling time of 750 ns. Specified region-region contact percent was calculated from the total of number of contacts representing the CHC-CHC, CHC-Cterm, and Cterm-Cterm. CHC is defined as residues 17-21; Cterm is defined as residues 30-42.

Finally, to characterize the shapes of the formed tetramers, moments of inertia ($I_1$, $I_2$, $I_3$) and eccentricity ($e$) were calculated from semiaxes $a$, $b$, and $c$ as follows [233, 234]:

$$I_1 = \frac{2}{5}(b^2 + c^2)$$
$$I_2 = \frac{2}{5}(c^2 + a^2)$$
$$I_3 = \frac{2}{5}(a^2 + b^2)$$

Shape parameters from these moments of inertia can be defined by a prolate ellipsoid (rod) when $I_1 \approx I_2 > I_3$, oblate ellipsoid (disc) when $I_1 \approx I_2 < I_3$, and sphere when $I_1 \approx I_2 \approx I_3$. Eccentricity ($e$) of the tetramer can also indicate its shape based on a 0 → 1 scale, with $e = 0$ representing a perfect sphere and $e = 1$ representing a rod. Eccentricity is calculated as follows:

$$e = \sqrt{1 - \frac{c^2}{a^2}}$$

From simulations in solution, the simulated $A\beta_{42}$ tetramer structures more closely resembled an oblate ellipsoid (disc) shape with an eccentricity value of 0.79 ± 0.03 (Table 4.4). This finding is in contrast to the mass spectrometry (MS) results of Bernstein et al. [229] who determined a linear structure for the $A\beta_{42}$ tetramer described as two dimer units that connected and were

separated by an angle of 120°, but it is in agreement with the disc-shape $A\beta_{42}$ pentamer structure as described by Ahmed et al. using transmission electron microscopy (TEM) and atomic force microscopy (AFM) [235]. Solution and experimental conditions could greatly influence the structure of $A\beta_{42}$ tetramer, leading to this difference in results. MS is an *in vacuo* technique, whereas TEM and AFM experiments were performed in a hydrated, salt-containing environment. The influence of solution conditions on $A\beta_{42}$ oligomerization is confirmed by formation of a disc-shaped $A\beta_{42}$ pentamer observed in conditions similar to those utilized in these simulations [235]. The formation of an oblate ellipsoid (disc-shaped) tetramer is also shown in Figure 4.S2 by the more compact tetramers, with all peptides being in contact with one another, as compared to the proposed linear tetramer structure [229]. This compact structure has potential for additional $A\beta_{42}$ binding given the heterogeneous (hydrophobic and hydrophobic) SASA of the $A\beta_{42}$ tetramer.

**Table 4.4.** Average moments of inertia ($I_1$, $I_2$, $I_3$) and eccentricity values ($e$) for $A\beta_{42}$ tetramers [a]

| System | $I_1$ ($10^4$ amu *nm$^2$) | $I_2$ ($10^4$ amu *nm$^2$) | $I_3$ ($10^4$ amu *nm$^2$) | $e$ |
|---|---|---|---|---|
| Tetramer Formation | 2.3 ± 0.1 | 3.2 ± 0.3 | 3.8 ± 0.3 | 0.79 ± 0.03 |
| Tetramer + POPC | 2.8 ± 0.3 | 7.0 ±1.0 | 8.0 ± 1.0 | 0.91 ± 0.01 |
| Tetramer + Raft | 6.0 ± 2.0 | 55.0 ± 43.0 | 58.0 ± 44.0 | 0.97 ± 0.02 |

[a] Average represents moments of inertia and eccentricity values of $A\beta_{42}$ tetramers averaged over the final 250 ns of three replicate trajectories for a cumulative sampling time of 750 ns for the indicated system, with corresponding standard deviations.

### 4.4.2 Modulation of $A\beta_{42}$ Tetramer Structure by Membranes

The representative structures from the last 250 ns of each of the three replicates from tetramer formation simulations were placed in the presence of pure POPC or raft model membranes (Figure 4.1, Table 4.S1). Analysis focused on the extent to which the $A\beta_{42}$ tetramer disrupted the model membranes and how the membranes would influence the nature of the inter-peptide interactions within the $A\beta_{42}$ tetramer.

The time taken for the $A\beta_{42}$ tetramer to bind to the POPC membrane varied across the replicates (Figure 4.S4), ranging from 32 to 245 ns. The $A\beta_{42}$ tetramer interacted with the raft membrane quickly, with the longest replicate taking only 56 ns to bind to the membrane (Figure 4.S4). In all POPC and raft simulations, once the $A\beta_{42}$ tetramer bound to the model membrane, it did not release from the membrane. Secondary structure evolution of $A\beta_{42}$ was of primary interest when first studying the effects of a membrane on $A\beta_{42}$ tetramer arrangement. The β-strand content of the Aβ tetramer was maintained in the presence of the POPC membrane (34 ± 5% vs. 32 ± 6% in water and bound to the membrane, respectively, Table 4.1). A slight increase in β-strand structure content was observed in the presence of a raft membrane (34 ± 5% vs. 40 ± 6%). To try to understand the increase in β-strand structure in the presence of the raft membrane, other structural features of the tetramer were considered. From examination of the structures, it appeared that the tetramer became more elongated in the presence of the raft membrane than in the presence of the POPC membrane. This change was borne out by $R_g$ values of the $A\beta_{42}$ tetramer, which increased to a statistically significant degree in the presence of POPC and raft membranes as compared to the structure in the absence of membranes (Table 4.2). An $R_g$ of 1.6

± 0.1 nm was observed for the $A\beta_{42}$ tetramer in solution, whereas an Aβ tetramer $R_g$ of 2.1 ± 0.2 nm and 2.4 ± 0.3 nm was observed after binding to the POPC membrane and raft membrane, respectively (Table 4.2). SASA was also calculated for the $A\beta_{42}$ tetramer in solution (100 ± 2 $nm^2$) and bound to the membrane. A slight increase in SASA was observed for the Aβ tetramer in the presence of POPC (105 ± 5 $nm^2$) and raft membranes (108 ± 2 $nm^2$, Table 4.S3). The slight increase in $R_g$ and SASA in the presence of a raft membrane compared to a POPC membrane agrees with, and potentially explains, the measurable increase in percent β-strand structure of the $A\beta_{42}$ tetramer in the presence of a raft, compared to pure POPC. The more extended $A\beta_{42}$ tetramer structure in the presence of the raft membrane could allow for extension of β-strand structure.

Finally, the elongation and loss of the spherical structure of the tetramer in the presence of POPC and raft membranes can be observed visually (Figure 4.2 and Figure 4.S2) and was calculated through moments of inertia and eccentricity values. After binding to the POPC membrane, the $A\beta_{42}$ tetramer became elongated, converting to a more rod-like ellipsoid structure, as demonstrated by an increase in eccentricity value (0.91 ± 0.01) as compared to the $A\beta_{42}$ tetramer in solution (0.79 ± 0.03, Table 4.4). Considerable variation in moments of inertia values was observed when the $A\beta_{42}$ tetramer bound to a raft membrane, showing further elongation into a prolate ellipsoid shape, with an eccentricity value of 0.97 ± 0.02 (Table 4.4). In the presence of both the POPC and raft membranes, the $A\beta_{42}$ tetramer adopted two larger moments and one smaller moment indicating progression towards a more prolate ellipsoid (rod-shape) as compared to the $A\beta_{42}$ tetramer in solution. In $A\beta_{42}$ tetramer and raft simulations, this degree of difference in the two larger moments as compared to the smaller moment is greater, as influenced by the increased elongation and β-strand content of the $A\beta_{42}$ tetramer when bound to the raft membrane compared to the POPC membrane. In addition, this extent of difference between $I_2$, $I_3$ values and $I_1$ is consistent with the degree of change in $R_g$ values of the $A\beta_{42}$ tetramer in the presence of a raft membrane. The degree in difference between $I_1$, $I_2$, $I_3$ values is consistent with other reported moments of inertia values for ellipsoid shapes [234]. Irrespective of membrane type, the $A\beta_{42}$ tetramer became more elongated and rod-like, which has been experimentally determined to be a property of on-pathway protofibrils of Aβ [236], leading us to conclude that membranes serve to modulate the shape of the $A\beta_{42}$ tetramer and cause rearrangement into on-pathway, rod-shaped aggregate structures from an oblate ellipsoid $A\beta_{42}$ tetramer in solution.

Given that membranes reduce the dimensionality of diffusion of molecules in solution from three dimensions to two, self-diffusion coefficients of the $A\beta_{42}$ tetramer bound to POPC and raft membranes were calculated. Significant decreases in self-diffusion coefficients were observed for the Aβ tetramer bound to POPC and raft membranes, as compared to the in-solution structure for tetramer formation simulations. The average self-diffusion coefficient calculated in the x-y plane for the $A\beta_{42}$ tetramer bound to POPC was reduced by approximately half relative to its value in solution, and further reduced in half when bound to the cholesterol-rich raft (Table 4.S2). The reduced diffusion at the membrane interface suggests strong peptide-lipid interactions and potential for nucleation due to decreased mobility. This finding also supports the "carpeting effect" model of $A\beta_{42}$-membrane interactions [191], in that the tetramer bound to both POPC and raft membranes elongates and coats the membrane surface to varying degrees as compared to structures in solution. Both membranes induced the conversion to more rod-like, on-pathway structures, and this effect was greatest in the cholesterol-rich rafts. This finding

indicates these specialized lipid microdomains that contain cholesterol are influential in the pathological aggregation pathway of Aβ and agree with current literature on lipid rafts being linked to Aβ aggregation [237].

Lastly, reorganization of inter-peptide contacts was observed in the presence of the raft membrane. Non-specific interactions between CHC-CHC, CHC-Cterm, and Cterm-Cterm domains were observed in solution when bound to the POPC membrane. However, after binding to the raft membrane, CHC-CHC contacts increased measurably and consistently across the three replicates, whereas Cterm-Cterm interactions decreased in a corresponding manner (Table 4.3). This intriguing rearrangement of the $A\beta_{42}$ tetramer in the presence of the raft membrane was due to the formation of two major hydrophobic nuclei (Figure 4.S3). In addition, the degree of elongation was more noticeable in the presence of the raft membrane, which is caused rearrangement of inter-peptide interactions. Ultimately, these simulations show rafts cause more substantial elongation and rearrangement of the tetramer than pure POPC membranes, implicating the raft microdomains in modulating the structure of Aβ tetramers to contribute to on-pathway Aβ fibril formation.

### 4.4.3 Perturbation of POPC and Raft Membranes by the $A\beta_{42}$ Tetramer

Membrane perturbation induced by the $A\beta_{42}$ tetramer was quantified in terms of deuterium order parameters ($S_{CD}$), area per lipid (APL), bilayer thickness, and density profiles. An increase in $S_{CD}$ and bilayer thickness, coupled with a decrease in APL, indicates tighter lipid packing and subsequent elongation of lipid tails. Density profiles of the membrane were also calculated to determine if $A\beta_{42}$ tetramer binding caused an increased penetration of water into the glycerol region of the membrane or affected lipid headgroup and lipid tail properties. Control membrane systems (without any peptide) were simulated for 1 μs in to serve as a control for understanding the role of the $A\beta_{42}$ tetramer on membrane perturbation. In the control simulations, APL and bilayer thickness averaged over the last 250 ns were 62 ± 1 $Å^2$ and 3.9 ± 0.1 nm for POPC, and 41.2 ± 0.1 $Å^2$ and 4.3 ± 0.2 nm for the raft membrane (Table 4.5). These metrics compare well with literature values [178, 238], indicating that 1 μs is adequate to achieve sufficient sampling, and that the force field model used in the present work adequately represents lipid dynamic and structural properties.

$A\beta_{42}$ tetramer binding and insertion into the POPC membrane caused an average 42% decrease in APL, coupled with a 10% increase in bilayer thickness (Table 4.5). Deuterium order parameters were also substantially increased compared to both the control POPC membrane $S_{CD}$ value and the $S_{CD}$ value from simulations of monomeric Aβ with a POPC membrane (A.M.B and D.R.B. – submitted) (Figure 4.3). Simulations of monomeric $A\beta_{42}$ with a POPC membrane were performed in the same conditions as this study and were utilized in this figure as a comparison to show extent of monomeric $A\beta_{42}$ vs. tetramer $A\beta_{42}$ perturbation on POPC and raft membranes. Density profiles also show that upon $A\beta_{42}$ tetramer binding, the lipids packed in a way that caused the lipid tails to interdigitate at the bilayer interface (Figure 4.S5, 4.S6). In addition, the density of the interacting leaflet headgroup decreased as compared to the control and non-interacting leaflet headgroup, indicating the compactness of the lipid headgroups as a result of $A\beta_{42}$ tetramer binding. Raft membranes resisted major perturbation by the $A\beta_{42}$ tetramer, resulting in only a 15% decrease in APL and no change in overall bilayer thickness (Table 4.5). Deuterium order parameter analysis also indicated minimal increase in $S_{CD}$ value for $A\beta_{42}$

tetramer binding as compared to the control and monomeric $A\beta_{42}$ $S_{CD}$ values (Figure 4.3). Density profiles showed no interdigitation between leaflets, and little to no change in density of the interacting leaflet headgroup was observed as compared to the control and non-interacting leaflet (Figure 4.S5). These results show that the presence of cholesterol in a raft membrane attenuates major perturbation such as that observed in the pure POPC membrane when either monomeric or tetrameric $A\beta_{42}$ bind. The neuroprotective role of cholesterol upon $A\beta_{42}$ binding has also been shown experimentally by AFM [162].

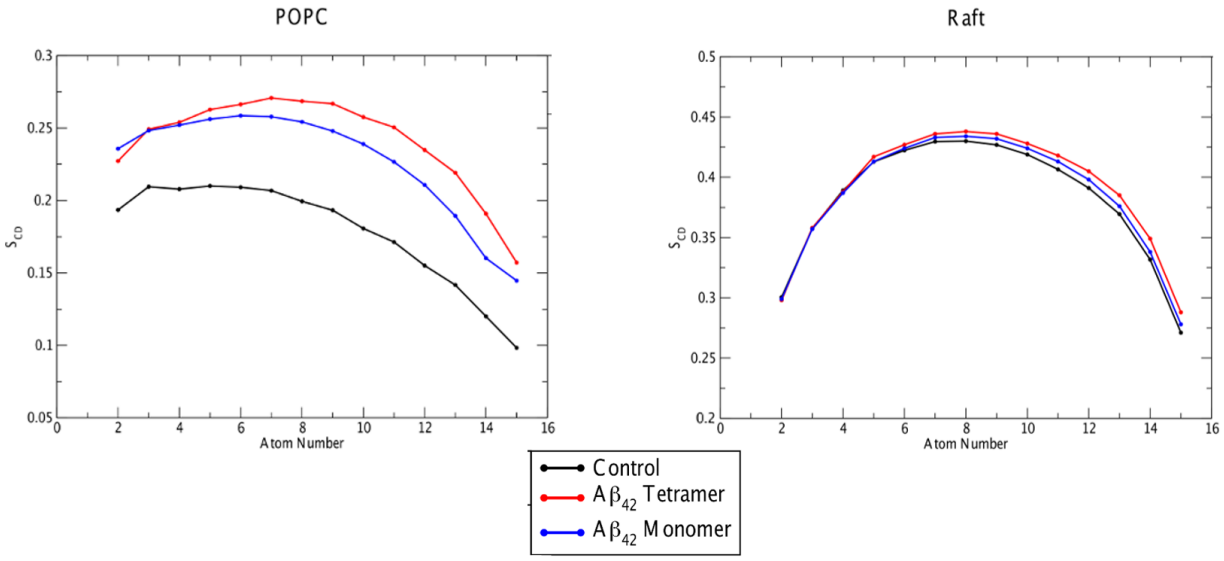


**Figure 4.3.** Average leaflet deuterium order parameters ($S_{CD}$) of palmitoyl (sn-1) chain of POPC lipids in model membrane simulations. For clarity, only the sn-1 chain is shown; however, parameters were also analyzed for the sn-2 chain and showed similar trends. Control (no peptide present) parameters for each carbon in the lipid chain are shown in black, with the average parameter over three replicates during the last 250 ns of simulation time shown for $AB_{42}$ tetramer (red) and monomer (blue) membrane simulations.

**Table 4.5.** Membrane properties after tetramer interaction. Averages, with corresponding standard deviation and % difference from controls, are shown for area per lipid head group (APL) and bilayer thickness analysis metrics. [a,b, c]

| | APL (Å$^2$) | Bilayer Thickness (nm) |
|---|---|---|
| Tetramer + POPC | 36 ± 5 (-42%) | 4.3 ± 0.1 (+10%) |
| Tetramer + Raft | 35 ± 3 (-15%) | 4.3 ± 0. 1 (±0%) |

[a] Average for represents APL and thickness for the indicated simulation, averaged over the final 250 ns of three replicate trajectories for a cumulative sampling time of 750 ns. [b] Control APL (Å$^2$) values, averaged over the last 250 ns of simulation time of a membrane only simulation are: 62 ± 1 (POPC) and 41.2 ± 0.1 (Raft)[c] Control bilayer thickness values, averaged over the last 250 ns of simulation time of a membrane only simulation are: 3.9 ± 0.1 (POPC) and 4.3 ± 0.2 (Raft)

In addition to studying the degree of perturbation on POPC and raft membranes caused by Aβ tetramer binding, it was of interest to determine if any residues of the peptide had an increased probability of participating in peptide-membrane interactions. Distance plots, which represent the position of the center of mass (COM) of each residue in the Aβ tetramer relative to the COM of the bilayer, were generated to determine if a certain amino acid type or position was more likely to be found at the membrane interface and to determine depth of insertion. Due to the large volume of data and the presence of four peptides, individual distance plots are provided for clarity, with the composite showing trends among the replicates. Positively charged residues Arg-5, Lys-16, Lys-28, and the highly polar N-terminal region of $A\beta_{42}$ frequently sampled regions close to or below the phosphate region of the POPC membrane across all replicates to a greater degree than any other observed amino acid type (Figure 4.4, Figure 4.S7). Lipid packing and a rigid membrane-water interface is not observed for a pure POPC membrane [239], aiding in explaining the ability of these positively charged residues to insert into the lipid headgroup region. Residue penetration into the raft membrane was not as deep as compared to the POPC membrane (Figure 4.4) and may result from the raft membrane being less fluid than a POPC membrane [240]. This observation is tied to the small APL of the raft membrane, indicating tight packing of phospholipid (POPC and PSM) headgroups to shield cholesterol from the water interface, thereby preventing the insertion of positively charged residues into the phosphate region of the lipid headgroups. This lack of insertion by positively charged residues into the lipid headgroup region of the raft membrane could result in consequent rearrangement of the $A\beta_{42}$ tetramer to adjust to the presence of this more rigid membrane headgroup region as compared to POPC (Figure 4.4, 4.S7). The influence of the headgroup rigidity of a raft on $A\beta_{42}$ tetramer binding is also shown by the peripheral association of the $A\beta_{42}$ tetramer with the raft membrane and the amount of buried surface area of the tetramer on the membrane (Figure 4.4,Table 4.S5). There is a significant decrease in buried/non-SASA of the $A\beta_{42}$ tetramer in the presence of the raft membrane compared to the $A\beta_{42}$ tetramer bound to the POPC membrane (Table 4.S5), even

though the $A\beta_{42}$ tetramer is more elongated in the presence of a raft. A largely hydrophilic surface of the $A\beta_{42}$ tetramer is observed in contact with the headgroup region of the raft, which influenced the inter-peptide rearrangement to form to hydrophobic nuclei (Figure 4.S7). The lack of insertion into the phosphate region of the membrane in raft simulations of these positively charged residues could relate to the decreased perturbation of the raft membrane by the $A\beta_{42}$ tetramer (Table 4.4, Figure 4.3) and account for the observed rearrangement as a result of cholesterol presence and rigidity of a raft membrane.

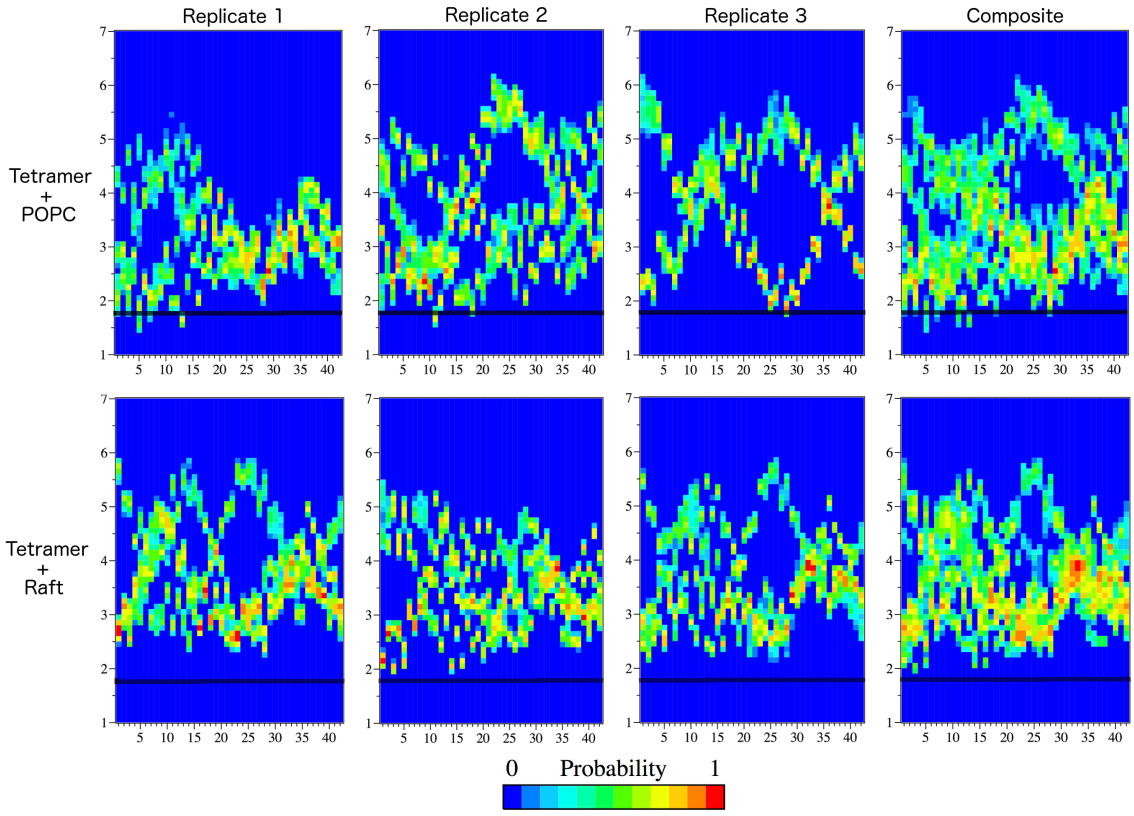


**Figure 4.4.** Normalized frequency of Aβ residue COM position at a distance, along the z-axis (membrane normal) relative to the COM of the bilayer. The residues of Aβ are given along the x-axis, while the y-axis corresponds to the COM-COM distance. The black dotted line indicates the position of the phosphorus atom in the lipid headgroup. A plot from each replicate is shown, as well as the composite of all replicates in order to show overall features of the ensembles.

## 4.5 Conclusions

Understanding the formation of low-molecular-weight $A\beta_{42}$ oligomers and consequential oligomer-membrane interactions are essential into providing mechanistic detail related to AD toxicity as caused by $A\beta_{42}$. The present work sought to understand the aggregation mechanism of an $A\beta_{42}$ tetramer and subsequent $A\beta_{42}$ tetramer-membrane interactions. The $A\beta_{42}$ tetramer formed in a stepwise manner, with each peptide binding individually until a relatively compact, oblate ellipsoid tetramer was formed. The formed $A\beta_{42}$ tetramer elongated in the presence of both POPC and raft model membranes, showing the influence of membranes on tetramer

structure. Rearrangement of inter-peptide contacts was observed in the presence of the raft membrane, in addition to a decrease in insertion depth of positively charged residues into the phosphate region of the membrane. $A\beta_{42}$ tetramer binding significantly perturbed POPC membranes, whereas the raft membrane remained relatively unperturbed by $A\beta_{42}$ tetramer binding. This observation further shows the influence of cholesterol on maintaining membrane integrity in the presence of $A\beta_{42}$ binding. These peptide-membrane interactions support the carpeting-effect model proposed for $A\beta_{42}$ toxicity on membranes [191] and reveal the role membrane environments in modulating Aβ fibril formation, ultimately yielding insight into mechanism of $A\beta_{42}$ toxicity and the potential for aggregation events to proceed in the presence of a membrane environment.

## 4.6 Acknowledgments

The authors thank Advanced Research Computing at Virginia Tech for computing time on the BlueRidge supercomputer and the Virginia Tech College of Agriculture and Life Sciences for the Graduate Teaching Scholars Fellowship (to A.M.B).

## 4.7 Supporting Information

**Table 4.S1.** Details of Systems and Initial Tetramer Membrane Distances.

| Membrane | Membrane Composition | System Dimensions (*x*, *y*, *z*, in nm) after energy minimization | Number of Ions | Minimum Distance between Tetramer and Membrane (nm) |
|---|---|---|---|---|
| POPC | 128 POPC | 6.34 x 6.31 x 18 | $Na^+$: 77<br>$Cl^-$ : 65 | Rep 1: 2.5<br>Rep 2: 2.5<br>Rep 3: 2.6 |
| Raft | 129 POPC<br>119 PSM<br>121 Cholesterol | 8.75 x 8.75 x 18 | $Na^+$: 136<br>$Cl^-$ : 124 | Rep 1: 3.4<br>Rep 2: 3.4<br>Rep 3: 3.5 |

**Table 4.S2.** Average diffusion coefficients of $A\beta_{42}$ tetramers, with corresponding standard deviation. [a]

| System | D ($cm^2\ s^{-1}$) |
|---|---|
| Tetramer Formation | $2.6 \pm 0.8 \times 10^{-6}$ |
| Tetramer + POPC | $1.4 \pm 0.3 \times 10^{-6}$ |
| Tetramer + Raft | $0.6 \pm 0.2 \times 10^{-6}$ |

[a] Average represents diffusion coefficient of $A\beta_{42}$ tetramers in the indicated simulation, averaged over the final 250 ns of three replicate trajectories for a cumulative sampling time of 750 ns, with corresponding standard deviations.

**Table 4.S3.** Average solvent accessible surface area (SASA) of $A\beta_{42}$ tetramers, with corresponding standard deviation. [a,b,c]

| System | Hydrophobic ($nm^2$) | Hydrophilic ($nm^2$) | Total SASA ($nm^2$) |
|---|---|---|---|
| Starting Structure | 70 ± 1 | 58 ± 1 | 128 ± 1 |
| Tetramer Formation | 54 ± 1 | 46 ± 1 | 100 ± 2 |
| Tetramer + POPC | 56 ± 4 | 49 ± 3 | 105 ± 5 |
| Tetramer + Raft | 57 ± 1 | 51 ± 1 | 108 ± 2 |

[a] Average represents SASA of $A\beta_{42}$ tetramers in the indicated simulation, averaged over the final 250 ns of three replicate trajectories for a cumulative sampling time of 750 ns, with corresponding standard deviations. [b] Starting structure average was calculated at the onset of MD simulations for the first 20 ns of simulation time. [c] An atom is determined to be hydrophilic if $|q| > 0.2$

**Table 4.S4.** Average SASA of POPC and raft membranes, with corresponding standard deviation. [a, b,c]

| System | Hydrophobic ($nm^2$) | Hydrophilic ($nm^2$) | Total SASA ($nm^2$) |
|---|---|---|---|
| Control POPC | 115 ±1 | 214 ± 1 | 329 ± 9 |
| Control Raft | 208 ± 1 | 401 ± 2 | 609 ± 2 |
| Tetramer + POPC | 112 ± 2 | 202 ± 3 | 314 ± 5 |
| Tetramer + Raft | 200 ± 3 | 400 ± 4 | 600 ± 7 |

[a] Average represents SASA of model membranes with $A\beta_{42}$ tetramers bound, averaged over the final 250 ns of three replicate trajectories for a cumulative sampling time of 750 ns, with corresponding standard deviations. [b] The control membrane averages presented represent the average over the last 250 ns of one simulation of the membrane only. [c] An atom is determined to be hydrophilic if $|q| > 0.2$

**Table 4.S5.** Average buried surface area of $A\beta_{42}$ tetramers, as calculated by (((SASA of membrane) + (SASA of $A\beta_{42}$ tetramers) – (SASA of peptide-membrane unit))/2), with corresponding standard deviation. [a, b]

| System | Hydrophobic ($nm^2$) | Hydrophilic ($nm^2$) | Total SASA ($nm^2$) |
|---|---|---|---|
| Tetramer + POPC | 6 ± 1 | 23 ± 4 | 29 ± 4 |
| Tetramer + Raft | 7 ± 3 | 16 ± 1 | 23 ± 1 |

[a] Average represents SASA of sidechain residues of $A\beta_{42}$ tetramers averaged over the final 250 ns of three replicate trajectories for a cumulative sampling time of 750 ns, with corresponding standard deviations. [b] An atom is determined to be hydrophilic if $|q| > 0.2$

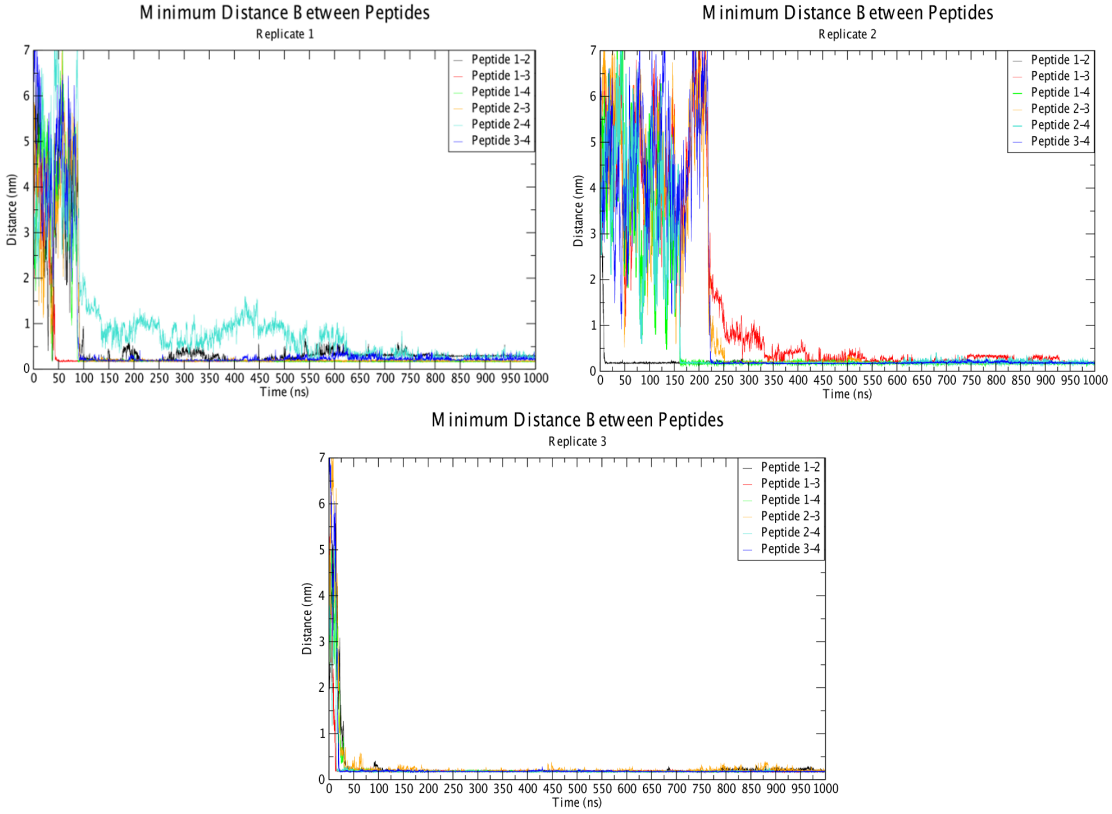


**Figure 4.S1.** Minimum distance between peptides (denoted as peptides 1, 2, 3, and 4) during tetramer formation. The minimum distance plots show the time and order of events for inter-peptide interaction.

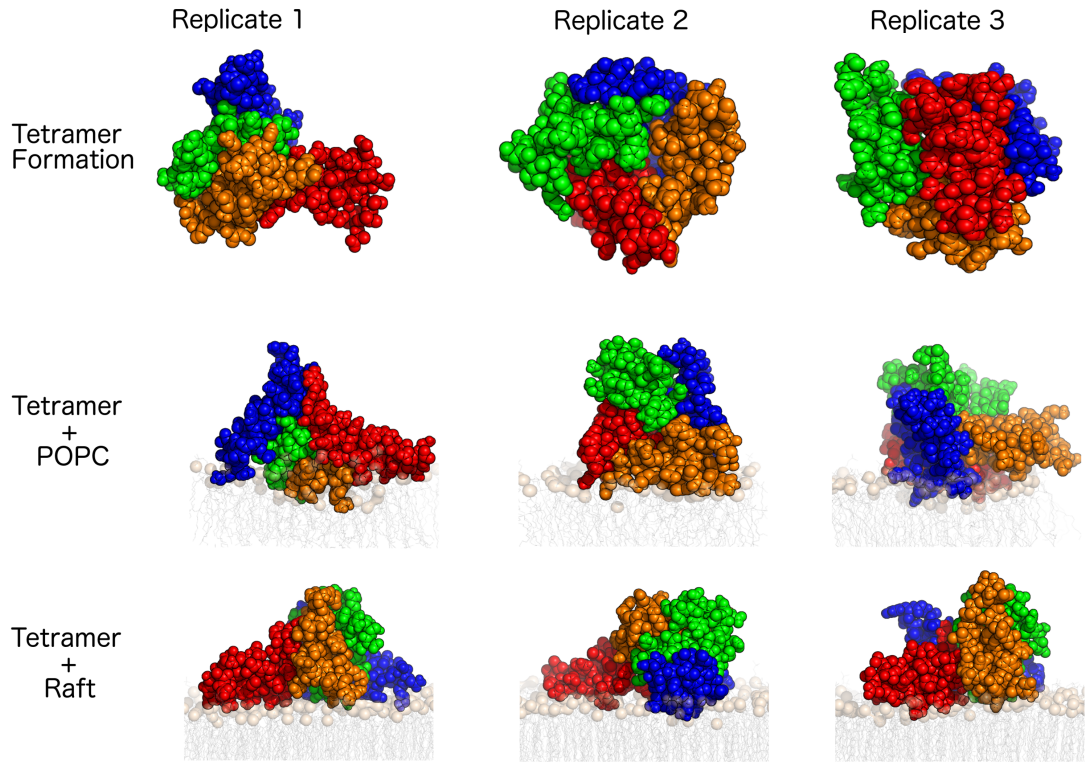


**Figure 4.S2.** Dominant morphologies of tetramer formation and tetramer-membrane interactions highlighting multimeric state. Representative images from the central structure of the first cluster (for clustering size, see Figure 4.2), with the peptides shown as spheres and colored orange, green, blue, or red for respective peptide number (1-4). Membranes are shown as grey sticks, with the phosphorus atoms shown as tan spheres for perspective.

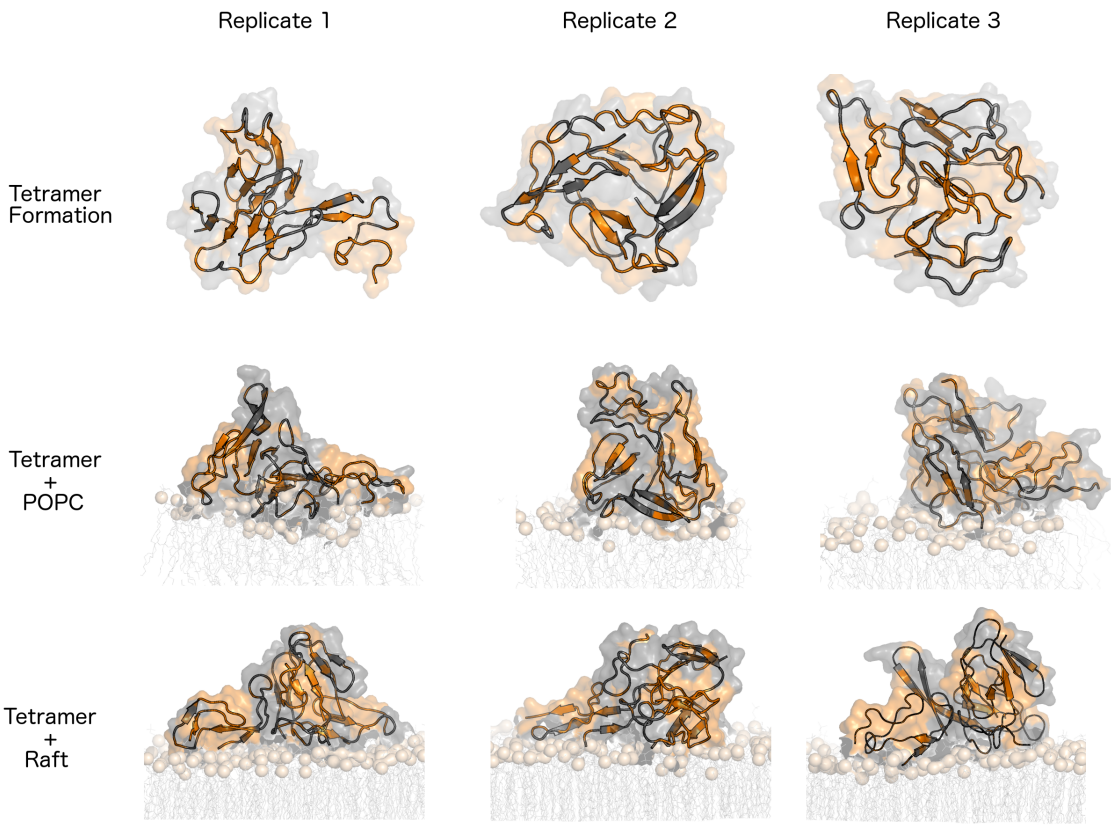


**Figure 4.S3.** Dominant morphologies of tetramer formation and tetramer-membrane interactions highlighting hydrophobic regions. Representative images from the central structure of the first cluster (for clustering size, see Figure 4.2), with the peptides shown as cartoon and surface, orange for hydrophobic residues and grey for hydrophilic. Membranes are shown as grey sticks, with the phosphorus atoms shown as tan spheres for perspective.

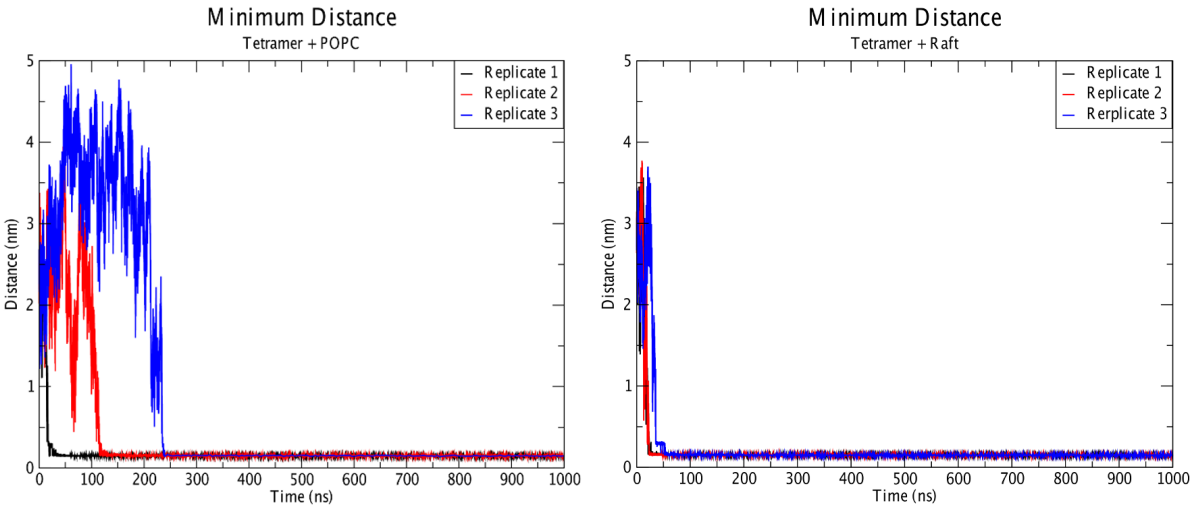


**Figure 4.S4.** Minimum distance between tetramer and POPC or raft membrane. The minimum distance plots show the time of interaction between the tetramer unit and membrane. For replicate 1 Tetramer + raft simulations, the time of contact is similar to replicate two and the two lines partially overlay.

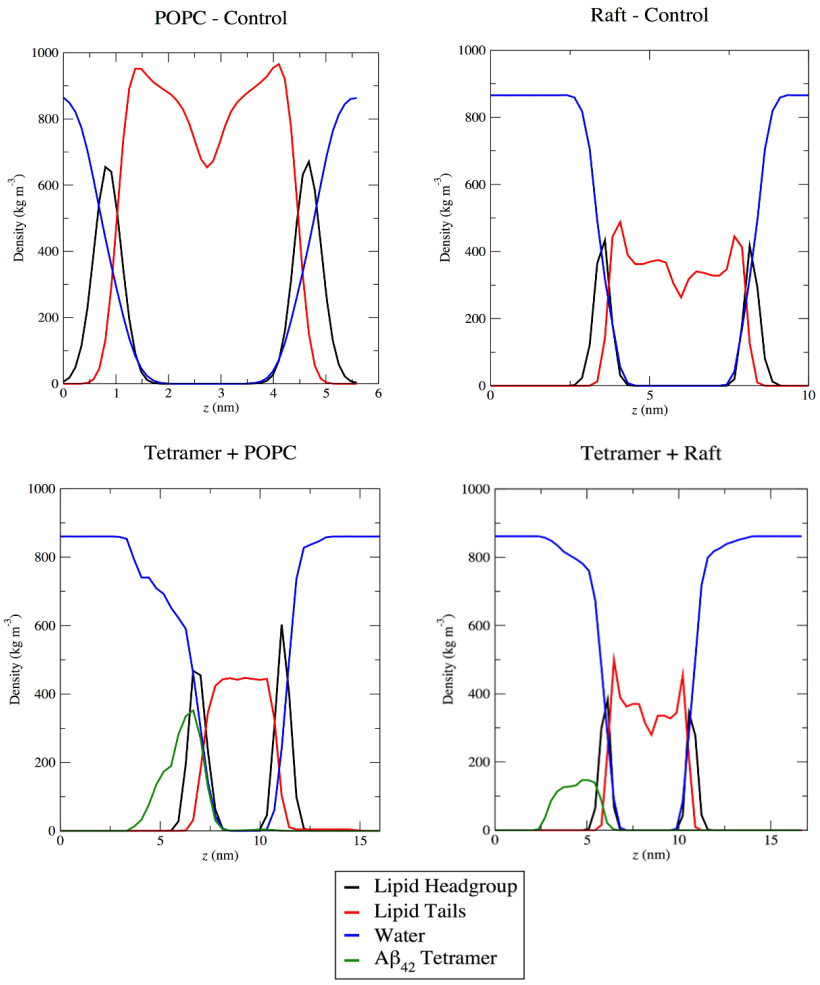


**Figure 4.S5.** Membrane (PC lipids), water, and protein density profiles for tetramer + POPC and raft membrane simulations. Note the flattening of the density at the core of the Tetramer + POPC profile indicates interdigitation of the PC lipid tails that is not observed in the control POPC membrane.

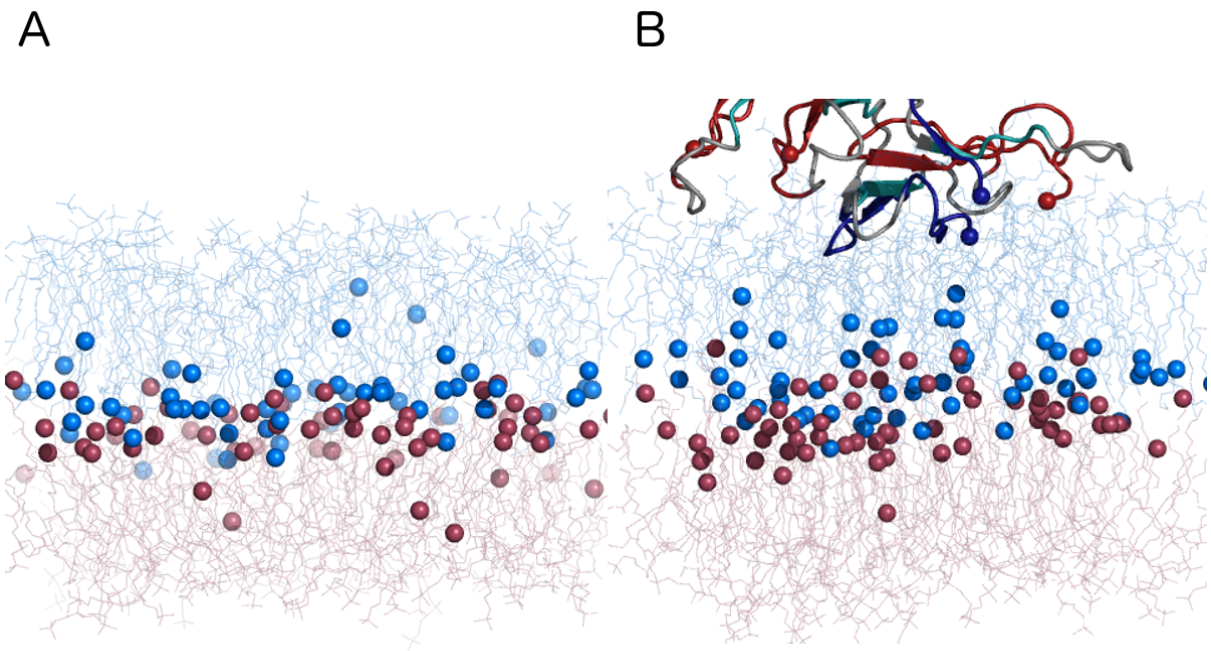


**Figure 4.S6.** Visual representation of interdigitation at bilayer interface for POPC membrane (A) POPC control and (B) POPC + Tetramer. Lipids are shown as sticks, with the terminal carbon of each chain shown as spheres, colored by leaflet (blue and red). The tetramer is shown for perspective and is rendered as in Figure 4.1.

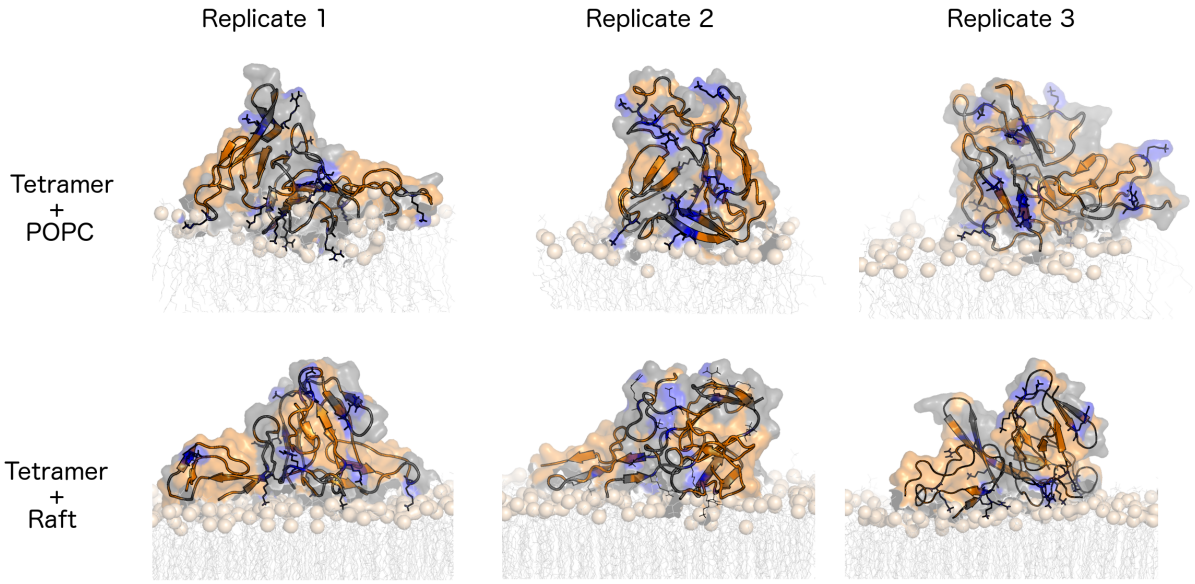


**Figure 4.S7.** Dominant morphologies of tetramer formation and tetramer-membrane interactions highlighting hydrophobic regions. Representative images from the central structure of the first cluster (for clustering size, see Figure 4.2), with the peptides shown as cartoon and surface, orange for hydrophobic residues, blue sticks for Arg-5, Lys-16, and Lys-28, and grey for all other hydrophilic residues. Membranes are shown as grey sticks, with the phosphorus atoms shown as tan spheres for perspective.

# 5 Molecular Dynamics Simulations of IAPP: Insight into the Influence of Primary Sequence on the Peptide In Solution and Interacting with Model Membranes

Anne M. Brown[1] and David R. Bevan[1]

[1]Department of Biochemistry (0308), Virginia Polytechnic Institute and State University, 201 Engel Hall, Blacksburg, VA 24061.

**Attribution:** AMB performed all of the data collection, analysis, and prepared the manuscript with editorial support from DRB. All authors collectively conceived the initial project idea and direction. AMB is responsible for pending submission of the completed manuscript and response to reviewers.

## 5.1 Abstract

Type 2 diabetes mellitus (T2D), classified as noninsulin-dependent diabetes, is a complex metabolic disorder drastically increasing in prevalence worldwide. A characteristic feature of T2D is the deposition of islet amyloid polypeptide (IAPP) in the pancreatic islets of Langerhans. It is currently unknown if IAPP aggregation is a cause or consequence of T2D, but it does lead to β-cell dysfunction and death, exacerbating the effects of T2D. Interestingly, the rat (*Rattus norvegicus*) form of IAPP (rIAPP) does not exhibit the toxicity as observed with the human form (hIAPP). In this work, molecular dynamics (MD) simulations were used to study the influence of primary sequence on secondary and tertiary structures of hIAPP and rIAPP in solution and in the presence of three model membranes. It was observed that hIAPP had an increased affinity for zwitterionic (PC) model membranes and caused significantly more membrane perturbation as compared to rIAPP. No difference in affinity or degree of membrane perturbation was observed for hIAPP interacting with an anionic (PS) model membrane as compared to rIAPP. Cholesterol was observed to attenuate the perturbation of membranes caused by IAPP. The amyloidogenic core, residues 20-29, in hIAPP was found to influence depth and type of insertion into model membranes, whereas Arg-18 in rIAPP influenced peptide affinity and type of insertion into model membranes. These findings indicate a potential target towards diminishing IAPP-membrane interactions and characterizing the fundamental interactions of hIAPP and rIAPP with model membranes on the atomistic scale.

## 5.2 Introduction

Type 2 diabetes mellitus (T2D), classified as noninsulin-dependent diabetes, is a complex metabolic disorder drastically increasing in prevalence worldwide [10]. T2D is diagnosed by the presence of high blood glucose levels caused by insulin resistance and eventually insufficient insulin production. As T2D progresses, there is a transition in T2D from a compensated phase of insulin resistance to a decompensated phase of hypoinsulinemia and hyperglycemia [12, 241, 242]. The advancement into the decompensated phase of T2D is associated with an overall reduction in the number of functional insulin-producing β-cells, ultimately creating a deficit in insulin secretion and further exacerbating the effects of insulin resistance in the body [242]. The progression from the compensated phase to the decompensated phase of T2D has been linked to increased levels of islet amyloid polypeptide (IAPP, also referred to as amylin) in the pancreatic islets of Langerhans [243]. The role of IAPP in T2D progression has been established, with IAPP being found in amyloid deposits in and around β-cells, with these amyloid deposits being linked to deleterious effects on β-cells and T2D pathogenesis [42].

Functionally, IAPP is a regulatory peptide that contributes to glycemic control by acting locally in the islets to inhibit insulin and glucagon secretion and by binding to receptors in the brain to slow gastric emptying and provide satiety regulation [12, 45, 46]. Insulin and IAPP are co-secreted from β-cells at a molar ratio of 1:100 (insulin:IAPP) in healthy individuals; this ratio changes to 1:20 in T2D patients [244, 245]. IAPP is a 37-residue peptide that is cleaved from an 89-residue preproprotein, which contains a 22-residue signal peptide and a 67-residue proislet amyloid polypeptide (proIAPP) [47]. The signal peptide directs the preproprotein to the endoplasmic reticulum (ER) where the signal peptide is cleaved, generating proIAPP. ProIAPP processing occurs in secretory vesicles by prohormone convertases 2 and 1/3 (PC2 and PC1/3), which are the same proteases that process proinsulin. PC1/3 cleaves IAPP at the N-terminus and PC2 cleaves at the C-terminus [48]. Following this cleavage event, carboxypeptidase E (CPE) removes a lysine and arginine at the C-terminus, exposing a glycine residue that is amidated by peptidylglycine alpha-amidating monooxygenase (PAM) [246]. A disulfide bond is formed between two cysteine residues in the N-terminal region (Cys2 and Cys7), resulting in biologically active IAPP [12, 48].

Biologically active, monomeric IAPP is classified as an intrinsically disordered protein (IDP), with its structure in solution being metastable and adopting either a random coil structure, an α-helical conformation, or a β-strand/hairpin conformation dependent on the stage in the aggregation pathway [247]. The transition from an α-helical conformation to a β-strand/hairpin conformation is a critical component in the aggregation pathway of human IAPP (hIAPP) *in vivo,* in that it leads to the β-strand/hairpin conformation adopted by hIAPP in fibillar form [248-250]. Secondary structure properties of IAPP, specifically the transition from an α-helical conformation to a β-strand/hairpin conformation, can be used to assess the progression of the peptide along the aggregation pathway and its toxic potential [251]. hIAPP has been found to disrupt the β–cell membrane and cause cytotoxicity [252-254], and in turn the membrane influences hIAPP structure by stabilizing an α-helical intermediate suggested to be a critical component in the aggregation pathway of hIAPP *in vivo* [255-258]. Finally, the rat variant, species *Rattus norvegicus*, of IAPP (rIAPP), which differs from hIAPP at six residues (Figure 5.1), does not form aggregates and is classified as non-cytotoxic [259]. Herein, it is hypothesized

that the primary structure of IAPP is influential on folding state and toxicity, and by comparing hIAPP and rIAPP, insight on toxic properties can be elucidated.

The primary toxic species of IAPP are pre-fibrillar, early stage oligomers of the peptide [260, 261]. Understanding IAPP structural features in its monomeric form prior to aggregation, in various environments, is essential to providing a foundation for understanding the aggregation process and mechanistic details related to the toxicity of IAPP oligomers on β–cells. Given the difficulty in working with monomeric or low-molecular-weight oligomers of IAPP experimentally due to aggregation rates and stability, theoretical methods such as molecular dynamics (MD) simulations can aid in describing the conformational state of the peptide in solution and in the presence of various model membranes. In this work, six replicates each of hIAPP and rIAPP were simulated in physiological solution (water and 150 mM NaCl) to assess differences in structure in solution. The resulting structures of hIAPP and rIAPP from these simulations were compared to various computational studies [247, 262] and experimental work [251, 263-265] to confirm their relevance as representative structures of IAPP. To assess the cytotoxicity of each peptide, each solution structure of IAPP was placed at least 2.4 nm away from model membranes of differing composition to assess the effect of IAPP on membrane stability and of the membrane on structural elements of IAPP. Three model membranes consisting of lipids that are prevalent in eukaryotic plasma membranes were utilized in this work to give insight into the role of lipid type on IAPP-membrane interactions [163, 164]. The model membranes utilized in this study also serve as a basis to compare to experimental work on IAPP-membrane interactions [266-268]. Each IAPP-membrane simulation was run for 1 μs, with six replicates of each hIAPP and rIAPP in the presence of three membranes, resulting in an extensive sampling time of 36 μs.

## 5.3 Methods

### 5.3.1 System Construction – Solution Structures of hIAPP and rIAPP

The starting structure of IAPP in the simulations was generated from an NMR structure in micelles (PDB ID: 2L86) [60]. This structure is for full-length (residues 1-37) hIAPP, has a disulfide bond between Cys-2 and Cys-7, and is C-terminally amidated to represent the biologically active form of IAPP. RIAPP coordinates were generated by taking the 2L86 NMR structure and changing six residues, H18R, F23L, A25P, I26V, S28P, and S29P (Figure 5.1), using DeepView-Swiss-PdbViewer [176] (http://www.expasy.org/spdbv/). The lowest energy rotamer of each altered amino acid side chain was selected. To begin simulations of hIAPP and rIAPP in the presence of model membranes, the hIAPP NMR structure and the rIAPP structure generated from DeepView were subjected to MD simulations in a physiologically relevant solution environment (water and 0.150 M NaCl) for 400 ns to obtain six different solution structures of each IAPP variant to place in the presence of model membranes. These simulations of hIAPP or rIAPP in solution were built by centering the structures in a dodecahedral box with a minimum solute-box distance of 1.0 nm and solvating with SPC water [114]. $Na^+$ and $Cl^-$ ions were added to mimic a concentration of 0.150 M NaCl and to maintain a net-neutral system. Six replicates of both hIAPP and rIAPP were performed and represent independent trajectories starting with different random starting velocities in a canonical (NVT) ensemble. Representative structures were chosen from these replicates to be placed in the presence of model membranes based on root-mean-square deviation (RMSD) clustering of backbone atom structures over the last 100 ns of simulation time with a cutoff of 0.2 nm.

**hIAPP:** KCNTATCATQ$_{10}$RLANFLVHSS$_{20}$NNFGAILSST$_{30}$NVGSNTY$_{37}$
**rIAPP:** KCNTATCATQ$_{10}$RLANFLVRSS$_{20}$NNLGPVLPPT$_{30}$NVGSNTY$_{37}$

**Figure 5.1.** Sequence comparison of human and rat IAPP. Residues are colored to represent hydrophobic (black), polar (green), and positively charged (blue) side chains.

### 5.3.2 System Construction – IAPP-membrane simulations

Each structure of hIAPP and rIAPP derived from RMSD clustering as described above (Figure 5.S1), was randomly placed above a model membrane so that the minimum atom distance between a protein atom and membrane atom was at least 2.4 nm (Table 5.S1). Model membranes used in this work include: **(1)** palmitoyloleoylphosphatidylcholine (POPC), **(2)** palmitoyloleoylphosphatidylserine (POPS), **(3)** raft [1:1:1 POPC:cholesterol:palmitoylsphingomyelin (PSM)]. The coordinates and topologies for the membranes utilized in these simulations were based on previous work [71, 178, 180]. Six replicates each of hIAPP and rIAPP, with each replicate containing a representative structure as based on RMSD clustering from replicates 1-6 of the IAPP solution structure simulations, were run for each model membrane. Details of membrane composition, size, and minimum distance of hIAPP or rIAPP to the membrane are shown in Table S1. IAPP-membrane systems were constructed in a cubic box with a minimum solute-box distance of 1.0 nm and solvated with SPC water [114]. As with IAPP solution structure simulations, $Na^+$ and $Cl^-$ ions were added to mimic a concentration of 0.150 M NaCl and to maintain a net-neutral system. In total, 18 simulations of at least 1 μs were run with hIAPP and the three membrane systems and 18 simulations were run

with rIAPP and the three membrane systems, totaling 36 μs of simulation time for peptide-membrane simulations. For simulations of hIAPP and rIAPP with POPC membranes, three replicates were not converged for at least 100 ns when reaching 1 μs of simulation time and were extended an additional 200 ns in order to perform analysis metrics on converged, completed simulations. Backbone RMSD clustering was performed on IAPP-membrane simulations in order to obtain representative structures and positions of hIAPP or rIAPP relevant to the model membrane, with the center structure of the largest cluster chosen as representative of the last 100 ns of simulation time for these IAPP-membrane interactions.

### 5.3.3 MD Simulation Protocol

All simulations, including IAPP in solution and IAPP-membrane simulations described above, were performed using the GROMACS software package, version 4.6.0 [68, 115] and the GROMOS53A6 force field [70]. Energy minimization on the solution structure simulations and IAPP-membrane simulations was performed using the steepest descent method. System equilibration was performed in two steps for IAPP in solution simulations, canonical (NVT) and isothermal-isobaric (NPT). System equilibration was performed in three steps for IAPP-membrane simulations, NVT, annealing, and NPT. NVT was applied to the system for 100 ps using the Berendsen weak coupling method [116] to maintain temperature at 310 K. For IAPP-membrane simulations, annealing was performed to linearly heat the system from 100 to 310 K, at 1 bar pressure for 1 ns using the Berendsen algorithm [116]. NPT was performed to maintain temperature (310 K) and pressure (1 bar) using the Nosé-Hoover thermostat [74, 75] and Parrinello-Rahman barostat [76, 77]. For all equilibration steps, position restraints were imposed on all peptide heavy atoms. Restraints were released at the start of MD simulations. All simulations were performed using three-dimensional periodic boundary conditions, with bond lengths being constrained using P-LINCS [117] with an integration time step of 2 fs. Nonbonded interaction cutoffs were set to 1.4 nm for IAPP solution structure simulations, whereas they were set to 1.2 nm for IAPP-membrane simulations. The smooth particle mesh Ewald (PME) method [79, 80] using cubic interpolation and Fourier grid spacing of 0.16 nm was utilized to calculate long-range electrostatic interactions for all simulations. A control simulation of each model membrane containing no peptide was run for 1 μs under the MD protocol described above to serve as a comparison to the degree or type of perturbation caused to the membrane by IAPP interaction.

### 5.3.4 Analysis

IAPP solution structure simulations and IAPP-membrane simulations were determined to be complete and converged after backbone RMSD and secondary structure analysis reported no major structural changes during at least the last 100 ns of simulation time. Secondary structure was evaluated according to the DSSP algorithm [118]. All analysis was performed using programs within the GROMACS program suite or scripts written in-house. Deuterium order parameter analysis was performed to assess the order of the lipid acyl chains, relative to the bilayer normal, using Equation (1).

$$-S_{CD} = \langle \frac{3cos^2\theta - 1}{2} \rangle \quad (1)$$

where θ is the angle between the C-D bond and bilayer normal and angle brackets represent that the θ value is averaged over all equivalent atoms (e.g., all C2 on the lipid acyl chain) over the

time period analyzed. Analysis on area-per-lipid (APL) and membrane bilayer thickness was performed using GridMAT-MD [182] to assess for degree and type of perturbation caused by IAPP interaction or binding. Binding is defined in this work as IAPP interacting with and maintaining interaction (e.g. no release from the membrane) with the model membrane from first point of IAPP-membrane interaction. All averages presented represent the average of six replicates for that simulation set, as averaged over the last 100 ns of simulation time. Averages over the last 100 ns of simulation time were deemed appropriate as a standard comparison across all IAPP-membrane interactions given the transient interaction observed by rIAPP in multiple simulations and to equally compare against and assess the role of lipid type in these IAPP-membrane interactions. Bound classifications of rIAPP-POPC simulations are for replicates 3 and 4, where the peptide interacted with and bound to the membrane. Unbound classifications of rIAPP-POPC simulations are for replicates 1,2,5, and 6, where rIAPP transiently interacted with the membrane and did not maintain a bound state with POPC (Figure 5.2). PyMOL was used for visualization of results [120]. Results were subjected to statistical analysis using a two-tailed *t*-test, with statistical significance determined if $p < 0.05$.

## 5.4 Results and Discussion

### 5.4.1 Secondary Structure of hIAPP and rIAPP in Solution

To begin simulations of hIAPP and rIAPP in solution and in the presence of various model membranes, particular care was given to the choice of force field. The GROMOS53A6 force field was utilized given its agreement in simulating hIAPP [269] compared to 2D- infrared (2D IR) spectroscopy experiments [270-272]. Six replicates each of hIAPP and rIAPP in solution were simulated for 400 ns and determined to be converged given results from block averaging of RMSD and RMSD clustering (Figure 5.S1, 5.S2). Simulations of hIAPP in solution resulted in two primary structures being sampled, with three replicates converging at a structure that contained antiparallel β-strand structure and three replicates converging at a structure that was mostly unstructured coil with short β-strand structure in the C-terminal region. Markov state models constructed from MD simulations have suggested that the conformation of the hIAPP peptide in solution is essentially random, sampling metastable states that adopt the observed secondary structure elements discussed above [247]. Thus, the starting structures of hIAPP presented and utilized in this work (Figure 5.S1) have been observed in other computational [262] and experimental work [273] and exemplify representative structures of hIAPP to place in the presence of model membranes.

IAPP can be divided into three regions: the N-terminal region (residues 1-19), the primary amyloidogenic region (residues 20-29) and the C-terminal region (residues 30-37) [274, 275]. Residues 20-29 represent the "amyloidogenic core" of hIAPP fibrils [276-279], with residues 23-27 constituting the FGAIL region of hIAPP that influences the aggregation and lag phase of hIAPP [273]. The FGAIL region has been observed through 2D IR spectroscopy and isotope labeling to adopt transient β-sheet structure, with the FGAIL region first adopting a β-sheet structure that transitions into the loop region of the fibril. The structures adopted by the FGAIL region indicate stages in the aggregation pathway. It is hypothesized that the structures influence the aggregation of hIAPP and explain variation in lag phase studies [273]. The all-atom MD simulations of hIAPP in solution in this study show the FGAIL region sampling both of these conformations (loop or β-sheet structure), representing extensive sampling of on-pathway structures of the hIAPP monomer (Figure 5.S1). The position of the FGAIL region in starting structures also influenced depth of insertion into a POPC membrane and is discussed further below.

Simulations of rIAPP in solution generated a primarily coiled structure that included a small amount of α-helical structure, which was not observed with hIAPP (Table 5.1). Circular dichroism (CD) studies report that rIAPP is globally disordered and adopts a mostly random coiled structure, in agreement with the structures generated in these simulations [275, 280]. The percentage of random coil in rIAPP structures was significantly greater than in hIAPP (84 ± 5 vs. 69 ± 8, respectively), while hIAPP structures contained a statistically higher percentage of β-sheet structure as compared to rIAPP (31 ± 9 vs. 11 ± 4) (Table 5.1). β-strand structure is indicative of on-pathway aggregation events and in monomeric form, represents a pre-fibrillar hIAPP species [273]. The reduced amount of β-sheet structure in rIAPP is consistent with its lack of ability to aggregate and reduced propensity to form amyloid as compared to hIAPP.

**Table 5.1.** Average secondary structure composition (shown in %) of hIAPP or rIAPP .[a]

| | Coil | | β-strand | | α-helix | |
|---|---|---|---|---|---|---|
| System | hIAPP | rIAPP | hIAPP | rIAPP | hIAPP | rIAPP |
| Solution | 69 ± 8 | 84 ± 5 | 31 ± 9 | 11 ± 4 | 0 ± 0 | 5 ± 8 |
| POPC | 68 ± 9 | 84 ± 9 | 32 ± 9 | 16 ± 9 | 0 ± 0 | 0 ± 0 |
| POPS | 68 ± 9 | 82 ± 6 | 32 ± 9 | 15 ± 6 | 0 ± 0 | 3 ± 7 |
| Raft | 71 ± 12 | 85 ± 4 | 28 ± 12 | 13 ± 5 | 0 ± 0 | 2 ± 5 |

[a] Percentages represent averages over the final 100 ns of simulation time for three replicates of each system, with corresponding standard deviations.

### 5.4.2 Electrostatic Forces Drive hIAPP and rIAPP Interactions with Model Membranes

To begin detailing IAPP-membrane interactions and orientation relevant to the bilayer normal, Williamson et al. suggests a parallel self-association of IAPP with the membrane that correlates with membrane toxicity and potential amyloid structure [281]. In the presented simulations where hIAPP or rIAPP interacted and bound to the membrane, the peptide primarily oriented parallel to the membrane (Figure 5.2, Figure 5.S3-5.S8). The parallel orientation of the peptide to the membrane is observed in all simulations of hIAPP + POPC and POPS and rIAPP + POPS. In the presence of raft membranes, this parallel orientation was observed to lesser extent indicating the potential for orientation of IAPP in the presence of a raft membrane to influence the degree of insertion and membrane perturbation.

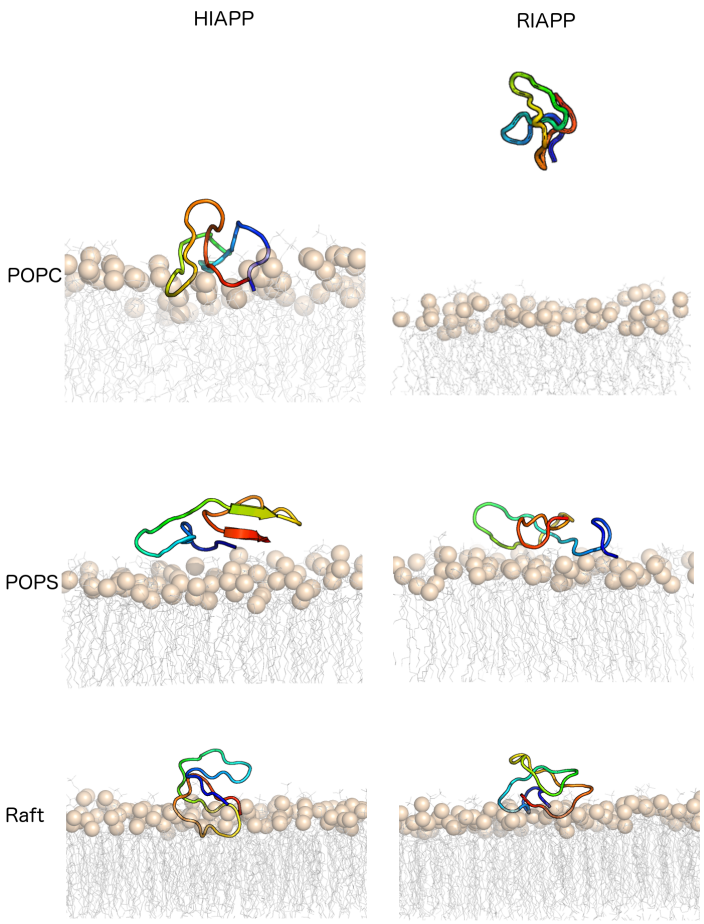


**Figure 5.2.** Dominant morphologies of IAPP interaction with model membranes from RMSD clustering. A representative replicate from each simulation set was chosen for clarity. The representative replicate was chosen based on similarity to secondary structure average. The structures shown are the central structure of the first cluster, as based on RMSD clustering with a cutoff of 0.2 nm. The peptide is shown as a cartoon, colored in rainbow from N-terminus (blue) to C-terminus (red). Lipids are shown as gray lines, with the phosphate atom shown as tan sphere for perspective

To further expand upon the parallel orientation of IAPP relative to the bilayer normal of model membranes, short range Lennard-Jones (LJ-SR) and Coulomb (Coul-SR) interaction energies were calculated. Larger energies associated with LJ-SR represent van der Waals forces prevailing in guiding interaction and binding energies, whereas larger Coul-SR interaction energies represent electrostatic forces driving binding. Interaction energies were first calculated to aid in explaining the unexpected, transient interaction of rIAPP with POPC model membranes (Figures 5.2 and 5.3, Figure 5.S4). Time for peptide-membrane interactions varied across peptide and lipid type (Figure 5.3); however, in simulations of rIAPP + POPC, four out of six replicates transiently interacted with the POPC membrane and did not stay bound. For these replicates, we have classified them as unbound (U), whereas the other two replicates in this simulation set remained bound (B) to the POPC membrane (Figures 5.S3, 5.S4). For distance measurements and interaction energies, we have separated out these calculations into U and B states when

necessary. For membrane perturbation analysis, we did not separate these states in order to assess overall POPC perturbation when both transient and stable interactions of rIAPP with POPC were present. The interaction energies for the unbound state of rIAPP + POPC simulations also confirmed the transient interaction of rIAPP with POPC (Table 5.2) and represent a lack of affinity for the membrane as compared to hIAPP. Similar trends for rIAPP when compared to hIAPP have been reported from studies using sucrose gradient centrifugation assays and CD titrations [258].

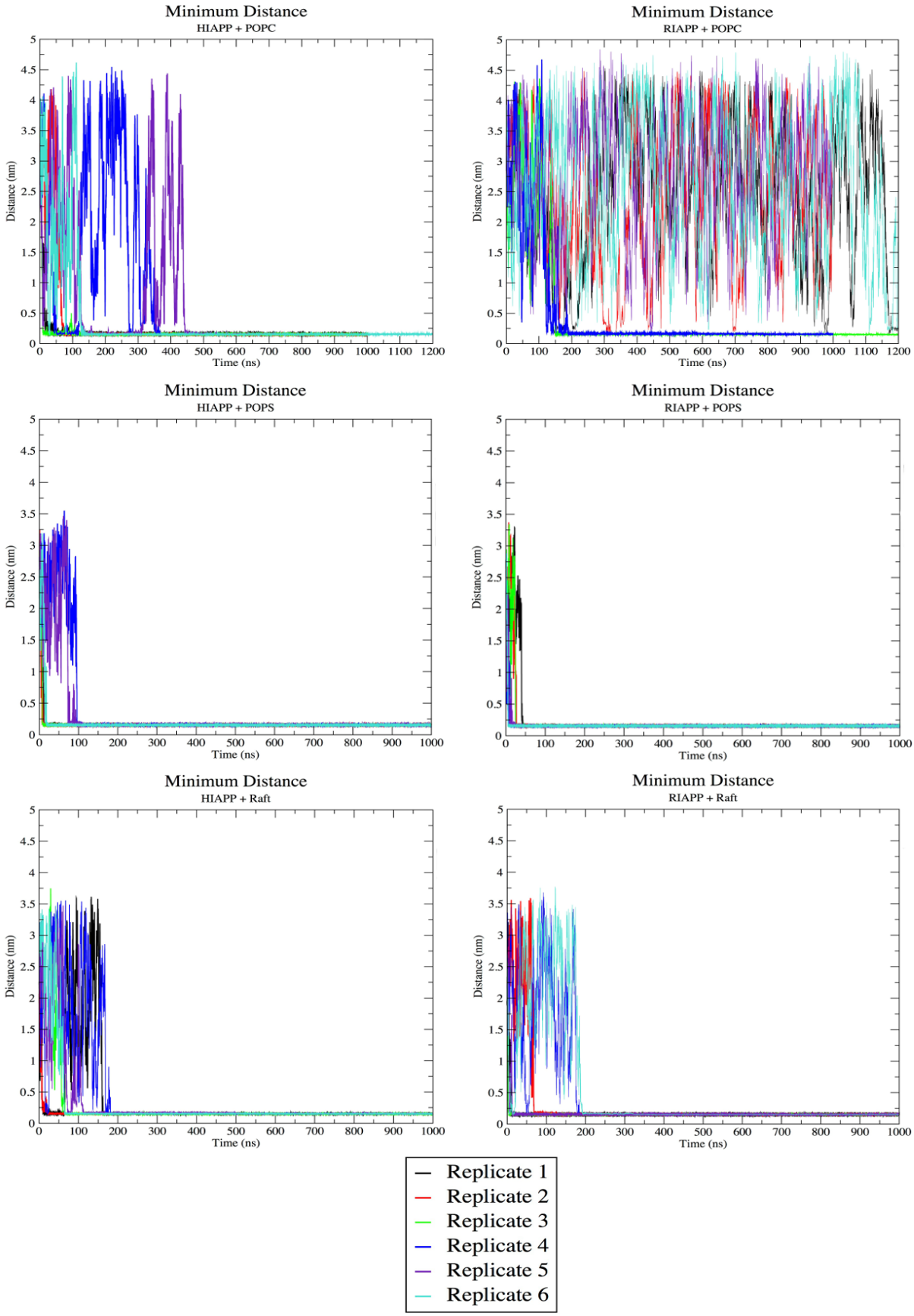


**Figure 5.3.** Minimum distance between IAPP and model membranes. The minimum distance plots show the time of interaction between hIAPP or rIAPP and respective membrane. Distance (nm) is plotted with respect to time (ns).

In all replicates of hIAPP in the presence of POPC, POPS, and raft bilayers, as well as rIAPP in the presence of POPS and raft bilayers, the peptides interacted with the membrane and remained bound after the initial interaction. Coul-SR interactions were determined to be the dominating interaction force (Table 5.2). Electrostatic forces are driving peptide-membrane interactions, with hIAPP having a larger total binding interaction energy in the presence of raft and POPC membranes as compared to POPS (Table 5.2). Larger total binding interaction energies for POPC and raft membranes as compared to POPS are also observed in rIAPP-membrane simulations where rIAPP remained bound to the model membrane throughout the simulation. Interestingly, a measurable increase in Coul-SR and total interaction energy was observed for all rIAPP-membrane interactions as compared to all hIAPP-membrane interactions. This increase in electrostatic interaction energies, can be related back to the influence of the primary sequence on IAPP-membrane interactions, given that rIAPP has one more positively charged amino acid as compared to hIAPP (Arg-18 in rat, His-18 in human). The influence of Arg-18, which can participate in two more hydrogen bonds than His-18, in rIAPP-membrane interaction is also confirmed by a measurable increase in hydrogen bonds between rIAPP and the membrane in the presence POPS and raft membranes (Table 5.3). From these results, it is concluded that the more positively charged rIAPP sequence has greater electrostatic drive to interact with POPS membranes, agreeing with experimental work that proposed rIAPP has greater affinity towards and was able to cause membrane leakage with a POPS membrane [257].

**Table 5.2.** Average IAPP-membrane short Lennard-Jones (LJ-SR) and Coulomb (Coul-SR) interaction energies.[a,b]

| | LJ-SR (kJ x $10^2$) | | | Coul-SR (kJ x $10^2$) | | | Total (LJ-SR+Coul-SR) (kJ x $10^2$) | | |
|---|---|---|---|---|---|---|---|---|---|
| System | hIAPP | rIAPP | | hIAPP | rIAPP | | hIAPP | rIAPP | |
| | | U | B | | U | B | | U | B |
| POPC | -3 ± 1 | 0 ± 0 | -4 ± 1 | -11 ± 2 | -1 ± 0.1 | -12 ± 6 | -15 ± 3 | -1 ± 0.1 | -17 ± 5 |
| POPS | -2 ± 1 | -2 ± 1 | | -11± 2 | -13± 4 | | -13 ± 2 | -15 ± 4 | |
| Raft | -3 ± 1 | -4 ± 2 | | -12 ± 1 | -15 ± 2 | | -15 ± 2 | -19 ± 4 | |

[a] Percentages represent averages over the final 100 ns of simulation time for three replicates of each system, with corresponding standard deviations.
[b] U represents the simulations where rIAPP did not stay bound to POPC, B represents the simulations where rIAPP did bind and maintain interaction with POPC.

**Table 5.3.** Average number of peptide-membrane hydrogen bonds .[a]

| | Number of Hydrogen Bonds | |
|---|---|---|
| System | hIAPP | rIAPP |
| POPC | 13 ± 3 | 5 ± 7 |
| POPS | 14 ± 3 | 16 ± 6 |
| Raft | 15 ± 3 | 20 ± 4 |

[a] Percentages represent averages over the final 200 ns of simulation time for three replicates of each system, with corresponding standard deviations.

To give a more detailed perspective into the electrostatic forces driving IAPP-membrane interactions, distance plots measuring the center of mass (COM) of each residue relative to the center of the bilayer were generated (Figure 5.4). In the two replicates of rIAPP + POPC where the peptide maintained interaction throughout the simulation, residues 15-18 inserted into the bilayer below the phosphate atom. When rIAPP did stay bound to the membrane, Arg-18 in rIAPP was also shown to form significantly more hydrogen bonds with model membranes, indicating this residues role in providing difference between hIAPP and rIAPP-peptide zwitterionic membrane interactions (POPC and raft) (Figure 5.5). These rIAPP residue interactions with a POPC membrane differs from hIAPP + POPC membrane interactions, where residues 20-29 inserted below the phosphate atom of the POPC bilayer (Figure 5.4). It is worth mentioning that in hIAPP+POPC simulations, the FGAIL region (residues 23-27) sampled a loop structure and represent a structure further down the aggregation pathway as shown by 2D IR spectroscopy [273], the degree and depth of insertion was much greater than when the FGAIL region sampled β-strand structure (Figure 5.S9). This is an interesting observation and potentially relates to the hIAPP structure in the aggregation pathway greatly influencing membrane interactions and toxicity.

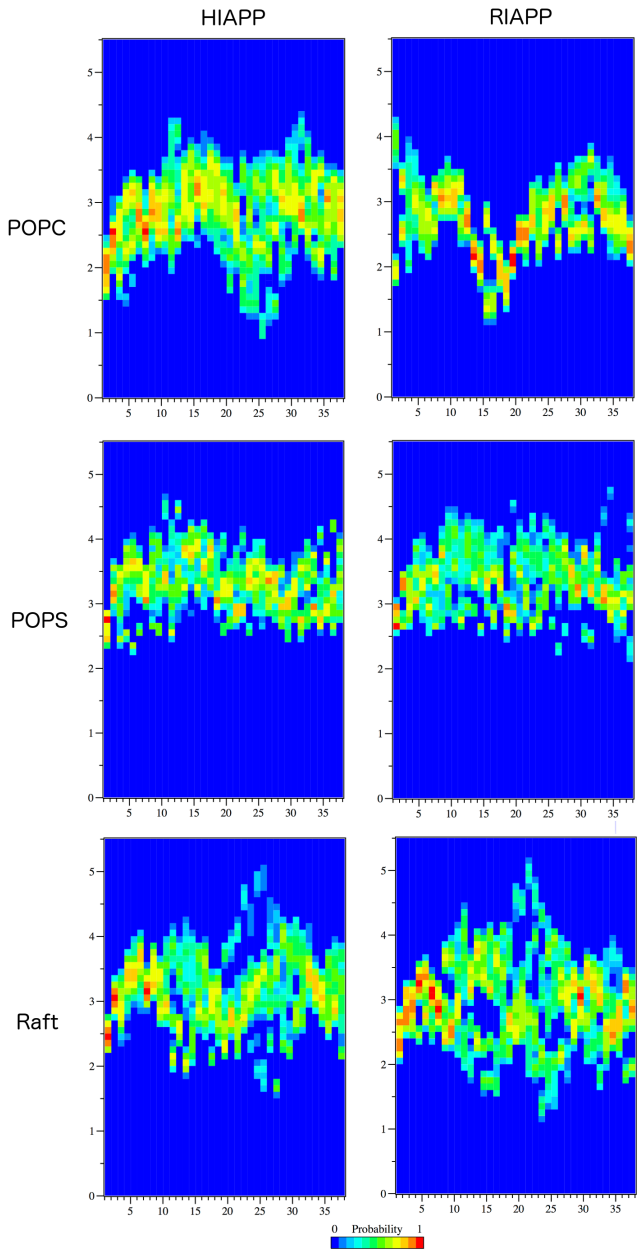


**Figure 5.4.** Global normalization of the frequency of IAPP residue center of mass (COM) occurrence at a distance, on the z-axis, from the COM of the membrane bilayer**.** Each plot contains all data points from 6 replicates over the last 100 ns of simulation time except for rIAPP + POPC, which only contain replicates in which the peptide bound and stayed bound to the membrane. Residue number and distance (nm) are plotted on the x- and y- axis, respectively.

Depth of insertion into raft membranes by either hIAPP or rIAPP differed, with rIAPP residues 15-18 inserting deeper into the leaflet as compared to hIAPP (Figure 5.4), further supporting the influence of Arg-18 in rIAPP on peptide-membrane interactions. Depth of insertion was not observed to the same extent in IAPP-raft simulations as compared to IAPP-POPC simulations,

indicating a difference in penetration ability as caused by lipid type. NMR experiments indicate that membrane composition does affect membrane permeabilization, with cholesterol modulating affinity and degree of perturbation of hIAPP [282]. In the presence of an anionic membrane, POPS, there was no observable differences in residue insertion depth between rIAPP and hIAPP. This finding further supports a lack of known experimental difference in toxicity as caused by either hIAPP or rIAPP in the presence of a POPS membrane [257]. Overall, these simulation studies propose that the amyloidogenic core of IAPP, residues 20-29, in hIAPP is implicated as key regions for membrane insertion in zwitterionic membranes with and without the presence of cholesterol. This difference from rIAPP- zwitterionic membrane centers around the presence of Arg-18, which may aid in attenuating the ability of the amyloidogenic core in rIAPP to interact and insert into zwitterionic membranes. This finding brings forward the role and influence of Arg-18 in rIAPP, whereas primary focus has been on the presence of proline residues in the 20-29 region of rIAPP as compared to hIAPP (Figure 5.1).

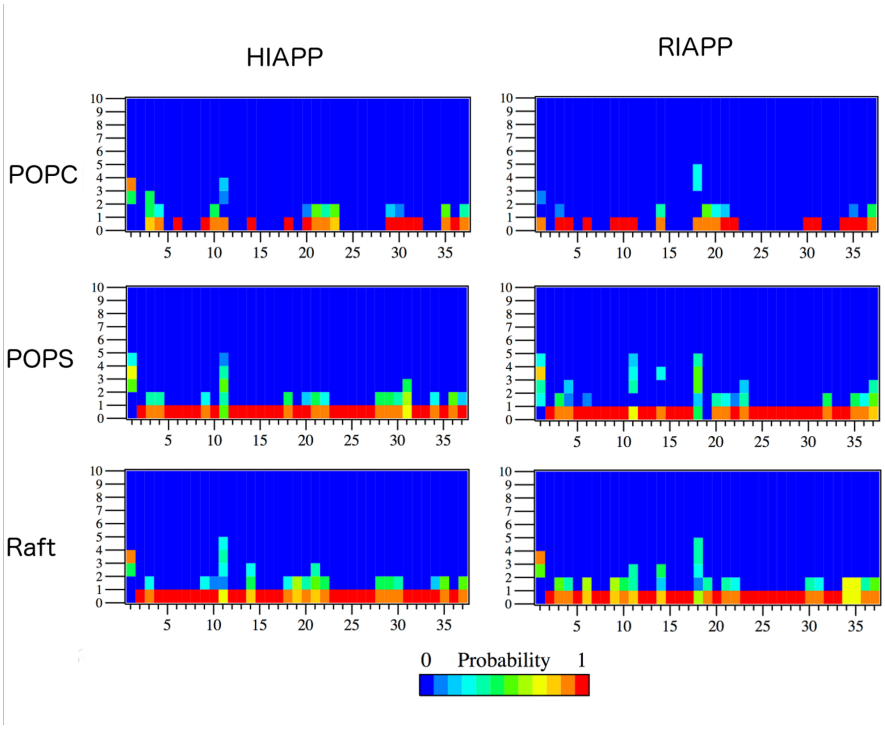


**Figure 5.5.** Probability distribution of the occurrence and amount of hydrogen bonds between IAPP side chains and the respective membrane. Each plot contains all data points from 6 replicates in each simulation over the last 100 ns of simulation time. Residue number and hydrogen bond number are plotted on the x- and y- axis, respectively.

After assessing and characterizing the type of interaction of IAPP with model membranes, assessment on changes in secondary structure as based on membrane interactions was performed. IAPP adopts a predominantly random structure in solution; however, it has been reported that after binding to a membrane surface, specifically anionic membranes like POPS, monomeric IAPP transiently adopts a partial α-helical structure before proceeding to form aggregates [256, 257, 281]. In the MD studies reported herein, no differences in relative amounts of secondary

structure were observed in hIAPP or rIAPP when comparing the structure in solution and the structure in the presence of or bound to model membranes (Table 1). hIAPP does maintain necessary β-strand structure in order to proceed through the aggregation pathway in the presence of a membrane [258]. In addition, no increase of β-strand structure was observed in rIAPP in the presence of a membrane, consistent with known behavior [280]. The difference between the MD simulations and NMR studies indicates the lack of stabilization or generation of α-helical structure of IAPP in the presence of membranes may be due to limitations of the force field used and the energetic progression of IAPP towards β-strand structure as part of the aggregation pathway. A free energy diagram of the transition state of IAPP structure in the presence of a membrane is also described by Williamson et al. and aids in explaining this observation in our MD simulations [281].

### 5.4.3 Degree and Extent of Membrane Perturbation as A Result of hIAPP or rIAPP Binding

After assessing the structural difference of hIAPP and rIAPP in solution and subsequent interactions with model membranes, it was of interest to evaluate membrane perturbation as caused by these membrane-interaction events. Several mechanisms of toxicity have been proposed as a result of IAPP-membrane interactions with the most prevalent being the membrane disruption hypothesis [192, 255]. Electron microscopy studies show that oligomeric IAPP disrupts membranes in three possible ways: the formation of transmembrane pores, nonspecific membrane disruption, or membrane fragmentation through the growth of amyloid fibrils on the membrane surface [50, 51]. In the current study, assessment of membrane perturbation as caused by full-length hIAPP and rIAPP membrane perturbation was assessed by deuterium order parameters, area-per-lipid, and bilayer thickness to provide more insight into the nonspecific general disruption of lipid bilayers as caused by monomeric IAPP.

Controversy exists on the ability of hIAPP and rIAPP monomers to cause membrane disruption, with some suggesting that the monomer does not cause membrane disruption [253] and while others propose both monomeric hIAPP and rIAPP can cause ion leakage depending on lipid type [257]. Oligomerization of IAPP before or at the membrane surface may be implicated in toxicity to a greater extent [283], but it has also been proposed that the structure differences (α-helical vs. β-strand structure) and stage in on-pathway aggregation events of the IAPP monomer explain variations in toxic properties of IAPP [284]. APL, bilayer thickness, and deuterium order parameter analysis of the current simulations show that all lipid types tested were disrupted to varying extents based on peptide. POPC lipids were disrupted by hIAPP to the greatest extent as compared to POPS and raft model membranes. A 21% decrease in APL as compared to control simulations for POPC lipids after hIAPP binding was observed, as compared to a 17% and 5% decrease for POPS and raft lipids, respectively (Table 5.4). Bilayer thickness measurements were consistent with this trend, indicating that zwitterionic and anionic membranes are perturbed by hIAPP binding (Table 5.5). $S_{CD}$ values from deuterium order parameter analysis further confirm the increase in order of lipid tails as a result of hIAPP binding, with the most greatest increase in order observed in POPC and POPS membranes (Figure 5.6). There was no observable change in $S_{CD}$ values in the presence of a raft membrane after hIAPP interactions. Therefore, given the decrease in perturbation in the presence of a raft membrane and the difference in depth of residue interaction as compared to POPC (Figure 5.4), it is concluded that cholesterol modulates

membrane perturbation. The ability of hIAPP to significantly disrupt POPC and POPS model membranes does support the nonspecific membrane perturbation hypothesis.

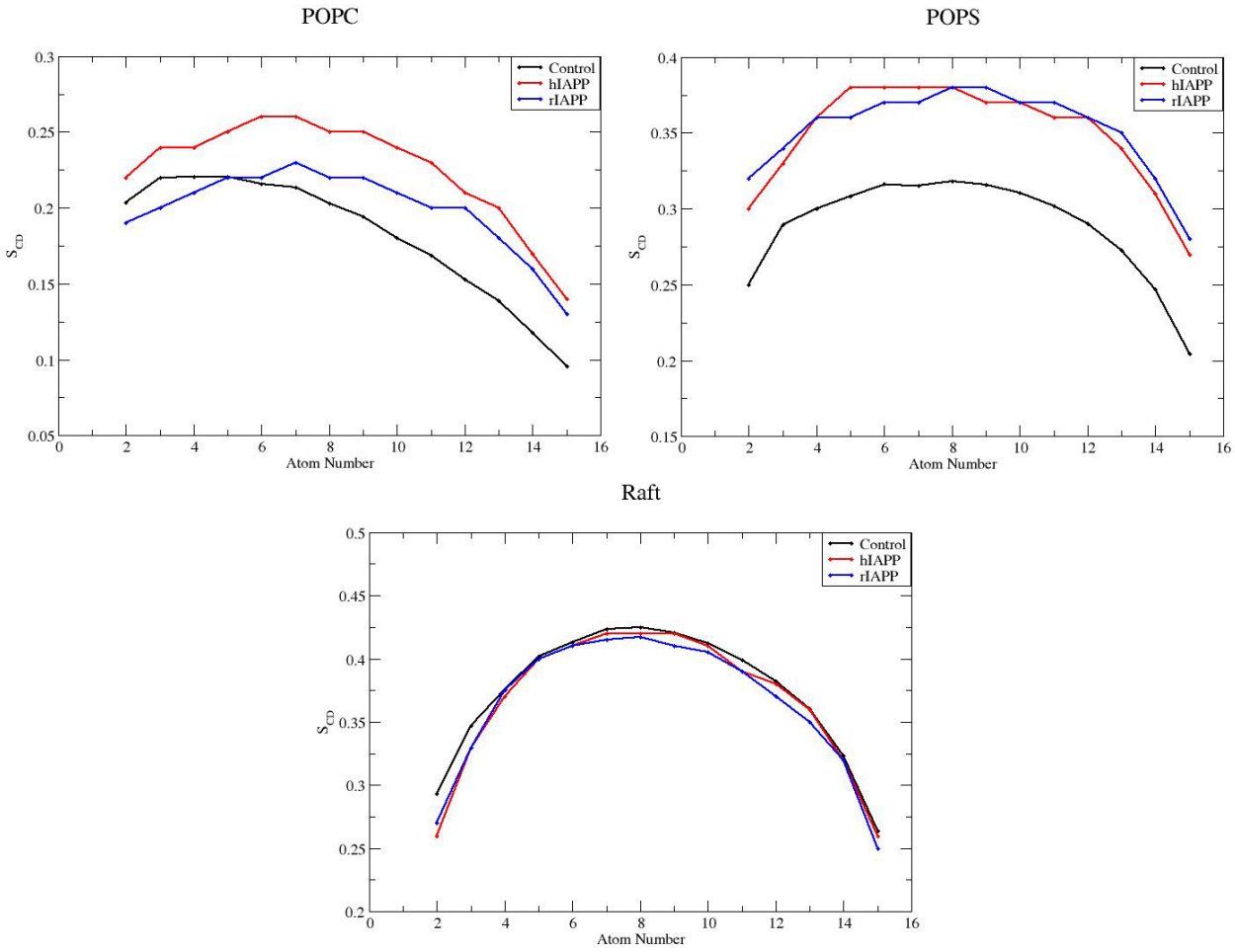


**Figure 5.6.** Average leaflet deuterium order parameters with and without IAPP presence. Average deuterium order parameters ($S_{CD}$) of palmitoyl (sn-1) chain of PO lipids in model membrane simulations. For clarity, only the sn-1 chain is shown; however, parameters were also analyzed on the sn-2 chain and showed similar trends. Control (no peptide present) parameters for each carbon in the lipid chain are shown in black, with the average parameter over six replicates being shown for hIAPP (red) and rIAPP (blue) for each membrane simulation set.

No disruptions of raft membranes were observed for rIAPP-raft interactions, with significantly less perturbation caused to POPC as a result of transient interactions with rIAPP (Tables 5.4 and 5.5, Figure 5.6). Interestingly, rIAPP caused comparable perturbation to anionic POPS membranes, agreeing well with experimental work on the toxicity as caused by rIAPP [257]. Given the similarity in residue insertion depth for hIAPP and rIAPP with POPS, this similarity in degree of membrane perturbation indicates that lipid type is extremely influential on extent of membrane perturbation as caused by IAPP. rIAPP did not disrupt POPC, POPS, and raft model membranes to the same degree as hIAPP, indicating that lipid type influences peptide affinity as shown by transient interactions of rIAPP with POPC (Figure 5.3) and degree of perturbation. This finding aids in explaining reports of a non-amyloidogenic variant of IAPP (rIAPP) causing

membrane disruption, in that it is dependent on the lipid type tested. Environmental factors, such as the membrane environment, have been implicated recently in other amyloid peptides (amyloid β-peptide) as being extremely influential on structure and toxicity [145]. As a result of the current MD study, it is hypothesized that similar trends in toxicity influenced by the environment are true for IAPP as well and should be considered in experimental design and conclusions.

**Table 5.4.** Area per lipid head group (mean ± SD) in $Å^2$ (% difference from controls) for the interacting leaflet over the last 100 ns of each trajectory. [a]

| | Control | hIAPP | rIAPP |
|---|---|---|---|
| POPC | 62 ± 1 | 50 ± 1(-21%)* | 56 ± 1 (-9%)* † |
| POPS | 51 ± 1 | 43 ± 2 (-17%)* | 44 ± 1 (-15%) |
| Raft | 41.2 ± 0.1 | 39 ± 1 (-5%)* | 41 ± 1 (± 0%) |

[a] Statistically significant differences from controls are designated with an asterisk, statistically significant differences between hIAPP and rIAPP are designated with an obelisk.

**Table 5.5.** Bilayer thickness (mean ± SD) in nm (% difference from controls) over the last 100 ns of each trajectory.

| | Control | hIAPP | rIAPP |
|---|---|---|---|
| POPC | 3.9 ± 0.1 | 4.2 ± 0.1 (+7%)* | 4.0 ± 0.1 (+2%) |
| POPS | 4.5 ± 0.1 | 4.7 ± 0.1(+4%) | 4.7 ± 0.1 (+4%) |
| Raft | 4.3 ± 0.2 | 4.3 ± 0.1 (± 0%) | 4.3 ± 0.1(± 0%) |

[a] Statistically significant differences from controls are designated with an asterisk.

### 5.4.4 Conclusions

Molecular dynamics (MD) simulations were used to study the influence of secondary and tertiary structures of hIAPP and rIAPP in solution and in the presence of three model membranes. It is of interest to determine the influence of primary sequence and environment on IAPP given reported differences in toxicity. rIAPP does not exhibit toxicity to β-cells and does not form aggregates in experimental studies, which are observed with hIAPP. Therefore, understanding of key amino acids related to peptide-membrane interactions is of interest. The presented simulation work shows significant differences in secondary structure between hIAPP and rIAPP, with hIAPP adopting more β-strand structure in solution as compared to rIAPP (Table 5.1). In the presence of model membranes, it was observed that the amyloidogenic core (residues 20-29) of hIAPP inserted into the zwitterionic model membranes (POPC and raft) to a greater extent as compared to anionic an membrane (POPS). It is hypothesized that rIAPP-membrane interactions are mediated by Arg-18, a finding that suggests that Arg-18 in rIAPP plays an important role in contributing to the lack of toxicity of rIAPP. Finally, lipid type was found to influence degree of perturbation. Both rIAPP and hIAPP disrupted an anionic POPS membrane, but rIAPP had decreased affinity and perturbation of zwitterionic membranes (POPC and raft) compared to hIAPP, showing the influence of both sequence and lipid type on peptide-membrane affinity. These simulations provide physiochemical insight into differences observed in hIAPP and rIAPP secondary structure, as well as indicating the amyloidogenic core as being an influence on type and degree of perturbation for hIAPP. To further elucidate the nonspecific membrane disruption

hypothesis of IAPP, this study found that hIAPP binding caused a more rigid, ordered membrane as a result of peptide insertion.

## 5.5 Acknowledgments

The authors thank Advanced Research Computing at Virginia Tech for computing time on the BlueRidge supercomputer and the Virginia Tech College of Agriculture and Life Sciences for the Graduate Teaching Scholars Fellowship (to A.M.B.).

## 5.6 Supporting Information

**Table 5.S1.** Details of System Contents and Initial IAPP-Membrane Distances.

| Membrane | Membrane Composition | System Dimensions (*x*, *y*, *z*, in nm) after energy minimization | Minimum Distance between IAPP and Membrane (nm) | |
|---|---|---|---|---|
| | | | Human IAPP | Rat IAPP |
| POPC | 128 POPC | 6.34 x 6.31 x 16 | Rep 1: 3.2<br>Rep 2: 3.0<br>Rep 3: 3.3<br>Rep 4: 2.8<br>Rep 5: 2.9<br>Rep 6: 3.3 | Rep 1: 3.0<br>Rep 2: 3.3<br>Rep 3: 3.1<br>Rep 4: 2.9<br>Rep 5: 3.1<br>Rep 6: 2.9 |
| POPS | 128 POPS | 5.48 x 5.7 x 16 | Rep 1: 3.0<br>Rep 2: 3.0<br>Rep 3: 3.1<br>Rep 4: 2.6<br>Rep 5: 2.8<br>Rep 6: 2.9 | Rep 1: 2.7<br>Rep 2: 3.0<br>Rep 3: 2.8<br>Rep 4: 2.6<br>Rep 5: 2.7<br>Rep 6: 2.7 |
| Raft | 129 POPC<br>119 PSM<br>121 Cholesterol | 8.75 x 8.75 x 16 | Rep 1: 2.8<br>Rep 2: 2.6<br>Rep 3: 3.0<br>Rep 4: 2.4<br>Rep 5: 2.5<br>Rep 6: 2.9 | Rep 1: 2.8<br>Rep 2: 3.0<br>Rep 3: 2.7<br>Rep 4: 2.6<br>Rep 5: 2.9<br>Rep 6: 2.7 |

**Table 5.S2.** Average radius of gyration of IAPP.[a]

| | $R_g$ (nm) | |
|---|---|---|
| System | hIAPP | rIAPP |
| Solution | 1.0 ± 0.1 | 1.0 ± 0.1 |
| POPC | 1.0 ± 0.1 | 1.1 ± 0.1 |
| POPS | 1.0 ± 0.1 | 1.1 ± 0.1 |
| Raft | 1.0 ± 0.1 | 1.0 ± 0.2 |

[a] Percentages represent averages over the final 100 ns of simulation time for six replicates of each system, with corresponding standard deviations.

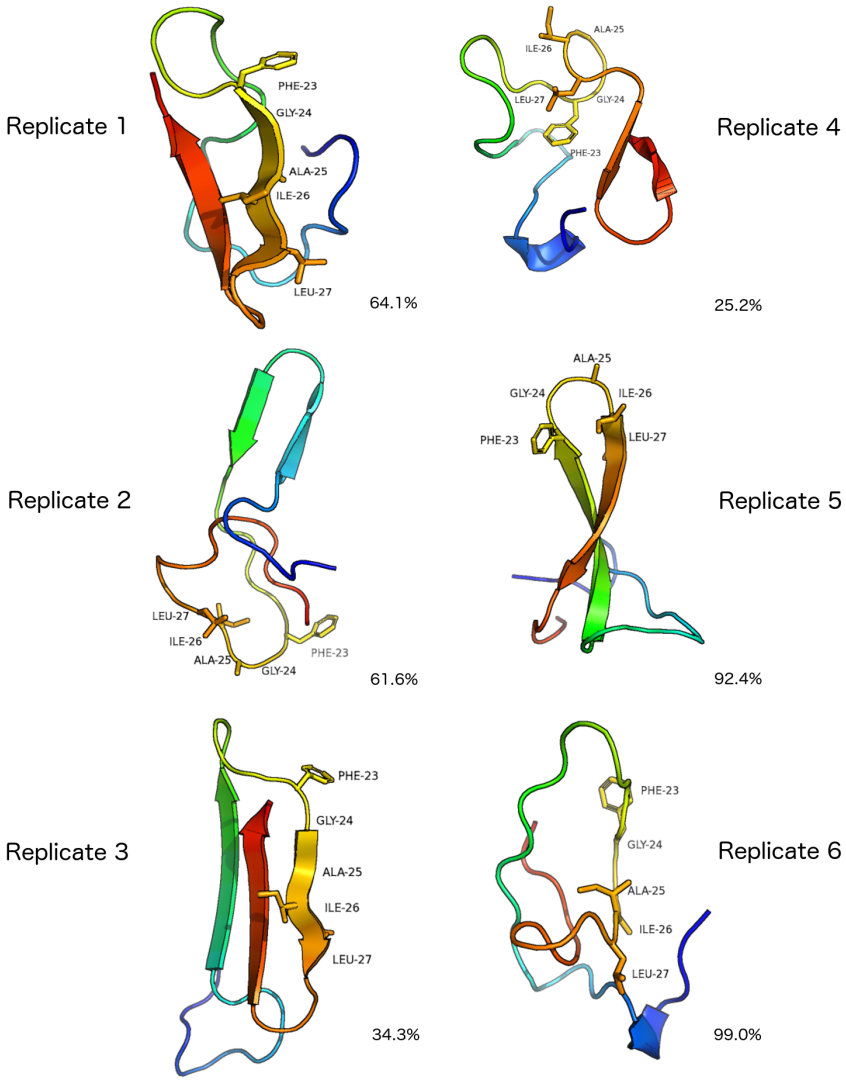


**Figure 5.S1.** Dominant morphologies of hIAPP in solution from RMSD clustering. Representative images from the central structure of the first cluster of each are shown with corresponding percentage indicating the percentage of frames in last 100 ns of simulation time that sample the shown structure. hIAPP is shown as cartoon and colored by rainbow, with the N-terminus shown as blue and the C-terminus shown as red. Residues 23-27, representing the FGAIL region are shown as sticks and labeled.

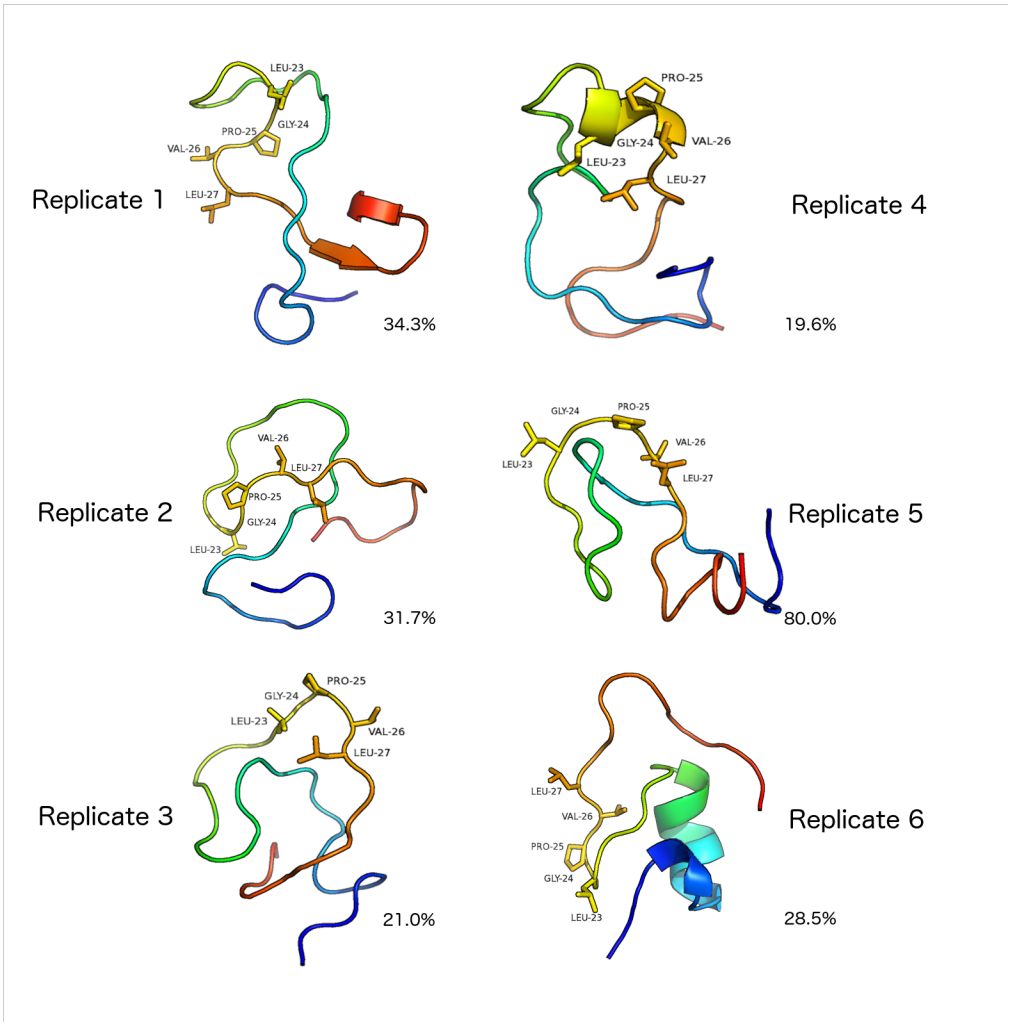


**Figure 5.S2.** Dominant morphologies of rIAPP in solution from RMSD clustering. Representative images from the central structure of the first cluster of each are shown with corresponding percentage indicating the percentage of frames in last 100 ns of simulation time that sample the shown structure. rIAPP is shown as cartoon and colored by rainbow, with the N-terminus shown as blue and the C-terminus shown as red. Residues 23-27, representing the LGPVL region are shown as sticks and labeled.

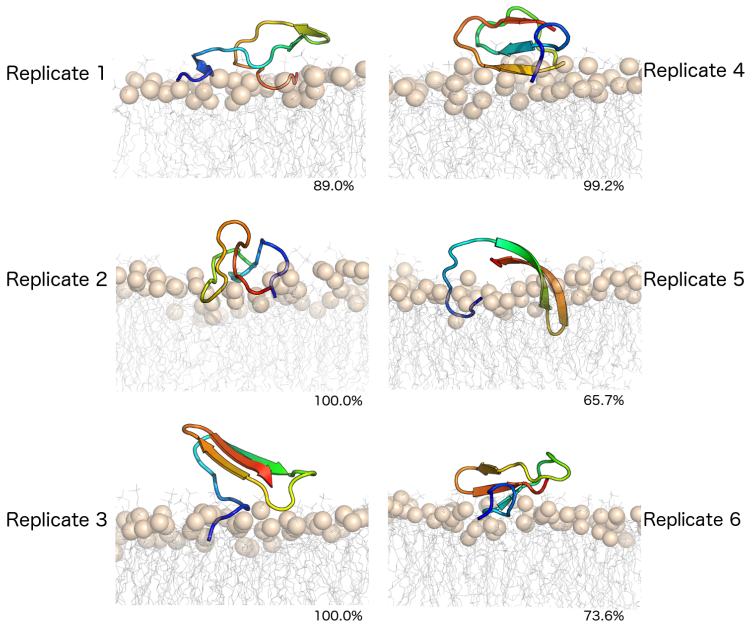


**Figure 5.S3.** Dominant morphologies of hIAPP interacting with POPC from RMSD clustering. Representative images from the central structure of the first cluster of each are shown with corresponding percentage indicating the percentage of frames in last 100 ns of simulation time that sample the shown structure. hIAPP is shown as cartoon and colored by rainbow, with the N-terminus shown as blue and the C-terminus shown as red. The membrane is colored by grey sticks, with the phosphate atom show as a tan sphere for perspective.

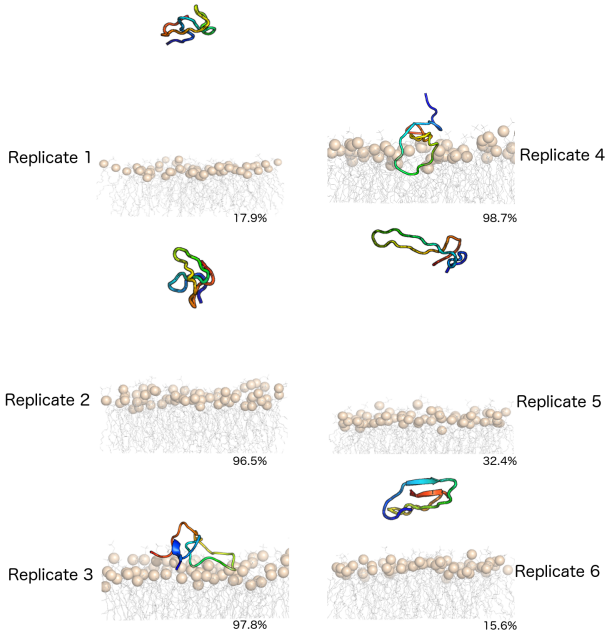


**Figure 5.S4.** Dominant morphologies of rIAPP interacting with POPC from RMSD clustering. Representative images from the central structure of the first cluster of each are shown with corresponding percentage indicating the percentage of frames in last 100 ns of simulation time that sample the shown structure. rIAPP and the membrane are colored as in Figure S3.

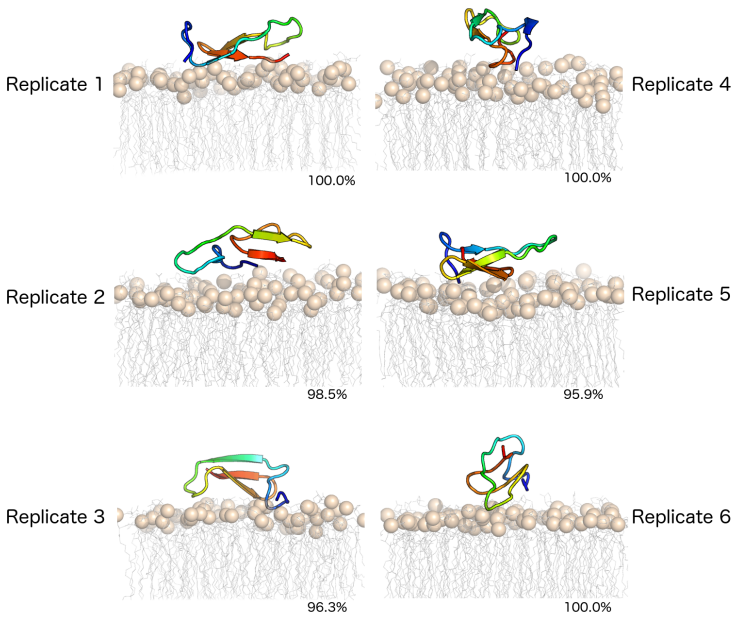


**Figure 5.S5.** Dominant morphologies of hIAPP interacting with POPS from RMSD clustering. Representative images from the central structure of the first cluster of each are shown with corresponding percentage indicating the percentage of frames in last 100 ns of simulation time that sample the shown structure. hIAPP and POPS membrane are colored as in Figure S3.

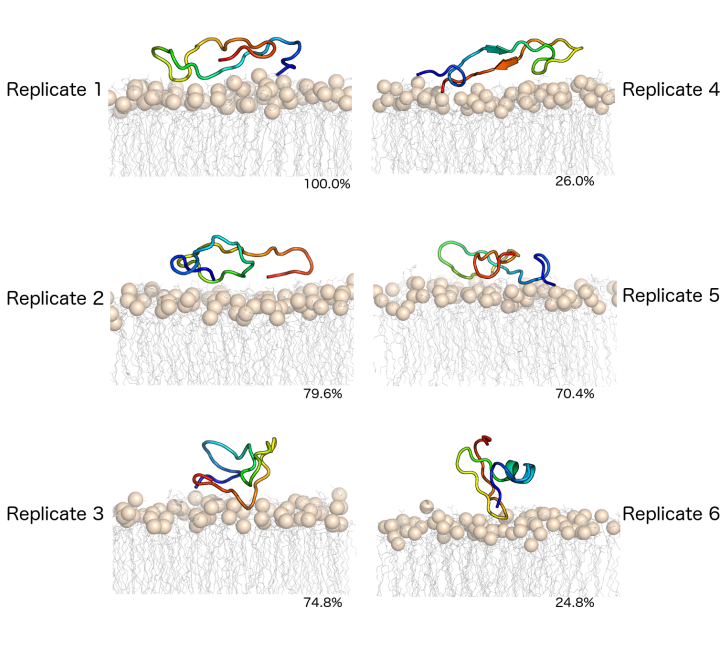


**Figure 5.S6.** Dominant morphologies of rIAPP interacting with POPS from RMSD clustering. Representative images from the central structure of the first cluster of each are shown with corresponding percentage indicating the percentage of frames in last 100 ns of simulation time that sample the shown structure. rIAPP and POPS membrane are colored as in Figure S3.

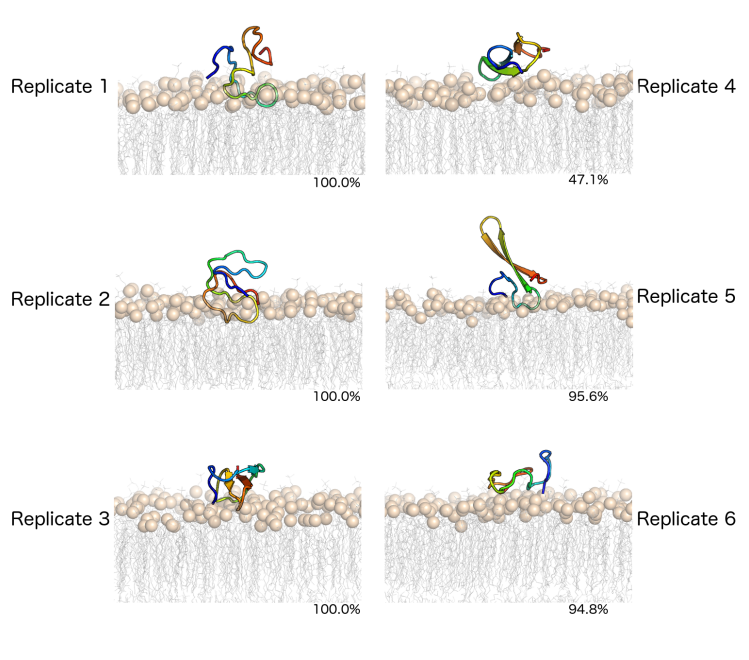


**Figure 5.S7.** Dominant morphologies of hIAPP interacting with raft from RMSD clustering. Representative images from the central structure of the first cluster of each are shown with corresponding percentage indicating the percentage of frames in last 100 ns of simulation time that sample the shown structure. hIAPP and raft membrane are colored as in Figure S3

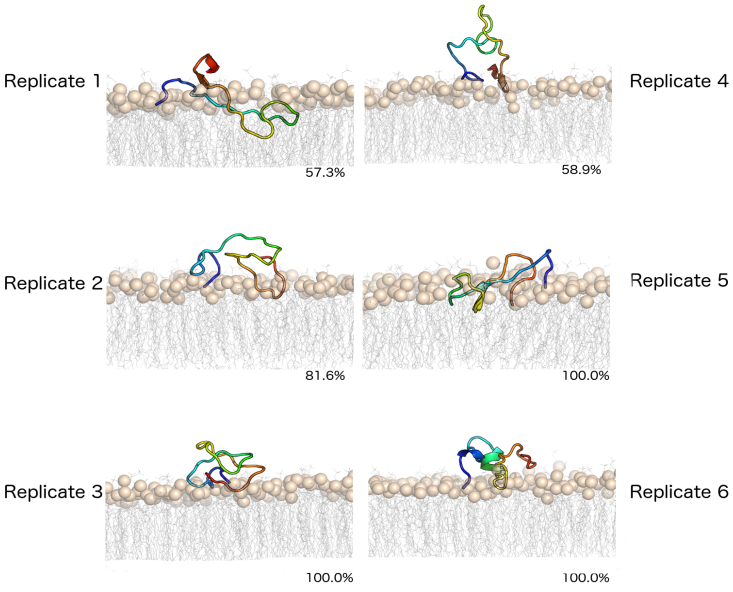


**Figure 5.S8.** Dominant morphologies of rIAPP interacting with raft from RMSD clustering. Representative images from the central structure of the first cluster of each are shown with corresponding percentage indicating the percentage of frames in last 100 ns of simulation time that sample the shown structure. rIAPP and raft membrane are colored as in Figure S3.

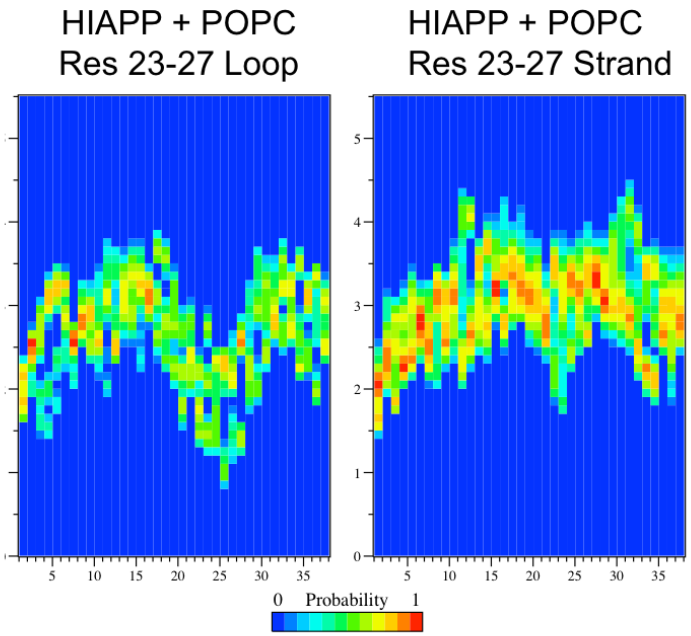


**Figure 5.S9.** Global normalization of the frequency of hIAPP residue center of mass (COM) flynnoccurrence at a distance, on the z-axis, from the COM of the membrane bilayer, as dependent of secondary structure of residues 23-27**.** Res 23-27 Loop represents replicates 2,4, and 5, which adopted a loop structure in residues 23-27. Res 23-27 Strand represents replicates 1,3, and 6, which adopted β-strand structure in residues. Each plot contains all data points from respective replicates over the last 100 ns of simulation time. Residue number and distance (nm) are plotted on the x- and y- axis, respectively.

# 6 Conclusions

Understanding the influence of sequence and environment (model membranes, salt, pH, peptide concentration) on amyloid proteins is of great interest due to their association with many incurable diseases. The work presented here sought to determine the influence of these factors on two amyloid proteins, Aβ and IAPP, and give insight into mechanistic detail associated with the toxicity and aggregation capabilities of these peptides. Interestingly, many of these amyloidogenic peptides share common characteristics such as size, structural changes while on-pathway for aggregation, and difference in toxicity based on sequence. To begin project design, it was noted that both Aβ and IAPP were similarly sized peptides (40/42 residues and 37 residues, respectively), of which both had rat variants that were noted to not express the same phenotype as their human-derived counterparts. Human and rat Aβ differ by three residues (R5G, Y10F, H13R) and human IAPP (HIAPP) and rat IAPP (RIAPP) differ by six residues (H18R, F23L, A25P, I26V, S28P, S29P). Given this change in primary sequence, it was of interest to determine how this sequence variation presents itself as a lack of phenotype of the disease states of AD and T2D in the rat. These residue differences between forms of each peptide may provide insight into the reduced aggregation, membrane perturbation, and cell death that is seen in rats [12, 54, 55]. By comparing the membrane interactions and binding events of human Aβ, HIAPP, rat Aβ and RIAPP with model membranes, similarities and differences have become apparent in degree and type interaction dependent on both peptide and lipid type. By exploring the influence of sequence on toxicity, a greater understanding of the mechanism and specific residue interactions that lead to membrane perturbation and cell death can be achieved. What kind of connections can be made that may be an overarching property of amyloid proteins? Can molecular dynamics (MD) simulations provide insight into residues that may be driving these peptide-membrane interactions that result in toxicity? How can MD simulations be utilized to start understanding aggregation pathways (e.g., tetramer formation)? These questions prompted the work and experimental design presented in this dissertation.

Studying the interactions of Aβ and IAPP in solution and in the membrane environment experimentally is challenging. Aβ and IAPP are prone to rapid aggregation in an aqueous solution, a process that interferes with techniques such as NMR, circular dichroism, and neutron and x-ray diffraction [12, 43, 53, 56, 57]. Molecular modeling, specifically MD simulations, can provide insight into molecular phenomena including protein folding/misfolding and protein-membrane interactions. The work presented sought to utilize these computational techniques in order to (1) determine the influence of oxidation state, solution conditions, and pH on monomeric Aβ and provide rational for conflicting experimental data (Chapter 2), (2) assess the role of sequence and lipid type on interactions of monomeric human and rat Aβ and model membranes (Chapter 3), (3) utilize unbiased, all-atom MD simulations to gain insight into Aβ tetramer formation and Aβ-tetramer membrane interactions (Chapter 4), and (4) assess the role of sequence and lipid type of HIAPP and RIAPP on model membrane. In total, over 56 μs of simulation time was performed for the discussed simulations and to answer the above questions. Simulations on the microsecond level are at an advanced point for the field, especially for peptide-membrane simulations.

In Chapter 2, we determined that oxidation of Met35 in monomeric $A\beta_{40}$ resulted in a decrease in C-terminal β-strand formation, a behavior that was influenced by solution conditions. Across all conditions, irrespective of peptide protonation state or solution ionic strength, oxidation of Met35 resulted in a decrease in β-strand content in the C-terminal region of $A\beta_{40}$, indicating that it is a global property of $Met35^{ox}$ to attenuate on-pathway aggregation events of Aβ. pH did not influence secondary structure elements to a great extent in $A\beta_{40}$; however increased salt concentration did produce a small decrease in β-strand content. It was concluded that the presence or absence of salt will influence the folding and secondary structure content $A\beta_{40}$, directly relating to differences in experimental studies surrounding aggregation rates of the peptide [101, 103]. Therefore, one of the biggest results that came from this study and influenced subsequent chapters and work is that it is important to interpret experimental studies in light of the different outcomes that arise simply by virtue of differences in solution pH and ionic strength. This is emphasized in Chapter 4, as solution conditions most likely influences Aβ oligomer formation, as shown through experimental and computational work. Understanding properties like oxidation state and the influence of solution conditions on Aβ folding will allow for further investigations to determine which molecular events give rise to the devastating characteristics of AD.

Chapter 3 took note to include solution conditions that mimicked a physiologically relevant environment and placed monomeric human and rat $A\beta_{42}$ in the presence of five model membranes. Starting structure and position of the peptide were found to be influential on Aβ-membrane interactions in these simulations as compared to previous computational studies. By placing $A\beta_{42}$ above and outside of long-range interactions with model membranes, we were able to test how extracellular, monomeric human $A\beta_{42}$ or rat $A\beta_{42}$ interacted with model membranes. This approach has not been utilized in previous MD simulations and gives a new perspective on $A\beta_{42}$–membrane interactions and the influence of sequence, most notably a change in position of an arginine. Only two model membranes were found to influence the secondary structure of human $A\beta_{(42)}$, POPC and raft. This lack of influence of model membranes on secondary structure of $A\beta_{42}$ could be due to the already equilibrated structure utilized in these peptide-membrane simulations. This is something to consider for subsequent simulations; various starting structures that range in α-helical and β-strand content. While it did make experimental sense to equilibrate the Aβ peptide before being placed in a membrane environment, there may be a threshold on how much β-strand content the peptide can adopt in the presence of a membrane. Relating to how human $A\beta_{42}$ and rat $A\beta_{42}$ influenced membrane stability, both were found to cause membrane perturbation, to varying extents based on lipid composition that resulted in the membrane becoming more gel-like and rigid. Cholesterol and ganglioside-GM1 attenuated the degree of perturbation that $A\beta_{42}$ exerted on the model membranes, a result also observed in $A\beta_{42}$-tetramer simulations. Finally, these simulations determined that positively charged residues were a key influence and a driving force in Aβ-membrane interactions. This observation may explain why targeting these residues has been successful in inhibiting the toxicity of Aβ [198, 199]. Herein, the role of sequence in these peptide-membrane interactions highlighted that differences in human and rat Aβ secondary structure, membrane perturbation, and lipid affinity were due to due to the change of position of arginine (R5G, H13R). This study rationalizes the role of lipid type and sequence on Aβ-membrane interactions and demonstrates that a non-Aβ factor, membranes, is an important factor to consider.

Chapter 4 was designed due to results obtained in Chapter 3, in that POPC membranes were perturbed to the greatest extent as compared to other lipid types and that cholesterol-rich raft membranes appeared to be attenuate perturbation effects of monomeric $A\beta_{42}$ binding. Therefore, simulations were constructed to assess the ability of all-atom MD simulations to provide insight into $A\beta_{42}$ tetramer formation and $A\beta_{42}$ tetramer-membrnae interactions. It is not currently known what $A\beta_{42}$ species (monomer, dimer, tetramer, dodecamer, etc.) causes the greatest membrane perturbation and results in neuronal cell death [229, 230]. A question at the beginning of the study included how does $A\beta_{42}$ tetramer binding and interaction with POPC and raft membranes influence membrane integrity as compared to monomeric $A\beta_{42}$. It was determined that the $A\beta_{42}$ tetramer perturbed POPC membranes to a greater extent than monomeric $A\beta_{42}$, but the raft membrane remained resilient to $A\beta_{42}$-tetramer perturbation as caused by binding. Positively charged residues, Arg-5, Lys-16, and Lys-28 were still found to influence orientation and insert into the headgroup region of POPC, similar to monomeric $A\beta_{42}$. This further supported the claim that positively charged residues were driving forces in $A\beta_{42}$-membrane interactions and provide a valid target for drug design. This finding also supports the role of cholesterol as being neuroprotective to the membrane environment with $A\beta_{42}$ binding. Finally, this study also provided an avenue to explore the overall shape of an $A\beta_{42}$ tetramer in solution and in the presence of a membrane. It was found that the membrane environment influenced the shape of the $A\beta_{42}$ tetramer to be more rod-like, indicating progression to on-pathway aggregation and seeding events. These peptide-membrane interactions in both Chapter 3 and 4 supports the carpeting-effect model proposed for $A\beta_{42}$ toxicity on membranes [191] and reveals the role membrane environments in modulating Aβ fibril formation, ultimately yielding insight into mechanism of $A\beta_{42}$ toxicity and the potential for aggregation events to proceed in the presence of a membrane environment.

Finally, Chapter 5 sought to simulate another amyloid peptide in the presence of POPC, POPS, and raft model membranes. These simulations could ultimately shed light into properties of IAPP-membrane interactions and serve as a starting point to compare peptide-membrane interactions of amyloidogenic peptides. One of the first findings in this study was the ability of rat IAPP to transiently interact with a POPC membrane in four out of six simulations. This transient interaction was not observed in any other peptide-membrane simulation and is unique to this peptide. This transient interaction also spurred the extension of simulations from 300 ns to 1 μs, with six replicates, to determine if any MD simulation artifacts were resulting in this rat IAPP and POPC interaction. Rat IAPP interactions with POPS and raft membranes did not produce the same transient interactions, indicating it was solely the properties of the POPC membrane resulting in this lack of binding affinity. Finally, Arg-18 was identified as a residue responsible for influencing rIAPP peptide-membrane interactions with anionic membranes and aids in explaining the curious nature of this peptide in peptide-membrane studies. IAPP is natively unfolded in its monomeric state in solution, which was observed in the in-solution simulations performed, and has helical characteristics in the presence of a membrane [42]. Human and rat IAPP secondary structure were not influenced by the membrane environment in any way in these simulations and did not adopt any helical characteristics in the presence of membranes; however, interesting sampling was observed with human IAPP in solution. Residues 20-29 of human IAPP (SNNFGAILSS) are classified as one of the most amyloidogenic sequences known and this region, specifically residues 23-27 is reported to either be involved in a loop region or in a β-strand region, depending progression in the aggregation cascade to fiber

formation [285]. MD simulations of human IAPP in solution showed equal sampling of both these structures, with the type of secondary structure associated with the 23-27 residue region then influencing area of insertion into the membrane.

To cohesively tie these separate studies together, it was of interest to analyze and compare degree of membrane perturbation between Aβ and IAPP. In the presence of a POPS membrane, rat versions of both Aβ and IAPP locally perturbed the membrane to the greatest extent, with rat Aβ providing the greatest overall amount of perturbation to this lipid type. In the presence of a POPC membrane, human Aβ and human IAPP perturbed in the same manner and to the same degree/extent, by causing an increase in lipid order and contributed to a more rigid membrane environment. Rat Aβ and IAPP did not disrupt a POPC membrane to the extent at which the human variants did, indicating an interesting trend. Rat versions of both peptides appear to have greater effect on membrane perturbation by binding to an anionic POPS membrane than a POPC and raft membrane. Controversy has arisen lately disputing the "non-toxicity" of rat IAPP, which could be supported by its ability to bind to and disrupt POPS membranes [286] rather than POPC. More systematic studies comparing both Aβ and IAPP in various environments are necessary in understanding amyloidogenicity, especially after the discussion non-peptide factors influencing the toxicity and aggregation potential of Aβ[145]. Finally, some future experiments would include mutating the human version of Aβ to have the mutation only at position 5 (R5G), in order to assess the lack of this residue in peptide toxicity. A similar mutation in IAPP, centering on Arg-18 in rIAPP would also be of interest. The role of positively charged residues and their influence on peptide-membrane interactions is an interesting area to continue research in and study as potential therapeutic targets.

The work presented focused on studying two of these peptides individually; however, it is proposed that greater insight into amyloidogenic pathways can be gained by studying several of these peptides and comparatively assessing similarities and differences utilizing the same experimental conditions [287]. The occurrence of multiple amyloid peptides in aggregates has also been proposed [288]; however, mechanistic action related to protein-protein interaction and aggregation pathways related to these peptides remain elusive. In addition, many age-related diseases are associated with amyloid peptides. By using MD simulations, future directions include performing extensive studies utilizing various amyloid peptides in the same environment to test degree and type of aggregation pathways and membrane disruption events. With this objective, answers surrounding the how and in what ways do amyloid proteins act in similar environments and how do these similarities and differences relate to the disease state and possibly aging can be answered. By selectively combining various amyloid proteins in order understand multi-peptide aggregation pathways. By focusing the scope of future work on multiple peptides and aggregation pathway trends on a more macro-level, new insight and experimental approach can be provided to the field and provide novel insight and direction. Given the prevalence and severity of amyloid-related diseases and the lack of therapeutics that offer any type of attenuation of the disease, insights into mechanistic detail is essential in successfully developing novel therapeutics for these amyloid diseases.

# 7 Bibliography


1. Kyle, R. A. (2001) Amyloidosis: a convoluted story, *Br J Haematol.* **114**, 529-538.
2. Ramírez-Alvarado, M., Merkel, J. S. & Regan, L. (2000) A systematic exploration of the influence of the protein stability on amyloid fibril formation in vitro, *Proc Natl Acad Sci USA.* **97**, 8979-8984.
3. Nilsson, M. R. (2004) Techniques to study amyloid fibril formation in vitro, *Methods.* **34**, 151-160.
4. Kayed, R., Head, E., Thompson, J. L., McIntire, T. M., Milton, S. C., Cotman, C. W. & Glabe, C. G. (2003) Common Structure of Soluble Amyloid Oligomers Implies Common Mechanism of Pathogenesis, *Science.* **300**, 486-489.
5. Alzheimer's Association 2015 Alzheimer's Disease Facts and Figures.
6. Blass, J. P. (1996) Age-Associated Memory Impairment and Alzheimer's Disease, *J Am Geriatr Soc.* **44**, 209-211.
7. Alzheimer's Disease International (2012) World Alzheimer Report.
8. Roberson, E. D. & Mucke, L. (2006) 100 Years and Counting: Prospects for Defeating Alzheimer's Disease, *Science.* **314**, 781-784.
9. National Institute on Aging Alzheimer's Disease and Education Referral Center (2012) Alzheimer's Disease Medications Fact Sheet.
10. Center for Disease Control and Prevention (2011) National Diabetes Fact Sheet.
11. International Diabetes Federation (2012) Diabetes Atlas.
12. Westermark, P., Andersson, A. & Westermark, G. T. (2011) Islet Amyloid Polypeptide, Islet Amyloid, and Diabetes Mellitus, *Physiol Rev.* **91**, 795-826.
13. Hardy, J. & Higgins, G. (1992) Alzheimer's disease: the amyloid cascade hypothesis, *Science.* **256**, 184-185.
14. Masters, C. L., Simms, G., Weinman, N. A., Multhaup, G., McDonald, B. L. & Beyreuther, K. (1985) Amyloid plaque core protein in Alzheimer disease and Down syndrome, *Proc Natl Acad Sci U S A.* **82**, 4245-4249.
15. Selkoe, D. J. (2000) The origins of Alzheimer disease: a is for amyloid, *JAMA.* **283**, 1615-7.
16. Hardy, J. & Selkoe, D. J. (2002) The Amyloid Hypothesis of Alzheimer's Disease: Progress and Problems on the Road to Therapeutics, *Science.* **297**, 353-356.
17. Simmons, L. K., May, P. C., Tomaselli, K. J., Rydel, R. E., Fuson, K. S., Brigham, E. F., Wright, S., Lieberburg, I., Becker, G. W. & Brems, D. N. (1994) Secondary structure of amyloid beta peptide correlates with neurotoxic activity in vitro, *Mol Pharmacol.* **45**, 373-379.
18. Wang, Q., Wang, Y. & Lu, H. P. (2013) Revealing the secondary structural changes of amyloid β peptide by probing the spectral fingerprint characters, *J Raman Spectrosc*. **44,** 670-674.
19. Bitan, G., Kirkitadze, M. D., Lomakin, A., Vollers, S. S., Benedek, G. B. & Teplow, D. B. (2003) Amyloid β-protein (Aβ) assembly: Aβ40 and Aβ42 oligomerize through distinct pathways, *Proc Natl Acad Sci USA.* **100**, 330-335.
20. Bitan, G., Vollers, S. S. & Teplow, D. B. (2003) Elucidation of Primary Structure Elements Controlling Early Amyloid β-Protein Oligomerization, *J Biol Chem.* **278**, 34882-34889.

21. Jarrett, J. T., Berger, E. P. & Lansbury, P. T. (1993) The carboxy terminus of the .beta. amyloid protein is critical for the seeding of amyloid formation: Implications for the pathogenesis of Alzheimer's disease, *Biochemistry.* **32**, 4693-4697.
22. Rohan de Silva, H. A., Jen, A., Wickenden, C., Jen, L. S., Wilkinson, S. L. & Patel, A. J. (1997) Cell-specific expression of beta-amyloid precursor protein isoform mRNAs and proteins in neurons and astrocytes, *Brain Res Mol Brain Res.* **47**, 147-56.
23. Isacson, O., Seo, H., Lin, L., Albeck, D. & Granholm, A. C. (2002) Alzheimer's disease and Down's syndrome: roles of APP, trophic factors and ACh, *Trends Neurosci.* **25**, 79-84.
24. Small, S. A. & Gandy, S. (2006) Sorting through the Cell Biology of Alzheimer's Disease: Intracellular Pathways to Pathogenesis, *Neuron.* **52**, 15-31.
25. Steiner, H., Fluhrer, R. & Haass, C. (2008) Intramembrane Proteolysis by γ-Secretase, *J Biol Chem.* **283**, 29627-29631.
26. Thinakaran, G. & Koo, E. H. (2008) Amyloid Precursor Protein Trafficking, Processing, and Function, *J Biol Chem.* **283**, 29615-29619.
27. Lazarov, O. & Demars, M. P. (2012) All in the Family: How the APPs Regulate Neurogenesis, *Front Neurosci.* **6**.
28. Steinbach, J. P., Müller, U., Leist, M., Li, Z.-W., Nicotera, P. & Aguzzi, A. (1998) Hypersensitivity to seizures in β-amyloid precursor protein deficient mice, *Cell Death Differ.* **5**, 858.
29. Lee, M. R., Lee, D., Shin, S. K., Kim, Y. H. & Choi, C. Y. (2008) Inhibition of APP intracellular domain (AICD) transcriptional activity via covalent conjugation with Nedd8, *Biochem Biophys Res Commun.* **366**, 976-81.
30. Vassar, R., Bennett, B. D., Babu-Khan, S., Kahn, S., Mendiaz, E. A., Denis, P., Teplow, D. B., Ross, S., Amarante, P., Loeloff, R., Luo, Y., Fisher, S., Fuller, J., Edenson, S., Lile, J., Jarosinski, M. A., Biere, A. L., Curran, E., Burgess, T., Louis, J.-C., Collins, F., Treanor, J., Rogers, G. & Citron, M. (1999) β-Secretase Cleavage of Alzheimer's Amyloid Precursor Protein by the Transmembrane Aspartic Protease BACE, *Science.* **286**, 735-741.
31. Koo, E. H. & Squazzo, S. L. (1994) Evidence that production and release of amyloid beta-protein involves the endocytic pathway, *J Biol Chem.* **269**, 17386-9.
32. Tomita, S., Kirino, Y. & Suzuki, T. (1998) Cleavage of Alzheimer's amyloid precursor protein (APP) by secretases occurs after O-glycosylation of APP in the protein secretory pathway. Identification of intracellular compartments in which APP cleavage occurs without using toxic agents that interfere with protein metabolism, *J Biol Chem.* **273**, 6277-84.
33. De Strooper, B., Iwatsubo, T. & Wolfe, M. S. (2012) Presenilins and γ-Secretase: Structure, Function, and Role in Alzheimer Disease, *Cold Spring Harb Perspect Med.* **2**, a006304.
34. Higgins, L. S., Murphy, G. M., Forno, L. S., Catalano, R. & Cordell, B. (1996) P3 beta-amyloid peptide has a unique and potentially pathogenic immunohistochemical profile in Alzheimer's disease brain, *Am J Pathol* **149**, 585-596.
35. Pearson, H. A. & Peers, C. (2006) Physiological roles for amyloid β peptides, *J Physiol.* **575**, 5-10.
36. Bush, A. I. (2003) The metallobiology of Alzheimer's disease, *Trends Neurosci.* **26**, 207-214.
37. Kamenetz, F., Tomita, T., Hsieh, H., Seabrook, G., Borchelt, D., Iwatsubo, T., Sisodia, S. & Malinow, R. (2003) APP Processing and Synaptic Function, *Neuron.* **37**, 925-937.

38. Soscia, S. J., Kirby, J. E., Washicosky, K. J., Tucker, S. M., Ingelsson, M., Hyman, B., Burton, M. A., Goldstein, L. E., Duong, S., Tanzi, R. E. & Moir, R. D. (2010) The Alzheimer's Disease-Associated Amyloid β-Protein Is an Antimicrobial Peptide, *PLoS One.* **5**, e9505.
39. Dixon, R. A. & Chopra, I. (1986) Polymyxin B and polymyxin B nonapeptide alter cytoplasmic membrane permeability in *Escherichia coli*, *J Antimicrob Chemother.* **18**, 557-563.
40. Opie, E. L. (1901) On the relation of chronic interstitial pancreatitis to the islands of langerhans and to diabetes melutus, *J. Exp. Med.* **5**, 397-428.
41. Westermark, P., Wernstedt, C., Wilander, E., Hayden, D. W., O'Brien, T. D. & Johnson, K. H. (1987) Amyloid fibrils in human insulinoma and islets of Langerhans of the diabetic cat are derived from a neuropeptide-like protein also present in normal islet cells, *Proc Natl Acad Sci USA.* **84**, 3881-3885.
42. Westermark, P. (2011) Amyloid in the islets of Langerhans: Thoughts and some historical aspects, *Ups J Med Sci.* **116**, 81-89.
43. Sciacca, Michele F. M., Milardi, D., Messina, Grazia M. L., Marletta, G., Brender, Jeffrey R., Ramamoorthy, A. & La Rosa, C. (2013) Cations as Switches of Amyloid-Mediated Membrane Disruption Mechanisms: Calcium and IAPP, *Biophys J.* **104**, 173-184.
44. Duan, Y., Wu, C., Chowdhury, S., Lee, M. C., Xiong, G., Zhang, W., Yang, R., Cieplak, P., Luo, R., Lee, T., Caldwell, J., Wang, J. & Kollman, P. (2003) A point-charge force field for molecular mechanics simulations of proteins based on condensed-phase quantum mechanical calculations, *J Comput Chem.* **24**, 1999-2012.
45. Hull, R. L., Westermark, G. T., Westermark, P. & Kahn, S. E. (2004) Islet Amyloid: A Critical Entity in the Pathogenesis of Type 2 Diabetes, *J Clin Endocrinol Metab.* **89**, 3629-3643.
46. Kahn, S. E., Andrikopoulos, S. & Verchere, C. B. (1999) Islet amyloid: a long-recognized but underappreciated pathological feature of type 2 diabetes, *Diabetes.* **48**, 241-253.
47. Mosselman, S. (1989) The complete islet amyloid polypeptide precursor is encoded by two exons, *FEBS Lett.* **247**, 154-158.
48. Sanke, T., Bell, G. I., Sample, C., Rubenstein, A. H. & Steiner, D. F. (1988) An islet amyloid peptide is derived from an 89-amino acid precursor by proteolytic processing, *J Biol Chem.* **263**, 17243-6.
49. Kayed, R., Sokolov, Y., Edmonds, B., McIntire, T. M., Milton, S. C., Hall, J. E. & Glabe, C. G. (2004) Permeabilization of Lipid Bilayers Is a Common Conformation-dependent Activity of Soluble Amyloid Oligomers in Protein Misfolding Diseases, *J Biol Chem.* **279**, 46363-46366.
50. Engel, M. F. M. (2009) Membrane permeabilization by Islet Amyloid Polypeptide, *Chem Phys Lipids.* **160**, 1-10.
51. Zhang, Y.-J., Shi, J.-M., Bai, C.-J., Wang, H., Li, H.-Y., Wu, Y. & Ji, S.-R. (2012) Intra-membrane Oligomerization and Extra-membrane Oligomerization of Amyloid-β Peptide Are Competing Processes as a Result of Distinct Patterns of Motif Interplay, *J Biol Chem.* **287**, 748-756.
52. Zhao, J., Luo, Y., Jang, H., Yu, X., Wei, G., Nussinov, R. & Zheng, J. (2012) Probing ion channel activity of human islet amyloid polypeptide (amylin), *Biochim Biophys Acta.* **1818**, 3121-3130.
53. Zhang, Y., Luo, Y., Deng, Y., Mu, Y. & Wei, G. (2012) Lipid Interaction and Membrane Perturbation of Human Islet Amyloid Polypeptide Monomer and Dimer by Molecular Dynamics Simulations, *PLoS One.* **7**, e38191.

54. Fox, A., Snollaerts, T., Errecart Casanova, C., Calciano, A., Nogaj, L. A. & Moffet, D. A. (2010) Selection for Nonamyloidogenic Mutants of Islet Amyloid Polypeptide (IAPP) Identifies an Extended Region for Amyloidogenicity, *Biochemistry.* **49**, 7783-7789.
55. Istrate, Andrey N., Tsvetkov, Philipp O., Mantsyzov, Alexey B., Kulikova, Alexandra A., Kozin, Sergey A., Makarov, Alexander A. & Polshakov, Vladimir I. (2012) NMR Solution Structure of Rat Aβ(1–16): Toward Understanding the Mechanism of Rats' Resistance to Alzheimer's Disease, *Biophys J.* **102**, 136-143.
56. Cao, P., Abedini, A. & Raleigh, D. P. (2013) Aggregation of islet amyloid polypeptide: from physical chemistry to cell biology, *Curr Opin Struct Biol.* **23**, 82-89.
57. Zhang, Y. J., Shi, J. M., Bai, C. J., Wang, H., Li, H. Y., Wu, Y. & Ji, S. R. (2012) Intra-membrane oligomerization and extra-membrane oligomerization of amyloid-beta peptide are competing processes as a result of distinct patterns of motif interplay, *J Biol Chem.* **287**, 748-56.
58. Jayasinghe, S. A. & Langen, R. (2007) Membrane interaction of islet amyloid polypeptide, *Biochim Biophys Acta.* **1768**, 2002-2009.
59. Kakio, A., Yano, Y., Takai, D., Kuroda, Y., Matsumoto, O., Kozutsumi, Y. & Matsuzaki, K. (2004) Interaction between amyloid β-protein aggregates and membranes, *J Pept Sci.* **10**, 612-621.
60. Nanga, R. P., Brender, J. R., Vivekanandan, S. & Ramamoorthy, A. (2011) Structure and membrane orientation of IAPP in its natively amidated form at physiological pH in a membrane environment, *Biochim Biophys Acta.* **1808**, 2337-42.
61. Palmblad, M., Westlind-Danielsson, A. & Bergquist, J. (2002) Oxidation of Methionine 35 Attenuates Formation of Amyloid β-Peptide 1–40 Oligomers, *J Biol Chem.* **277**, 19506-19510.
62. Davis, C. H. & Berkowitz, M. L. (2009) Interaction Between Amyloid-β (1–42) Peptide and Phospholipid Bilayers: A Molecular Dynamics Study, *Biophys J.* **96**, 785-797.
63. Davis, C. H. & Berkowitz, M. L. (2010) A molecular dynamics study of the early stages of amyloid-β(1–42) oligomerization: The role of lipid membranes, *Proteins: Struct, Funct, Bioinf.* **78**, 2533-2545.
64. Lemkul, J. A. & Bevan, D. R. (2009) Perturbation of membranes by the amyloid β-peptide – a molecular dynamics study, *FEBS J.* **276**, 3060-3075.
65. Lemkul, J. A. & Bevan, D. R. (2011) Lipid composition influences the release of Alzheimer's amyloid β-peptide from membranes, *Protein Sci.* **20**, 1530-1545.
66. Milardi, D., Sciacca, M. M., Pappalardo, M., Grasso, D. & Rosa, C. (2011) The role of aromatic side-chains in amyloid growth and membrane interaction of the islet amyloid polypeptide fragment LANFLVH, *Eur Biophys J.* **40**, 1-12.
67. Xu, W., Wei, G., Su, H., Nordenskiöld, L. & Mu, Y. (2011) Effects of cholesterol on pore formation in lipid bilayers induced by human islet amyloid polypeptide fragments: A coarse-grained molecular dynamics study, *Physical Review E.* **84**, 051922.
68. Pronk, S., Páll, S., Schulz, R., Larsson, P., Bjelkmar, P., Apostolov, R., Shirts, M. R., Smith, J. C., Kasson, P. M., van der Spoel, D., Hess, B. & Lindahl, E. (2013) GROMACS 4.5: a high-throughput and highly parallel open source molecular simulation toolkit, *Bioinformatics.* **29**, 845-854.
69. Van Der Spoel, D., Lindahl, E., Hess, B., Groenhof, G., Mark, A. E. & Berendsen, H. J. C. (2005) GROMACS: Fast, flexible, and free, *J Comput Chem.* **26**, 1701-1718.
70. Oostenbrink, C., Villa, A., Mark, A. E. & Van Gunsteren, W. F. (2004) A biomolecular force field based on the free enthalpy of hydration and solvation: The GROMOS force-field parameter sets 53A5 and 53A6, *J Comput Chem.* **25**, 1656-1676.

71. Berger, O., Edholm, O. & Jähnig, F. (1997) Molecular dynamics simulations of a fluid bilayer of dipalmitoylphosphatidylcholine at full hydration, constant pressure, and constant temperature, *Biophys J.* **72**, 2002-2013.
72. Gerben, S. R., Lemkul, J. A., Brown, A. M. & Bevan, D. R. (2013) Comparing atomistic molecular mechanics force fields for a difficult target: a case study on the Alzheimer's amyloid β-peptide, *J Biomol Struct Dyn*, 1-16.
73. Olubiyi, O. O. & Strodel, B. (2012) Structures of the amyloid beta-peptides Abeta1-40 and Abeta1-42 as influenced by pH and a D-peptide, *J Phys Chem B.* **116**, 3280-91.
74. Hoover, W. G. (1985) Canonical dynamics: Equilibrium phase-space distributions, *Phys Rev A.* **31**, 1695-1697.
75. Nosé, S. (2002) A molecular dynamics method for simulations in the canonical ensemble, *Mol Phys.* **100**, 191-198.
76. Nosé, S. & Klein, M. L. (1983) Constant pressure molecular dynamics for molecular systems, *Mol Phys.* **50**, 1055-1076.
77. Parrinello, M. & Rahman, A. (1981) Polymorphic transitions in single crystals: A new molecular dynamics method, *J Appl Phys.* **52**, 7182-7190.
78. Berendsen, H. J. C., Postma, J. P. M., Gunsteren, W. F. & Hermans, J. (1981) Interaction Models for Water in Relation to Protein Hydration in *Intermolecular Forces* (Pullman, B., ed) pp. 331-342, Springer Netherlands.
79. Darden, T., York, D. & Pedersen, L. (1993) Particle mesh Ewald: An N log(N) method for Ewald sums in large systems, *J Chem Phys.* **98**, 10089-10092.
80. Essmann, U., Perera, L., Berkowitz, M. L., Darden, T., Lee, H. & Pedersen, L. G. (1995) A smooth particle mesh Ewald method, *J Chem Phys.* **103**, 8577-8593.
81. Kumar-Singh, S., Theuns, J., Van Broeck, B., Pirici, D., Vennekens, K. l., Corsmit, E., Cruts, M., Dermaut, B., Wang, R. & Van Broeckhoven, C. (2006) Mean age-of-onset of familial alzheimer disease caused by presenilin mutations correlates with both increased Aβ42 and decreased Aβ40, *Hum Mutat.* **27**, 686-695.
82. Yip, C. M., Darabie, A. A. & McLaurin, J. (2002) Aβ42-Peptide Assembly on Lipid Bilayers, *J Mol Biol.* **318**, 97-107.
83. Kirkitadze, M. D., Bitan, G. & Teplow, D. B. (2002) Paradigm shifts in Alzheimer's disease and other neurodegenerative disorders: The emerging role of oligomeric assemblies, *J Neurosci Res.* **69**, 567-577.
84. Chow, V., Mattson, M., Wong, P. & Gleichmann, M. (2010) An Overview of APP Processing Enzymes and Products, *Neuromolecular Med.* **12**, 1-12.
85. Demuro, A., Parker, I. & Stutzmann, G. E. (2010) Calcium Signaling and Amyloid Toxicity in Alzheimer Disease, *J Biol Chem.* **285**, 12463-12468.
86. Atwood, C. S., Scarpa, R. C., Huang, X., Moir, R. D., Jones, W. D., Fairlie, D. P., Tanzi, R. E. & Bush, A. I. (2000) Characterization of Copper Interactions with Alzheimer Amyloid β Peptides, *J Neurochem.* **75**, 1219-1233.
87. Bousejra-ElGarah, F., Bijani, C., Coppel, Y., Faller, P. & Hureau, C. (2011) Iron(II) Binding to Amyloid-β, the Alzheimer's Peptide, *Inorg Chem.* **50**, 9024-9030.
88. Guilloreau, L., Combalbert, S., Sournia-Saquet, A., Mazarguil, H. & Faller, P. (2007) Redox Chemistry of Copper–Amyloid-β: The Generation of Hydroxyl Radical in the Presence of Ascorbate is Linked to Redox-Potentials and Aggregation State, *ChemBioChem.* **8**, 1317-1325.
89. Hewitt, N. & Rauk, A. (2009) Mechanism of Hydrogen Peroxide Production by Copper-Bound Amyloid Beta Peptide: A Theoretical Study, *J Phys Chem B.* **113**, 1202-1209.

90. Markesbery, W. R. (1997) Oxidative Stress Hypothesis in Alzheimer's Disease, *Free Radic Biol Med.* **23**, 134-147.
91. Butterfield, D. A., Drake, J., Pocernich, C. & Castegna, A. (2001) Evidence of oxidative damage in Alzheimer's disease brain: central role for amyloid β-peptide, *Trends Mol Med.* **7**, 548-554.
92. Choi, J., Levey, A. I., Weintraub, S. T., Rees, H. D., Gearing, M., Chin, L.-S. & Li, L. (2004) Oxidative Modifications and Down-regulation of Ubiquitin Carboxyl-terminal Hydrolase L1 Associated with Idiopathic Parkinson's and Alzheimer's Diseases, *J Biol Chem.* **279**, 13256-13264.
93. Lauderback, C. M., Hackett, J. M., Huang, F. F., Keller, J. N., Szweda, L. I., Markesbery, W. R. & Butterfield, D. A. (2001) The glial glutamate transporter, GLT-1, is oxidatively modified by 4-hydroxy-2-nonenal in the Alzheimer's disease brain: the role of Aβ1–42, *J Neurochem.* **78**, 413-416.
94. Markesbery, W. R., Kryscio, R. J., Lovell, M. A. & Morrow, J. D. (2005) Lipid peroxidation is an early event in the brain in amnestic mild cognitive impairment, *Ann Neurol.* **58**, 730-735.
95. Smith, M. A., Richey Harris, P. L., Sayre, L. M., Beckman, J. S. & Perry, G. (1997) Widespread Peroxynitrite-Mediated Damage in Alzheimer's Disease, *J Neurosci.* **17**, 2653-2657.
96. Butterfield, D. A. & Lauderback, C. M. (2002) Lipid peroxidation and protein oxidation in Alzheimer's disease brain: potential causes and consequences involving amyloid β-peptide-associated free radical oxidative stress, *Free Radic Biol Med.* **32**, 1050-1060.
97. Butterfield, D. A. & Sultana, R. (2011) Methionine-35 of AB: Importance for Oxidative Stress in Alzheimer Disease, *J Amino Acids.* **2011**.
98. Kanski, J., Varadarajan, S., Aksenova, M. & Butterfield, D. A. (2002) Role of glycine-33 and methionine-35 in Alzheimer's amyloid β-peptide 1–42-associated oxidative stress and neurotoxicity, *Biochim Biophys Acta.* **1586**, 190-198.
99. Schöneich, C. (2002) Redox Processes of Methionine Relevant to β-Amyloid Oxidation and Alzheimer's Disease, *Arch Biochem Biophys.* **397**, 370-376.
100. Hou, L., Kang, I., Marchant, R. E. & Zagorski, M. G. (2002) Methionine 35 Oxidation Reduces Fibril Assembly of the Amyloid Aβ-(1–42) Peptide of Alzheimer's Disease, *J Biol Chem.* **277**, 40173-40176.
101. Hou, L., Shao, H., Zhang, Y., Li, H., Menon, N. K., Neuhaus, E. B., Brewer, J. M., Byeon, I.-J. L., Ray, D. G., Vitek, M. P., Iwashita, T., Makula, R. A., Przybyla, A. B. & Zagorski, M. G. (2004) Solution NMR Studies of the Aβ(1−40) and Aβ(1−42) Peptides Establish that the Met35 Oxidation State Affects the Mechanism of Amyloid Formation, *J Am Chem Soc.* **126**, 1992-2005.
102. Watson, A. A., Fairlie, D. P. & Craik, D. J. (1998) Solution Structure of Methionine-Oxidized Amyloid β-Peptide (1−40). Does Oxidation Affect Conformational Switching?†,‡, *Biochemistry.* **37**, 12700-12706.
103. Snyder, S. W., Ladror, U. S., Wade, W. S., Wang, G. T., Barrett, L. W., Matayoshi, E. D., Huffaker, H. J., Krafft, G. A. & Holzman, T. F. (1994) Amyloid-beta aggregation: selective inhibition of aggregation in mixtures of amyloid with different chain lengths, *Biophys J.* **67**, 1216-1228.
104. Ciccotosto, G. D., Tew, D., Curtain, C. C., Smith, D., Carrington, D., Masters, C. L., Bush, A. I., Cherny, R. A., Cappai, R. & Barnham, K. J. (2004) Enhanced Toxicity and Cellular Binding of a Modified Amyloid β Peptide with a Methionine to Valine Substitution, *J Biol Chem.* **279**, 42528-42534.

105. Kuo, Y.-M., Kokjohn, T. A., Beach, T. G., Sue, L. I., Brune, D., Lopez, J. C., Kalback, W. M., Abramowski, D., Sturchler-Pierrat, C., Staufenbiel, M. & Roher, A. E. (2001) Comparative Analysis of Amyloid-β Chemical Structure and Amyloid Plaque Morphology of Transgenic Mouse and Alzheimer's Disease Brains, *J Biol Chem.* **276**, 12991-12998.
106. Hensley, K., Hall, N., Subramaniam, R., Cole, P., Harris, M., Aksenov, M., Aksenova, M., Gabbita, S. P., Wu, J. F., Carney, J. M., Lovell, M., Markesbery, W. R. & Butterfield, D. A. (1995) Brain Regional Correspondence Between Alzheimer's Disease Histopathology and Biomarkers of Protein Oxidation, *J Neurochem.* **65**, 2146-2156.
107. Subbarao, K. V., Richardson, J. S. & Ang, L. C. (1990) Autopsy Samples of Alzheimer's Cortex Show Increased Peroxidation In Vitro, *J Neurochem.* **55**, 342-345.
108. Sarroukh, R., Cerf, E., Derclaye, S., Dufrêne, Y., Goormaghtigh, E., Ruysschaert, J.-M. & Raussens, V. (2011) Transformation of amyloid β(1–40) oligomers into fibrils is characterized by a major change in secondary structure, *Cell Mol Life Sci.* **68**, 1429-1438.
109. Xu, Y., Shen, J., Luo, X., Zhu, W., Chen, K., Ma, J. & Jiang, H. (2005) Conformational transition of amyloid β-peptide, *Proc Natl Acad Sci USA.* **102**, 5403-5407.
110. Ma, K., Clancy, E. L., Zhang, Y., Ray, D. G., Wollenberg, K. & Zagorski, M. G. (1999) Residue-Specific pKa Measurements of the β-Peptide and Mechanism of pH-Induced Amyloid Formation, *J Am Chem Soc.* **121**, 8698-8706.
111. Stine, W. B., Dahlgren, K. N., Krafft, G. A. & LaDu, M. J. (2003) In Vitro Characterization of Conditions for Amyloid-β Peptide Oligomerization and Fibrillogenesis, *J Biol Chem.* **278**, 11612-11622.
112. Wood, S. J., Maleeff, B., Hart, T. & Wetzel, R. (1996) Physical, Morphological and Functional Differences between pH 5.8 and 7.4 Aggregates of the Alzheimer's Amyloid Peptide A β, *J Mol Biol.* **256**, 870-877.
113. Geerke, D. P., Oostenbrink, C., van der Vegt, N. F. A. & van Gunsteren, W. F. (2004) An Effective Force Field for Molecular Dynamics Simulations of Dimethyl Sulfoxide and Dimethyl Sulfoxide−Water Mixtures, *J Phys Chem B.* **108**, 1436-1445.
114. Berendsen, H. J. C., Postma, J. P. M., van Gunsteren, W. F. & Hermans, J. (1981) Interaction models for water in relation to protein hydration, *Intermolecular Forces*, 331-342.
115. Hess, B., Kutzner, C., van der Spoel, D. & Lindahl, E. (2008) GROMACS 4: Algorithms for Highly Efficient, Load-Balanced, and Scalable Molecular Simulation, *J Chem Theory Comput.* **4**, 435-447.
116. Berendsen, H. J. C., Postma, J. P. M., van Gunsteren, W. F., DiNola, A. & Haak, J. R. (1984) Molecular dynamics with coupling to an external bath, *J Chem Phys.* **81**, 3684-3690.
117. Hess, B. (2007) P-LINCS: A Parallel Linear Constraint Solver for Molecular Simulation, *J Chem Theory Comput.* **4**, 116-122.
118. Kabsch, W. & Sander, C. (1983) Dictionary of protein secondary structure: Pattern recognition of hydrogen-bonded and geometrical features, *Biopolymers.* **22**, 2577-2637.
119. Daura, X., Gademann, K., Jaun, B., Seebach, D., van Gunsteren, W. F. & Mark, A. E. (1999) Peptide Folding: When Simulation Meets Experiment, *Angew Chem Int Ed.* **38**, 236-240.
120. MacKerell, A. D., Bashford, D., Bellott, Dunbrack, R. L., Evanseck, J. D., Field, M. J., Fischer, S., Gao, J., Guo, H., Ha, S., Joseph-McCarthy, D., Kuchnir, L., Kuczera, K., Lau, F. T. K., Mattos, C., Michnick, S., Ngo, T., Nguyen, D. T., Prodhom, B., Reiher, W. E., Roux, B., Schlenkrich, M., Smith, J. C., Stote, R., Straub, J., Watanabe, M., Wiórkiewicz-Kuczera, J., Yin, D. & Karplus, M. (1998) All-Atom Empirical Potential for Molecular Modeling and Dynamics Studies of Proteins, *J Phys Chem B.* **102**, 3586-3616.

121. Pike, C. J., Walencewicz-Wasserman, A. J., Kosmoski, J., Cribbs, D. H., Glabe, C. G. & Cotman, C. W. (1995) Structure-Activity Analyses of β-Amyloid Peptides: Contributions of the β25–35 Region to Aggregation and Neurotoxicity, *J Neurochem.* **64**, 253-265.
122. Zhang, S., Iwata, K., Lachenmann, M. J., Peng, J. W., Li, S., Stimson, E. R., Lu, Y. a., Felix, A. M., Maggio, J. E. & Lee, J. P. (2000) The Alzheimer's Peptide Aβ Adopts a Collapsed Coil Structure in Water, *J Struct Biol.* **130**, 130-141.
123. Cornell, W. D., Cieplak, P., Bayly, C. I., Gould, I. R., Merz, K. M., Ferguson, D. M., Spellmeyer, D. C., Fox, T., Caldwell, J. W. & Kollman, P. A. (1995) A Second Generation Force Field for the Simulation of Proteins, Nucleic Acids, and Organic Molecules, *J Am Chem Soc.* **117**, 5179-5197.
124. García, A. E. & Sanbonmatsu, K. Y. (2002) α-Helical stabilization by side chain shielding of backbone hydrogen bonds, *Proc Natl Acad Sci USA.* **99**, 2782-2787.
125. Hornak, V., Abel, R., Okur, A., Strockbine, B., Roitberg, A. & Simmerling, C. (2006) Comparison of multiple Amber force fields and development of improved protein backbone parameters, *Proteins: Struct, Funct, Bioinf.* **65**, 712-725.
126. Kollman, P. A. (1996) Advances and Continuing Challenges in Achieving Realistic and Predictive Simulations of the Properties of Organic and Biological Molecules, *Acc Chem Res.* **29**, 461-469.
127. Nymeyer, H. & García, A. E. (2003) Simulation of the folding equilibrium of α-helical peptides: A comparison of the generalized Born approximation with explicit solvent, *Proc Natl Acad Sci USA.* **100**, 13934-13939.
128. Wang, J., Cieplak, P. & Kollman, P. A. (2000) How well does a restrained electrostatic potential (RESP) model perform in calculating conformational energies of organic and biological molecules?, *J Comput Chem.* **21**, 1049-1074.
129. MacKerell, A. D., Feig, M. & Brooks, C. L. (2004) Extending the treatment of backbone energetics in protein force fields: Limitations of gas-phase quantum mechanics in reproducing protein conformational distributions in molecular dynamics simulations, *J Comput Chem.* **25**, 1400-1415.
130. Kaminski, G. A., Friesner, R. A., Tirado-Rives, J. & Jorgensen, W. L. (2001) Evaluation and Reparametrization of the OPLS-AA Force Field for Proteins via Comparison with Accurate Quantum Chemical Calculations on Peptides, *J Phys Chem B.* **105**, 6474-6487.
131. Scott, W. R. P., Hünenberger, P. H., Tironi, I. G., Mark, A. E., Billeter, S. R., Fennen, J., Torda, A. E., Huber, T., Krüger, P. & van Gunsteren, W. F. (1999) The GROMOS Biomolecular Simulation Program Package, *J Phys Chem A.* **103**, 3596-3607.
132. Schmid, N., Eichenberger, A., Choutko, A., Riniker, S., Winger, M., Mark, A. & Gunsteren, W. (2011) Definition and testing of the GROMOS force-field versions 54A7 and 54B7, *Eur Biophys J.* **40**, 843-856.
133. Best, R. B., Buchete, N.-V. & Hummer, G. (2008) Are Current Molecular Dynamics Force Fields too Helical?, *Biophys J.* **95**, L07-L09.
134. Sgourakis, N. G., Yan, Y., McCallum, S. A., Wang, C. & Garcia, A. E. (2007) The Alzheimer's Peptides Aβ40 and 42 Adopt Distinct Conformations in Water: A Combined MD / NMR Study, *J Mol Biol.* **368**, 1448-1457.
135. Olubiyi, O. O. & Strodel, B. (2012) Structures of the Amyloid β-Peptides Aβ1–40 and Aβ1–42 as Influenced by pH and a d-Peptide, *J Phys Chem B.* **116**, 3280-3291.

136. Triguero, L., Singh, R. & Prabhakar, R. (2008) Comparative Molecular Dynamics Studies of Wild-Type and Oxidized Forms of Full-Length Alzheimer Amyloid β-Peptides Aβ(1−40) and Aβ(1−42), *J Phys Chem B.* **112**, 7123-7131.
137. Valerio, M., Porcelli, F., Zbilut, J. P., Giuliani, A., Manetti, C. & Conti, F. (2008) pH Effects on the Conformational Preferences of Amyloid β-Peptide (1–40) in HFIP Aqueous Solution by NMR Spectroscopy, *ChemMedChem.* **3**, 833-843.
138. Burdick, D., Soreghan, B., Kwon, M., Kosmoski, J., Knauer, M., Henschen, A., Yates, J., Cotman, C. & Glabe, C. (1992) Assembly and aggregation properties of synthetic Alzheimer's A4/beta amyloid peptide analogs, *J Biol Chem.* **267**, 546-554.
139. Klug, G. M. J. A., Losic, D., Supundi, Subasinghe, S., Aguilar, M.-I., Martin, L. L. & Small, D. H. (2003) β-Amyloid protein oligomers induced by metal ions and acid pH are distinct from those generated by slow spontaneous ageing at neutral pH, *Eur J Biochem.* **270**, 4282-4293.
140. Melnikova, I. (2007) Therapies for Alzheimer's disease, *Nat Rev Drug Discov.* **6**, 341-342.
141. Higgins, L. S., Murphy, G. M., Forno, L. S., Catalano, R. & Cordell, B. (1996) P3 beta-amyloid peptide has a unique and potentially pathogenic immunohistochemical profile in Alzheimer's disease brain, *Am J Pathol.* **149**, 585-596.
142. Pauwels, K., Williams, T. L., Morris, K. L., Jonckheere, W., Vandersteen, A., Kelly, G., Schymkowitz, J., Rousseau, F., Pastore, A., Serpell, L. C. & Broersen, K. (2012) Structural Basis for Increased Toxicity of Pathological Aβ42:Aβ40 Ratios in Alzheimer Disease, *J Biol Chem.* **287**, 5650-5660.
143. Ferreira, S. T. & Klein, W. L. (2011) The Aβ oligomer hypothesis for synapse failure and memory loss in Alzheimer's disease, *Neurobiol Learn Mem.* **96**, 529-543.
144. Sepulveda, F. J., Parodi, J., Peoples, R. W., Opazo, C. & Aguayo, L. G. (2010) Synaptotoxicity of Alzheimer Beta Amyloid Can Be Explained by Its Membrane Perforating Property, *PLoS One.* **5**, e11820.
145. Roychaudhuri, R., Zheng, X., Lomakin, A., Maiti, P., Condron, M. M., Benedek, G. B., Bitan, G., Bowers, M. T. & Teplow, D. B. (2015) Role of Species-Specific Primary Structure Differences in Aβ42 Assembly and Neurotoxicity, *ACS Chem Neurosci.* **6**, 1941-1955.
146. Ambroggio, E. E., Kim, D. H., Separovic, F., Barrow, C. J., Barnham, K. J., Bagatolli, L. A. & Fidelio, G. D. (2005) Surface Behavior and Lipid Interaction of Alzheimer β-Amyloid Peptide 1–42: A Membrane-Disrupting Peptide, *Biophys J.* **88**, 2706-2713.
147. Terzi, E., Hölzemann, G. & Seelig, J. (1997) Interaction of Alzheimer β-Amyloid Peptide(1−40) with Lipid Membranes, *Biochemistry.* **36**, 14845-14852.
148. Zhao, L. N., Chiu, S.-W., Benoit, J., Chew, L. Y. & Mu, Y. (2011) Amyloid β Peptides Aggregation in a Mixed Membrane Bilayer: A Molecular Dynamics Study, *J Phys Chem B.* **115**, 12247-12256.
149. Lemkul, J. A. & Bevan, D. R. (2013) Aggregation of Alzheimer's amyloid beta-peptide in biological membranes: a molecular dynamics study, *Biochemistry.* **52**, 4971-80.
150. Dies, H., Toppozini, L. & Rheinstädter, M. C. (2014) The Interaction between Amyloid-β Peptides and Anionic Lipid Membranes Containing Cholesterol and Melatonin, *PLoS One.* **9**, e99124.
151. Kirsch, C., Eckert, G. P. & Mueller, W. E. (2002) Cholesterol attenuates the membrane perturbing properties of β-amyloid peptides, *Amyloid.* **9**, 149-160.
152. Lockhart, C. & Klimov, D. K. (2014) Alzheimer's Aβ10–40 Peptide Binds and Penetrates DMPC Bilayer: An Isobaric–Isothermal Replica Exchange Molecular Dynamics Study, *J Phys Chem B.* **118**, 2638-2648.

153. Coles, M., Bicknell, W., Watson, A. A., Fairlie, D. P. & Craik, D. J. (1998) Solution structure of amyloid beta-peptide(1-40) in a water-micelle environment. Is the membrane-spanning domain where we think it is?, *Biochemistry.* **37**, 11064-77.
154. Ege, C., Majewski, J., Wu, G., Kjaer, K. & Lee, K. Y. C. (2005) Templating Effect of Lipid Membranes on Alzheimer's Amyloid Beta Peptide, *Chemphyschem.* **6**, 226-229.
155. Kim, S. & Klimov, D. (2013) Binding to the lipid monolayer induces conformational transition in Aβ monomer, *J Mol Model.* **19**, 737-750.
156. Davis, C. H. & Berkowitz, M. L. (2009) Structure of the Amyloid-β (1−42) Monomer Absorbed To Model Phospholipid Bilayers: A Molecular Dynamics Study, *J Phys Chem B.* **113**, 14480-14486.
157. Poojari, C., Kukol, A. & Strodel, B. (2013) How the amyloid-beta peptide and membranes affect each other: an extensive simulation study, *Biochim Biophys Acta.* **1828**, 327-39.
158. Yu, X., Wang, Q., Pan, Q., Zhou, F. & Zheng, J. (2013) Molecular interactions of Alzheimer amyloid-[small beta] oligomers with neutral and negatively charged lipid bilayers, *Phys Chem Chem Phys.* **15**, 8878-8889.
159. Bucciantini, M., Rigacci, S. & Stefani, M. (2014) Amyloid Aggregation: Role of Biological Membranes and the Aggregate–Membrane System, *J Phys Chem Lett.* **5**, 517-527.
160. Manna, M. & Mukhopadhyay, C. (2013) Binding, Conformational Transition and Dimerization of Amyloid-β Peptide on GM1-Containing Ternary Membrane: Insights from Molecular Dynamics Simulation, *PLoS One.* **8**, e71308.
161. Sasahara, K., Morigaki, K. & Shinya, K. (2013) Effects of membrane interaction and aggregation of amyloid beta-peptide on lipid mobility and membrane domain structure, *Phys Chem Chem Phys.* **15**, 8929-39.
162. Seghezza, S., Diaspro, A., Canale, C. & Dante, S. (2014) Cholesterol Drives Aβ(1–42) Interaction with Lipid Rafts in Model Membranes, *Langmuir.* **30**, 13934-13941.
163. Devaux, P. F. (1991) Static and dynamic lipid asymmetry in cell membranes, *Biochemistry.* **30**, 1163-1173.
164. Ikeda, M., Kihara, A. & Igarashi, Y. (2006) Lipid asymmetry of the eukaryotic plasma membrane: functions and related enzymes, *Biol Pharm Bull.* **29**, 1542-6.
165. Sonnino, S., Mauri, L., Chigorno, V. & Prinetti, A. (2007) Gangliosides as components of lipid membrane domains, *Glycobiology.* **17**, 1r-13r.
166. Tsui-Pierchala, B. A., Encinas, M., Milbrandt, J. & Johnson, E. M., Jr. (2002) Lipid rafts in neuronal signaling and function, *Trends Neurosci.* **25**, 412-7.
167. Chishti, M. A., Yang, D.-S., Janus, C., Phinney, A. L., Horne, P., Pearson, J., Strome, R., Zuker, N., Loukides, J., French, J., Turner, S., Lozza, G., Grilli, M., Kunicki, S., Morissette, C., Paquette, J., Gervais, F., Bergeron, C., Fraser, P. E., Carlson, G. A., George-Hyslop, P. S. & Westaway, D. (2001) Early-onset Amyloid Deposition and Cognitive Deficits in Transgenic Mice Expressing a Double Mutant Form of Amyloid Precursor Protein 695, *J Biol Chem.* **276**, 21562-21570.
168. Jawhar, S., Wirths, O., Schilling, S., Graubner, S., Demuth, H.-U. & Bayer, T. A. (2011) Overexpression of Glutaminyl Cyclase, the Enzyme Responsible for Pyroglutamate Aβ Formation, Induces Behavioral Deficits, and Glutaminyl Cyclase Knock-out Rescues the Behavioral Phenotype in 5XFAD Mice, *J Biol Chem.* **286**, 4454-4460.
169. Oddo, S., Caccamo, A., Shepherd, J. D., Murphy, M. P., Golde, T. E., Kayed, R., Metherate, R., Mattson, M. P., Akbari, Y. & LaFerla, F. M. (2003) Triple-Transgenic Model of

Alzheimer's Disease with Plaques and Tangles: Intracellular Aβ and Synaptic Dysfunction, *Neuron.* **39**, 409-421.
170. Glenner, G. G. & Wong, C. W. (1984) Alzheimer's disease: initial report of the purification and characterization of a novel cerebrovascular amyloid protein, *Biochem Biophys Res Commun.* **120**, 885-90.
171. Shivers, B. D., Hilbich, C., Multhaup, G., Salbaum, M., Beyreuther, K. & Seeburg, P. H. (1988) Alzheimer's disease amyloidogenic glycoprotein: expression pattern in rat brain suggests a role in cell contact, *EMBO J.* **7**, 1365-70.
172. Vaughan, D. W. & Peters, A. (1981) The structure of neuritic plaque in the cerebral cortex of aged rats, *J Neuropathol Exp Neurol.* **40**, 472-87.
173. Nasica-Labouze, J., Nguyen, P. H., Sterpone, F., Berthoumieu, O., Buchete, N.-V., Coté, S., De Simone, A., Doig, A. J., Faller, P., Garcia, A., Laio, A., Li, M. S., Melchionna, S., Mousseau, N., Mu, Y., Paravastu, A., Pasquali, S., Rosenman, D. J., Strodel, B., Tarus, B., Viles, J. H., Zhang, T., Wang, C. & Derreumaux, P. (2015) Amyloid β Protein and Alzheimer's Disease: When Computer Simulations Complement Experimental Studies, *Chem Rev.* **115**, 3518-3563.
174. Kotler, S. A., Walsh, P., Brender, J. R. & Ramamoorthy, A. (2014) Differences between amyloid-[small beta] aggregation in solution and on the membrane: insights into elucidation of the mechanistic details of Alzheimer's disease, *Chem Soc Rev.* **43**, 6692-6700.
175. Crescenzi, O., Tomaselli, S., Guerrini, R., Salvadori, S., D'Ursi, A. M., Temussi, P. A. & Picone, D. (2002) Solution structure of the Alzheimer amyloid beta-peptide (1-42) in an apolar microenvironment. Similarity with a virus fusion domain, *Eur J Biochem.* **269**, 5642-8.
176. Guex, N. & Peitsch, M. C. (1997) SWISS-MODEL and the Swiss-PdbViewer: an environment for comparative protein modeling, *Electrophoresis.* **18**, 2714-23.
177. Leekumjorn, S., Wu, Y., Sum, A. K. & Chan, C. (2008) Experimental and Computational Studies Investigating Trehalose Protection of HepG2 Cells from Palmitate-Induced Toxicity, *Biophys J.* **94**, 2869-2883.
178. Niemelä, P. S., Ollila, S., Hyvönen, M. T., Karttunen, M. & Vattulainen, I. (2007) Assessing the Nature of Lipid Raft Membranes, *PLoS Comput Biol.* **3**, e34.
179. Tieleman, D. P., Forrest, L. R., Sansom, M. S. P. & Berendsen, H. J. C. (1998) Lipid Properties and the Orientation of Aromatic Residues in OmpF, Influenza M2, and Alamethicin Systems: Molecular Dynamics Simulations, *Biochemistry.* **37**, 17554-17561.
180. Tieleman, D. P., Sansom, M. S. P. & Berendsen, H. J. C. (1999) Alamethicin Helices in a Bilayer and in Solution: Molecular Dynamics Simulations, *Biophys J.* **76**, 40-49.
181. Bachar, M. & Becker, O. M. (2000) Protein-induced membrane disorder: a molecular dynamics study of melittin in a dipalmitoylphosphatidylcholine bilayer, *Biophys J.* **78**, 1359-1375.
182. Allen, W. J., Lemkul, J. A. & Bevan, D. R. (2009) GridMAT-MD: A grid-based membrane analysis tool for use with molecular dynamics, *J Comput Chem.* **30**, 1952-1958.
183. Hoyer, W., Gronwall, C., Jonsson, A., Stahl, S. & Hard, T. (2008) Stabilization of a beta-hairpin in monomeric Alzheimer's amyloid-beta peptide inhibits amyloid formation, *Proc Natl Acad Sci U S A.* **105**, 5099-104.
184. Zhang, M., Zhao, J. & Zheng, J. (2014) Molecular understanding of a potential functional link between antimicrobial and amyloid peptides, *Soft Matter.* **10**, 7425-7451.
185. Sgourakis, N. G., Merced-Serrano, M., Boutsidis, C., Drineas, P., Du, Z., Wang, C. & Garcia, A. E. (2011) Atomic-level characterization of the ensemble of the Abeta(1-42) monomer

in water using unbiased molecular dynamics simulations and spectral algorithms, *J Mol Biol.* **405**, 570-83.
186. Shen, L. & Ji, H.-F. (2011) Comparative study on the conformational stability of human and murine amyloid β peptide, *Comp Theor Chem.* **972**, 44-47.
187. Brown, A. M., Lemkul, J. A., Schaum, N. & Bevan, D. R. (2014) Simulations of monomeric amyloid β-peptide (1–40) with varying solution conditions and oxidation state of Met35: Implications for aggregation, *Arch Biochem Biophys.* **545**, 44-52.
188. Costantini, S., Colonna, G. & Facchiano, A. M. (2006) Amino acid propensities for secondary structures are influenced by the protein structural class, *Biochem Biophys Res Commun.* **342**, 441-451.
189. Klimov, D. K. & Thirumalai, D. (2003) Dissecting the Assembly of Aβ16–22 Amyloid Peptides into Antiparallel β Sheets, *Structure.* **11**, 295-307.
190. Mason, R. P., Jacob, R. F., Walter, M. F., Mason, P. E., Avdulov, N. A., Chochina, S. V., Igbavboa, U. & Wood, W. G. (1999) Distribution and fluidizing action of soluble and aggregated amyloid beta-peptide in rat synaptic plasma membranes, *J Biol Chem.* **274**, 18801-7.
191. Williams, T. L. & Serpell, L. C. (2011) Membrane and surface interactions of Alzheimer's Aβ peptide – insights into the mechanism of cytotoxicity, *FEBS J.* **278**, 3905-3917.
192. Butterfield, S. M. & Lashuel, H. A. (2010) Amyloidogenic Protein–Membrane Interactions: Mechanistic Insight from Model Systems, *Angew Chem Int Ed.* **49**, 5628-5654.
193. Kakio, A., Nishimoto, S.-i., Yanagisawa, K., Kozutsumi, Y. & Matsuzaki, K. (2002) Interactions of Amyloid β-Protein with Various Gangliosides in Raft-Like Membranes: Importance of GM1 Ganglioside-Bound Form as an Endogenous Seed for Alzheimer Amyloid†, *Biochemistry.* **41**, 7385-7390.
194. Kremer, J. J., Pallitto, M. M., Sklansky, D. J. & Murphy, R. M. (2000) Correlation of β-Amyloid Aggregate Size and Hydrophobicity with Decreased Bilayer Fluidity of Model Membraneskkk, *Biochemistry.* **39**, 10309-10318.
195. Muller, W. E., Eckert, G. P., Scheuer, K., Cairns, N. J., Maras, A. & Gattaz, W. F. (1998) Effects of beta-amyloid peptides on the fluidity of membranes from frontal and parietal lobes of human brain. High potencies of A beta 1-42 and A beta 1-43, *Amyloid.* **5**, 10-5.
196. Muller, W. E., Koch, S., Eckert, A., Hartmann, H. & Scheuer, K. (1995) beta-Amyloid peptide decreases membrane fluidity, *Brain Res.* **674**, 133-6.
197. Lockhart, C., Kim, S. & Klimov, D. K. (2012) Explicit Solvent Molecular Dynamics Simulations of Aβ Peptide Interacting with Ibuprofen Ligands, *J Phys Chem B.* **116**, 12922-12932.
198. Sinha, S., Lopes, D. H., Du, Z., Pang, E. S., Shanmugam, A., Lomakin, A., Talbiersky, P., Tennstaedt, A., McDaniel, K., Bakshi, R., Kuo, P. Y., Ehrmann, M., Benedek, G. B., Loo, J. A., Klarner, F. G., Schrader, T., Wang, C. & Bitan, G. (2011) Lysine-specific molecular tweezers are broad-spectrum inhibitors of assembly and toxicity of amyloid proteins, *J Am Chem Soc.* **133**, 16958-69.
199. Sinha, S., Lopes, D. H. J. & Bitan, G. (2012) A Key Role for Lysine Residues in Amyloid β-Protein Folding, Assembly, and Toxicity, *ACS Chem Neurosci.* **3**, 473-481.
200. Stefani, M. (2004) Protein misfolding and aggregation: new examples in medicine and biology of the dark side of the protein world, *Bba Mol Basis Dis.* **1739**, 5-25.
201. Beel, A. J. & Sanders, C. R. (2008) Substrate Specificity of γ-Secretase and Other Intramembrane Proteases, *CMLS.* **65**, 1311-1334.

202. Vardy, E. R., Catto, A. J. & Hooper, N. M. (2005) Proteolytic mechanisms in amyloid-beta metabolism: therapeutic implications for Alzheimer's disease, *Trends Mol Med.* **11**, 464-72.
203. Jarrett, J. T., Berger, E. P. & Lansbury, P. T., Jr. (1993) The carboxy terminus of the beta amyloid protein is critical for the seeding of amyloid formation: implications for the pathogenesis of Alzheimer's disease, *Biochemistry.* **32**, 4693-7.
204. Jarrett, J. T., Berger, E. P. & Lansbury, P. T., Jr. (1993) The C-terminus of the beta protein is critical in amyloidogenesis, *Ann N Y Acad Sci.* **695**, 144-8.
205. Dahlgren, K. N., Manelli, A. M., Stine, W. B., Jr., Baker, L. K., Krafft, G. A. & LaDu, M. J. (2002) Oligomeric and fibrillar species of amyloid-beta peptides differentially affect neuronal viability, *J Biol Chem.* **277**, 32046-53.
206. Baglioni, S., Casamenti, F., Bucciantini, M., Luheshi, L. M., Taddei, N., Chiti, F., Dobson, C. M. & Stefani, M. (2006) Prefibrillar amyloid aggregates could be generic toxins in higher organisms, *J Neurosci.* **26**, 8160-7.
207. Glabe, C. C. (2005) Amyloid accumulation and pathogensis of Alzheimer's disease: significance of monomeric, oligomeric and fibrillar Abeta, *Subcell Biochem.* **38**, 167-77.
208. Klein, W. L., Stine, W. B., Jr. & Teplow, D. B. (2004) Small assemblies of unmodified amyloid beta-protein are the proximate neurotoxin in Alzheimer's disease, *Neurobiol Aging.* **25**, 569-80.
209. Caughey, B. & Lansbury, P. T. (2003) Protofibrils, pores, fibrils, and neurodegeneration: separating the responsible protein aggregates from the innocent bystanders, *Annu Rev Neurosci.* **26**, 267-98.
210. Ross, C. A. & Poirier, M. A. (2005) What is the role of protein aggregation in neurodegeneration?, *Nat Rev Mol Cell Biol.* **6**, 891-898.
211. Glabe, C. G. (2008) Structural Classification of Toxic Amyloid Oligomers, *J Biol Chem.* **283**, 29639-29643.
212. Baumketner, A., Bernstein, S. L., Wyttenbach, T., Bitan, G., Teplow, D. B., Bowers, M. T. & Shea, J.-E. (2006) Amyloid β-protein monomer structure: A computational and experimental study, *Protein Sci.* **15**, 420-428.
213. Kayed, R. & Glabe, C. G. (2006) Conformation‐Dependent Anti‐Amyloid Oligomer Antibodies in *Methods Enzymol* pp. 326-344, Academic Press.
214. Deshpande, A., Mina, E., Glabe, C. & Busciglio, J. (2006) Different conformations of amyloid beta induce neurotoxicity by distinct mechanisms in human cortical neurons, *J Neurosci.* **26**, 6011-8.
215. Kayed, R., Canto, I., Breydo, L., Rasool, S., Lukacsovich, T., Wu, J., Albay, R., 3rd, Pensalfini, A., Yeung, S., Head, E., Marsh, J. L. & Glabe, C. (2010) Conformation dependent monoclonal antibodies distinguish different replicating strains or conformers of prefibrillar Abeta oligomers, *Mol Neurodegener.* **5**, 57.
216. Teplow, D. B., Lazo, N. D., Bitan, G., Bernstein, S., Wyttenbach, T., Bowers, M. T., Baumketner, A., Shea, J. E., Urbanc, B., Cruz, L., Borreguero, J. & Stanley, H. E. (2006) Elucidating amyloid beta-protein folding and assembly: A multidisciplinary approach, *Acc Chem Res.* **39**, 635-45.
217. Wise-Scira, O., Xu, L., Kitahara, T., Perry, G. & Coskuner, O. (2011) Amyloid-beta peptide structure in aqueous solution varies with fragment size, *J Chem Phys.* **135**, 205101.
218. Yang, M. & Teplow, D. B. (2008) Amyloid beta-protein monomer folding: free-energy surfaces reveal alloform-specific differences, *J Mol Biol.* **384**, 450-64.

219. Barz, B. & Urbanc, B. (2012) Dimer formation enhances structural differences between amyloid beta-protein (1-40) and (1-42): an explicit-solvent molecular dynamics study, *PLoS One.* **7**, e34345.
220. Urbanc, B., Cruz, L., Ding, F., Sammond, D., Khare, S., Buldyrev, S. V., Stanley, H. E. & Dokholyan, N. V. (2004) Molecular Dynamics Simulation of Amyloid β Dimer Formation, *Biophys J.* **87**, 2310-2321.
221. Meral, D. & Urbanc, B. (2013) Discrete Molecular Dynamics Study of Oligomer Formation by N-Terminally Truncated Amyloid β-Protein, *J Mol Biol.* **425**, 2260-2275.
222. Urbanc, B., Cruz, L., Yun, S., Buldyrev, S. V., Bitan, G., Teplow, D. B. & Stanley, H. E. (2004) In silico study of amyloid beta-protein folding and oligomerization, *Proc Natl Acad Sci U S A.* **101**, 17345-50.
223. Zhang, T., Zhang, J., Derreumaux, P. & Mu, Y. (2013) Molecular mechanism of the inhibition of EGCG on the Alzheimer Abeta(1-42) dimer, *J Phys Chem B.* **117**, 3993-4002.
224. Tofoleanu, F. & Buchete, N. V. (2012) Molecular interactions of Alzheimer's Abeta protofilaments with lipid membranes, *J Mol Biol.* **421**, 572-86.
225. Yates, E. A., Owens, S. L., Lynch, M. F., Cucco, E. M., Umbaugh, C. S. & Legleiter, J. (2013) Specific domains of Abeta facilitate aggregation on and association with lipid bilayers, *J Mol Biol.* **425**, 1915-33.
226. Zhao, L. N., Chiu, S. W., Benoit, J., Chew, L. Y. & Mu, Y. (2011) Amyloid beta peptides aggregation in a mixed membrane bilayer: a molecular dynamics study, *J Phys Chem B.* **115**, 12247-56.
227. Strodel, B., Lee, J. W. L., Whittleston, C. S. & Wales, D. J. (2010) Transmembrane Structures for Alzheimer's Aβ1−42 Oligomers, *J Am Chem Soc.* **132**, 13300-13312.
228. The PyMOL Molecular Graphics System, Version 1.5.0.4 in, Schrödinger, LLC.
229. Bernstein, S. L., Dupuis, N. F., Lazo, N. D., Wyttenbach, T., Condron, M. M., Bitan, G., Teplow, D. B., Shea, J.-E., Ruotolo, B. T., Robinson, C. V. & Bowers, M. T. (2009) Amyloid-β protein oligomerization and the importance of tetramers and dodecamers in the aetiology of Alzheimer's disease, *Nat Chem.* **1**, 326-331.
230. Shankar, G. M., Li, S., Mehta, T. H., Garcia-Munoz, A., Shepardson, N. E., Smith, I., Brett, F. M., Farrell, M. A., Rowan, M. J., Lemere, C. A., Regan, C. M., Walsh, D. M., Sabatini, B. L. & Selkoe, D. J. (2008) Amyloid-beta protein dimers isolated directly from Alzheimer's brains impair synaptic plasticity and memory, *Nat Med.* **14**, 837-42.
231. Sakono, M. & Zako, T. (2010) Amyloid oligomers: formation and toxicity of Abeta oligomers, *FEBS J.* **277**, 1348-58.
232. Nag, S., Sarkar, B., Bandyopadhyay, A., Sahoo, B., Sreenivasan, V. K. A., Kombrabail, M., Muralidharan, C. & Maiti, S. (2011) Nature of the Amyloid-β Monomer and the Monomer-Oligomer Equilibrium, *J Biol Chem.* **286**, 13827-13833.
233. Abel, S., Sterpone, F., Bandyopadhyay, S. & Marchi, M. (2004) Molecular Modeling and Simulations of AOT−Water Reverse Micelles in Isooctane: Structural and Dynamic Properties, *J Phys Chem B.* **108**, 19458-19466.
234. Martinez, A. V., Dominguez, L., Małolepsza, E., Moser, A., Ziegler, Z. & Straub, J. E. (2013) Probing the Structure and Dynamics of Confined Water in AOT Reverse Micelles, *J Phys Chem B.* **117**, 7345-7351.
235. Ahmed, M., Davis, J., Aucoin, D., Sato, T., Ahuja, S., Aimoto, S., Elliott, J. I., Van Nostrand, W. E. & Smith, S. O. (2010) Structural conversion of neurotoxic amyloid-[beta]1-42 oligomers to fibrils, *Nat Struct Mol Biol.* **17**, 561-567.

236. Cheng, I. H., Scearce-Levie, K., Legleiter, J., Palop, J. J., Gerstein, H., Bien-Ly, N., Puoliväli, J., Lesné, S., Ashe, K. H., Muchowski, P. J. & Mucke, L. (2007) Accelerating Amyloid-β Fibrillization Reduces Oligomer Levels and Functional Deficits in Alzheimer Disease Mouse Models, *J Biol Chem.* **282**, 23818-23828.
237. Rushworth, J. V. & Hooper, N. M. (2011) Lipid Rafts: Linking Alzheimer's Amyloid-B; Production, Aggregation, and Toxicity at Neuronal Membranes, *Int J Alzheimers Dis.* **2011**.
238. Elmore, D. E. (2006) Molecular dynamics simulation of a phosphatidylglycerol membrane, *FEBS Lett.* **580**, 144-148.
239. Zhou, F. & Schulten, K. (1995) Molecular Dynamics Study of a Membrane-Water Interface, *J Phys Chem B.* **99**, 2194-2207.
240. Hancock, J. F. (2006) Lipid rafts: contentious only from simplistic standpoints, *Nat Rev Mol Cell Biol.* **7**, 456-62.
241. Hayden, M. R. (2002) Islet amyloid, metabolic syndrome, and the natural progressive history of type 2 diabetes mellitus, *Jop.* **3**, 126-38.
242. Weir, G. C. & Bonner-Weir, S. (2004) Five stages of evolving beta-cell dysfunction during progression to diabetes, *Diabetes.* **53 Suppl 3**, S16-21.
243. Guardado-Mendoza, R., Davalli, A. M., Chavez, A. O., Hubbard, G. B., Dick, E. J., Majluf-Cruz, A., Tene-Perez, C. E., Goldschmidt, L., Hart, J., Perego, C., Comuzzie, A. G., Tejero, M. E., Finzi, G., Placidi, C., La Rosa, S., Capella, C., Halff, G., Gastaldelli, A., DeFronzo, R. A. & Folli, F. (2009) Pancreatic islet amyloidosis, beta-cell apoptosis, and alpha-cell proliferation are determinants of islet remodeling in type-2 diabetic baboons, *Proc Natl Acad Sci U S A.* **106**, 13992-7.
244. Knight, J. D., Williamson, J. A. & Miranker, A. D. (2008) Interaction of membrane-bound islet amyloid polypeptide with soluble and crystalline insulin, *Protein Sci.* **17**, 1850-6.
245. Pieber, T. R., Stein, D. T., Ogawa, A., Alam, T., Ohneda, M., McCorkle, K., Chen, L., McGarry, J. D. & Unger, R. H. (1993) Amylin-insulin relationships in insulin resistance with and without diabetic hyperglycemia, *Am J Physiol.* **265**, E446-53.
246. Bradbury, A. F. & Smyth, D. G. (1991) Peptide amidation, *Trends Biochem Sci.* **16**, 112-115.
247. Qiao, Q., Bowman, G. R. & Huang, X. (2013) Dynamics of an Intrinsically Disordered Protein Reveal Metastable Conformations That Potentially Seed Aggregation, *JACS.* **135**, 16092-16101.
248. Fu, L., Liu, J. & Yan, E. C. Y. (2011) Chiral sum frequency generation spectroscopy for characterizing protein secondary structures at interfaces, *J Am Chem Soc.* **133**, 8094.
249. Hebda, J. A. & Miranker, A. D. (2009) The Interplay of catlysis and toxicity by amyloid intermediates: insights from type II diabetes, *Annu Rev Biophys.* **38**, 125.
250. Jayasinghe, S. A. & Langen, R. (2005) Lipid membranes modulate the structure of islet amyloid polypeptide, *Biochemistry.* **44**, 12113.
251. Kayed, R., Bernhagen, J., Greenfield, N., Sweimeh, K., Brunner, H., Voelter, W. & Kapurniotu, A. (1999) Conformational transitions of islet amyloid polypeptide (IAPP) in amyloid formation in vitro, *J Mol Biol.* **287**, 781-96.
252. Anguiano, M., Nowak, R. J. & Lansbury, P. T., Jr. (2002) Protofibrillar islet amyloid polypeptide permeabilizes synthetic vesicles by a pore-like mechanism that may be relevant to type II diabetes, *Biochemistry.* **41**, 11338-43.

253. Janson, J., Ashley, R. H., Harrison, D., McIntyre, S. & Butler, P. C. (1999) The mechanism of islet amyloid polypeptide toxicity is membrane disruption by intermediate-sized toxic amyloid particles, *Diabetes.* **48**, 491-8.
254. Mirzabekov, T. A., Lin, M. C. & Kagan, B. L. (1996) Pore formation by the cytotoxic islet amyloid peptide amylin, *J Biol Chem.* **271**, 1988-92.
255. Hebda, J. A. & Miranker, A. D. (2009) The interplay of catalysis and toxicity by amyloid intermediates on lipid bilayers: insights from type II diabetes, *Annu Rev Biophys.* **38**, 125-52.
256. Jayasinghe, S. A. & Langen, R. (2005) Lipid membranes modulate the structure of islet amyloid polypeptide, *Biochemistry.* **44**, 12113-9.
257. Knight, J. D., Hebda, J. A. & Miranker, A. D. (2006) Conserved and cooperative assembly of membrane-bound alpha-helical states of islet amyloid polypeptide, *Biochemistry.* **45**, 9496-508.
258. Knight, J. D. & Miranker, A. D. (2004) Phospholipid catalysis of diabetic amyloid assembly, *J Mol Biol.* **341**, 1175-87.
259. Green, J., Goldsbury, C., Mini, T., Sunderji, S., Frey, P., Kistler, J., Cooper, G. & Aebi, U. (2003) Full-length rat amylin forms fibrils following substitution of single residues from human amylin, *J Mol Biol.* **326**, 1147-56.
260. Goldsbury, C. S., Cooper, G. J., Goldie, K. N., Muller, S. A., Saafi, E. L., Gruijters, W. T., Misur, M. P., Engel, A., Aebi, U. & Kistler, J. (1997) Polymorphic fibrillar assembly of human amylin, *J Struct Biol.* **119**, 17-27.
261. Green, J. D., Goldsbury, C., Kistler, J., Cooper, G. J. & Aebi, U. (2004) Human amylin oligomer growth and fibril elongation define two distinct phases in amyloid formation, *J Biol Chem.* **279**, 12206-12.
262. Singh, S., Chiu, C. C., Reddy, A. S. & de Pablo, J. J. (2013) alpha-helix to beta-hairpin transition of human amylin monomer, *J Chem Phys.* **138**, 155101.
263. Cort, J. R., Liu, Z., Lee, G. M., Huggins, K. N., Janes, S., Prickett, K. & Andersen, N. H. (2009) Solution state structures of human pancreatic amylin and pramlintide, *Protein Eng Des Sel.* **22**, 497-513.
264. Williamson, J. A. & Miranker, A. D. (2007) Direct detection of transient alpha-helical states in islet amyloid polypeptide, *Protein Sci.* **16**, 110-7.
265. Yonemoto, I. T., Kroon, G. J., Dyson, H. J., Balch, W. E. & Kelly, J. W. (2008) Amylin proprotein processing generates progressively more amyloidogenic peptides that initially sample the helical state, *Biochemistry.* **47**, 9900-10.
266. Kegulian, N. C., Sankhagowit, S., Apostolidou, M., Jayasinghe, S. A., Malmstadt, N., Butler, P. C. & Langen, R. (2015) Membrane Curvature-sensing and Curvature-inducing Activity of Islet Amyloid Polypeptide and Its Implications for Membrane Disruption, *J Biol Chem.* **290**, 25782-25793.
267. McHenry, A. J., Brender, J. R., Hartman, K. & Ramamoorthy, A. Lipid Composition and Raft Domain Formation on the IAPP-Membrane Interaction: The Role of Cholesterol on the Inhibition of IAPP (Amylin) Fibrilization and the Reduction of Membrane Disruption in Model Liposomes and Mouse Pancreatic Islets, *Biophys J.* **100**, 541a.
268. Pannuzzo, M., Raudino, A. & Böckmann, R. A. (2014) Peptide-induced membrane curvature in edge-stabilized open bilayers: A theoretical and molecular dynamics study, *The Journal of Chemical Physics.* **141**, 024901.
269. Singh, S., C. C. Chiu, A. S. Reddy and J. J. de Pablo (2013). Alpha-helix to beta-hairpin transition of human amylin monomer. *J Chem Phys* **131,** 155101.

270. Middleton, C. T., Marek, P., Cao, P., Chiu, C. C., Singh, S., Woys, A. M., de Pablo, J. J., Raleigh, D. P. & Zanni, M. T. (2012) Two-dimensional infrared spectroscopy reveals the complex behaviour of an amyloid fibril inhibitor, *Nat Chem.* **4**, 355-60.
271. Reddy, A. S., Wang, L., Singh, S., Ling, Y. L., Buchanan, L., Zanni, M. T., Skinner, J. L. & de Pablo, J. J. (2010) Stable and metastable states of human amylin in solution, *Biophys J.* **99**, 2208-16.
272. Wang, L., Middleton, C. T., Singh, S., Reddy, A. S., Woys, A. M., Strasfeld, D. B., Marek, P., Raleigh, D. P., de Pablo, J. J., Zanni, M. T. & Skinner, J. L. (2011) 2DIR spectroscopy of human amylin fibrils reflects stable beta-sheet structure, *J Am Chem Soc.* **133**, 16062-71.
273. Buchanan, L. E., Dunkelberger, E. B., Tran, H. Q., Cheng, P.-N., Chiu, C.-C., Cao, P., Raleigh, D. P., de Pablo, J. J., Nowick, J. S. & Zanni, M. T. (2013) Mechanism of IAPP amyloid fibril formation involves an intermediate with a transient β-sheet, *Proc Natl Acad Sci USA.*. **110**, 19285-19290.
274. Engel, M. F., Yigittop, H., Elgersma, R. C., Rijkers, D. T., Liskamp, R. M., de Kruijff, B., Hoppener, J. W. & Antoinette Killian, J. (2006) Islet amyloid polypeptide inserts into phospholipid monolayers as monomer, *J Mol Biol.* **356**, 783-9.
275. Jaikaran, E. T., Higham, C. E., Serpell, L. C., Zurdo, J., Gross, M., Clark, A. & Fraser, P. E. (2001) Identification of a novel human islet amyloid polypeptide beta-sheet domain and factors influencing fibrillogenesis, *J Mol Biol.* **308**, 515-25.
276. Glenner, G. G., David Eanes, E. & Wiley, C. A. (1988) Amyloid fibrils formed from a segment of the pancreatic islet amyloid protein, *Biochem Biophys Res Commun.* **155**, 608-614.
277. Porat, Y., Mazor, Y., Efrat, S. & Gazit, E. (2004) Inhibition of Islet Amyloid Polypeptide Fibril Formation: A Potential Role for Heteroaromatic Interactions, *Biochemistry.* **43**, 14454-14462.
278. Tenidis, K., Waldner, M., Bernhagen, J., Fischle, W., Bergmann, M., Weber, M., Merkle, M.-L., Voelter, W., Brunner, H. & Kapurniotu, A. (2000) Identification of a penta- and hexapeptide of islet amyloid polypeptide (IAPP) with amyloidogenic and cytotoxic properties, *J Mol Biol.* **295**, 1055-1071.
279. Westermark, P., Engström, U., Johnson, K. H., Westermark, G. T. & Betsholtz, C. (1990) Islet amyloid polypeptide: pinpointing amino acid residues linked to amyloid fibril formation, *Proc Natl Acad Sci USA.* **87**, 5036-5040.
280. Padrick, S. B. & Miranker, A. D. (2001) Islet amyloid polypeptide: identification of long-range contacts and local order on the fibrillogenesis pathway, *J Mol Biol.* **308**, 783-94.
281. Williamson, J. A., Loria, J. P. & Miranker, A. D. (2009) Helix stabilization precedes aqueous and bilayer-catalyzed fiber formation in islet amyloid polypeptide, *J Mol Biol.* **393**, 383-96.
282. Caillon, L., Duma, L., Lequin, O. & Khemtemourian, L. (2014) Cholesterol modulates the interaction of the islet amyloid polypeptide with membranes, *Mol Membr Biol.* **31**, 239-49.
283. Janson, J., Ashley, R. H., Harrison, D., McIntyre, S. & Butler, P. C. (1999) The mechanism of islet amyloid polypeptide toxicity is membrane disruption by intermediate-sized toxic amyloid particles, *Diabetes.* **48**, 491-498.
284. Guo, C., Cote, S., Mousseau, N. & Wei, G. (2015) Distinct helix propensities and membrane interactions of human and rat IAPP(1-19) monomers in anionic lipid bilayers, *J Phys Chem B.* **119**, 3366-76.
285. Zhang, T. O., Buchanan, L. E. & Zanni, M. T. (2014) Insights into amylin aggregation by 2D IR spectroscopy, *Biomedical Spectroscopy and Imaging.* **3**, 189-196.

286. Milton, N. G. & Harris, J. R. (2013) Fibril formation and toxicity of the non-amyloidogenic rat amylin peptide, *Micron.* **44**, 246-53.
287. Götz, J., Lim, Y.-A. & Eckert, A. (2013) Lessons from two prevalent amyloidoses—what amylin and Aβ have in common, *Front Aging Neurosci.* **5**, 38.
288. Yan, L.-M., Velkova, A. & Kapurniotu, A. (2014) Molecular characterization of the hetero-assembly of β-amyloid peptide with islet amyloid polypeptide, *Curr Pharm Des.* **20**, 1182-1191.

# 8 Appendices

## 8.1 Appendix A: Executive summary

**Executive summary of additional published works**

The articles summarized below were written and published in peer-reviewed journals during the course of the predoctoral period. As the articles do not pertain directly to completion of the dissertation work but were essential in my research and professional development, they are summarized here below the full citation for the papers.

> Gerben, S. R., Lemkul, J. A., **Brown, A. M**., and Bevan, D. R. (2013) "Comparing atomistic molecular mechanics force fields for a difficult target: a case study on the Alzheimer's amyloid β-peptide." *J. Biomol. Struct. Dyn.* **32** (11),1-16.

Molecular simulation methods can augment experimental techniques to understand misfolding and aggregation pathways with atomistic resolution, but the reliability of these predictions is a function of the parameters used for the simulation. This study sought to comparatively assess various force fields (AMBER03, CHARMM22 + CMAP, GROMOS96 53A6, GROMOS96 54A7, and OPLS-AA) on the secondary structure of Aβ. Herein, it was determined that the GROMOS96 53A6 force field best simulated Aβ as compared to experimental results. My role in this study consisted of aiding in analysis methods utilized and drawing conclusions based on data. I performed secondary structure and clustering analysis and aiding in manuscript completion. I was involved in reviewing and editing the full manuscript before and during the review process. This paper is the most relevant to my primary research of all the papers included in the appendices, given that it provided a solid argument for force field selection for my simulations and gave me confidence in the simulated Aβ structures, as related to secondary structure changes.

> Congdon, M.D., Kharel, Y., **Brown, A.M**., Lewis, S.N., Thorpe, S.B., Bevan, D.R., Lynch, K.R., and Santos, W. L. "Structure-activity relationship studies and molecular modeling of naphthalene-based sphingosine kinase 2 inhibitors" *J. Med. Chem. Letters.*

This publication sought to determine the structure-activity relationship between naphthalene-based inhibitors and sphingosine kinase 2 (SphK2). In addition, determination of key residues for binding specificity in SphK2 was achieved. This is a collaborative project where I performed part of the homology modeling and analysis of the SphK2 structure, the molecular docking on compounds into SphK2, and assessed key residues for binding specificity. This project did not include MD simulations, but increased my skill set in various computational techniques and provided solid foundation for utilized computational techniques in drug design. I was involved in reviewing and editing the full manuscript before and during the review process.

> Miller, D.V., **Brown, A.M.,** Xu, H., Bevan, D.R., and White, R.H. (2015) "Elucidating the Role of a Conserved Cysteine in Adenine Deaminase." *Proteins: Structure, Function, and Bioinformatics.*

This study centered around characterization of the previously uncharacterized adenine demaminase (Ade) and hypoxanthine/guanine phosphoribosyltransferasest and their involvement in purine salvage in *Methanocaldococcus jannaschii*. A conserved cysteine (C127, *M. jannaschii* numbering) was examined due to its high conservation in bacterial and archaeal homologues. To assess the role of this highly conserved cysteine in *M. jannaschii* Ade, site directed mutagenesis and molecular dynamics simulations were performed. Detailed molecular docking and dynamics studies revealed adenine was unable to properly orient in the active site in the C127A and C127S Ade model, giving insight into the role of the conserved cysteine in maintaining active site structure. I performed all molecular dynamics simulations and analysis, in addition to providing insight and analysis to homology modeling and molecular docking results. I was involved in writing, reviewing, and editing the full manuscript before and during the review process.

## 8.2 Appendix B: Input files for MD simulations

### 8.2.1 Isochoric-isothermal ensemble (NVT) – Peptide in Solution

```
title       = NVT equilibration
define      = -DPOSRES  ; position restrain the protein
; Run parameters
integrator  = md        ; leap-frog integrator
nsteps      = 50000     ; 2 * 50000 = 100 ps
dt      = 0.002     ; 2 fs
; Output controli
nstxout     = 5000      ; save coordinates every 0.2 ps
nstvout     = 5000      ; save velocities every 0.2 ps
nstenergy   = 5000      ; save energies every 0.2 ps
nstlog      = 5000      ; update log file every 0.2 ps
; Bond parameters
continuation    = no        ; first dynamics run
constraint_algorithm = lincs    ; holonomic constraints
constraints = all-bonds ; all bonds (even heavy atom-H bonds) constrained
lincs_iter  = 1     ; accuracy of LINCS
lincs_order = 4     ; also related to accuracy
```

```
; Neighborsearching
ns_type     = grid      ; search neighboring grid cells
nstlist     = 5     ; 10 fs
rlist       = 0.9       ; short-range neighborlist cutoff (in nm)
rcoulomb    = 0.9       ; short-range electrostatic cutoff (in nm)
rvdw        = 1.4       ; short-range van der Waals cutoff (in nm)
; Electrostatics
coulombtype = PME       ; Particle Mesh Ewald for long-range electrostatics
pme_order   = 4     ; cubic interpolation
fourierspacing  = 0.16      ; grid spacing for FFT
; Temperature coupling is on
tcoupl      = V-rescale ; modified Berendsen thermostat
tc-grps     = Protein Non-Protein   ; two coupling groups - more accurate
tau_t       = 0.1   0.1 ; time constant, in ps
ref_t       = 310   310 ; reference temperature, one for each group, in K
; Pressure coupling is off
pcoupl      = no        ; no pressure coupling in NVT
; Periodic boundary conditions
pbc     = xyz       ; 3-D PBC
; Dispersion correction
DispCorr    = EnerPres  ; account for cut-off vdW scheme
; Velocity generation
gen_vel     = yes       ; assign velocities from Maxwell distribution
gen_temp    = 310       ; temperature for Maxwell distribution
gen_seed    = -1        ; generate a random seed
```

### 8.2.2 Isochoric-isothermal ensemble (NVT) – Peptide-Membrane System for GROMOS53A6 Force Field

```
Title       = NPT simulation for a protein+membrane
cpp     = /usr/bin/cpp
define      = -DPOSRES -DPOSRES_LIPID
; Run parameters
integrator  = md
dt          = 0.002
nsteps      = 50000     ; 100 ps
nstcomm     = 1
; Output parameters
nstxout     = 0
nstvout     = 0
nstfout     = 0
nstlog      = 1000
nstenergy   = 1000
; Bond parameters
constraint_algorithm    = lincs
constraints             = all-bonds
continuation            = no        ; starting up
; Twin-range cutoff scheme, parameters for Gromos96
nstlist     = 5
ns_type     = grid
rlist       = 1.2
```

```
rcoulomb    = 1.2
rvdw        = 1.2
; PME electrostatics parameters
coulombtype = PME
fourierspacing  = 0.12
fourier_nx  = 0
fourier_ny  = 0
fourier_nz  = 0
pme_order   = 4
ewald_rtol  = 1e-5
optimize_fft    = yes
; Berendsen temperature coupling is on in three groups
Tcoupl      = Berendsen
tc_grps     = Protein POPC_SM_CHOL  SOL_NA_CL
tau_t       = 0.1 0.1 0.1
ref_t       = 100 100 100
; Pressure coupling is not on
Pcoupl      = no
; Generate velocities is on
gen_vel     = yes
gen_temp    = 100
gen_seed    = -1
; Periodic boundary conditions are on in all directions
pbc     = xyz
; Long-range dispersion correction
DispCorr    = EnerPres
```

### 8.2.3 Isochoric-isothermal ensemble (NVT) – Peptide-Membrane System for GROMOS53A6 Force Field

```
title       =  NPT equilibration
define      = -DPOSRES  ; position restrain the protein
; Run parameters
integrator  = md        ; leap-frog integrator
nsteps      = 50000     ; 2 * 50000 = 100 ps
dt      = 0.002     ; 2 fs
; Output control
nstxout     = 5000      ; save coordinates every 0.2 ps
nstvout     = 5000      ; save velocities every 0.2 ps
nstenergy   = 5000      ; save energies every 0.2 ps
nstlog      = 5000      ; update log file every 0.2 ps
; Bond parameters
continuation    = yes       ; Restarting after NVT
constraint_algorithm = lincs    ; holonomic constraints
constraints = all-bonds ; all bonds (even heavy atom-H bonds) constrained
lincs_iter  = 1     ; accuracy of LINCS
lincs_order = 4     ; also related to accuracy
; Neighborsearching
ns_type     = grid      ; search neighboring grid cells
nstlist     = 5     ; 10 fs
```

```
rlist       = 0.9       ; short-range neighborlist cutoff (in nm)
rcoulomb    = 0.9       ; short-range electrostatic cutoff (in nm)
rvdw        = 1.4       ; short-range van der Waals cutoff (in nm)
; Electrostatics
coulombtype = PME       ; Particle Mesh Ewald for long-range electrostatics
pme_order   = 4     ; cubic interpolation
fourierspacing  = 0.16      ; grid spacing for FFT
; Temperature coupling is on
tcoupl      = V-rescale ; modified Berendsen thermostat
tc-grps     = Protein Non-Protein   ; two coupling groups - more accurate
tau_t       = 0.1   0.1 ; time constant, in ps
ref_t       = 310   310 ; reference temperature, one for each group, in K
; Pressure coupling is on
pcoupl      = Parrinello-Rahman ; Pressure coupling on in NPT
pcoupltype  = isotropic ; uniform scaling of box vectors
tau_p       = 2.0       ; time constant, in ps
ref_p       = 1.0       ; reference pressure, in bar
compressibility = 4.5e-5    ; isothermal compressibility of water, bar^-1
refcoord_scaling = com
; Periodic boundary conditions
pbc     = xyz       ; 3-D PBC
; Dispersion correction
DispCorr    = EnerPres  ; account for cut-off vdW scheme
; Velocity generation
gen_vel     = no        ; Velocity generation is off
```

### 8.2.4 Isothermal-isobaric ensemble (NPT) – Peptide-Membrane System for GROMOS53A6 Force Field

```
title       = NPT simulation for a protein+membrane
define      = -DPOSRES
; Run parameters
integrator  = md
dt          = 0.002
nsteps      = 500000        ; 1000 ps (1 ns)
nstcomm     = 1
refcoord_scaling = com
; Output parameters
nstxout     = 50000
nstvout     = 50000
nstfout     = 50000
nstlog      = 5000
nstenergy   = 5000
; Bond parameters
constraint_algorithm    = lincs
constraints             = all-bonds
continuation            = yes       ; continuing from annealing
; Twin-range cutoff scheme, parameters for Gromos96
nstlist     = 5
ns_type     = grid
rlist       = 1.2
```

```
rcoulomb    = 1.2
rvdw        = 1.2
; PME electrostatics parameters
coulombtype     = PME
fourierspacing  = 0.12
fourier_nx      = 0
fourier_ny      = 0
fourier_nz      = 0
pme_order       = 4
ewald_rtol      = 1e-5
optimize_fft    = yes
; Berendsen temperature coupling is on in three groups
Tcoupl      = Nose-Hoover
tc_grps     = Protein POPC_SM_CHOL  SOL_NA_CL
tau_t       = 1.0 1.0 1.0
ref_t       = 310 310 310
; Pressure coupling is on
Pcoupl      = Parrinello-Rahman
pcoupltype  = semiisotropic
tau_p       = 2.0
compressibility = 4.5e-5 4.5e-5
ref_p       = 1.0 1.0
; Generate velocities is off
gen_vel     = no
; Periodic boundary conditions are on in all directions
pbc     = xyz
; Long-range dispersion correction
DispCorr    = EnerPres
```

### 8.2.5 Production MD – Peptide in Solution for GROMOS53A6 Force Field

```
title       =  MD equilibration
; Run parameters
integrator  = md        ; leap-frog integrator
nsteps      = 12500000  ; 2 * 50000 = 100 ps
dt      = 0.002     ; 2 fs
; Output control
nstxout     = 0     ; save coordinates every 0.2 ps
nstvout     = 0     ; save velocities every 0.2 ps
nstenergy   = 5000      ; save energies every 0.2 ps
nstlog      = 5000      ; update log file every 0.2 ps
nstxtcout   = 5000      ; frame every 10 ps
; Bond parameters
continuation    = yes       ; Restarting after NVT
constraint_algorithm = lincs    ; holonomic constraints
constraints = all-bonds ; all bonds (even heavy atom-H bonds) constrained
lincs_iter  = 1     ; accuracy of LINCS
lincs_order = 4     ; also related to accuracy
; Neighborsearching
ns_type     = grid      ; search neighboring grid cells
```

```
nstlist     = 5     ; 10 fs
rlist       = 0.9       ; short-range neighborlist cutoff (in nm)
rcoulomb    = 0.9       ; short-range electrostatic cutoff (in nm)
rvdw        = 1.4       ; short-range van der Waals cutoff (in nm)
; Electrostatics
coulombtype = PME       ; Particle Mesh Ewald for long-range electrostatics
pme_order   = 4     ; cubic interpolation
fourierspacing  = 0.16      ; grid spacing for FFT
; Temperature coupling is on
tcoupl      = V-rescale ; modified Berendsen thermostat
tc-grps     = Protein Non-Protein   ; two coupling groups - more accurate
tau_t       = 0.1   0.1 ; time constant, in ps
ref_t       = 310   310 ; reference temperature, one for each group, in K
; Pressure coupling is on
pcoupl      = Parrinello-Rahman ; Pressure coupling on in NPT
pcoupltype  = isotropic ; uniform scaling of box vectors
tau_p       = 2.0       ; time constant, in ps
ref_p       = 1.0       ; reference pressure, in bar
compressibility = 4.5e-5    ; isothermal compressibility of water, bar^-1
; Periodic boundary conditions
pbc     = xyz       ; 3-D PBC
; Dispersion correction
DispCorr    = EnerPres  ; account for cut-off vdW scheme
; Velocity generation
gen_vel     = no        ; Velocity generation is off
```

### 8.2.6 Production MD – Peptide-Membrane System for GROMOS53A6 Force Field

```
title       = NPT simulation for a membrane protein
; Run parameters
integrator  = md
dt          = 0.002
tinit       = 0
nsteps      = 12500000      ; 25000 ps (25 ns)
nstcomm     = 1
refcoord_scaling = com
; Output parameters
nstxout     = 0
nstvout     = 0
nstfout     = 0
nstlog      = 5000
nstenergy   = 5000
nstxtcout   = 5000
; Bond parameters
constraint_algorithm    = lincs
constraints         = all-bonds
continuation            = yes       ; continuing from annealing
; Twin-range cutoff scheme, parameters for Gromos96
nstlist     = 5
```

```
ns_type     = grid
rlist       = 1.2
rcoulomb    = 1.2
rvdw        = 1.2
; PME electrostatics parameters
coulombtype     = PME
fourierspacing  = 0.12
fourier_nx  = 0
fourier_ny  = 0
fourier_nz  = 0
pme_order   = 4
ewald_rtol  = 1e-5
optimize_fft    = yes
; Berendsen temperature coupling is on in three groups
Tcoupl      = Nose-Hoover
tc_grps     = Protein POPC_SM_CHOL  SOL_NA_CL
tau_t       = 1.0 1.0 1.0
ref_t       = 310 310 310
; Pressure coupling is on
Pcoupl      = Parrinello-Rahman
pcoupltype  = semiisotropic
tau_p       = 2.0
compressibility = 4.5e-5 4.5e-5
ref_p       = 1.0 1.0
; Generate velocities is off
gen_vel     = no
; Periodic boundary conditions are on in all directions
pbc     = xyz
; Long-range dispersion correction
DispCorr    = EnerPres
```